Properties of Stripe Phases in Transition Metal Oxides

Marcin Raczkowski

Ph.D. Thesis
under the supervision of
Prof. dr. Andrzej M. Oleś
Prof. dr. Raymond Frésard

JAGELLONIAN UNIVERSITY
Marian Smoluchowski Institute of Physics
Condensed Matter Theory Department

UNIVERSITE DE CAEN
BASSE–NORMANDIE
Laboratoire de Cristallographie
et Sciences des Matériaux
Crismat-ENSICAEN

KRAKÓW, May 2005

Abstract

Stripe phases are common complex phases encountered in doped nickelates and cuprates. They are characterized by the combined spin and charge modulation, with periodicity decreasing upon doping down to saturation. The orientation and filling of domain walls differ from cuprates to nickelates but the microscopic reasons of the observed differences remain unsettled. In this Thesis we show that the stripe phases depend significantly on strong electron correlations typical of these compounds. By determining phase diagrams of the extended one-band Hubbard model, relevant for the cuprates, and of the two-band Hubbard model, appropriate for the nickelates, we show that the location of the proper stripe phase in the phase diagram corresponds in each case to the parameter regime relevant for the studied compounds. In particular, it is shown that the filled diagonal stripe phases observed in the nickelates are a generic feature of the model with two e_g electrons. In contrast, an adequate description of the half-filled vertical stripes in the cuprates involves a proper treatment of strong electron correlations in the t-t'-U model.

Contents

Acknowledgments

First of all, I would like to thank both my supervisors, Profs. Andrzej M. Oleś and Raymond Frésard, for their enthusiasm and many inspiring ideas that were an essential ingredient for this Thesis.

Prof. Andrzej M. Oleś inspired and guided much of the work presented here. I also owe him my thanks for the critical reading of the manuscript. His relentless effort enabled me to weed out some inconsistencies and to polish the writing.

It is my pleasure to acknowledge a close collaboration with Prof. Raymond Frésard. I enjoyed much our physics discussions and consider them as some of the most fun and interesting parts of my Ph.D. studies. Without his great advice and suggestions, this Thesis could not have been accomplished. On top, I thank him for being much more than a host during my stay in Caen.

I am grateful to Prof. Józef Spałek, head of Condensed Matter Theory Department in the Institute of Physics at the Jagellonian University, for being the main force behind the development of a powerful computer cluster, on which the overwhelming majority of calculations was carried out. Additionally, I thank my colleague Edward M. Görlich for installing and maintaining the cluster software.

I am greatly indebted to Profs. Bernard Raveau and Antoine Maignan, former and present head of Laboratoire de Cristallographie et Sciences des Matériaux CRISMAT, who gave me the opportunity to work in Caen.

I also wish to thank Prof. Charles Simon for being a co-ordinator of my Marie Curie fellowship.

During my stay in Caen I enjoyed the company of many good friends. In particular, I would like to mention Sylvie Hébert, Silvana Mercone, Jacques Noudem, Michaël Pollet, and Joseph Scola, together with whom I laughed at physics, physicists and life in general. Special thanks go to Delphine Flahaut and Yannic Klein who explained to me that French is easy once you know how to read French words.

This Thesis was financially supported by a Marie Curie fellowship of the European Community program under number HPMT2000-141. Further, I acknowledge financial support from the Polish State Committee of Scientific Research (KBN) under Projects No. 5 P03B 055 20, 5 P03B 036 21, and 1 P03B 068 26.

Kraków, May 2005 Marcin Raczkowski

Chapter 1

Introduction

'Good order is the foundation of all things.'
Edmund Burke (1729 - 1797), Irish philosopher

Interest in transition-metal oxides has never been restricted to the most spectacular phenomenon of the high-T_c superconductivity, but also concerns, *inter alia*, metal-insulator transitions, colossal magnetoresistance, and orbital ordering [1, 2]. Recent progress in this field has been made possible by the development of various novel experimental techniques, sophisticated theoretical methods, and new physical concepts. In particular, charge localization and the tendency of doped holes towards self-organization into stripped patterns is one of the most interesting current topics in the physics of strongly correlated electron systems and fascinates not only as an exceptional phenomenon but also offers a framework for interpreting a broad range of experimental results [3, 4].

The stripe instability was predicted on the basis of Hartree-Fock (HF) calculations before their experimental confirmation, in the two-band model for CuO_2 planes of layered $La_{2-x}Sr_xCuO_4$ (LSCO), including $Cu(3d_{x^2-y^2})$ and $O(2p_{x(y)})$ states [5], as well as in the effective single-band Hubbard model [6–9]. These calculations yielded solutions with a phase separation manifested in formation of nonmagnetic lines of holes, one-dimensional (1D) domain walls or stripes, which separate antiferromagnetic (AF) domains of opposite phases. Such states result from the competition between the superexchange interaction, which stabilize the AF long-range order in the parent Mott insulator, and the kinetic energy of doped holes. Indeed, the magnetic energy is gained when electrons occupy the neighboring sites and their spins order as in the Néel state, whereas the kinetic energy is gained when the holes can move and the AF order is suppressed along a domain wall (DW) . Thus, a stripe phase provides the best compromise between the AF order and the kinetic energy of doped holes.

However, the debate on the microscopic origin of the stripe instability is far from closed. Two main scenarios, based on a Ginzburg-Landau free energy, for the driving mechanism of the stripe phase have been discussed [10, 11]. In the first one, stripes are charge-density waves with large periodicity arising from the Fermi surface instability with the transition being spin driven [5]. A general feature of such an instability is a gap/pseudogap precisely on the Fermi surface. Hence, the spacing between DWs is equal to $1/x$, with x denoting doping level so as to maintain a gap/pseudogap on the Fermi surface. In this scenario spin and charge order occur at the same temperature or charge stripe order sets in only after spin order has developed.

An alternative scenario comes from the Coulomb-frustrated phase separation suggesting that stripe formation is commonly charge driven. Indeed, using the Ising model, it has been shown that competition between long range Coulomb interactions and short range attraction between holes leads to formation of stripes [12]. In this case Ginzburg-Landau considerations lead to an onset of charge order prior to spin order as the temperature is lowered, supported by the experimental findings in $La_{2-x-y}Nd_ySr_xCuO_4$ (Nd-LSCO) [13] and $La_{2-x}Sr_xNiO_4$ (LSNO) [14, 15]. However, the above analysis does not take into account spin fluctuations which might be crucial for the nature of the phase transition by precluding the spins from ordering at the charge-order temperature [16]. Moreover, the conjecture that long range Coulomb forces are required to stabilize stripe phases has been challenged by the studies of the t-J model, in which the DW structures were obtained without such interactions [17].

This Thesis is mainly concerned with stability and properties of stripe phases in two-dimensional (2D) LSCO and in isostructural LSNO. With increasing doping x, LSCO very quickly undergoes a transition from an AF insulator to a paramagnetic (PM) metal in which a superconducting phase occurs for somewhat higher doping at low temperatures. Conversely, LSNO remains an insulator up to large hole concentrations $x \simeq 1$ [1]. Therefore, it is particularly surprising that in spite of these differences, stripe phases appear in both compounds. However, despite intense theoretical studies over the last decade as well as accumulating experimental evidence on the properties of these compounds, many questions concerning formation of DWs remain unsettled. First of all, one would like to understand the microscopic reasons of the observed differences, between the cuprates and nickelates, in the filling of DWs. In Nd-LSCO [13, 18–22] and LSCO [23], one finds the so-called *half-filled* stripes, with the density of one doped hole per two atoms along DWs. In contrast, it is clear from variety of experiments that magnetic states within doped NiO_2 planes of the nickelates are the *filled* stripes with density of one doped hole per one atom in a DW [14, 15, 24–29].

The question of filling is not the only difference between the nickelate and the cuprate stripes, however. Neutron diffraction measurements performed on Nd-LSCO revealed that magnetic peaks are displaced from the AF maximum at $\mathbf{Q}_{AF} = (\pi, \pi)$ to the points $\mathbf{Q}_s = \pi(1 \pm 2\epsilon, 1)$ and $\mathbf{Q}_s = \pi(1, 1 \pm 2\epsilon)$ and the shift ϵ depends linearly on hole doping $\epsilon \simeq x$ for $x < 1/8$, while it is almost constant at higher doping. These values correspond to a superposition of *vertical* (01) and *horizontal* (10) DWs. The essentially identical modulation and doping dependence of ϵ was observed in superconducting crystals of LSCO with $x > 0.05$. Conversely, experiments on LSNO established that spin order is characterized by the wave vectors $\mathbf{Q}_s = \pi(1 \pm \epsilon, 1 \pm \epsilon)$ with $\epsilon \simeq x$ for $x < 1/3$, corresponding to a constant charge of one hole/Ni ion along a *diagonal* DW, in agreement with HF predictions made in the pioneering works [5–9].

Several methods have been employed to investigate the stripe phases which go beyond the HF approximation, such as: Density Matrix Renormalization Group (DMRG) [17, 30], Slave-Boson Approximation (SBA) [31–33], variational local ansatz approximation [34], Exact Diagonalization (ED) of finite clusters [35], analytical approach based on variational trial wave function within the string picture [36], Dynamical Mean Field Theory (DMFT) [37], Cluster Perturbation Theory (CPT) [38], and Quantum Monte Carlo (QMC) [39, 40]. They all address the crucial role of local electron correlations in stabilizing of the half-filled stripe phases in the cuprates. In spite of this huge effort, it remains unclear whether DWs are centered on rows of metal atoms, hereafter named site-centered (SC) stripes, or if they are centered on rows of oxygen atoms bridging the two neighboring metal sites, the so-called bond-centered (BC) stripes.

Although no clear evidence was presented as yet, it seems that the degeneracy of $3d$ orbitals might play a role in stabilizing filled stripes in the nickelates. In the simplest picture for the cuprates, the Cu^{3+} ions forming DWs are spinless, while the Cu^{2+} of the AF domains carry spin $S = 1/2$. In the nickelates, filled DWs are formed of the Ni^{3+} ions ($S = 1/2$), whereas the AF domains consist of Ni^{2+} ions ($S = 1$). Therefore, a realistic Hamiltonian for LSNO has to contain, besides the $|x^2 - y^2\rangle$ orbital usually included in the cuprate oxide models, the $|3z^2 - r^2\rangle$ orbital at each ion, so as to account for the high spin state ($S = 1$) in the stoichiometric compound.

The main purpose of the present study is to investigate formation of both SC and BC stripe phases in either CuO_2 plane for the superconducting cuprates or NiO_2 plane for the insulating nickelates, using a *realistic* effective Hamiltonians. For stable phases we determine charge and magnetization densities, double occupancy, kinetic and magnetic energies, and investigate the role of a finite electron-lattice coupling. The stability of stripe phases is related to their electronic structure and it is studied within the Hartree Approximation (HA) and the SBA. Our studies should provide the microscopic reasons for the observed differences, between the cuprates and the nickelates as well as in the filling of the DWs in both systems. In addition, we will also investigate the role of the second orbital for the relative stability of stripe phases in the nickelates.

1.1 Outline of the Thesis

The structure of the Thesis is as follows. In Chapter 2 we review briefly the current literature on stripe phases both in the cuprates and the nickelates, as well as discuss the most prominent theoretical and experimental findings.

Chapter 3 starts with a discussion of the so-called solitonic mechanism responsible for the robust stability of DWs. Next using the HA, we investigate relative stability of filled stripes within the 2D Hubbard model with anisotropic nearest-neighbor hopping t. We also discuss changes in the stability of such phases in the extended Hubbard model due to both the next-neighbor hopping t' and the nearest-neighbor Coulomb interaction V, as well as to the lattice degrees of freedom i.e., induced by the static Peierls electron-lattice coupling. Next, we attempt to stabilize the half-filled stripe phase involving an on-wall spin-density wave (SDW) in the t-t'-U model. Finally, we compare static hole-hole and spin-spin correlation functions for the considered stripes.

Chapter 4 begins with an introduction to the spin-rotation-invariant slave-boson (SRI SB) representation of the Hubbard model. We then describe reciprocal space representation which is based on the stripe periodicity and provides a possibility to perform calculations on large (up to 144×144) clusters. Further, we investigate the stability of filled and half-filled stripes in the t-t'-U model. We also examine the effect of a proper treatment of strong electrons correlations by comparing the slave-boson (SB) charge and spin density profiles with the ones obtained in the HA. Next, we perform systematic studies of an array of stripe phases with a different length of the unit cell which enables us to establish the behavior of the incommensurability ϵ, optimal stripe filling ν, the chemical potential μ, as well as the density of states (DOS) as a function of doping. Finally, we analyze the melting of stripe phases in the overdoped regime $x \geq 0.3$ and show that the spin and charge order disappear simultaneously.

Chapter 5 deals with systems with orbital degeneracy such as layered nickelates or manganites. In Section 5.1 we introduce a *realistic model* with the e_g electrons and next, in Section 5.2, we solve exactly a two-site molecule with either e_g or t_{2g} orbitals at quarter-filling in order to get more insight into the role of orbital degeneracy in possible magnetic and orbital instabilities. Furthermore, in Section 5.3, we determine a phase diagram of the model in the HA and compare our results with the previous ED solutions. In particular, we address the occurrence of orbitally polarized states due to the inequivalent orbitals, and their interplay with FM and AF spin order. We also discuss the role played by the Hund's exchange coupling J_H and by the crystal field orbital splitting E_z in stabilizing one of the competing phases. Finally, in Section 5.4, we shall investigate the behavior of ϵ, ν, and μ in the stripe ground state, similarly as we have done in Chapter 4 within the single-band Hubbard model for the cuprates. For this purpose we use the HA and show that the filled diagonal BC stripes observed in the nickelates appear naturally within the effective model for the e_g electrons, whereas a simplified equivalent band model, i.e., doubly degenerated Hubbard (DDH) model, fails to reproduce the experimental data. Finally, we summarize our results in Chapter 6 which also includes an outlook for possible future research.

Chapter 2

Experimental signatures of stripes

Experimentally, stripe phases are most clearly detected in insulating compounds with a static stripe order, but there is growing evidence of fluctuating stripe correlations in metallic and superconducting materials.

The most direct evidence for stripe phases in doped antiferromagnets has come from neutron scattering studies in which charge and spin modulations are identified by the appearance of some extra incommensurate (IC) Bragg peaks. The positions of such superstructure peaks provide information about the spatial period and orientation of the modulation. In fact, neutrons do not scatter from charge incommensurations directly, but instead are sensitive to nuclear displacements induced by the charge modulation. The lattice modulation is also measurable with electron and x-ray diffraction. However, sometimes appropriate crystals for such experiments are not available and one has to resort to other methods capable of probing local order. These methods include nuclear magnetic resonance (NMR), nuclear quadruple resonance (NQR), muon spin rotation (μSR), scanning tunneling microscopy (STM), and transmission electron microscopy (TEM) [41]. Furthermore, angle-resolved photoemission spectroscopy (ARPES), angle-integrated photoemission spectroscopy (AIPES), as well as x-ray photoemission (XPS) and ultraviolet photoemission (UPS) spectroscopies all provide an essential information about conspicuous changes in the electronic structure when stripes set in [42]. Finally, a distinct imprint of the 1D spin-charge modulation on transport properties should be detectable as the in-plane anisotropy of the resistivity and the Hall coefficient R_H.

2.1 Cuprates

The abundance of the current evidence on various types of stripe order as well as the recent ARPES results on the spectral weight of the cuprate superconductors is contained in a few available review articles [41, 42]. Historically, the first compelling evidence for both magnetic and charge order in the cuprates, was accomplished in a neodymium codoped compound $La_{2-x-y}Nd_ySr_xCuO_4$. For

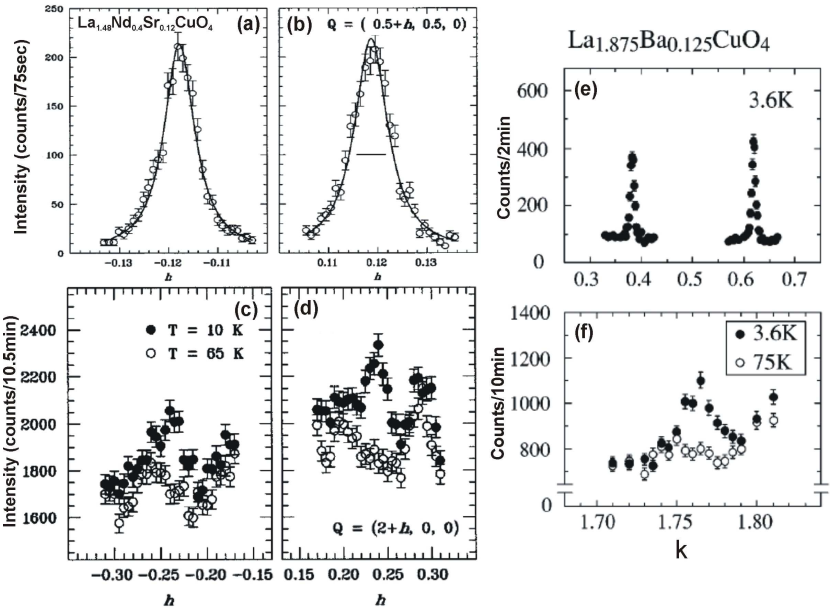

Figure 2.1: IC magnetic (a,b) and charge peaks (c,d) in $La_{1.6-x}Nd_{0.4}Sr_xCuO_4$ at $x = 0.12$, after Ref. 18. Right panels show analogous IC magnetic (e) and charge (f) peaks in $La_{2-x}Ba_xCuO_4$ at $x = 1/8$, after Ref. 47. In both compounds, appearance of static stripes is associated with the low-temperature tetragonal (LTT) structural distortion.

$y = 0.4$ and $x = 0.12$, Tranquada *et al.* [13] found that the magnetic scattering is not characterized by the 2D AF wave vector $(1/2, 1/2)$ [1], but by IC peaks at the wave vectors $(1/2 \pm \epsilon, 1/2)$ with $\epsilon = 0.118$, as depicted in Fig. 2.1 (a,b). Moreover, inspired by the pioneering works suggesting that the staggered magnetization undergoes a phase shift of π at the charge DWs [5–9], the authors found additional charge order peaks that split by $(\pm 2\epsilon, 0)$ about a fundamental Bragg peak such as $(2, 0)$, precisely at the expected position $2\epsilon = 0.236$ [*cf.* Fig. 2.1 (c,d)]. Unfortunately, in an early study, Tranquada *et al.* [19] detected only magnetic IC peaks at higher doping levels $x = 0.15$ and $x = 0.2$. However, systematic NQR studies of Nd-LSCO suggest indeed the presence of charge stripe order throughout the entire superconducting region $0.07 \leq x \leq 0.25$ [21]. Also in a more recent study, both charge and spin superlattice peaks at $x = 0.15$ were recently found in the neutron diffraction experiments by Wakimoto *et al.* [22].

In fact, the reason why static stripes could be detected in this compound is a structural transition from the low temperature orthorhombic (LTO) to the low temperature tetragonal (LTT) phase, induced by the substitution for La ions by isovalent Nd ions. This, in turn, provides a pinning potential for dynamic stripes and stabilizes the charge order. Evidence of a similar pinning potential has also

---

[1] For convenience, throughout Chapter 2 we follow the convention used in experiments.

been found both in the μSR and NQR studies of $La_{2-x-y}Eu_ySr_xCuO_4$ (Eu-LSCO) with $y \simeq 0.2$ [43, 44]. Moreover, the connection between the LTT phase and the appearance of charge and spin stripe order has been clearly demonstrated both in the neutron scattering and x-ray diffraction studies on $La_{2-x-y}Ba_ySr_xCuO_4$ (Ba-LSCO) with $y = 1/8$ [45, 46]. Finally, static IC charge $(2 \pm 2\epsilon, 0)$ and magnetic $(1/2 \pm \epsilon, 1/2)$ peaks have been detected within the LTT phase of $La_{2-x}Ba_xCuO_4$ (LBCO) with $x = 1/8$ [47]. Note that the position of the peaks and the established incommensurability $\epsilon = 0.118$ are exactly the same as those obtained by Tranquada *et al.* [18] for Nd-LSCO. Notably, the charge order peaks always appear at somewhat higher temperature than the magnetic ones, indicating that the stripe order is driven by the charge instability.

Let us now discuss the experimental evidence of slowly fluctuating stripes in $La_{2-x}Sr_xCuO_4$. The main difference between the Ba and Sr codoped system is the fact that the latter undergoes a structural phase transition from the high-temperature tetragonal (HTT) phase to the LTO phase. As a consequence, in the superconducting regime $x \geq 0.06$, the LSCO system exhibits purely *dynamic* magnetic correlations which give rise to IC peaks at the wave vector $(1/2 \pm \epsilon, 1/2)$ specified in tetragonal lattice units $2\pi/a_{tetra}$. In seminal inelastic neutron scattering studies, Yamada *et al.* [23] established a remarkably simple relation $\epsilon \simeq x$ for $0.06 \leq x \leq 0.12$ with a lock-in effect at $\epsilon \simeq 1/8$ for larger x.

In contrast, in the insulating spin-glass regime of LSCO $x \leq 0.055$, quasielastic neutron scattering experiments with the main weight at zero frequency demonstrate that IC magnetic peaks are located at the wave vectors $(1/2 \pm \epsilon/\sqrt{2}, 1/2 \pm \epsilon/\sqrt{2})$ [48–50]. This phenomenon has often been interpreted as the existence of static diagonal stripes, even though no signatures of a charge modulation were observed. Another possible explanation is formation of a short ranged spiral order as its chirality also breaks the translational symmetry of the square lattice by a clockwise or anticlockwise twist [51]. Remarkably, even though the spin modulation changes from a diagonal to vertical/horizontal one to Cu-O bonds at x around 0.06, ϵ follows the doping x reasonably well over the entire range $0.03 \leq x \leq 0.12$, as shown in Fig. 2.2. In fact, just for $x = 0.06$, both diagonal ($\epsilon = 0.053$) and vertical/horizontal ($\epsilon = 0.049$) IC spin modulations have been found to coexist [50]. In a stripe model this corresponds to a constant density of 0.5 (0.7) holes per Cu atom in the DWs in the vertical/horizontal (diagonal) stripe phases, respectively, because of the difference in Cu spacings in the two geometries, i.e., $a_{ortho} = \sqrt{2}a_{tetra}$. In contrast, in the narrow region $0.02 \leq x \leq 0.024$, IC magnetic peaks are located at the wave vector $(1/2 \pm \epsilon/2, 1/2 \pm \epsilon/2)$ with $\epsilon \simeq x$ corresponding to a constant charge of one hole/Cu ion along a diagonal DW [52–54]. However, below $x = 0.02$, this does not hold anymore and the incommensurability gets locked with the value $\epsilon \simeq 0.014$ [54].

Unfortunately, any concomitant charge ordering has not yet been detected in LSCO. Nevertheless, by comparing the data based on the wipeout effect of ^{63}Cu NQR charge order parameter in LSCO with the ones obtained from charge stripe

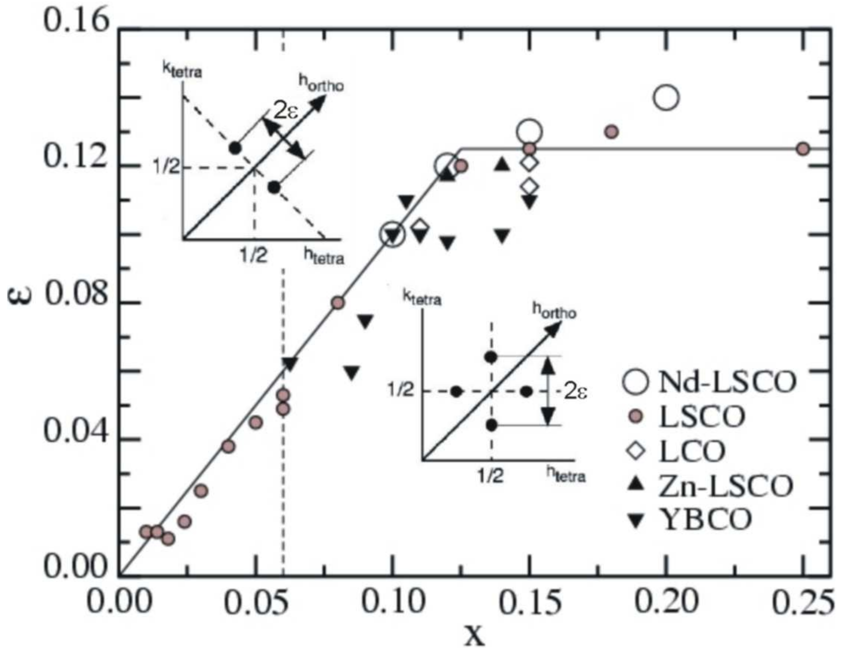

Figure 2.2: Summary of experimental data illustrating the doping dependence of incommensurability ϵ in the cuprates. Results have been obtained by different groups: Nd-LSCO (Refs. 13, 18–20); LSCO (Refs. 23, 48–50, 53, and 54); LCO (Ref. 58); Zn-LSCO (Refs. 59 and 60); YBCO (Refs. 61 and 67–69). In LSCO, ϵ has been defined as a distance from the IC peak position to the AF wave vector $(1/2, 1/2)$ either in the orthorhombic ($x < 0.06$) or tetragonal ($x > 0.06$) notation, whereas at $x = 0.06$, both definitions are used due to the coexistence of diagonal and parallel to the Cu-O bonds spin modulations.

compounds as (Nd,Eu,Ba)-LSCO, Hunt *et al.* [55] concluded that a similar stripe instability exists in LSCO over the whole underdoped superconducting region $1/16 \leq x \leq 1/8$. It is also worth mentioning that a very compiling evidence for its existence has been established in the measurements of the in-plane resistivity and the dynamical infrared conductivity anisotropy [56, 57].

Experimental detection of IC magnetic peaks in the LTO phase of LSCO suggests that the LTT structure is not essential for the appearance of stripes. This conjecture has been confirmed in experiments on the oxygen doped $La_2CuO_{4+\delta}$ (LCO) with the orthorhombic crystal structure [58]. It is also supported by the evidence for *static* IC magnetic peaks in another orthorhombic compound $La_{2-x}Sr_xCu_{1-y}Zn_yO_4$ (Zn-LSCO) with y up to 0.03, even though attempts to observe the charge order peaks were unsuccessful [59, 60]. In fact, Zn substitution pins the stripe fluctuations similarly to the rare-earth elements. However, in contrast to the latter, it does not induce a structural transition to the LTT phase, but provides randomly distributed pinning centers that promote meandering of

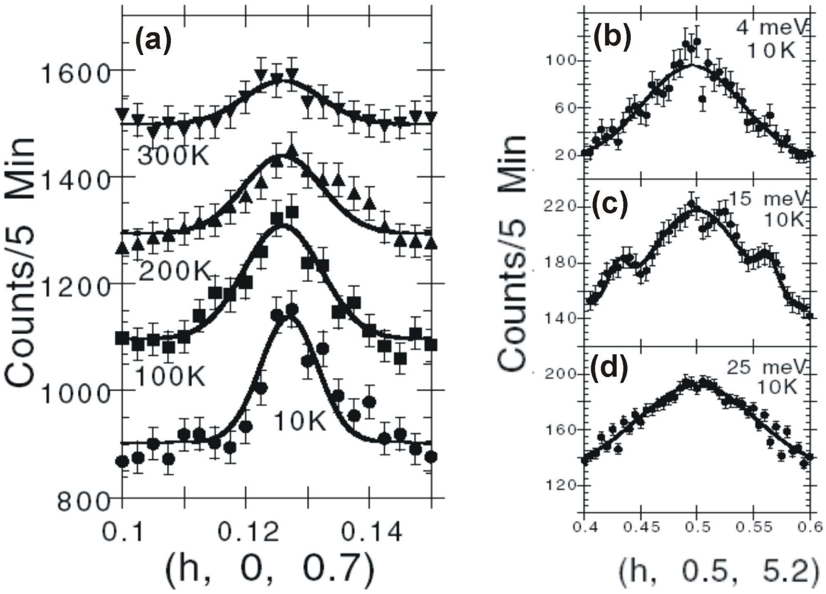

Figure 2.3: Neutron scattering measurements of: (a) static charge order and (b)-(d) magnetic fluctuations for YBCO$_{6.35}$, after Ref. 69.

stripes and correspondingly broadens IC peaks.

An important question is whether charge stripes appear solely in monolayered lanthanum compounds or if they are a generic feature of all the cuprates. The latter conjecture seems to be supported by inelastic neutron scattering experiments on bilayered YBa$_2$Cu$_3$O$_{6+\delta}$ (YBCO) that have identified the presence of IC spin fluctuations throughout its entire superconducting regime [61]. In fact, as the doped charge is nontrivially distributed between the CuO$_2$ planes and CuO chains, it is very difficult to determine the precise doping level x in the CuO$_2$ sheet of YBCO. One can only estimate it using either a relationship between the superconducting transition temperature T_c and x [61] or the empirical bond valence sum rule of Tallon *et al.* [62], $x = 0.21\delta - 0.023$.

However, despite seminal uncertainty concerning the orientation of the IC patterns at $\delta = 0.6$, which corresponds to an effective hole concentration $x \simeq 0.1$ [63], subsequent studies have revealed the presence of IC magnetic peaks at the wave vectors $(1/2 \pm 0.1, 1/2)$ and $(1/2, 1/2 \pm 0.1)$ [64–66]. Analogical IC magnetic superstructure has also been found at a slightly larger doping level $\delta = 0.7$ [67] as well as at $\delta = 0.85$ [68]. Moreover, systematic studies by Dai *et al.* [61] have shown that the incommensurability in YBCO increases initially with doping but it saturates faster than in LSCO, i.e., already at $x \simeq 0.1$ with the value $\epsilon \simeq 0.1$. Unfortunately, there is no any compelling explanation that would account for such a different behavior of ϵ in both systems.

Eventually, after continuous attempts, *static* charge order peaks have been

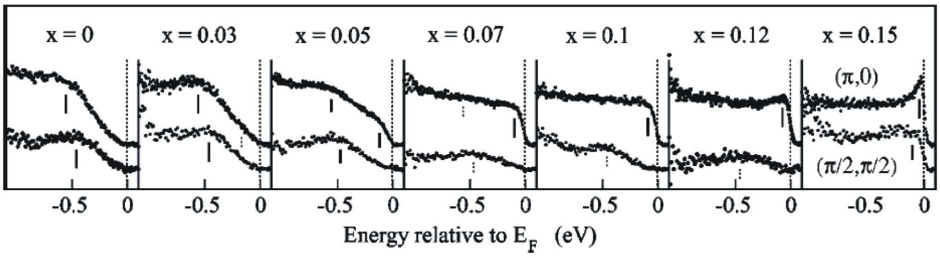

Figure 2.4: Comparison between the ARPES spectra at the momentum $(\pi, 0)$ and $(\pi/2, \pi/2)$ for LSCO, after Ref. 72. The latter were multiplied by a factor 2.

observed in $\mathrm{YBCO}_{6.35}$ at the wave vector $(0.127, 0, 0.7)$ which is almost precisely double the *dynamic* magnetic incommensuration $\epsilon = 0.0625$, as depicted in Fig. 2.3 [69]. This is 1/16, so the magnetic peaks correspond to the DWs separated by $d = 1/2\epsilon = 8$ lattice spacings with a constant charge density 0.5 hole/Cu ion. Therefore, an inspection of Fig. 2.2 suggests that ϵ in YBCO tends to saturate in the low doping regime as in LSCO below $x = 0.02$. However, in the latter case, a diagonal IC spin modulation with a charge of one hole/Cu ion has been observed [54]. Finally, we note that in spite of several attempts, no static charge order could be detected in $\mathrm{YBCO}_{6.5}$ and $\mathrm{YBCO}_{6.6}$.

Furthermore, although some neutron scattering experiments have been done on $\mathrm{Bi_2Sr_2CaCu_2O_{8+\delta}}$ (BSCCO), the probe has only produced weak evidence of the IC structure [70]. In contrast, Fourier transform of the recent STM data has revealed some IC peaks corresponding to a four-period modulation of the local density of states along the Cu-O bond direction, which may imply the existence of stripes [71]. Nevertheless, definite answer pertinent to the appearance of stripes in all the cuprates remains still unsettled and further experiments are required to reach an unambiguous conclusion, even though the summary of the experimental data illustrating doping dependence of the incommensurability ϵ in cuprates, depicted in Fig. 2.2, includes an array of compounds.

Tendency towards phase separation is also a starting point to understand doping evolution of the electronic structure in LSCO and Nd-LSCO. Fig. 2.4 illustrates the ARPES spectra at the $X = (\pi, 0)$ and $S = (\pi/2, \pi/2)$ points for LSCO at different doping levels [72]. The remarkable result is that even though in the insulating regime the data are solely characterized by a single high binding energy feature, one can also identify a second low-energy feature near the X point for $x = 0.05$. Upon further doping one observes a systematic transfer of spectral weight from the high- to the low-energy feature and finally a well-defined quasiparticle (QP) peak develops near the optimal doping. In contrast, the intensity near the S point remains suppressed for the entire underdoped regime so that a QP peak is observed only for $x \geq 0.15$.

The dispersion of the LSCO spectral features for different doping levels is

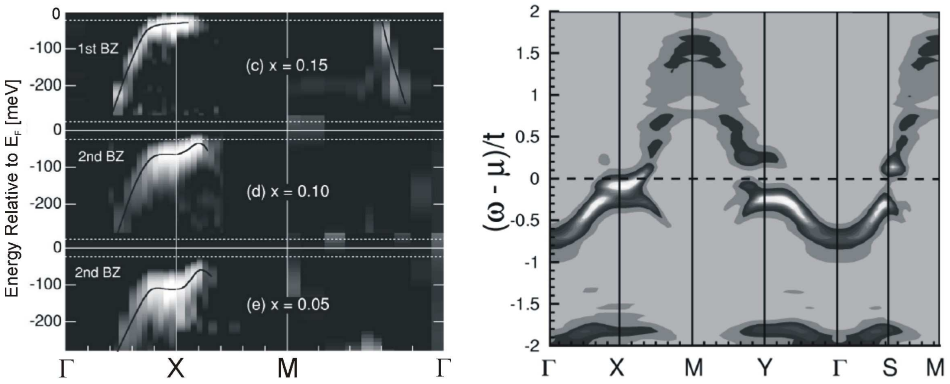

Figure 2.5: Band dispersion near the Fermi level for LSCO, measured by ARPES (left panel), after Ref. 73; theoretical gray-scaled intensity of spectral weight obtained using the Hubbard model within DMFT at $x = 1/12$ with $U = 12t$, along the main directions of the 2D Brillouin zone, with $\Gamma = (0,0)$, $X = (\pi,0)$, $Y = (0,\pi)$, $M = (\pi,\pi)$, and $S = (\pi/2,\pi/2)$ (right panel), after Ref. 37.

summarized in the left panel of Fig. 2.5. One can clearly see that the ARPES band dispersion possesses, extensively discussed in the literature, saddle point at the X point, the so-called flat band [73]. As hole doping increases, the flat band moves monotonically upwards and crosses the Fermi level E_F at $x \simeq 0.2$. This is reflected in the enhancement of the DOS at the chemical potential $N(\mu)$ observed by AIPES, as shown in the left panel of Fig. 2.6 [74].

The result is compared with a theoretical spectral function obtained using the Hubbard model with $U = 12t$ within the DMFT for a vertical (01) SC stripe at $x = 1/12$ [37]. As a consequence of the stripe order, the spectra along the $\Gamma{-}X{-}M$ path are not equivalent to those along the $\Gamma - Y - M$ one, with $\Gamma = (0,0)$ and $Y = (0,\pi)$. Note that, as in the experiment, the spectral weight along the $\Gamma - X$ direction is suppressed close to the Γ point and becomes enhanced at the X point. The flat QP band near the X point with a large intensity at the maximum below the chemical potential μ follows from a superposition of the dispersionless 1D metallic band along the x direction, formed by holes propagating along the vertical stripes, and an insulating band that stems from the AF domains. In contrast, an AF band at the Y point is characterized by a high binding energy well below μ and consequently the spectral weight at $\omega = \mu$ almost vanishes. Moreover, a distinct gap for charge excitations opens at μ near the S point. This gap follows indeed from the stripe structure — while the system may be metallic along the stripes, i.e., in the antinodal directions $\Gamma - X$ or $\Gamma - Y$, the low-energy excitations should be noticeably suppressed along the nodal direction $\Gamma - S$ crossing all the stripes. This conjecture is also supported either by the ED studies [35] or by the analytical approach based on variational trial wave function within the string picture [36], both applied to the t-t'-t''-J model, or by the CPT for the t-J model [38].

In fact, the low-energy spectral weight of Nd-LSCO at $x = 0.12$, a model compound for which the evidence of spin and charge stripe order is the strongest, is also mostly concentrated in flat regions along the $\Gamma - X$ and $\Gamma - Y$ directions, while there is little or no spectral weight along the $\Gamma - S$ direction [75]. On the other hand, ARPES spectra of both LSCO and Nd-LSCO at $x = 0.15$ have revealed not only the presence of flat bands around the X and Y points but also the existence of appreciable spectral weight at E_F in the nodal region [76]. While the observation of flat segments might be directly ascribed to 1D stripes [77], detection of nodal spectral weight poses a formidable task to develop a theory that would describe the electronic structure resembling the Fermi surface (FS) of a fully 2D system because, as it was already stressed out, the nodal spectral weight is expected to be suppressed in a static SC stripe picture [35–38]. Indeed, the experimentally established FS looks rather like the one arising from disorder or from dynamic fluctuating stripes [77].

Alternatively, guided by the CPT results showing that while the SC stripes yield little spectral weight near the nodal region, the BC ones reproduce quite well the nodal segments [38], Zhou *et al.* [76] have conjectured that the experimental FS may result from the coexistence of the SC and BC stripes. Within this framework, upon increasing doping the BC stripes are formed at the expense of the SC ones. This scenario is particularly interesting because it has been shown that the BC stripe, in contrast to its SC counterpart, enhances superconducting pairing correlations [78]. The relevance of a bond order at the doping level $x = 0.15$ is supported by recent studies of the ARPES spectra in a system with the BC stripes [79]. These studies have yielded pronounced spectral weight both in the nodal and antinodal directions, reproducing quite well the experimental results in Nd-LSCO and LSCO [76]. Furthermore, the stripe scenario would also explain the origin of the two components seen in the ARPES spectra at the X point near $x = 0.05$ (*cf.* Fig. 2.4). Indeed, the response from the AF insulating regions would be pushed to the high binding energies due to the Mott gap, whereas the charge stripes would be responsible for the other component near E_F.

Finally, existence of DWs should give rise to the appearance of new states inside the charge-transfer gap that would pin the chemical potential μ. Doping dependence of μ in LSCO deduced from XPS is depicted in the right panel of Fig. 2.6 [80]. This figure shows the suppression of the shift in the underdoped regime $x < 1/8$ where ϵ increases linearly (*cf.* Fig. 2.2). In contrast, in the overdoped region with a lock-in effect of ϵ, the number of stripes saturates, doped holes overflow into the AF domains, and μ moves fast with doping. The picture of broadened stripes and holes spreading out all over the AF domains is also indicated by the doping dependence of the resistivity and the Hall coefficient R_H in Nd-LSCO. Namely, a rapid decrease in the magnitude of R_H for doping level $x \leq 1/8$ at low temperature provides evidence for the 1D charge transport, whereas for $x > 1/8$, relatively large R_H suggests a crossover from the 1D to 2D charge transport [81]. Altogether, it appears that the metallic stripe picture does capture

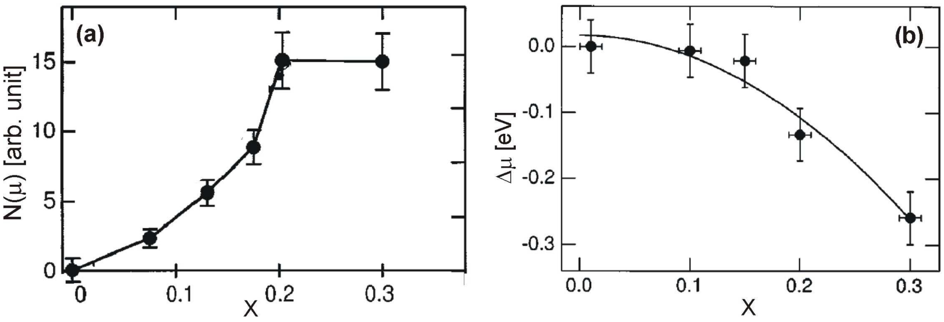

Figure 2.6: Doping dependence of: (a) DOS at the chemical potential μ, $N(\mu)$, after Ref. 74; (b) chemical potential shift $\Delta\mu$ in LSCO, after Ref. 80.

the essence of the low-lying physics for Nd-LSCO and LSCO systems.

Conversely, it is important to note that so far no evidence of IC peaks has been detected in any electron-doped cuprates superconductors. Instead, the neutron scattering experiments have established only *commensurate* spin fluctuations as in $Nd_{2-x}Ce_xCuO_4$ (NCCO), both in the superconducting and in normal state [82]. Moreover, observation of such peaks is consistent with the XPS measurements in NCCO showing that the chemical potential monotonously increases with electron doping [83].

2.2 Nickelates

Stripe order has also been observed in a number of nonsuperconducting doped antiferromagnets, such as layered manganites $(La,Nd)_{1-x}Sr_{1+x}MnO_4$ [84, 85]. Among them, LSNO and $La_2NiO_{4+\delta}$ (LNO) play plausibly the most prominent role. Indeed, neutron scattering measurements have revealed static stripe order in the LNO samples with $\delta = 0.105$, 0.125, as well as 0.133 [86–92], and even over a wider hole doping region $0.135 \leq x \leq 0.5$ in the case of LSNO [14, 15, 24–29]. Moreover, the IC stripe order persists up to $x = 0.7$ in the $Nd_{2-x}Sr_xNiO_4$ (NSNO) system [95], in which the LTO phase seems to extend to a higher doping region $x \leq 0.45$ as compared to the La compounds where the HTT phase is stabilized at the expense of the LTO structure already at $x \simeq 0.22$ [14]. Indications of a charge order in doped La_2NiO_4 were also found in electron [96] and x-ray diffraction studies [97–99]. Quite recently, the 1D nature of the stripe modulation within NiO_2 planes has been directly confirmed in the TEM studies of charge stripes in LSNO [100]. In addition, careful examination of the TEM images has shown that at a low temperature stripes are mainly centered on rows of Ni atoms. However, a mixture of the SC and BC stripes was also observed in some small regions of the sample.

In contrast to LSCO, charge and spin order in LSNO is characterized by the

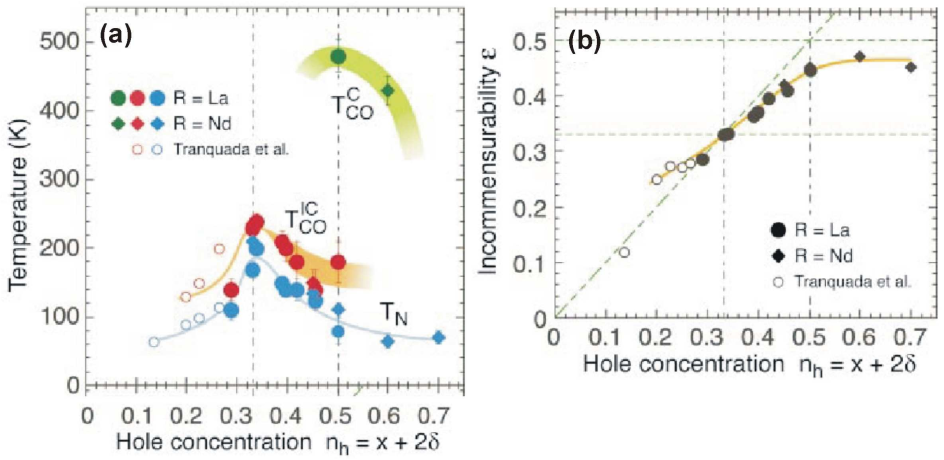

Figure 2.7: Summary of the results for $La_{2-x}Sr_xNiO_4$ (filled circles), $Nd_{2-x}Sr_xNiO_4$ (diamonds), and $La_{2-x}Sr_xNiO_{4+\delta}$ (empty circles) for different net dopant induced hole concentration $n_h = x + 2\delta$ dependence of: (a) transition temperature for a checkerboard-type charge order ($T_{\rm CO}^{\rm C}$) as well as a stripe-type charge ($T_{\rm CO}^{\rm IC}$) and spin ($T_{\rm N}$) order, and (b) incommensurability ϵ, after Ref. 29.

wave vectors (ϵ, ϵ) and $(1/2{\pm}\epsilon/2, 1/2{\pm}\epsilon/2)$, respectively, with $\epsilon \simeq x$ corresponding to a constant charge density of one hole/Ni ion along the diagonal stripe. Note that the behavior of ϵ is exactly the same as that found in the seminal HF calculations within the Hubbard model [5–9]. Later on, using the same approach applied to a more realistic four-band Peierls-Hubbard model for NiO_2 planes, Zaanen and Littlewood have shown that doped holes prone to form diagonal DWs, centered on rows of Ni atoms, with a tendency to have a ferromagnetic (FM) alignment of the reduced Ni spins at a DW [101]. In fact, subsequent multiband HF calculations have shown that depending on strength of the electron-lattice coupling, one can obtain either metal- or oxygen-centered structures [102]. Therefore, it appears that the semiclassical theory describes well the essence of stripe physics in the nickelates, even though recent inelastic neutron scattering in LSNO at $x = 1/3$ has revealed the existence of 1D AF correlations parallel to the stripe direction [93] instead of FM ones predicted in Ref. 101.

We proceed now to discuss a summary of the results concerning $La_{2-x}Sr_xNiO_4$, $Nd_{2-x}Sr_xNiO_4$, and $La_{2-x}Sr_xNiO_{4+\delta}$ shown in Fig. 2.7. Fig. 2.7(a) depicts the transition temperature for a checkerboard-type charge order ($T_{\rm CO}^{\rm C}$) as well as for a stripe-type charge ($T_{\rm CO}^{\rm IC}$) and spin ($T_{\rm N}$) order, as a function of the net dopant induced hole concentration $n_h = x+2\delta$, which accounts for the fact that each excess oxygen dopes two holes into NiO_2 planes. The data give a clear evidence that the stripe order is most stable at $n_h = 1/3$. Indeed, $T_{\rm CO}^{\rm IC}$ and $T_{\rm N}$ increase linearly with n_h, take a maximum at $n_h = 1/3$ with 240 and 180 K, respectively, and then decrease monotonously upon further doping. The particularly robust stability of stripes at $n_h = \epsilon = 1/3$ stems from the coincidence of the spin superlattice peaks at the wave vectors $(1/2 \pm \epsilon/2, 1/2 \pm \epsilon/2)$ with those of the charge order, given by (ϵ, ϵ). One should also note that, as illustrated in Fig. 2.7(b), ϵ starts to gradually deviate above $n_h = 1/3$ from the value given by the $\epsilon \simeq n_h$ law. In fact, the charge order is even more stable than the stripe order at $n_h = 1/2$ and forms a checkerboard pattern below the transition temperature $T_{\rm CO}^{\rm C} \simeq 480$ K. Remarkably, with decreasing temperature, a stripe charge order sets in below $T_{\rm CO}^{\rm IC} \simeq 180$ K and its incommensurability is twice as large as that of the spin order with the much lower onset temperature $T_N \simeq 80$ K [28, 29]. The low temperature competition of the checkerboard and stripe order at $n_h = 1/2$ has also been clearly indicated by the measurements of Raman and optical conductivity [103, 104]. Interestingly, above this doping, incommensurability tends to saturate rapidly with the value $\epsilon \simeq 0.44$ [95].

The unique stability of charge and spin order at $x = 1/3$ in LSNO has been the subject of intense studies that led to the discovery of distinct anomalies of transport, optical, and thermodynamic properties observed in an array of measurements. Here we only briefly discuss the most prominent results, summarized in Figs. 2.8 and 2.9. Fig. 2.8(a) illustrates the so-called commensurability effect [26]. Namely, one can clearly recognize that at $x = 1/3$, ϵ is almost temperature independent with the value $\epsilon = 1/3$. Moreover, incommensurability of two samples with a doping level slightly below and above $x = 1/3$, is a function of T with a tendency to approach 1/3 near $T_{\rm CO}^{\rm IC}$ at the expense of deviation from the $\epsilon \simeq x$ law. Apparently, charge order itself induces commensurate values of ϵ and such a commensurability effect seems to be an intrinsic property of the stripe order. On the other hand, concomitant tuning the hole density at the DWs suppresses the superexchange energy gain, best optimized when all the holes are accommodated within stripes. Therefore, it is the AF order that drives ϵ to approach the value given by the linear relation $\epsilon \simeq x$ below $T_{\rm N}$. Obviously, when $x = 1/3$, both effects cooperate which results in the locked-in value of $\epsilon \simeq 1/3$ over the whole $T < T_{\rm CO}^{\rm IC}$ range.

Next, let us focus on the phonon thermal conductivity κ in LSNO with $x = 1/3$ and $x = 1$ shown in Fig. 2.8(b). In the former case, the temperature dependence of κ exhibits a typical behavior for insulators, i.e., it possesses a clear maximum at low T and then decreases monotonously with increasing T [105]. The maximum originates from two competing effects. On the one hand, at very low T, κ increases owing to an increasing number of phonons, as in this case the mean free path is temperature independent. On the other hand, an exponentially growing number of scattering processes results in the suppression of κ at higher T. However, at $T_{\rm CO}^{\rm IC} = 240$ K a distinct kink occurs in the thermal conductivity. This peculiarity might be easily interpreted in the stripe framework. Indeed, fluctuating charge stripes might induce lattice fluctuations and such an additional scattering channel for phonons naturally explains the suppression of κ at $T_{\rm CO}^{\rm IC}$, whereas static stripes justify the typical insulating behavior of κ below $T_{\rm CO}^{\rm IC}$. In contrast, the thermal

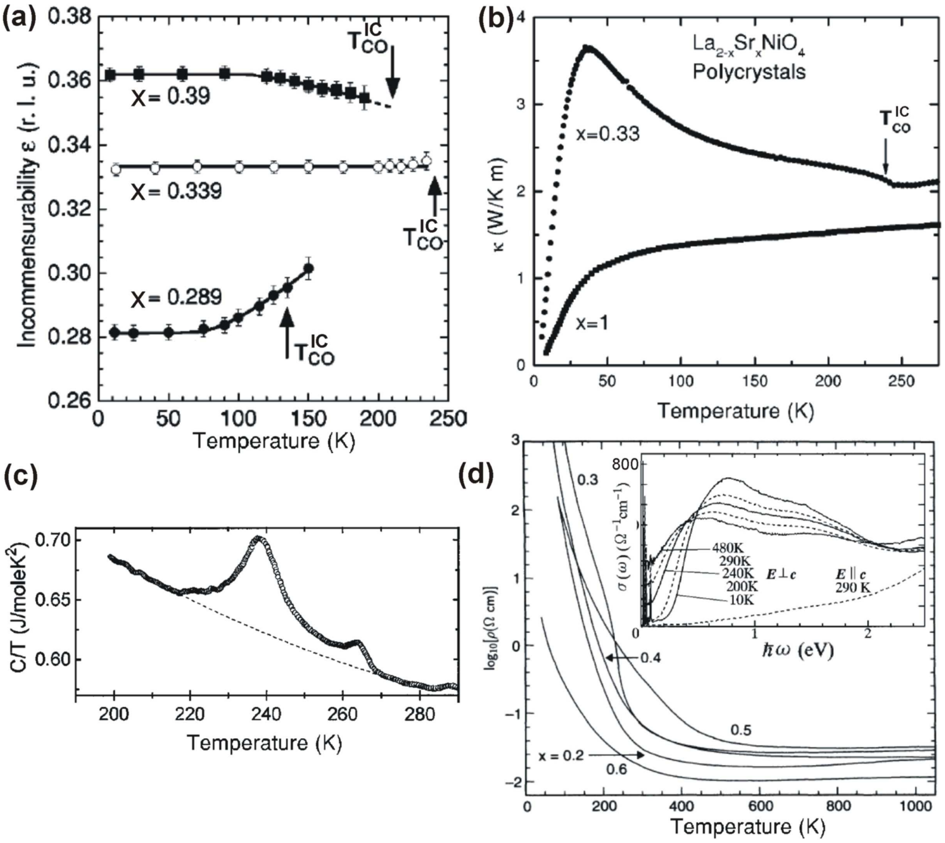

Figure 2.8: Temperature dependence of: (a) incommensurability ϵ ($x = 0.289$, 0.339, and 0.39), after Ref. 26; (b) phonon thermal conductivity κ, ($x = 1/3$ and 1.0), after Ref. 105; (c) specific heat C ($x = 1/3$), after Ref. 106, and (d) logarithmic resistivity $\log \rho$ ($x = 0.2$, 0.3, 0.4, 0.5, and 0.6), after Ref. 107 in LSNO. The inset in panel (d) shows the temperature dependence of the optical conductivity spectra $\sigma(\omega)$ in LSNO at $x = 1/3$, after Ref. 108.

conductivity of metallic sample with $x = 1$ differs remarkably from that of the insulating one and increases continously with T over the whole measured region.

Further, temperature dependence of the specific heat C, depicted in Fig. 2.8(c), shows a distinct anomaly at the same temperature $T_{\rm CO}^{\rm IC} = 240$ K suggesting a charge-order transition [106]. This conjecture is supported by the temperature dependence of the logarithmic resistivity $\log \rho$ shown in Fig. 2.8(d). Indeed, as expected for this transition, $\log \rho$ of the sample with $x = 0.3$ exhibits a steep increase precisely at 240 K [107]. Charge fluctuations around $T_{\rm CO}^{\rm IC} = 240$ K also lead to conspicuous changes in the optical conductivity spectra $\sigma(\omega)$ [108], as displayed in the inset of Fig. 2.8(d). Namely, at a high temperature $T > T_{\rm CO}^{\rm IC}$, only a broad peak is observed with a finite low-energy spectral weight. However, when T is decreased down to $T_{\rm CO}^{\rm IC}$, the low-energy weight below 0.4 eV is gradually

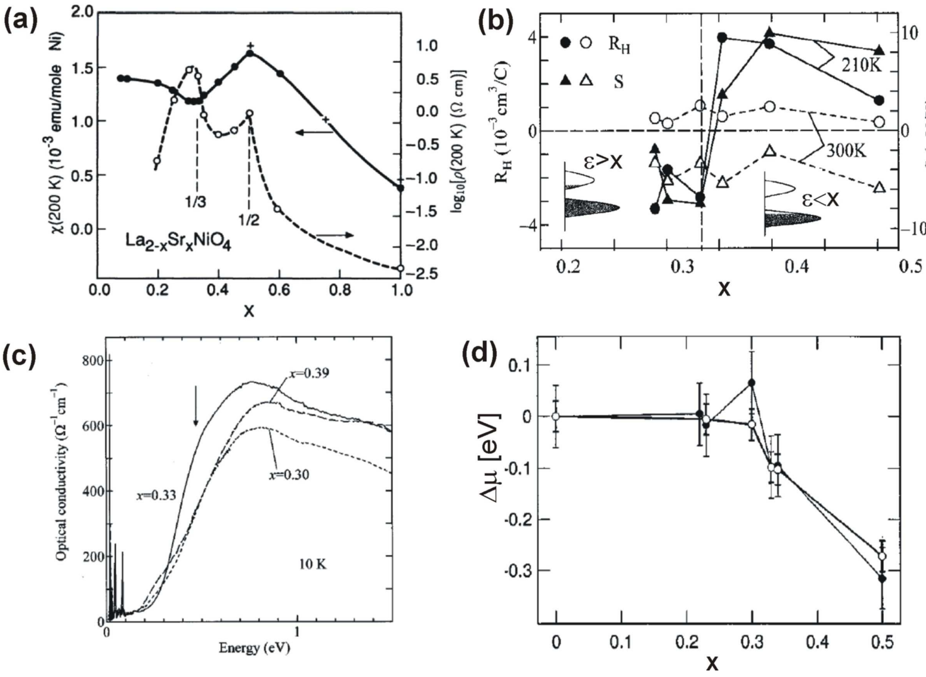

Figure 2.9: Doping dependence of: (a) the magnetic susceptibility χ and the logarithmic resistivity $\log \rho$ at 200 K, after Ref. 107; (b) Hall coefficient R_H (circles) and Seebeck coefficient S (triangles) at $T > T_{\mathrm{CO}}^{\mathrm{IC}}$ (empty symbols) and at $T < T_{\mathrm{CO}}^{\mathrm{IC}}$ (filled symbols); (c) the optical conductivity spectra at 10 K, and (d) the chemical potential shift $\Delta\mu$ deduced either from XPS (filled circles) or UPS (empty circles), after Ref. 110 in LSNO. Panels (b) and (c) are after Ref. 109.

transferred to higher energy so that opening of the charge gap is clearly observed.

A special character of $x = 1/3$ as well as $x = 1/2$ doping, is best seen in the magnetic susceptibility χ and logarithmic resistivity $\log \rho$, recorded at 200 K, showing distinct anomalies at these doping levels, as depicted in Fig. 2.9(a) [107]. In this context it is important to discuss a peculiar behavior of the Hall coefficient R_H (circles) and the Seebeck coefficient S (triangles) at two representative values of T below and above $T_{\mathrm{CO}}^{\mathrm{IC}} = 240$ K, i.e., 300 K (empty symbols) and 210 K (filled symbols), shown in Fig. 2.9(b). The Hall coefficient at 300 K is almost independent of doping and takes a small positive value corresponding to the order of one hole carrier per Ni site [109]. The Seebeck coefficient shows a similar nearly constant behavior taking, however, a negative value. In contrast, below $T_{\mathrm{CO}}^{\mathrm{IC}}$, both R_H and S change their signs from negative to positive at $x = 1/3$ and their absolute values are larger than those at 300 K. In addition, for samples with $x = 0.3$ and 0.33, R_H keeps decreasing with decreasing T, so that the number of carriers per Ni site gets reduced even down to 0.01.

These results indicate that the deviation of x from 1/3 can be considered as an electronlike ($x < 1/3$) or holelike ($x > 1/3$) carrier doping into the $\epsilon = 1/3$ charge-ordered insulator with three Ni sites in the unit cell. Hence, for the doping level $x = 1/3$ there is exactly one hole per unit cell and such a state is robust and may be considered as a half-filled state. Moreover, it would certainly retain this feature if the incommensurability followed precisely the relation $\epsilon = x$. However, as shown in Fig. 2.7(b), ϵ has a tendency to shift towards 1/3, for both sides of the $x = 1/3$ point, which has important implications for the sign of R_H. On the one hand, when x is less than 1/3, the number of holes is insufficient for filling up the mid-gap states entirely, i.e., the states inside the charge-transfer gap induced by stripe order, and in this case the mid-gap states contain some electrons which become carriers. On the other hand, for x larger than 1/3, the number of electrons is insufficient for entirely filling up the lower Hubbard band which contains holes. Consequently, R_H is expected to have an opposite sign to the $x < 1/3$ case (hole carriers).

Next, the unique stability of the $x = 1/3$ point induced by the stripe order should strongly affect the electronic structure. Indeed, as we have already seen in the inset of Fig. 2.8(d), the optical conductivity spectra $\sigma(\omega)$ below $T_{\rm CO}^{\rm IC}$, with the suppressed intensity in the low-energy region, imply that LSNO is an insulator with a finite charge gap. Remarkably, as illustrated in Fig. 2.8(c), for both $x = 0.3$ and 0.39 doping levels, the low-energy spectral weight is enhanced as compared to $x = 1/3$, demonstrating distinct anomalies in the electronic structure around $x = 1/3$.

Finally, Fig. 2.9(d) depicts the suppression of the chemical potential shift $\Delta\mu$ in LSNO for $x \leq 1/3$ deduced either from XPS (filled circles) or UPS (empty circles) [110]. Certainly, this phenomenon cannot be explained within a simple rigid-band framework in which μ is expected to shift downwards with hole doping. In fact, an increase of x in a system with a spatially uniform hole distribution should enhance the average hole-hole repulsion which, in turn, would result in a higher energy required to add one hole to the system, i.e., in a larger $|\mu|$. Therefore, the absence of $\Delta\mu$ implies that the average hole-hole repulsion remains nearly unaltered upon doping. Such a behavior might be easily explained within a stripe picture in which a constant hole density at the DWs is realized in the regime where ϵ increases linearly with increasing x. Moreover, as we have already pointed out, a similar suppression of the shift has been found below $x \leq 1/8$ in LSCO [*cf.* Fig. 2.6(b)], suggesting that an inhomogeneous charge distribution is a common feature of both systems.

Let us finish this Section off with another prominent neutron scattering experiment that sheds some light on the question concerning the SC or BC nature of the stripes. We refer here to a magnetic-field induced effect suggesting that the stripes in LNO are O-centered at high T with a tendency to formation of the Ni-centered ones at low T [91, 92]. Indeed, on cooling the sample with $\delta = 0.133$, charge order was found at $T_{\rm CO}^{\rm IC} \simeq 220$ K with a locked-in value of $\epsilon = 1/3$. On further cooling, the magnetic order was detected below $T_{\rm N} \simeq 111$ K, accompanied

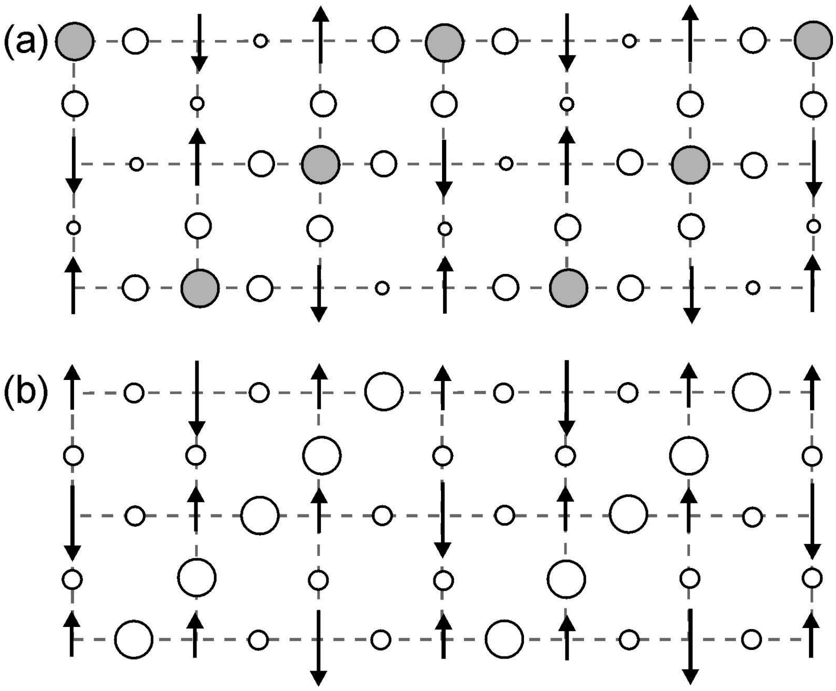

Figure 2.10: Schematic picture of the two possible stripe phases at high T in LNO with $\delta = 0.133$, as discussed in Refs. 91 and 92: (a) site-centered (SC), and (b) bond-centered (BC) domain walls with $\epsilon = 1/3$. The arrows indicate spins at Ni sites, open (shaded) circles stand for the excess charge density at O (Ni) atoms, respectively. The size of arrows (circles) is proportional to the magnetization (charge) density.

by a discontinuous jump in ϵ down to 0.295. Moreover, the incommensurability kept on decreasing and finally reached the value $\epsilon = 0.278$ at $T = 10$ K. Hence, one can conjecture that at low T, the measured incommensurability approaches the HF value $\epsilon = 2\delta = 0.266$.

Consider finally the $\epsilon = 1/3$ phase with two possible stripe arrangements: (*i*) with the SC stripes separating the AF domains comprising a pair of antiparallel spins, as shown in Fig. 2.10(a) or (*ii*) BC stripes, with the AF domains consisting of two $\uparrow$-spins and one $\downarrow$-spin, as depicted in Fig. 2.10(b). By looking at the magnetic structure it becomes clear that only the latter configuration might show a ferrimagnetic response, induced by a uniform magnetic field, in the PM phase at $T > T_{\mathrm{N}}$. Indeed, such a magnetization peak has been detected in a field of 6 T [91]. Therefore, assuming that the DWs are bond-centered in the high temperature regime, it has been concluded, based on the temperature dependence of ϵ, that cooling promotes the SC stripes.

Chapter 3

Semiclassical properties of filled stripes

As we already stated, the phenomenon of phase separation, manifesting itself in formation of nonmagnetic 1D domain walls, which separate AF domains of opposite phases is the most pronounced in Nd-LSCO around hole doping $x = 1/8$ [13, 18], where stripes are aligned along one of two equivalent lattice directions x (y), to which we refer as the horizontal (vertical) stripes. This is in contrast to the diagonal stripes inferred in the insulating nickelates LSNO [14, 15, 24–29] and LNO [86–92].

Even though the multiband HF calculations of Zaanen and Littlewood [101] are consistent with the observation of filled stripes in nickelates, by which is meant one doped hole per stripe unit cell, this approximation does not predict the half-filled stripes (one hole per every two atoms in a DW) observed in the cuprates [111]. In addition, charge transport is not possible in idealized filled stripes. Both these features indicate that it is necessary to go beyond the HF treatment of stripes by including local electron correlations which further influence the charge and spin distributions.

However, significant qualitative statements remain possible within the framework of the unrestricted mean-field theory. Indeed, early HF calculations for the 2D Hubbard model found that vertical stripes were favored for $U/t \lesssim 4$ and diagonal stripes formed at larger values of U [6–9]. Here, we extend these studies and determine a phase diagram of the Hubbard model with an anisotropic nearest-neighbor hopping t, by varying the on-site Coulomb repulsion U and investigating locally stable structures for representative hole doping levels $x = 1/8$ and $x = 1/6$. We also report the changes in stability of the stripe structures in the extended Hubbard model due to the next-neighbor hopping t' and to the nearest-neighbor Coulomb interaction V. Next, in order to gain a comprehensive understanding of the competition between different types of stripes in a realistic model, we include lattice degrees of freedom induced by a static Peierls electron-lattice coupling. Further, guided by the observation that negative t' ($t'/t < 0$) yields a positive kinetic energy contribution and hence it is suppressed by expelling holes from the AF domains and reinforcing the stripe order, we attempt to stabilize a half-filled stripe phase involving an on-wall spin-density wave as in Ref. 111. We argue that such a phase not only easily accommodates holes, but also redistributes them around domain walls so that the kinetic energy associated with next-neighbor hopping becomes negative despite negative t'. Consequently, it takes over in the regime of $t'/t \simeq -0.3$ appropriate for YBCO. Finally, we investigate and compare static hole-hole and spin-spin correlation functions of the considered stripes.

3.1 Solitonic mechanism of stripe formation

In what follows we describe the essential mechanism which favors stripe phases at finite doping, by considering only a small cluster consisting of three atoms filled by two electrons and one hole (with respect to half-filling with the electron density $n = 1$ per site). For simplicity we assume that the electrons are confined to the considered cluster owing to large Coulomb interaction $U \gg t$, and we do not take into account any interactions with the AF background. There are two possible candidates for the ground state. The first one corresponds to a hole added to three atoms of a single AF domain in which, if we suppose that a $\downarrow$-spin electron is replaced by a hole, the two remaining $\uparrow$-spin electrons can be found in one of three allowed configurations: $\{\uparrow, 0, \uparrow\}$, $\{\uparrow, \uparrow, 0\}$, and $\{0, \uparrow, \uparrow\}$ (the other configurations are excluded by the Pauli principle). Hence, this polaronic state gives the total energy,

$$E_P = -\sqrt{2}t, \tag{3.1}$$

and the Coulomb interaction U does not contribute.

A different situation is obtained when a hole occupies instead a DW separating two AF domains. Delocalization leads then to similar three configurations to those obtained above: $\{\uparrow, 0, \downarrow\}$, $\{\uparrow, \downarrow, 0\}$, and $\{0, \uparrow, \downarrow\}$, but in addition, three configurations with one doubly occupied site $\{\uparrow\downarrow, 0, 0\}$, $\{0, \uparrow\downarrow, 0\}$, and $\{0, 0, \uparrow\downarrow\}$, can be reached as excited states which cost Coulomb energy U. Moreover, three other configurations with interchanged $\uparrow$- and $\downarrow$- spins are then also accessible via the decay of double occupancies: $\{\downarrow, 0, \uparrow\}$, $\{\downarrow, \uparrow, 0\}$, and $\{0, \downarrow, \uparrow\}$. In the regime of large U, the total energy in the ground state can be found in a perturbative way and as a result one obtains,

$$E_S = -\sqrt{2}t - \frac{4t^2}{U}. \tag{3.2}$$

Therefore, the Hilbert space for the latter solitonic solution is larger and one finds that this solution is always more stable than the polaronic one [111]. The argument applies also to 2D systems, where the DWs are more stable than the lines of polarons in an AF background.

3.2 Vertical versus diagonal stripes

In this Section we attempt a systematic investigation of the properties and relative stability of filled vertical and diagonal stripes. We shall see that in spite of difficulty to stabilize the ground state with a half-filled DW, the mean-field framework is useful as providing a generic microscopic description of filled inhomogeneous structures.

3.2.1 Extended single-band Hubbard model

Starting point for the analysis of stripe structures is the extended single-band Hubbard model, which is widely accepted as the generic model for a microscopic description of the cuprate superconductors [112],

$$H = -\sum_{ij\sigma} t_{ij} c_{i\sigma}^{\dagger} c_{j\sigma} + U \sum_{i} n_{i\uparrow} n_{i\downarrow} + V \sum_{\langle ij \rangle} n_i n_j, \tag{3.3}$$

where the operator $c_{i\sigma}^{\dagger}$ ($c_{j\sigma}$) creates (annihilates) an electron with spin σ on lattice site i (j), and $n_i = c_{i\uparrow}^{\dagger} c_{i\uparrow} + c_{i\downarrow}^{\dagger} c_{i\downarrow}$ gives the electron density. The hopping t_{ij} is t on the bonds connecting nearest neighbors sites $\langle i, j \rangle$ and t' for second-neighbor sites, while the on-site and nearest-neighbor Coulomb interactions are, respectively, U and V.

The model can be solved self-consistently in real space within the HA, where the interactions are decoupled into products of one-particle terms becoming effective mean fields that act on each electron with the same strength. This approximation involves basically solving an eigenvalue problem. The obtained wavefunctions form a new potential and hence the Hamiltonian for a new eigenvalue problem. Typically, the new potential is chosen as some linear combination of the current and preceding potential. The iterations are continued until the input and output charge density and energy do not change within some prescribed accuracy. The most significant drawback of this method is that it neglects correlations. Electron correlation changes the system properties and manifests itself in the decrease of the ground state energy. The difference between the energy of the exact ground state and the energy obtained within the HA is thus called the correlation energy. It arises from the fact that an electron's movement is correlated with the electrons around it, and accounting for this effect lowers further the energy, beyond the independent electron approximation.

We do not consider noncollinear spin configurations, and use the most straightforward version of the HA with a product of two separate Slater determinants for up and down spins, whence,

$$n_{i\uparrow} n_{i\downarrow} \simeq n_{i\uparrow} \langle n_{i\downarrow} \rangle + \langle n_{i\uparrow} \rangle n_{i\downarrow} - \langle n_{i\uparrow} \rangle \langle n_{i\downarrow} \rangle. \tag{3.4}$$

A similar decoupling is performed for the nearest-neighbor Coulomb interaction. Calculations were performed on 12×12 (16×16) clusters for $x = 1/6$ ($x = 1/8$)

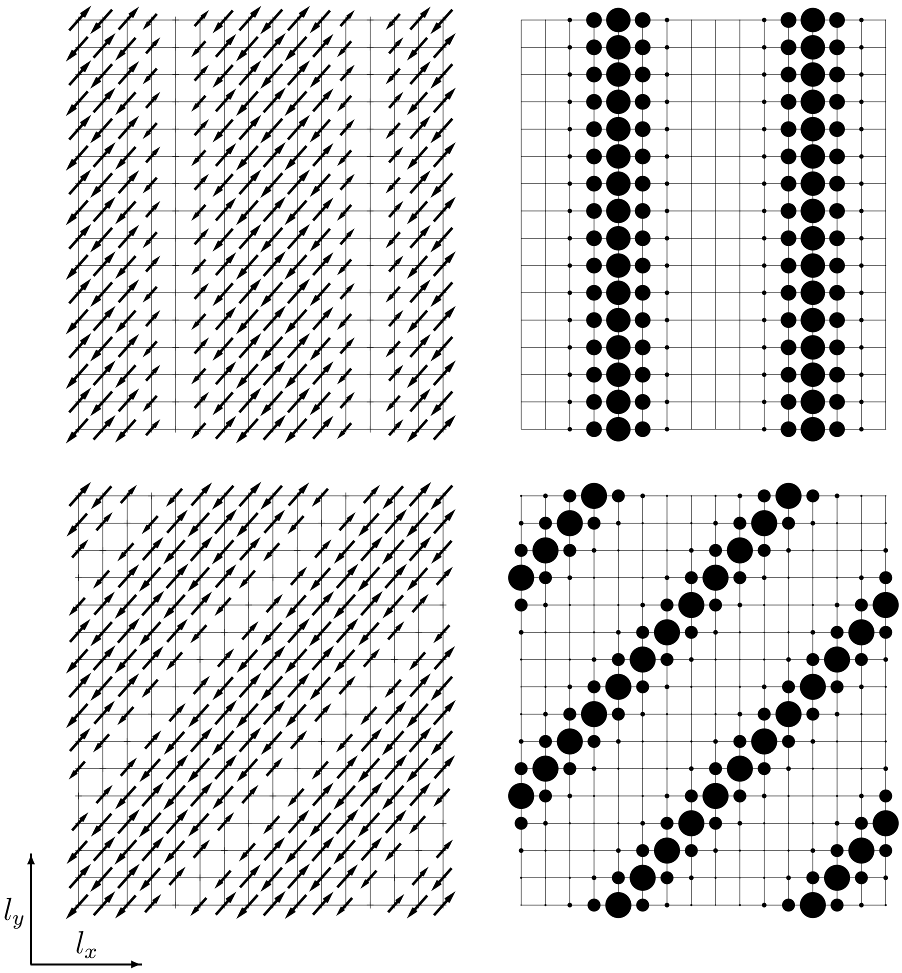

Figure 3.1: Vertical site-centered (VSC) and diagonal site-centered (DSC) stripe phases as found for $U/t = 5$ at hole doping $x = 1/8$. The length of arrows is proportional to the magnetization $\langle S_i^z \rangle$ and the hole density $\langle n_{\mathrm{h}i} \rangle$ is scaled by the diameter of black circles.

with periodic boundary conditions, and we obtain stable stripe structures with AF domains of width five atoms for $x = 1/6$ and seven atoms for $x = 1/8$. Typical solutions at $x = 1/8$ are shown in Fig. 3.1 with the local hole density,

$$\langle n_{\mathrm{h}i} \rangle = 1 - \langle n_{i\uparrow} + n_{i\downarrow} \rangle, \tag{3.5}$$

scaled by the diameter of the black circles and the length of the arrows being proportional to the amplitude of local magnetization density,

$$\langle S_i^z \rangle = \tfrac{1}{2} |\langle n_{i\uparrow} - n_{i\downarrow} \rangle|. \tag{3.6}$$

These structures possess nonmagnetic DWs with enhanced hole density which separate AF domains having hole density almost unchanged with respect to the

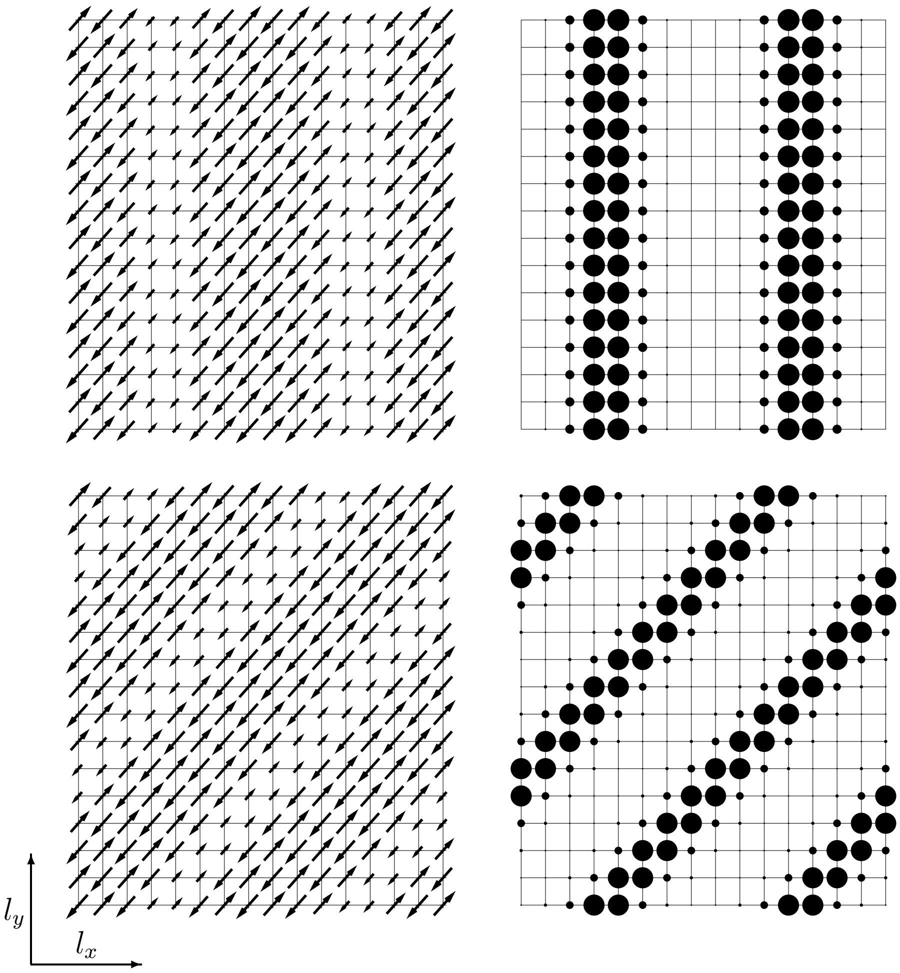

Figure 3.2: Vertical bond-centered (VBC) and diagonal bond-centered (DBC) stripe phases as found for $U/t = 5$ at hole doping $x = 1/8$. The meaning of the arrows and black circles as in Fig. 3.1.

undoped case. Note that the AF sites on each side of the DWs have a phase shift of π due to the solitonic mechanism described in Section 3.1. We compare the stability of such nonmagnetic SC domain walls with the BC stripe phases in which DWs are formed by pairs of magnetic atoms, as obtained by White and Scalapino [17] (*cf.* Fig. 3.2). In the three-band model, SC (BC) stripes correspond to DWs centered at metal (oxygen) sites, respectively [102, 113–116].

We begin by setting $t' = 0$ and $V = 0$ with a goal of elucidating the effects of hopping anisotropy on the stripes. This is motivated by the fact that the first detection of static stripes in both charge and spin sectors was accomplished in Nd-LSCO [13] indicating that rare-earth elements doping is in some way helpful for pinning of the stripe structure. Indeed, it produces a structural transition in the system from the LTO to LTT phase [117]. Both phases involve a distortion of the CuO_2 plane by rotation of the CuO_6 octahedra. In the LTO phase the tilt axis runs diagonally within the copper plane, such that all the oxygen atoms are displaced out of the plane. Conversely, in the LTT phase this rotation takes place around an axis oriented along the planar Cu−O bonds. Therefore, oxygen atoms on the tilt axis remain in the plane, while the ones in the perpendicular direction are displaced out of the plane. This provides a microscopic origin for in-plane anisotropies — the Cu−Cu hopping amplitude t depends on the Cu−O bond and it is isotropic in the LTO phase and anisotropic in the LTT one. For a physical tilt angle of order 5°, the relative anisotropy $\epsilon_t = |t_x - t_y|/t_y \simeq 1.5\%$ is weak [118, 119]. The direction with a larger hopping amplitude coincides with the direction of a stronger superexchange coupling J.

The possible relationship between this anisotropy and the onset of stripe phases has been intensively studied within anisotropic Hubbard ($t_x \neq t_y$) or t-J ($t_x \neq t_y$, $J_x \neq J_y$) models by means of various techniques: unrestricted HF approach [118], DMRG [119], and QMC method [39]. The in-plane anisotropies might also be represented theoretically by on-site potentials as in the QMC study by Riera [40]. All these studies have shown an enhanced tendency to forming stripe phases clearly seen either by the reduction their energy [118, 119] or by the appearance of IC peaks in the spin and charge structure factor [39, 40]. It appears that a finite anisotropy of the next-nearest hopping term t' might play a role in stabilizing diagonal incommensurate peaks observed in a spin-glass phase of LSCO ($0.02 \leqslant x \leqslant 0.06$) [48–50, 52–54]. Indeed, although the LTO phase is usually considered as isotropic, which is the case for nearest-neighbor hopping and interaction, a different length of the orthorhombic axes implies the need for an anisotropic t' parameter. Exact diagonalization studies incorporating such anisotropy found that it strongly strengthens hole correlations in one direction and suppresses them along the other, resulting in a 1D pattern of holes [120].

It turns out, however, that the variation of the ϵ_t anisotropy have only a little visible effect on the local hole density,

$$n_{\mathrm{h}}(l_x) = 1 - \langle n_{(l_x,0),\uparrow} + n_{(l_x,0),\downarrow} \rangle, \tag{3.7}$$

shown in Fig. 3.3 as a function of the x-direction coordinate l_x for a given y-direction coordinate $l_y = 0$, even at the unrealistically large 22% anisotropy level corresponding to $t_x/t = 1.1$ and $t_y/t = 0.9$. Similarly, the anisotropy does not modify the modulated magnetization density,

$$S_\pi(l_x) = (-1)^{l_x} \tfrac{1}{2} \langle n_{(l_x,0),\uparrow} - n_{(l_x,0),\downarrow} \rangle, \tag{3.8}$$

with a site dependent factor $(-1)^{l_x}$ compensating modulation of the staggered magnetization density within a single AF domain.

In contrast, the strong effect of finite anisotropy ϵ_t is clearly demonstrated by variation of the expectation values of the bond hopping terms along the x- and

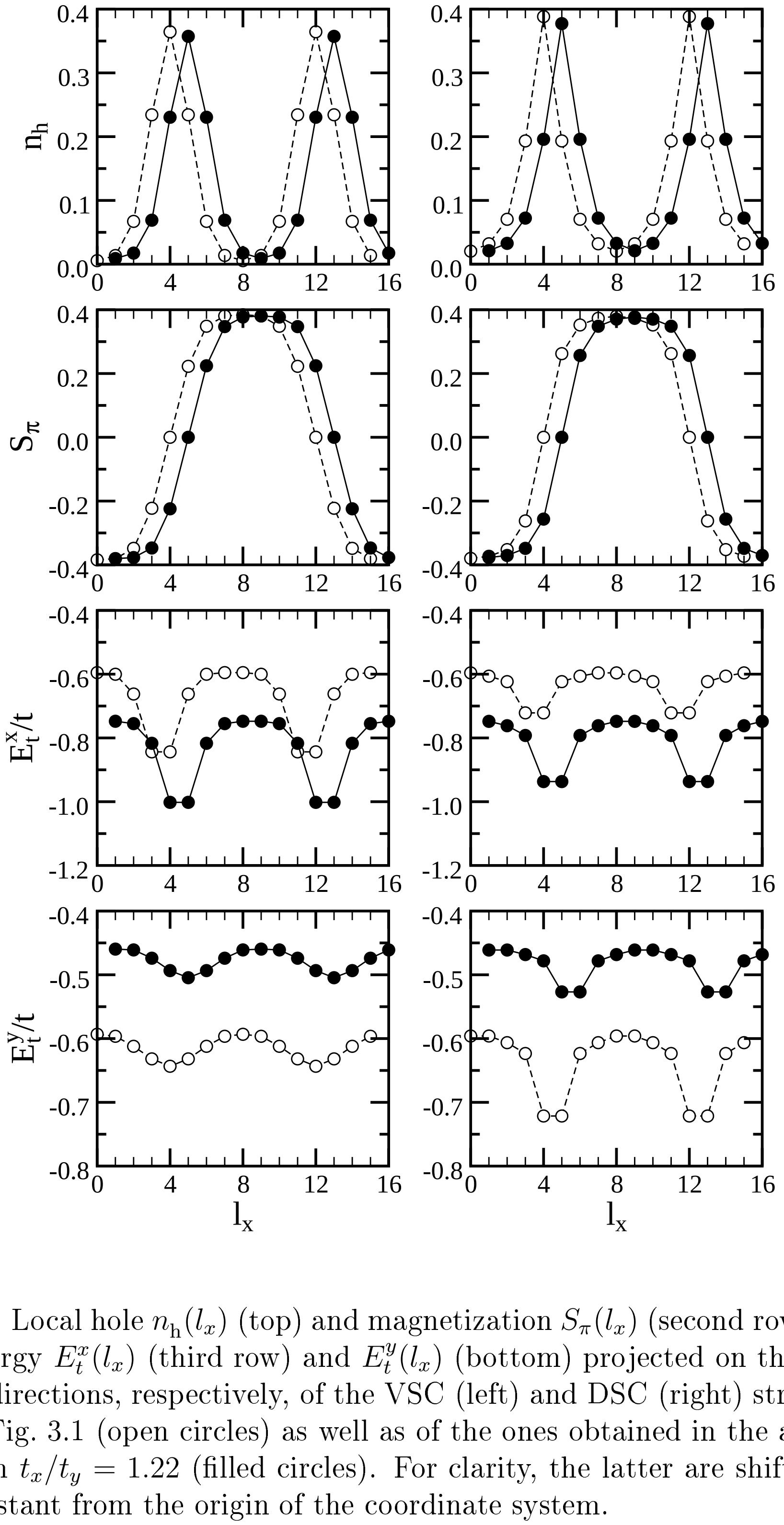

Figure 3.3: Local hole $n_{\rm h}(l_x)$ (top) and magnetization $S_\pi(l_x)$ (second row) density; kinetic energy $E_t^x(l_x)$ (third row) and $E_t^y(l_x)$ (bottom) projected on the bonds in the x-(y)-directions, respectively, of the VSC (left) and DSC (right) stripe phases shown in Fig. 3.1 (open circles) as well as of the ones obtained in the anisotropic model with $t_x/t_y = 1.22$ (filled circles). For clarity, the latter are shifted by one lattice constant from the origin of the coordinate system.

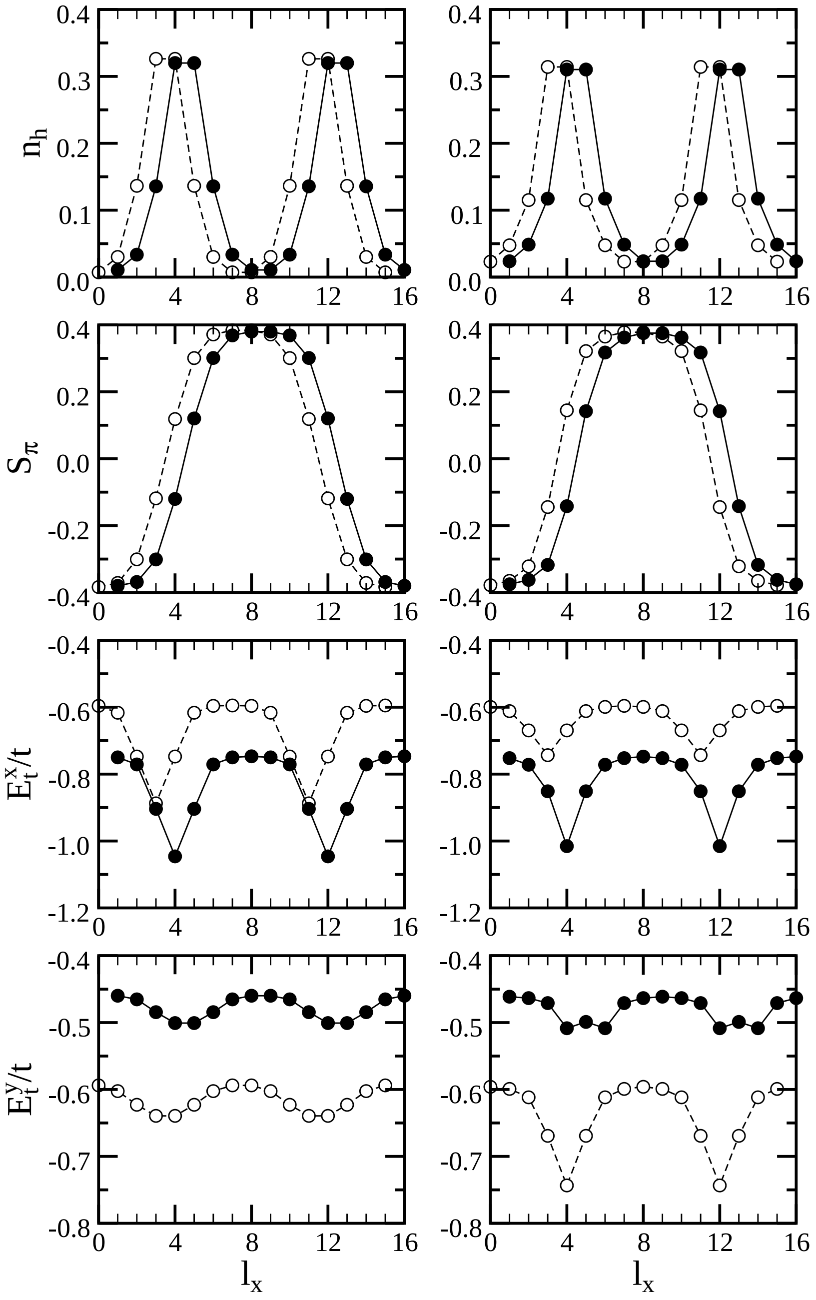

Figure 3.4: The same as in Fig. 3.3 but for the BC stripe phases.

y-directions,

$$E_t^x(l_x) = -t_x \sum_\sigma \left\langle c^\dagger_{(l_x,0),\sigma} c_{(l_x+1,0),\sigma} + h.c \right\rangle, \tag{3.9}$$

$$E_t^y(l_x) = -t_y \sum_\sigma \left\langle c^\dagger_{(l_x,0),\sigma} c_{(l_x,1),\sigma} + h.c \right\rangle. \tag{3.10}$$

	E_t^x/t	E_t^y/t	E_U/t	E_{tot}/t
VB(S)C	-0.6753	-0.6147	0.4900	-0.8000
DBC	-0.6375	-0.6375	0.4726	-0.8024
DSC	-0.6368	-0.6368	0.4696	-0.8040

Table 3.1: Site-normalized ground-state energy E_{tot}, kinetic energy (E_t^x, E_t^y), and potential energy E_U in the isotropic Hubbard model with $U/t = 5$ and $x = 1/8$ as obtained for different stripe phases: vertical site-centered (VSC), diagonal site-centered (DSC), vertical bond-centered (VBC) and diagonal bond-centered (DBC). In the HA, both types of vertical stripes are degenerate.

As we have learnt in Section 3.1, stripes are stabilized not by charge motion along them but by the transverse hopping. This was concluded from the previous HF studies which have clarified that the largest kinetic energy gains are obtained due to the hopping perpendicular to the stripes [111, 118]. These features are seen in Fig. 3.3. For the VSC stripes one finds a large anisotropy in the values of the kinetic energies (3.9) and (3.10), which becomes especially pronounced beside the stripes, and is strongly reinforced by the hopping anisotropy. Therefore, taking into account that the hopping between two different charge densities is favored over motion between equal densities, one should expect that transverse charge fluctuations will always tune the direction of DWs along the weaker hopping direction in the anisotropic model. Analogous conclusion based on Fig. 3.4 might be drawn concerning the orientation of the VBC stripes.

Regarding diagonal stripes, although a finite anisotropy in hopping is also reflected in the kinetic energy anisotropy, a system with either the DSC or DBC stripe pattern becomes topologically frustrated and consequently gains less energy compared to a system with vertical stripes, taking a full advantage of the anisotropy (*cf.* Tables 3.1 and 3.2). However, we shall see later on that the universal character of the solitonic mechanism which also applies to diagonal stripes stabilizes them in the Hubbard model with the next-neighbor hopping t' across the stripes.

The effect of an increasing anisotropy illustrates a phase diagram shown in Fig. 3.5 determined by varying U and the ratio t_x/t_y of the nearest-neighbor

	E_t^x/t	E_t^y/t	E_U/t	E_{tot}/t
DBC	-0.8143	-0.4807	0.4815	-0.8135
DSC	-0.8098	-0.4836	0.4793	-0.8141
VB(S)C	-0.8304	-0.4776	0.4938	-0.8142

Table 3.2: The same as in Table 3.1 but with the hopping anisotropy $\epsilon_t = 22\%$.

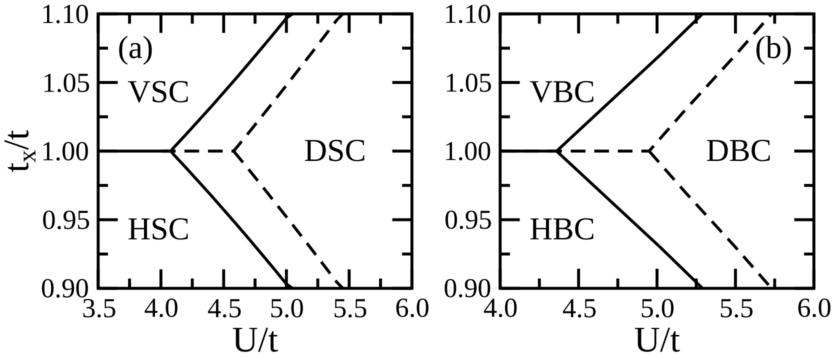

Figure 3.5: Phase diagrams for stable site-centered (a) and bond-centered (b) stripe structures obtained in the anisotropic Hubbard model ($t' = 0$, $V = 0$) on a 16×16 cluster for doping $x = 1/8$ (solid lines) and on a 12×12 cluster for $x = 1/6$ (dashed lines).

hoppings in the x- and y-directions, while maintaining constant $t = \frac{1}{2}(t_x + t_y)$. We observe the generic crossover from vertical to diagonal stripes with increasing Coulomb interaction reported in early HF studies [6, 7, 9]. The transition from the VSC to DSC stripes appears in the isotropic case at $U/t \simeq 4.1$ for $x = 1/8$, and at a higher value $U/t \simeq 4.6$ for $x = 1/6$ [*cf.* Fig. 3.5(a)]. The corresponding phase boundary between the VBC and DBC stripes is shifted towards stronger Coulomb interaction and occurs at $U/t \simeq 4.4$ (5.0) for $x = 1/8$ ($x = 1/6$), respectively [*cf.* Fig. 3.5(b)].

The results shown in Fig. 3.5 have a simple physical interpretation. Stripe phases occur as a compromise between, on the one hand, the AF interactions between magnetic ions and the local Coulomb interactions which favor charge localization, and the kinetic energy of doped holes which favors charge delocalization on the other hand. The kinetic energies in Table 3.1 show further that the vertical stripes are more favorable for charge dynamics. This result, which is not immediately obvious, has however a straightforward origin. Namely, the HA always leads to a large spin polarization since it is the only way to minimize the on-site Coulomb repulsion. Indeed, removal of a $\downarrow$-spin electron at site i leads to relaxation of the $\uparrow$-spin electron energy level at this site. As a consequence, an alternating on-site level shift develops yielding an energetical motivation for the symmetry breaking and forming the AF order. However, the renormalization of the double-occupancy energy involves a strong reduction of the kinetic energy in the $\downarrow$-spin channel between site i and its neighboring sites, as an electron incoming into this site encounters a high energy potential $U\langle n_{i\uparrow}\rangle$. Therefore, in the HA we shall be able to identify dynamically favorable stripe patterns only by comparing appropriate local magnetization densities.

For example, charge fluctuations occur more readily in the VSC stripe geometry presumably due to their greater overall width indicating weaker correlation

	i	1	2	3	4	5
VSC	$\langle n_{\mathrm{h}i} \rangle$	0.364	0.234	0.067	0.014	0.006
		(0.378)	(0.234)	(0.060)	(0.013)	(0.006)
	$\langle S_i^z \rangle$	0.000	0.222	0.348	0.381	0.384
		(0.000)	(0.234)	(0.357)	(0.382)	(0.384)
DSC	$\langle n_{\mathrm{h}i} \rangle$	0.388	0.193	0.070	0.032	0.020
		(0.405)	(0.195)	(0.066)	(0.028)	(0.017)
	$\langle S_i^z \rangle$	0.000	0.262	0.352	0.373	0.380
		(0.000)	(0.272)	(0.360)	(0.377)	(0.382)

Table 3.3: Local hole $\langle n_{\mathrm{h}i} \rangle$ and magnetization $\langle S_i^z \rangle$ density of the site-centered stripes shown in Fig. 3.1, all labeled by decreasing hole density in the x-direction. In parenthesis the values for the extended model with $t'/t = -0.15$ are given.

effects (*cf.* Fig. 3.3). This explains their stability at small U where the consequent cost in potential energy E_U becomes less relevant. By contrast, the DSC stripes are narrower having larger hole density along nonmagnetic DWs. Moreover, magnetization density of their nearest neighbor sites is markedly enhanced as compared to the corresponding VSC stripe magnetization as shown in Fig. 3.3 and Table 3.3. The former also illustrates that the bonds connecting DWs with their nearest neighboring sites perpendicularly to the walls, have the main contribution to the kinetic energy gain, in fact suppressed here by larger spin polarization. Taken together, the above features are reflected in a more localized character of the DSC stripes, with a lower net double occupancy and hence a more favorable on-site energy E_U (*cf.* Table 3.1). This clarifies the mechanism of the transition from the VSC to DSC stripes with increasing U.

Turning now to the analogous crossover between the BC stripes, we shall again compare local hole and magnetization densities on and around their DWs. In contrast to the SC case, a VBC stripe phase possesses larger hole density along DWs as illustrated in Fig. 3.2 and Table 3.4, suggesting that it is more localized than the DBC one. Nevertheless, a better renormalization of the double occupancy energy E_U by the latter (*cf.* Table 3.1) follows from a stronger spin polarization not only of the DW atoms but also their nearest neighbors (*cf.* Fig. 3.2 and Table 3.4). This enhancement is directly responsible for a great reduction of the kinetic energy along bonds joining these atoms. Correspondingly, it accounts for a crossover from the DBC to VBC stripes in the small U regime when the larger kinetic gain becomes crucial.

We would like to emphasize that the above transition between different types of stripe phases is not an artefact of the HA and occurs also between filled stripes obtained within more realistic approaches including local electron correlations. Indeed, slave-boson studies of the Hubbard model at the doping $x = 1/9$ have established that the transition from the filled VSC to DSC stripe phase appears

	i	1	2	3	4
VBC	$\langle n_{\mathrm{h}i} \rangle$	0.326	0.136	0.030	0.007
	$\langle S_i^z \rangle$	0.118	0.301	0.371	0.384
DBC	$\langle n_{\mathrm{h}i} \rangle$	0.314	0.115	0.047	0.023
		(0.323)	(0.110)	(0.046)	(0.021)
	$\langle S_i^z \rangle$	0.145	0.322	0.365	0.378
		(0.155)	(0.333)	(0.368)	(0.380)

Table 3.4: The same as in Table 3.3 but for the bond-centered stripes. VBC stripe is not stable in the extended hopping model with $t'/t = -0.15$.

at the value $U/t \simeq 5.7$, being much higher than that predicted by the HA yielding $U/t \simeq 3.8$ [31]. In this method, enhanced stability of the VSC stripes follows from an additional variational parameter per each site d_i, reducing the on-site energy without a strong suppression of the kinetic energy. Remarkably, the total energy difference between the vertical SC and BC stripes at both doping level is comparable to the accuracy of the present calculation. Such degeneracy was also reported in the HF studies of the charge-transfer model [113].

We have also considered the effect of a next-neighbor hopping t' on the relative stability of the stripes. There are numerous experimental and theoretical results which support the presence of finite t' in the cuprates. For example, recent slave-boson studies have revealed that the phenomena of the half-filled vertical stripes in LSCO requires a finite next-neighbor hopping $t'/t \simeq -0.2$ [33]. We shall however not pursue here this result as the influence of t' on the stripe phases within the SBA is extensively reported in Chapter 4. Instead, let us pause for a moment to clarify the influence of t' on the DOS as well as on the FS using a simple tight-binding model,

$$E(\mathbf{k}) = -2t(\cos k_x + \cos k_y) - 4t' \cos k_x \cos k_y. \tag{3.11}$$

By reduction from the CuO$_2$ multiband model to an effective single-band model it has been found that $t > 0$ and $t' < 0$ for a hole doped system, and $t < 0$ and $t' > 0$ in an electron doped system [112]. Although an accidental cancellation of the various contributions results in almost perfect electron-hole symmetry of the nearest-neighbor hopping t, the next-neighbor hopping t' asymmetry appears owing to the fact that the dominant contribution to the latter comes from a direct O-O hopping t_{pp} in the case of a hole hopping. On the contrary, an electron hopping follows from a third order Cu→O→O→Cu process, being therefore dominated by the Cu-O t_{pd} hopping.

In the noninteracting limit the role of t' is to shift the van Hove singularity away from the middle of the band either to higher or to lower energy depending on its sign. Fig. 3.6 shows the tight-binding DOS, centered at $\omega = 0$ with the condition $\int N(\omega)\omega d\omega = 0$, and the occupied states at the doping $x = 1/4$. In

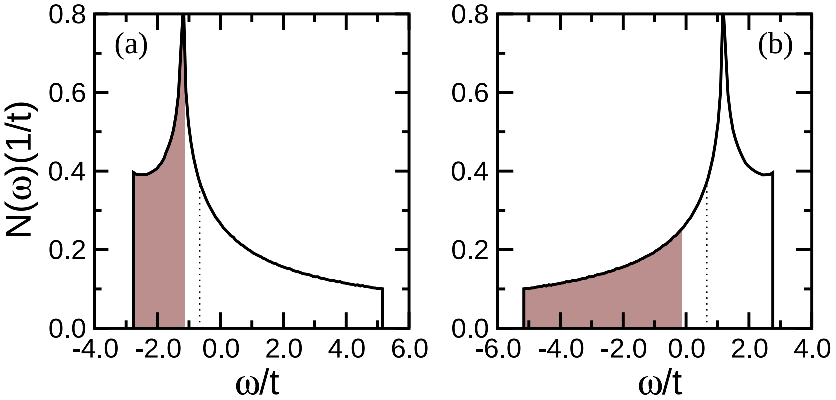

Figure 3.6: Effect of the next-neighbor hopping $t'/t = -0.3$ on the noninteracting 2D DOS at the doping $x = 1/4$: (a) hole doping ($t = 1$); (b) electron doping ($t = -1$). Dotted line shows the Fermi energy in the undoped case, whereas the gray area shows the states occupied by either electrons (a) or holes (b).

the hole-doped case, with the vacuum as the zero electron state, the van Hove singularity lies in the lower part of the band. Conversely, in the case of electron doping, with the vacuum as the zero hole state, the van Hove singularity is shifted towards higher energy part of the band, unoccupied by holes.

Apart from breaking the electron-hole symmetry, the extra parameter t' modifies the geometry of the FS of the free electrons so that it becomes more consistent with the FS topology seen by ARPES [73, 121, 122]. In the electron-doped system NCCO, the low-energy spectral weight at the doping $x = 0.04$ is concentrated in a small electron pocket around the $(\pm\pi, 0)$ and $(0, \pm\pi)$ points. Upon increasing doping, one observes both the modification of the hole pockets and the emergence of new low-lying spectral weights around $(\pm\pi/2, \pm\pi/2)$. Finally, at $x = 0.15$ the FS pieces evolve into a large holelike curve centered at $M = (\pi, \pi)$, as illustrated in Figs. 3.7(a)-(c). In contrast, it is clearly observed in LSCO that in the lightly doped regime $x = 0.03$ doped holes enter into the $(\pm\pi/2, \pm\pi/2)$ points [123], implying that the FS is holelike and centered at the M point. However, Figs. 3.7(d)-(f) depict that in the heavy overdoped regime $x = 0.3$ it converts into the electronlike FS around the $\Gamma = (0, 0)$ point.

Fig. 3.8(a) shows that the model (3.11) with $t' = 0$ has a nested square FS at half-filling which becomes electronlike and shrinks around the Γ point upon hole doping. However, addition of the negative $t' = -0.3$ removes the half-filled nesting and consequently the FS expands in the $(\pm k, 0)$ and $(0, \pm k)$ directions, while contracting along the nodal $(k, \pm k)$ and $(\pm k, k)$ directions due to a large gradient dE/dk along the latter. Indeed, the eigenenergy map, illustrated in Fig. 3.9(a), has in this case a valleylike character with a minimum at the Γ point. Therefore the FS turns into a holelike one with experimentally observed arcs [*cf.* Fig. 3.8(a)]. In contrast, the nearest neighbor hopping t' with the same sign as t interchanges

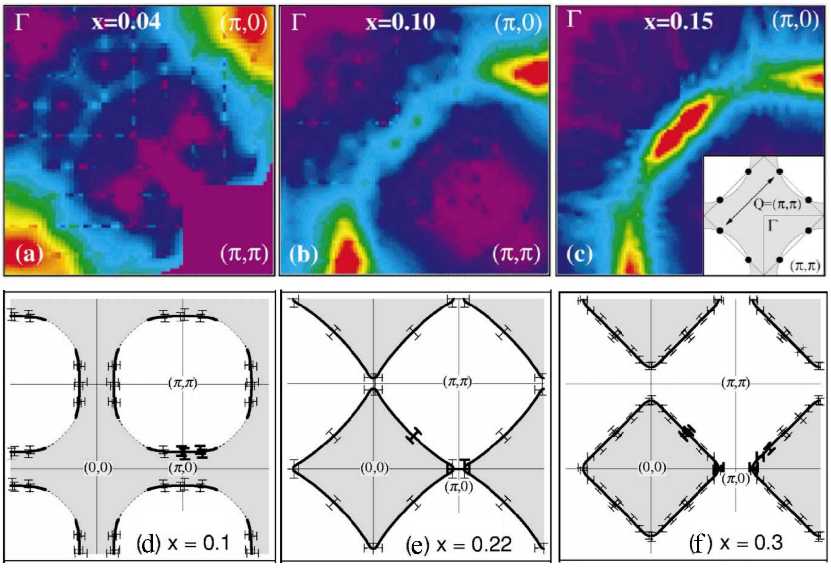

Figure 3.7: Fermi surface plots obtained from the ARPES experiments: (a)-(c) NCCO, after Ref. 122; (d)-(f) LSCO, after Ref. 73.

the expansion- and contraction directions which results in the electronlike FS.

Regarding the electron doped case with $t = -1$, shown in Fig. 3.8(b), positive $t' = 0.3$ (dark solid line) also leads to the appearance of arc segments of the FS and makes it closer to experimental observations. In this case, however, the

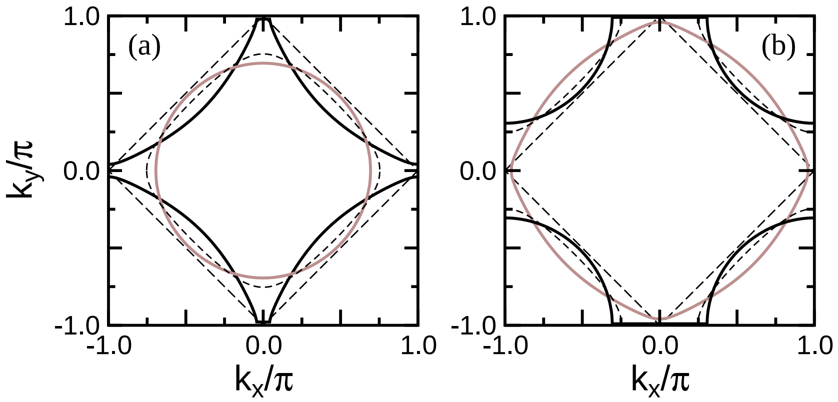

Figure 3.8: Tight-binding FS plots at the doping $x = 1/4$: (a) hole doping with $t = 1$ and: $t' = -0.3$ (black solid line), $t' = 0.3$ (gray solid line), and $t' = 0$ (dashed line); (b) electron doping with $t = -1$ and: $t' = 0.3$ (black solid line), $t' = -0.3$ (gray solid line), and $t' = 0$ (dashed line). The long-dashed line in both panels corresponds to the undoped case with $t' = 0$. The excessively large value of $|t'| = 0.3$ as compared to LSCO was chosen only for more clarity of the figure.

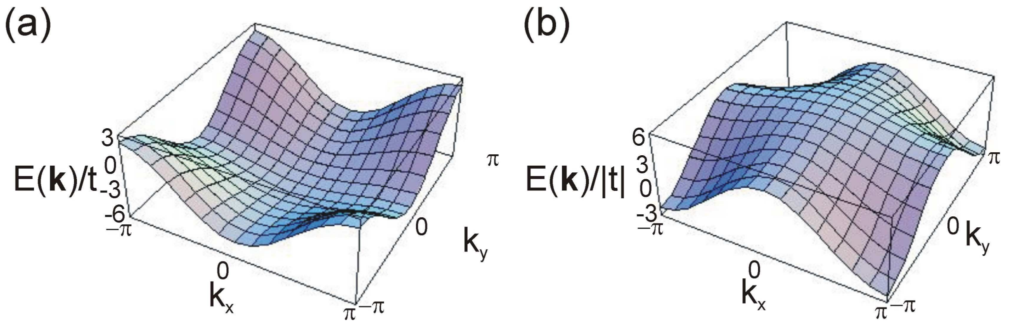

Figure 3.9: Eigenenergy maps of the tight-binding model (3.11) with $t'/t = -0.3$; (a) hole doping ($t = 1$); (b) electron doping ($t = -1$).

minimum energy is centered at the M point, as illustrated in Fig. 3.9(b). In passing, it should be noted that this FS describes the same situation as the one obtained with $t = 1$ and $t' = 0.3$, indicated by the gray solid line in Fig. 3.8(a). Indeed, the sign of t is less important being entirely equivalent to the (π, π) shift of the momentum without changing the corresponding eigenvalues. Consequently, in order to imitate the effect of hole and electron doping it is enough to study the Hamiltonian (3.3) only below half-filling and the alternation between two regimes is possible by the particle-hole transform,

$$c^{\dagger}_{i\sigma} \rightarrow (-1)^{i} c_{i\sigma}, \tag{3.12}$$

mapping the model (3.11) with $t' < 0$ in the one with $t' > 0$. Therefore, in order to avoid any further confusion concerning the signs of t and t' in Eq. (3.11), we set hereafter t to be positive; then a negative t' ($t'/t < 0$) corresponds to hole doping, whereas a positive one ($t'/t > 0$) indicates electron doping.

The remarkable differences of the electronic structure due to the broken hole-electron symmetry by t', result in different phase diagrams of LSCO and NCCO. In the former the long-range AF order is already suppressed in the lightly doped regime $x \simeq 0.03$, while in the latter the antiferromagnetism is known to be robust against electron doping, hence only *commensurate* spin fluctuations are observed at $x = 0.15$ [82]. The robustness of the commensurate spin fluctuations in the electron doped regime is consistent with the ED studies of the t-t'-J [124, 125] and t-t'-t''-J [126, 127] models. It is also supported by the conclusion that a negative t' promotes incommensuration at a lower doping level than a positive one, reached using the QMC technique applied to the extended Hubbard model [128]. Finally, the XPS measurements in NCCO show that the chemical potential monotonously increases with electron doping [83], whereas its shift is suppressed in the underdoped region of LSCO [80]. These data have been nicely reproduced in Ref. 126 for both compounds, except for the low doping regime of LSCO where stripes are expected. All these numerical and experimental results indicate that doped electrons might self-organize in a different way than holes that form DWs.

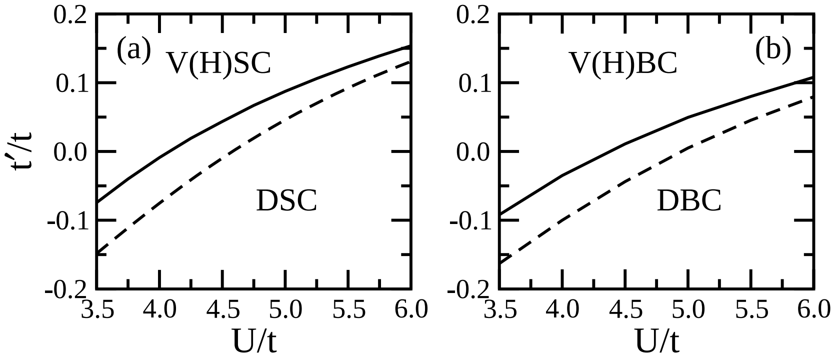

Figure 3.10: Phase boundaries for: (a) site-centered, and (b) bond-centered stripes as obtained in the extended Hubbard model with the next-neighbor hopping t' for doping $x = 1/8$ (solid line) and $x = 1/6$ (dashed line).

Nevertheless, stabile diagonal stripes with one doped electron per site in a DW have been obtained in the slave-boson studies of a more realistic extended three-band model [115], so the problem is still open.

Turning back to the competition between stripes in a doped system, Fig. 3.10(a) shows that negative t' stabilizes the DSC stripes, whereas positive t' favors the VSC ones, within the parameter range where t' does not drive a stripe melting. Analogous crossover from vertical stripes at small $|t'|$ to more complex in shape diagonal ones at $t'/t = -0.1$ and $t'/t = -0.2$ has been found in other HF studies [129]. The explanation is contained in Table 3.5: negative t' gives a positive kinetic energy contribution, which is much more readily minimized by the diagonal charge configuration. Indeed, despite the solitonic mechanism yielding a noticeable kinetic energy loss due to the transverse hopping $t'/t = -0.15$, the overall kinetic energy loss in the case of DSC stripes along the diagonal (11) and antidiagonal $(1\bar{1})$ directions is smaller than the corresponding one for the VSC stripe. A more careful analysis shows that hole propagation along the DSC stripe results in a contribution having the same sign as t'. However, it is entirely canceled by the ones coming from diagonal bonds of the AF domains so that $E_{t'}^{x-y} = 0$.

One observes further that positive t' reduces the anisotropy between the kinetic energy gains in the x- and y-directions for the VSC stripes, and makes their sum more favorable, while negative t' has the opposite effect. For the DSC stripes the total kinetic energy also follows the same trend. The explanation of these results can be found in the reinforcement of stripe order by a negative t' (*cf.* values in parenthesis in Table 3.3), which suppresses the hopping contributions, and its smearing out by positive t' where hopping is enhanced. These trends agree with the earlier finding within the DMFT that the VSC stripe phase is destabilized by kink fluctuations [130]. However, this stripe (dis)ordering tendency also leads to a considerably greater change in the Coulomb energy E_U, listed in Table 3.5, for the DSC than for VSC stripes, which contributes significantly to

	t'/t	E_t^x/t	E_t^y/t	$E_{t'}^{x-y}/t$	$E_{t'}^{x+y}/t$	E_U/t	E_{tot}/t
VSC	-0.15	-0.6876	-0.5886	0.0140	0.0140	0.4778	-0.7704
DBC	-0.15	-0.6279	-0.6279	0.0000	0.0183	0.4562	-0.7813
DSC	-0.15	-0.6275	-0.6275	0.0000	0.0188	0.4533	-0.7829
DBC	0.15	-0.6442	-0.6442	0.0000	-0.0282	0.4883	-0.8283
DSC	0.15	-0.6437	-0.6437	0.0000	-0.0279	0.4855	-0.8298
VB(S)C	0.15	-0.6612	-0.6372	-0.0169	-0.0169	0.4997	-0.8325

Table 3.5: Energies per site: ground-state energy E_{tot}, kinetic energy contributions for the bonds along (10) E_t^x, (01) E_t^y, (11) $E_{t'}^{x-y}$ and $(1\bar{1})$ $E_{t'}^{x+y}$ directions, as well as the potential energy E_U, all site-normalized, in the extended hopping Hubbard model with $U/t = 5$ and $x = 1/8$. VBC stripe is not stable at $t'/t = -0.15$.

the predominance of the former structure for negative t'. In fact, it follows from the increase of hole density within the nonmagnetic stripes and the magnetization density enhancement within the AF domains (*cf.* Table 3.3).

Like their SC counterparts, DBC stripes are also stabilized by negative t' resulting in a phase diagram shown in Fig. 3.10(b). In this case, expelling holes from the AF domains enhances not only magnetization of their atoms but also increases magnetic moment of the hole rich DWs, as illustrated in Table 3.4. This enhancement must, however, strongly suppress the dominant transverse kinetic energy gain of the VBC stripes. Therefore, the latter are already unstable at $t'/t = -0.15$.

It is worth noting that a finite diagonal hopping t' should directly affect the competition between the d-wave pairing correlations and stripes. Indeed, a systematic comparison of stripe and pairing instabilities within the DMRG framework has shown that when the stripes are weakened by positive t', the latter are strongly enhanced due to increasing pair mobility [30]. This effect is accompanied by a simultaneous enhancement of the AF correlations [127]. Conversely, negative t' reinforcing a static stripe order results in the suppression of pair formation in the underdoped region, both in the DMRG technique and Variational Monte Carlo (VMC) [131]. However, the enhanced pairing correlation, attributed to the change of the FS topology in LSCO, has been found in the optimally doped and overdoped regimes [132].

Finally, we investigate the changes in the stripe stability due to repulsive ($V > 0$) and attractive ($V < 0$) nearest-neighbor Coulomb interactions, which give the phase boundaries between the VSC and DSC stripe phases shown in Fig. 3.11(a). We have found that realistic repulsive V favors the latter. The tendency towards the DSC stripe formation at $V > 0$ is primarily due to a large difference between charge densities at the atoms of the DW itself and at all their nearest-neighbor sites, a situation which is avoided in the case of VSC stripe phases (*cf.* Fig. 3.1). Consequently, the former better optimize the repulsive potential energy component

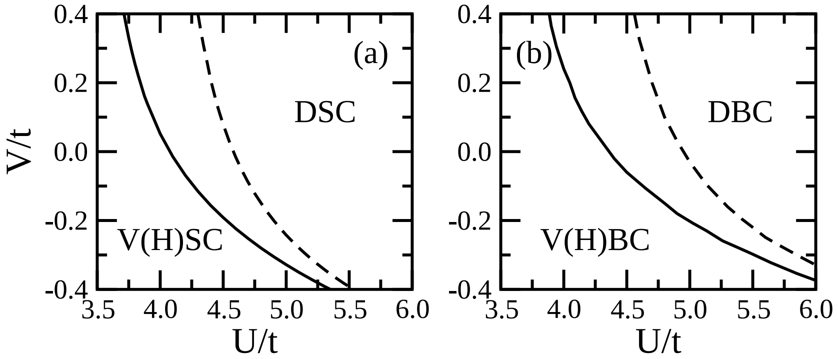

Figure 3.11: Phase diagrams for the site-centered (a) and bond-centered (b) stripes obtained in the extended Hubbard model with the nearest-neighbor Coulomb interaction V for doping $x = 1/8$ (solid line) and $x = 1/6$ (dashed line).

E_V, as shown by the data reported in Table 3.6. Similarly, the fact that the nearest-neighbor interaction V is well minimized only by inhomogeneous charge densities makes the DBC stripe phase more favorable than the VBC one, as shown in Fig 3.11(b). While this is also the leading mechanism for both diagonal stripe suppression at $V < 0$, the asymmetry of the curve in Fig. 3.11 arises from the fact that the lower U values at the transition favor the higher kinetic energy contributions available for the vertical stripes.

However, it has been argued based on the SBA that an increasing repulsive interaction V favors half-filled vertical stripes, hence the latter take over at $V/t \simeq 0.1$ in the parameter regime of $x = 1/8$ and $U/t = 10$ [32]. This finding could naturally explain the appearance of filled diagonal stripes in the nickelates, provided that they were characterized by a small V term, and the stability of the half-filled vertical ones in the Nd-codoped cuprates due to possibly larger V. It is also worth mentioning other HF [133] and variational [134] studies in which a variety of in-

	V/t	E_t^x/t	E_t^y/t	E_U/t	E_V/t	E_{tot}/t
DBC	-0.4	-0.6322	-0.6322	0.4626	-0.6194	-1.4212
DSC	-0.4	-0.6319	-0.6319	0.4602	-0.6193	-1.4229
VB(S)C	-0.4	-0.6655	-0.6083	0.4749	-0.6251	-1.4240
VB(S)C	0.4	-0.6838	-0.6214	0.5063	0.6207	-0.1782
DBC	0.4	-0.6424	-0.6424	0.4829	0.6176	-0.1843
DSC	0.4	-0.6412	-0.6412	0.4789	0.6171	-0.1864

Table 3.6: Energies per sites: ground-state energy E_{tot}, kinetic energy (E_t^x, E_t^y) and potential energy (E_U, E_V) components in the extended Hubbard model with the nearest-neighbor Coulomb interaction V for $U/t = 5$ and $x = 1/8$.

triguing stripe phases, coexisting at $V/t \simeq 1.5$ with charge order, has been found in a broad doping region.

In summary, we have shown that a competition between vertical (horizontal) and diagonal stripes dominates the behavior of the charge structures formed on doping the Hubbard model in the physically interesting regime of $3.5 \leq U/t \leq 6$ within the HA. The detailed charge distribution and the type of stripe order depend on the ratio U/t, on the value of the next-neighbor hopping t', and on the nearest-neighbor Coulomb interaction V.

3.2.2 Single-band Peierls-Hubbard Hamiltonian

In the preceding Section, we have demonstrated that a finite anisotropy of the transfer integral t can tip the balance between vertical and diagonal stripes. Here we will show that such anisotropy naturally emerges in a doped system with DWs, described by a single-band Peierls-Hubbard Hamiltonian,

$$H = -\sum_{ij\sigma} t_{ij}(u_{ij}) c^{\dagger}_{i\sigma} c_{j\sigma} + U \sum_{i} n_{i\uparrow} n_{i\downarrow} + \tfrac{1}{2} K \sum_{\langle ij \rangle} u^{2}_{ij}. \tag{3.13}$$

In this model we keep only the leading term and assume a linear dependence of the nearest neighbor hopping element t_{ij} on the lattice displacements u_{ij},

$$t_{ij}(u_{ij}) = t_0(1 + \alpha u_{ij}). \tag{3.14}$$

Furthermore, we include the elastic energy $\propto K$ which allows to investigate the stability of the system with respect to a given lattice deformation and to determine the equilibrium configuration. For convenience, we parametrize the electron-lattice coupling with a single quantity, $\lambda = \alpha^2 t_0/K$, with the parameter values $K/t_0 = 18\text{Å}^{-2}$ and $\alpha = 3\text{Å}^{-1}$ assumed following the earlier HF studies [111], but we note that a different choice could also give the same value of α. As previously, we focus on the doping $x = 1/8$ ($x = 1/6$) and perform the calculations on 16×16 (12×12) clusters, respectively, with periodic boundary conditions. Our calculations have shown that such clusters give the most stable filled stripe solutions for the selected doping levels. The model (3.13) was solved self-consistently in real space within the HA (3.4). Thereby, we used an approximate saddle-point formula for the equilibrium relation between the actual deformation u_{ij} of a given bond and the bond-charge density $\langle c^{\dagger}_{i\sigma} c_{j\sigma} \rangle$,

$$u^{(0)}_{ij} \simeq \frac{\alpha t_0}{K} \sum_{\sigma} \langle c^{\dagger}_{i\sigma} c_{j\sigma} + h.c. \rangle, \tag{3.15}$$

being a consequence of the linearity assumption in Eq. (3.14).

Quite generally, it is a widely held belief in a strong sensitivity of inhomogeneous doping states to small changes of λ, supported both by the HF [135, 136] and ED studies [137]. Further, it has been shown that the electron-lattice interaction favors DW solutions over other possible phases like isolated polarons or bipolarons [101, 111]. Finally, in Chapter 2 we have discussed some experiments suggesting that the nickel-centered stripes are favored at low temperature, whereas the oxygen-centered ones are stabilized at higher temperature [91, 92]. The transition might be easily explained by considering models with a temperature-dependent electron-lattice coupling. Indeed, an increasing elastic constant α, which modifies the nearest-neighbor Ni-O hopping, gradually changes oxygen-centered stripes into the nickel-centered ones, as in the HF studies of the four-band Peierls-Hubbard model. Such a Hamiltonian contains, besides the $|x^2-y^2\rangle$ orbitals usually included in the cuprate oxide models, the $|3z^2-r^2\rangle$ orbitals, that are necessary to account for the high spin state ($S=1$) in the undoped nickel oxides [102]. Certainly, with a stronger electron-lattice coupling, the system gains more kinetic energy owing to larger lattice distortions. However, as it was discussed in the preceding Section, the largest kinetic energy contributions are released on bonds around the DWs. Consequently, in the strong electron-lattice coupling regime (elastic constant α should be stiffer at lower temperatures), the diagonal metal-centered stripes with four oxygens neighboring each metal site are promoted over the oxygen-centered ones with two metal-oxygen bonds at the DWs (*cf.* Fig. 2.10). Therefore, a complete discussion of the stripe phase stability in correlated oxides has to include coupling to the lattice.

We turn now to the most important aspect of this Section. Figs. 3.12 and 3.13 illustrate the effect of the finite electron-lattice coupling $\lambda = 0.5$ on the SC and BC stripes, respectively. Both figures give a clear demonstration that, in contrast to the hopping anisotropy ϵ_t discussed above, finite λ markedly modifies both the local hole density (3.7) and modulated magnetization (3.8) [*cf.* also Table 3.3 with 3.7 (SC stripes) and Table 3.4 with 3.8 (BC stripes)]. Basically, the influence of λ resembles the effect of positive t', smearing out the stripe order by ejecting holes from the DWs, being however much stronger. In fact, hole delocalization not only suppresses the magnetization within the AF domains, but also noticeably quenches magnetic moments of the BC domain walls. These trends can be understood by considering energy increments: the kinetic E_t, on-site E_U, and elastic energy E_K, as explained below.

In general, a system described by the Hamiltonian (3.13) might be unstable towards lattice deformations only if the covalency increase is large enough to compensate both the E_U and E_K energy cost. Without the electron-lattice coupling, a compromise solution is mainly reached by developing a strong magnetic order in the AF domains, where a possible kinetic energy gain is irrelevant, and by forming nonmagnetic or weakly magnetic DWs with large hole density. As we have already shown, transverse charge fluctuations around the DWs yield the main kinetic energy contribution. However, enhanced covalency and mixing of the lower $\sim \epsilon_d$ and higher $\sim \epsilon_d + U$ energy states between a DW and the surrounding sites generate some not negligible amount of double occupancy,

$$D(l_x) = \langle n_{(l_x,0),\uparrow} n_{(l_x,0),\downarrow} \rangle . \tag{3.16}$$

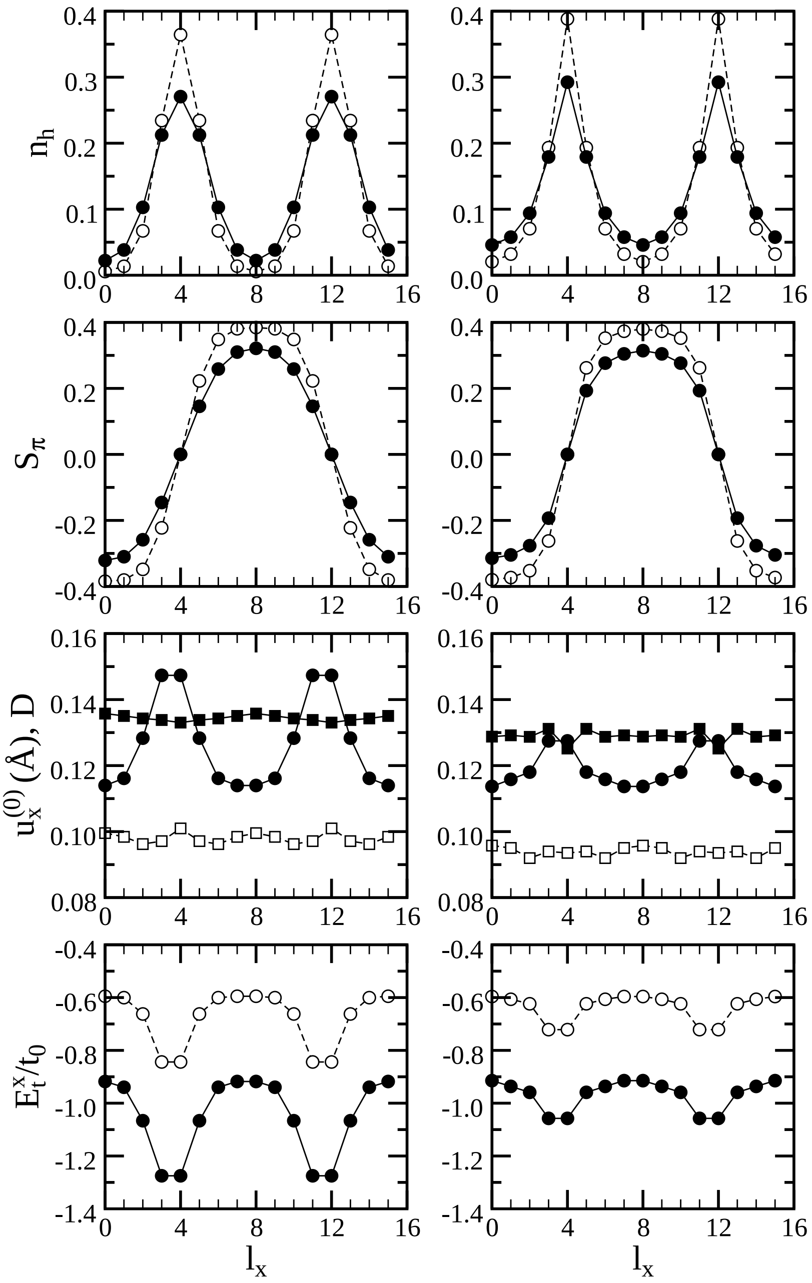

Figure 3.12: Local hole $n_{\mathrm{h}}(l_x)$ (top) and magnetization $S_\pi(l_x)$ (second row) density; fractional change of the length for the bonds to the right nearest-neighbor along the x-direction $u_x^{(0)}$ (circles) and double occupancy $D(l_x)$ (squares) (third row), as well as the kinetic energy $E_t^x(l_x)$ projected on the bonds in the x-direction (bottom) of the VSC (left) and DSC (right) stripe phases, as obtained in the Peierls-Hubbard model (3.13) with $U/t = 5$, $\lambda = 0.5$ and $x = 1/8$ (filled symbols). For comparison the result obtained with $\lambda = 0$ are shown by open symbols.

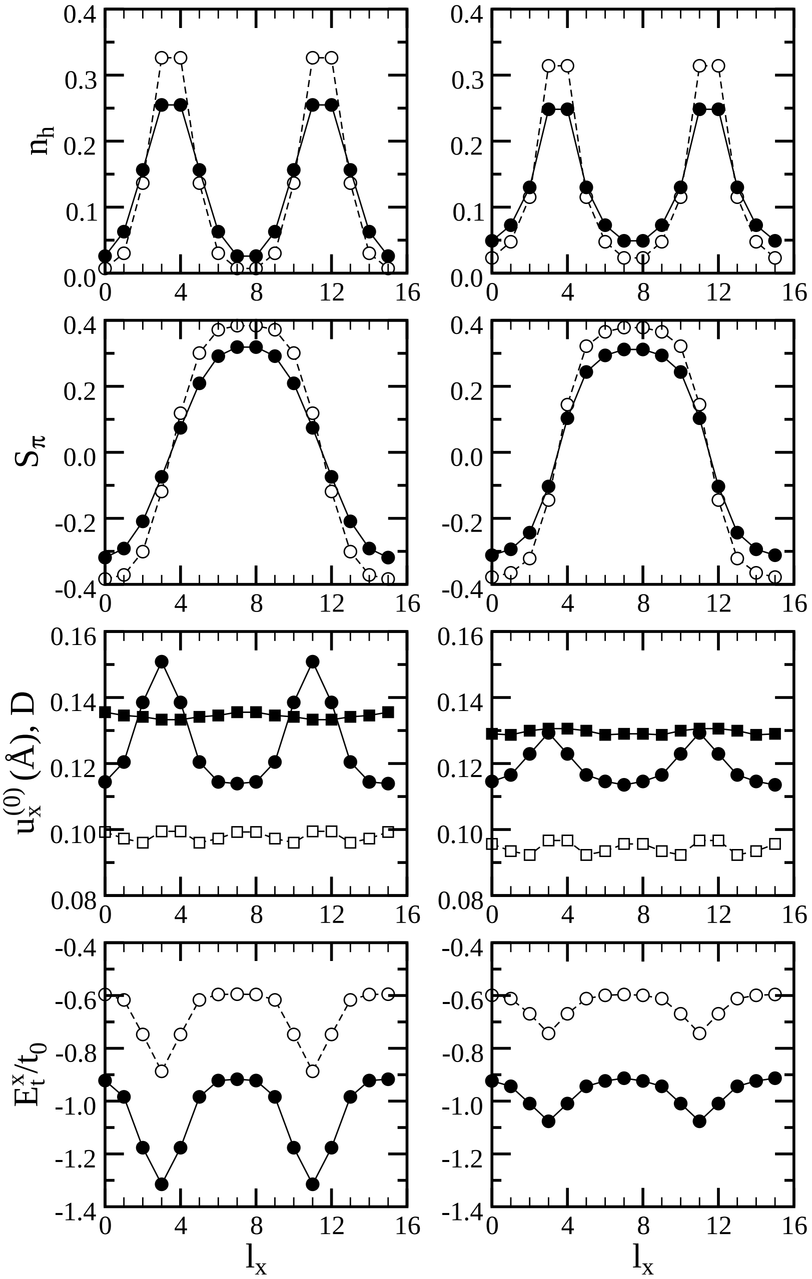

Figure 3.13: The same as in Fig. 3.12 but for the bond-centered stripes.

Indeed, in the $\lambda = 0$ case, double occupancy $D(l_x)$ reaches its maximum at the DWs, as illustrated in Figs. 3.12 and 3.13. The only exception is the DSC stripe phase (right panels of Fig. 3.12) with the largest $D(l_x)$ in the AF domains. As a consequence, the latter is the most localized one with the smallest kinetic energy gain (*cf.* Table 3.1).

The situation changes upon turning on the electron-lattice coupling. When

	i	1	2	3	4	5
VSC	$\langle n_{\mathrm{h}i}\rangle$	0.270	0.212	0.103	0.038	0.022
	$\langle S_i^z\rangle$	0.000	0.146	0.259	0.310	0.321
DSC	$\langle n_{\mathrm{h}i}\rangle$	0.292	0.179	0.094	0.058	0.046
	$\langle S_i^z\rangle$	0.000	0.193	0.277	0.305	0.314

Table 3.7: Local hole $\langle n_{\mathrm{h}i}\rangle$ and magnetization $\langle S_i^z\rangle$ density of the SC stripe phases, all labeled by decreasing hole density in the x-direction, in the Peierls-Hubbard model on a 16×16 cluster with $U/t = 5$, $\lambda = 0.5$ and $x = 1/8$.

the electrons couple to the lattice ($\lambda \neq 0$), the bonds contract, and the saddle point values of the distortions (3.15): $u_{ij}^{(0)} = \langle u_{ij}\rangle$ along (10) and (01) direction, respectively, are finite. However, a nonuniform charge distribution results in a different bondlength in the cluster. This is illustrated in Figs. 3.12 and 3.13 showing a fractional change of the length for the bonds to the right nearest-neighbor along the x-direction $u_x^{(0)}$ (third row). Although the values of $u_{ij}^{(0)}$ in the AF domains are also substantial, the largest lattice deformations $\sim \langle c_{i\sigma}^{\dagger} c_{j\sigma}\rangle$ appear either on the bonds connecting atoms of the DWs with their nearest neighbors (*cf.* Fig. 3.12), or on the bonds which join two atoms of the bond-centered DWs (*cf.* Fig. 3.13). Accordingly, a strengthening nearest neighbor hopping (3.14) enables a larger kinetic energy gain on these bonds (*cf.* bottom of Figs. 3.12 and 3.13).

In fact, the effect of increasing covalency is accompanied by partial quenching of magnetic moments. In order to appreciate this tendency, let us consider a site in the AF domain with larger density of ↑-spin electrons. Once the magnetization is reduced, it pushes up the corresponding ↑-spin energy level, forming the Lower Hubbard Band (LHB), and lowers that for the ↓-spin level, constituting originally the Upper Hubbard Band (UHB). As a result, the locally raised ↑-spin state becomes more mixed with the surrounding ↓-spin states, increasing simultaneously bond-charge density. At the same time, electrons, jumping forth and back between the central site occupied by the ↑-spin and its nearest neighbors filled by the ↓-spin, enhance considerably double occupancy $D(l_x)$, as shown in Figs. 3.12 and 3.13. Such weaker stripe order results in a more uniform distribution of $D(l_x)$.

	i	1	2	3	4
VBC	$\langle n_{\mathrm{h}i}\rangle$	0.255	0.156	0.063	0.026
	$\langle S_i^z\rangle$	0.074	0.209	0.291	0.319
DBC	$\langle n_{\mathrm{h}i}\rangle$	0.248	0.130	0.073	0.049
	$\langle S_i^z\rangle$	0.103	0.243	0.294	0.312

Table 3.8: The same as in Table 3.7 but for the BC stripe phases.

	E_t^x/t	E_t^y/t	E_U/t	E_K/t	$E_{\rm tot}/t$
DBC	-0.9679	-0.9679	0.6478	0.2548	-1.0332
DSC	-0.9670	-0.9670	0.6450	0.2544	-1.0346
VB(S)C	-1.0496	-0.9248	0.6719	0.2638	-1.0387

Table 3.9: Site-normalized ground-state energy $E_{\rm tot}$, kinetic energy (E_t^x, E_t^y) and potential energy (E_U, E_K) components, as obtained in the Peierls-Hubbard model with $U/t = 5$, $\lambda = 0.5$ and $x = 1/8$.

Nevertheless, the increase of the elastic energy and concomitant enhancement of the on-site energy, both owing to finite bond contractions (3.15), is compensated by the kinetic energy gain (*cf.* Tables 3.1 and 3.9).

We close this section with phase diagrams shown in Fig. 3.14. They were obtained by varying U and the coefficient α, while maintaining constant $K/t_0 = 18\text{Å}^{-2}$. The increased stability of vertical stripes follows from the relative stronger enhancement of the local hopping elements (3.14) (and consequently larger gain of the kinetic energy), especially on the bonds in the direction perpendicular to the DWs itself. However, although the arguments were given that Sr-doped La_2NiO_4 is stronger localized than its cuprate counterpart $La_{2-x}Sr_xCuO_4$, primarily due to the large effect of the electron-phonon coupling [138], neutron scattering studies revealed appearance of diagonal stripes within the NiO_2 planes [14]. In fact, the HF calculations of Zaanen and Littlewood, based on the four-band model with a finite electron-lattice coupling, have yielded a narrow charge stripe centered on a diagonal row of Ni atoms [101]. Hence, our result remains in contradiction both with the experimental data and with theory, so one may conclude that the single-band Hubbard model describes quite well CuO_2 planes but is insufficient to

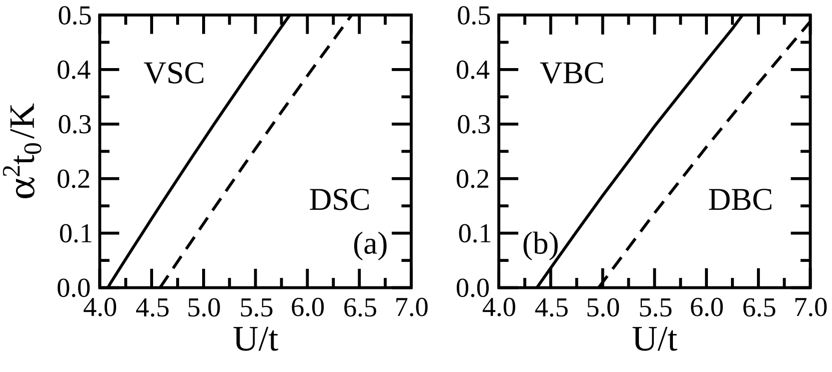

Figure 3.14: Phase diagrams for site-centered (a) and bond-centered (b) stripe structures as calculated from the Peierls-Hubbard model for doping $x = 1/8$ (solid line) and $x = 1/6$ (dashed line).

model a physical situation within NiO_2 ones. We shall return to this problem in Chapter 5 discussing stability of stripe phases obtained in a more appropriate for the nickelates two-band model.

3.3 Stability of half-filled stripes

So far we have only been concerned with the filled stripes. However, neutron experiments on the Nd-codoped LSCO cuprates reveal that the observed stripes are filled by one hole per two DWs, corresponding to the so-called half-filled stripes [13]. Unfortunately, the latter are only locally stable within the HF approximation. Even though some additional Hamiltonian terms like the nearest-neighbor Coulomb repulsion V may slightly enhance their stability, filled stripes remain always better solutions [111]. Nonetheless, we will show that under some circumstances, half-filled vertical site-centered (HVSC) stripes become energetically favored over the filled ones even in the HA.

The first important proviso involves a modulation in a charge or longitudinal spin channel, i.e., the period on the stripe should become four times the lattice constant [111]. Such a stripe with a quadrupling of the period due to the on-wall SDW is shown in the upper panel of Fig. 3.16. In order to understand this condition, let us discuss briefly how stripes modify the band structure of a simple antiferromagnet. In general, each filled DW induces formation of two unoccupied bands, i.e., one for the ↑-spin and another one for the ↓-spin, lying within the

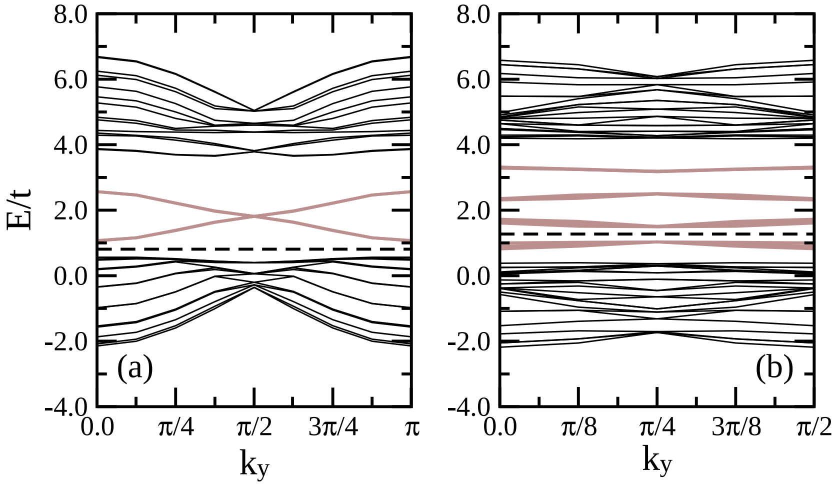

Figure 3.15: Band structure as a function of parallel momentum k_y, calculated from a unit cell of width $N_x = 16$ in the Hubbard model with $U/t = 5$, with a doubled (a) or quadrupled (b) Brillouin zone. Black (gray) line corresponds to the bulk (mid-gap) bands, respectively, whereas the dashed line indicates the Fermi level. (a) VSC stripe; (b) HVSC stripe.

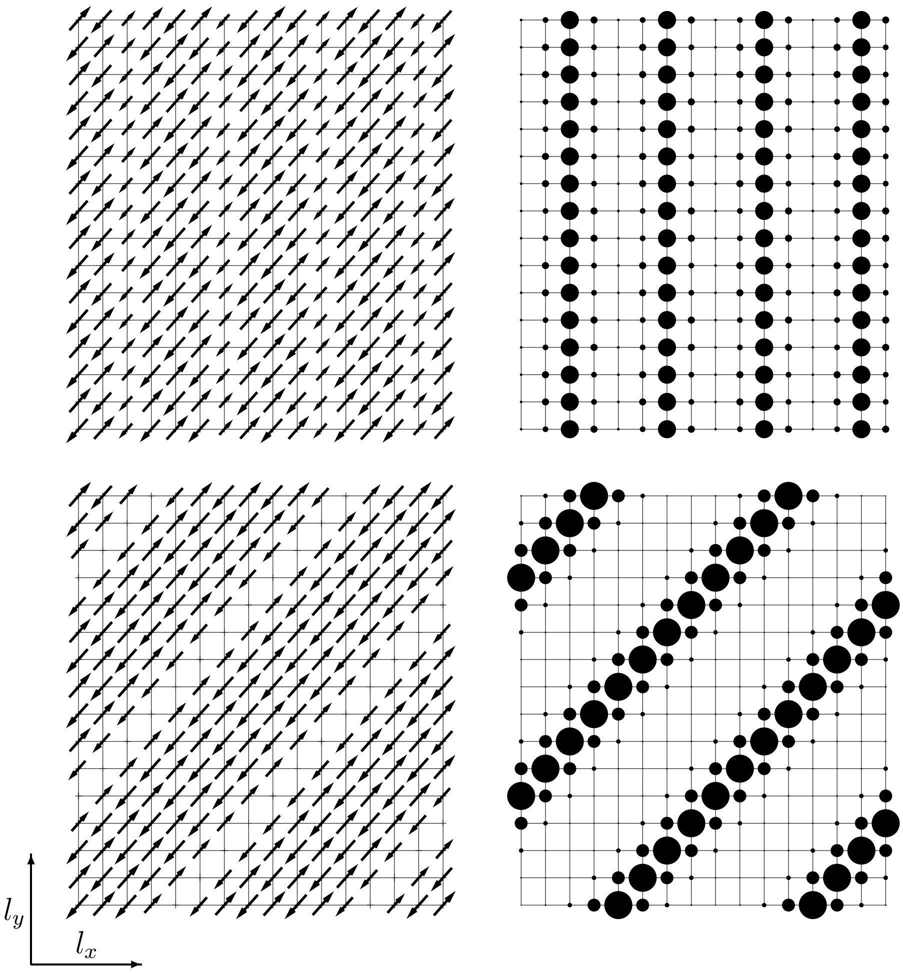

Figure 3.16: Half-filled vertical site-centered (HVSC) and filled diagonal site-centered (DSC) stripe phase as found for $U/t = 5$ and $t'/t = -0.3$ at hole doping $x = 1/8$. The length of arrows is proportional to the magnetization $\langle S_i^z \rangle$ and the hole density $\langle n_{\mathrm{h}i} \rangle$ is scaled by the diameter of black circles.

Mott-Hubbard gap, as illustrated in Fig. 3.15(a). Consequently, their special stability rests on a gap that opens in the symmetry broken state between the highest occupied state of the LHB and the bottom of the mid-gap band. One may ask what happens now if one decreases the doping level so as to get half-filled stripes without a period quadrupling? Certainly, the twofold degenerate mid-gap states become *quarter filled*, as there is only half a hole per one DW. Hence, any stringent reason for such a symmetry breaking with the Fermi level in the middle of the lower mid-gap band is absent. Therefore, one needs to lower the symmetry by a period quadrupling. This might be accomplished by introducing a SDW modulation along the DWs which leads to the band structure shown in Fig. 3.15(b), with a gap that opens up exactly at the Fermi energy.

	t'/t	E_t^x/t	E_t^y/t	$E_{t'}^{x-y}/t$	$E_{t'}^{x+y}/t$	E_U/t	$E_{\rm tot}/t$
HVSC	0.0	−0.5846	−0.6585	0.0000	0.0000	0.4627	−0.7804
VSC	0.0	−0.6753	−0.6147	0.0000	0.0000	0.4900	−0.8000
DSC	0.0	−0.6368	−0.6368	0.0000	0.0000	0.4696	−0.8040
DSC	−0.3	−0.6152	−0.6152	0.0000	0.0257	0.4379	−0.7668
HVSC	−0.3	−0.5786	−0.6198	−0.0080	−0.0080	0.4322	−0.7678

Table 3.10: Energies per site: ground-state energy $E_{\rm tot}$, kinetic energy contributions for the bonds along (10) E_t^x, (01) E_t^y, (11) $E_{t'}^{x-y}$ and $(1\bar{1})$ $E_{t'}^{x+y}$ directions, as well as the potential energy E_U of the HVSC, VSC and DSC stripe phases in the t-t'-U model with $U/t = 5$ and $x = 1/8$. VSC stripe is not stable at $t'/t = -0.3$.

However, in spite of better optimizing the potential energy E_U, the HVSC stripe phase represents only a local minimum of energy, being less stable than the filled V(D)SC one (*cf.* Table 3.10). Thus, guided by the observation that finite negative t' expels holes from the AF domains and reinforces the stripe order, we investigate whether this mechanism suffices to stabilize the former structure in the t-t'-U model.

In order to establish the role of t', let us first discuss Fig. 3.17 showing how the charge and spin configuration around the HVSC stripe is altered in the presence of increasing $|t'|$. In Fig. 3.17(a), which depicts the $t' = 0$ case, we label all inequivalent bond kinetic energies along the (10) ($\text{A}_x, \ldots, \text{D}_x$), (01) ($\text{A}_y, \ldots, \text{G}_y$), (11) (A,...,H), and $(1\bar{1})$ (in parenthesis) directions. The corresponding values are listed in Table 3.12. The most striking feature of the HVSC stripe phase is that the main kinetic energy gain is released not by transverse charge fluctuations but by on-wall hopping processes on the bonds C_y (F_y) connecting ferromagnetically (antiferromagnetically) coupled sites, respectively. Another interesting property

t'/t	l	1	2	3	4	5
0.00	$\langle n_{\rm h\mathit{l}} \rangle$	0.040	0.116	0.265	0.080	0.040
	$\langle S_l^z \rangle$	−0.369	0.325	−0.199	−0.348	0.369
−0.15	$\langle n_{\rm h\mathit{l}} \rangle$	0.040	0.101	0.268	0.092	0.040
	$\langle S_l^z \rangle$	−0.372	0.340	−0.199	−0.346	0.372
−0.30	$\langle n_{\rm h\mathit{l}} \rangle$	0.039	0.086	0.269	0.106	0.039
	$\langle S_l^z \rangle$	−0.375	0.355	−0.206	−0.344	0.375
−0.45	$\langle n_{\rm h\mathit{l}} \rangle$	0.036	0.072	0.270	0.122	0.036
	$\langle S_l^z \rangle$	−0.377	0.372	−0.221	−0.339	0.377

Table 3.11: Local hole $\langle n_{\rm h\mathit{l}} \rangle$ and magnetization $\langle S_l^z \rangle$ density of the HVSC stripe phase, all labeled by $l = (l_x, 0)$ (*cf.* Fig. 3.17).

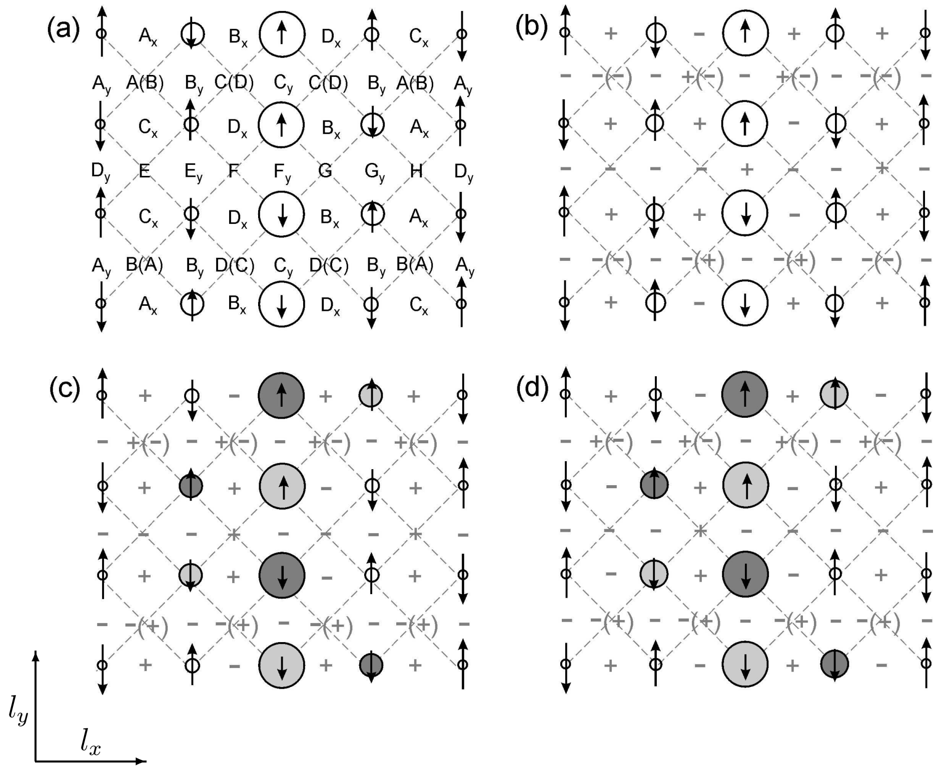

Figure 3.17: Rearrangement of the HVSC stripe order with increasing next-neighbor hopping $|t'|$: (a) $t'/t = 0$; (b) $|t'|/t = 0.15$; (c) $|t'|/t = 0.30$; (d) $|t'|/t = 0.45$. Capital letters label bond kinetic energies along the (10) (A$_x$, ... ,D$_x$), (01) (A$_y$, ... ,G$_y$), (11) (A, ... ,H), and (1$\bar{1}$) (in parenthesis) directions, listed in Table 3.12, while $+$ ($-$) correspond to the bond kinetic energy gain (lost), respectively, with respect to the $t' = 0$ case (U/t=5, $x = 1/8$). Shadow circles indicate two crossing zigzag lines along and between which moving holes gain the kinetic energy.

is that the system tries to regain some of the kinetic energy in the transverse direction by developing a charge-density wave (CDW) on nearest-neighbor sites to the DW itself. Indeed, although the charge distribution along the stripe is uniform, the on-wall SDW causes the CDW on both sides of the DW. This clearly promotes the hopping between the AF sites (bonds B_x) over the FM ones (bonds D_x).

Further, as reported in Table 3.11, the CDW is strongly influenced by finite t', being first almost entirely quenched when $t' = -0.15$ [*cf.* Fig. 3.17(b)] and then it is gradually restored [*cf.* Fig. 3.17(c)-(d)]. These trends are fully consistent with the DMFT studies of the effect of a single kink along the HVSC stripe [130]. It has been established that the energy cost of forming a kink increases slightly with increasing $|t'|$ up to $|t'|/t < 0.1$. However, further increase leads to the opposite effect and finally a wall with a kink becomes favored at $|t'|/t \simeq 0.3$.

	t'/t			
bond	0	-0.15	-0.30	-0.45
A_x	-0.6081	-0.6098	-0.6128	-0.6141
B_x	-0.6652	-0.6322	-0.5964	-0.5482
C_x	-0.6277	-0.6290	-0.6285	-0.6257
D_x	-0.4377	-0.4590	-0.4769	-0.4885
A_y	-0.6057	-0.5945	-0.5863	-0.5822
B_y	-0.6003	-0.5859	-0.5616	-0.5281
C_y	-0.8505	-0.8216	-0.7802	-0.7234
D_y	-0.5759	-0.5681	-0.5628	-0.5623
E_y	-0.6515	-0.6175	-0.5781	-0.5299
F_y	-0.7206	-0.7223	-0.6933	-0.6364
G_y	-0.6635	-0.6533	-0.6344	-0.6046
A	0.0000	0.0022	-0.0002	-0.0053
B	0.0000	0.0068	0.0164	0.0262
C	0.0000	-0.0343	-0.0761	-0.1300
D	0.0000	0.0252	0.0310	0.0128
E	0.0000	0.0039	0.0055	0.0033
F	0.0000	0.0046	-0.0071	-0.0367
G	0.0000	0.0180	0.0248	0.0164
H	0.0000	-0.0010	-0.0007	0.0020

Table 3.12: Bond kinetic energies along the (10) ($A_x,\ldots,D_x$), (01) ($A_y,\ldots,G_y$), (11) and ($1\bar{1}$) (A,...,H) directions around the HVSC stripe phase shown in Fig. 3.17.

Note, however, that although the overall shape of the brought back CDW is the same as of the initial one, the physical situation is fundamentally different. Namely, in the $t' = 0$ limit, it is energetically advantageous for the system to equalize hole density between sites connected by the bonds B_x (AF coupling), whereas in the large $|t'|$ limit, it rather tries to equalize hole density between sites connected by the bonds D_x (FM coupling). Accordingly, such a charge redistribution results in two crossing zigzag lines, which facilitate the propagation of holes. Indeed, each path consists of a -C-F- bond pattern along the (11) direction and analogous sequence in the ($1\bar{1}$) direction. Even though a moving hole gains kinetic energy on both type of bonds, a more significant gain is achieved on the FM bond C, being the driving force in the formation of zigzag pattern. It is also supported by a systematically growing kinetic energy gain with increasing $|t'|$ on the FM bond D_x connecting the zigzag paths (*cf.* Table 3.12). Finally, it is worth pointing out that a tendency towards the formation of zigzag chains with ferromagnetically ordered t_{2g} spins, has been widely observed in the CE phase of doped manganites such as $La_{0.5}Ca_{0.5}MnO_3$ and $Nd_{0.5}Sr_{0.5}MnO_3$ [139].

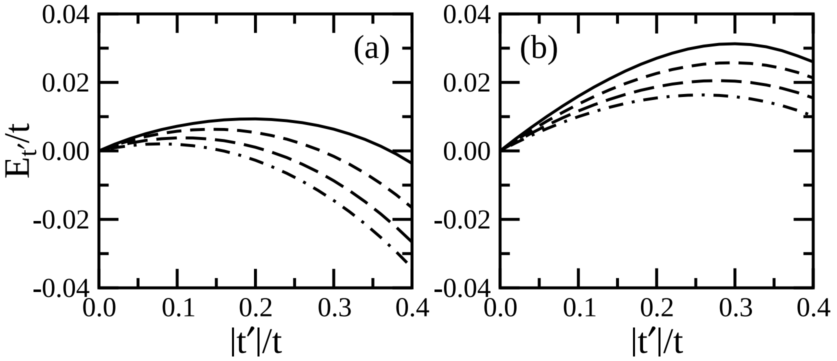

Figure 3.18: Average kinetic energy $E_{t'}$ per diagonal bond as a function of increasing next-neighbor hopping $|t'|$ for $U/t = 4$ (solid line), $U/t = 5$ (dashed line), $U/t = 6$ (long-dashed line), and $U/t = 7$ (dot-dashed line): (a) HVSC stripe phase; (b) DSC stripe phase.

The effect of increasing $|t'|$ on the kinetic energy per diagonal bond E_t' of the HVSC stripe phase illustrates Fig. 3.18(a). One observes that in the small $|t'|$ regime next-neighbor hopping processes cost energy and therefore they are suppressed by quenching the CDW order on sites next to the DW. However, towards larger $|t'|$, the kinetic energy associated with next-neighbor hopping becomes negative despite the negative sign of t'. This is possible by a change in coefficients of the Slater determinant such that on average the sign of the diagonal bond hopping term is negative. Consequently, the system develops a new CDW so as to optimize the $E_{t'}$ gain. In contrast, $E_{t'}$ of the filled DSC stripe phase remains

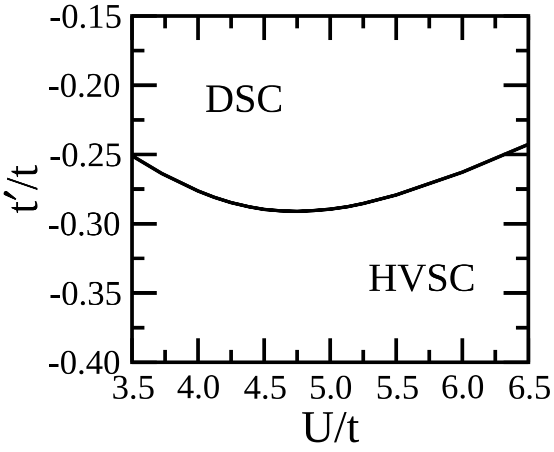

Figure 3.19: Phase boundary between filled diagonal site-centered (DSC) stripe phase and half-filled vertical site-centered (HVSC) one as obtained in the t-t'-U Hubbard model with doping $x = 1/8$.

positive even in the large $|t'| = 0.4t$ regime, as shown in Fig. 3.18(b). Moreover, increasing Coulomb repulsion U yields in this case only a small suppression of $E_{t'}$, whereas the same increase of U is reflected in much larger $E_{t'}$ gain of the HVSC stripe phase. This, together with a better on-site energy E_U, explains a broader region of their stability in the strongly correlated regime, as illustrated in Fig. 3.19. We interprete their enhanced stability in the small U regime as following from the melting of both stripe phases. Indeed, increased mobility of the holes released from the DSC stripes results in a faster, as compared to the HVSC case, enhancement of the $E_{t'}$ energy cost upon increasing $|t'|$.

In conclusion, we have found that the next-neighbor hopping t' plays an important role in affecting the relative stability between filled and half-filled stripe phases. However, the established value $|t'|/t \simeq 0.3$ opening a window for the stability of the HVSC stripe phase, is excessively large as compared to the model parameter $t'/t \simeq -0.1$ of LSCO compounds. This indicates that it is necessary to go beyond the HF treatment of the cuprate stripes by including local electron correlations, which will be the subject of Chapter 4. However, $t'/t \simeq -0.3$ corresponds to the value appropriate for $\mathrm{YBa_2Cu_3O_{6+\delta}}$ [140] and indeed half-filled vertical stripe phase has been reported in $\mathrm{YBa_2Cu_3O_{6.35}}$ [69], whereas only IC magnetic fluctuations have been observed at larger doping level region [61].

3.4 Static correlation functions

In order to make a direct comparison with experimental findings, we calculate a Fourier transform of the static hole-hole (spin-spin) correlation function, which gives the charge (magnetic) structure factor,

$$C(\mathbf{k}) = \frac{1}{N}\sum_{ij} e^{i\mathbf{k}(\mathbf{R}_i-\mathbf{R}_j)}\langle n_{\mathrm{h}i}\rangle\langle n_{\mathrm{h}j}\rangle, \tag{3.17}$$

$$S^z(\mathbf{k}) = \frac{1}{N}\sum_{ij} e^{i\mathbf{k}(\mathbf{R}_i-\mathbf{R}_j)}\langle S_i^z\rangle\langle S_j^z\rangle, \tag{3.18}$$

where the summations include all pairs $\{ij\}$ in a considered cluster with N sites. Let us first discuss the charge and spin response of the filled SC stripe phase, shown in Fig. 3.1, at the doping $x = 1/8$. The local hole (magnetization) density $\langle n_{\mathrm{h}i}\rangle$ ($\langle S_i^z\rangle$), respectively, of nonequivalent atoms used in Eqs. (3.17) and (3.18) are given in Table 3.3. In fact, the BC stripe phase shown in Fig. 3.2 has the same size of the magnetic unit cell. As a consequence, it gives practically the same neutron scattering pattern and, unfortunately, both structures are not distinguishable experimentally.

We observe, in both panels of Fig. 3.20, the dominating weight of $C(\mathbf{k})$ at the $\Gamma = (0,0)$ point, as it is usually found for a uniform distribution. However, periodically spaced with the distance $d = 8$ DWs give rise to additional charge Bragg peaks at $\mathbf{Q}_c^v = (\pm 2\pi\epsilon, 0)$ (VSC stripe phase) and $\mathbf{Q}_c^d = \pm(2\pi\epsilon, 2\pi\epsilon)$ (DSC

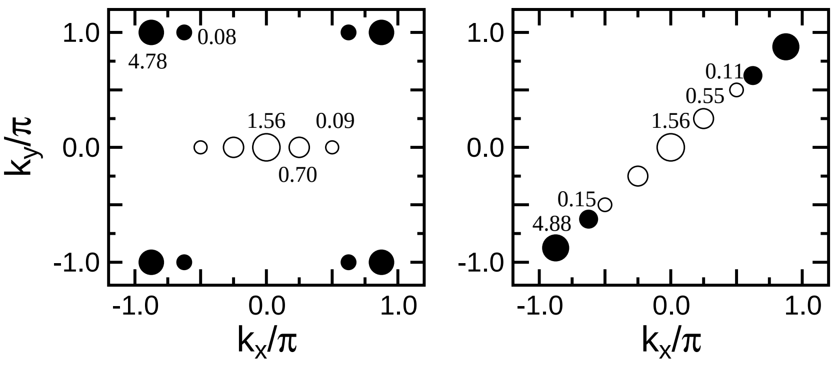

Figure 3.20: Reciprocal space pattern of the VSC (left panel) and DSC stripe phases (right panel) shown in Fig. 3.1 separated by $d = 8$ lattice spacings. Filled (open) circles correspond to the magnetic (charge) peaks, respectively. Bond-centered structures shown in Fig. 3.2 give practically the same patterns.

stripe phase) with $\epsilon = 1/8$. Moreover, instead of a single maximum at the $M = (\pi, \pi)$ point, characteristic of the AF phase, one finds for the VSC stripe phase a high intensity of the magnetic structure factor $S^z(\mathbf{k})$ at $\mathbf{Q}_s^v = \pi(1 \pm \epsilon, 1)$. Similarly, in the case of DSC stripe phase, the main weight of $S^z(\mathbf{k})$ is shifted towards $\mathbf{Q}_s^d = \pi(1 \pm \epsilon, 1 \pm \epsilon)$. Certainly, a twice larger value of the charge Bragg wave vector as compared to the magnetic one, follows from the fact that the staggered magnetization undergoes a phase-shift of π when crossing a DW. Consequently, due to antiphase AF domains, magnetic unit cell is twice as long as the charge unit cell. Note that maxima around the Γ (M) point in the charge (magnetic) structure factor, respectively, are accompanied by some higher harmonics (*cf.* Figs. 3.20 and 3.21). The appearance of similar weak satellites was also reported in Ref. 34.

Fig. 3.21 depicts reciprocal space pattern of the separated by $d = 6$ lattice

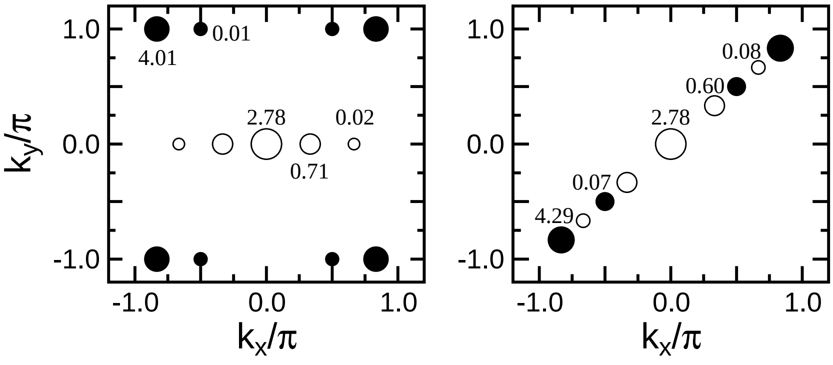

Figure 3.21: The same as in Fig. 3.21 but for doping $x = 1/6$. The stripes are separated by $d = 6$ lattice spacings.

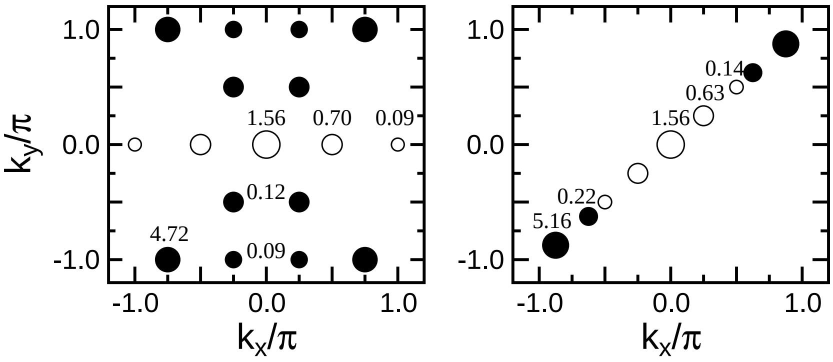

Figure 3.22: Reciprocal space pattern of the HVSC (left panel) and DSC stripe phases (right panel) shown in Fig. 3.16. The former (latter) are separated by $d = 4$ ($d = 8$) lattice spacings, respectively.

spacings stripes obtained at the higher doping $x = 1/6$. A smaller distance between the DWs results in a larger splitting $\propto \epsilon = 1/6$ of the charge (magnetic) structure factor maxima around the Γ (M), respectively. Correspondingly, even though the intensity of $C(\mathbf{k})$ at the Γ point is noticeably enhanced, the intensity of first harmonics at the wave vector $\mathbf{Q}_c^{v(d)}$ is nearly unaltered, meaning that average hole density at the DWs remains the same. In contrast, the intensity of the main magnetic peaks at $\mathbf{Q}_s^{v(d)}$ is strongly suppressed owing to a smaller magnetization density of the central AF domain atoms.

Experimentally, a diagonal stripe order with ϵ being approximately linear in x has been established up to $x = 1/2$ in doped $\mathrm{NiO_2}$ planes of LSNO [14, 15, 24–26, 29]. In contrast, neutron diffraction measurements on Nd-LSCO have demonstrated the existence of two kinds of IC magnetic maxima $\mathbf{Q}_s = \pi(1 \pm 2\epsilon, 1)$ and $\mathbf{Q}_s = \pi(1, 1 \pm 2\epsilon)$ corresponding to equally probable modulations along the (10) and (01) direction [13, 18, 19]. In this case, providing the evidence for charge order, Bragg peaks are distributed symmetrically around the Γ point at wave vectors $\mathbf{Q}_c = (\pm 4\pi\epsilon, 0)$ and $\mathbf{Q}_c = (0, \pm 4\pi\epsilon)$. Similar magnetic Bragg peaks $\mathbf{Q}_s$ have been resolved in LSCO with incommensurability ϵ that follows the relation $\epsilon \simeq x$ for $0.06 \leq x \leq 0.125$ [23]. Note, however, that the experimentally determined periodicity $d = 4$ for $x = 1/8$, corresponding to the half-filled stripes, differs from the HF prediction by a factor of 2 (*cf.* left panel of Fig. 3.20). One possibility of such a stripe order at $x = 1/8$ that possesses both magnetic and charge Bragg peaks precisely at the experimentally reported wave vectors $\mathbf{Q}_s$ and $\mathbf{Q}_c$ for the cuprates is shown in Fig. 3.16 (Fig. 3.22) in real (reciprocal) space, respectively. However, the on-wall SDW results in some extra magnetic harmonics at $\mathbf{Q}'_s = (\pm\pi/4, \pm\pi/2)$ and $\mathbf{Q}'_s = (\pm\pi/4, \mp\pi/2)$. Unfortunately, we are not aware of any experimental data that confirm the appearance of such Bragg peaks.

Finally, for comparative purposes we present, in the right panel of Fig. 3.22, reciprocal space pattern of the filled DSC stripe phase obtained in the t-t'-U model with $t' = -0.3$. Here, reinforcement of the stripe order by t' is best seen in the enhancement of $C(\mathbf{k})$ intensity at $\mathbf{Q}_c^d = (\pm\pi/4, \pm\pi/4)$ (larger hole density at the DWs) as well as in the larger weight of $S(\mathbf{k})$ at $\mathbf{Q}_s^d = (\pm\pi/8, \pm\pi/8)$ (stronger magnetization of the AF domains) (*cf.* Figs. 3.20 and 3.22).

Chapter 4

The slave-boson approach

In this Chapter we shall examine the role of strong electron correlations in stabilization of various stripe phases. A good starting point for a proper approximate treatment of strong correlations is the representation of the Hubbard model in terms of auxiliary fermions and bosons due to Kotliar and Ruckenstein (KR) [141]. The SBA has been applied successfully to a whole range of problems with local Coulomb interaction and is known to provide a realistic mean-field description of strongly correlated systems. It is quite encouraging that the ground state phase diagram obtained using KR approach for the 2D Hubbard model with homogeneous spiral, AF, FM, and PM phases shows a good agreement both with QMC simulations and the ED method [142]. The SBA was also used to investigate magnetic and charge correlations of the t-t'-U model [143], ground state of the Anderson lattice model [144, 145], and systems with orbital degeneracy [146–150]. Moreover, the unrestricted SBA has turned out to be a powerful tool in the description of inhomogeneous states, i.e., spin polarons and stripe phases both in the single- [31, 33] and three-band model [116] for the cuprates.

This Chapter is organized as follows. First, we present briefly the SRI SB representation of the Hubbard model and the saddle-point equations. Then, we introduce, based on stripe periodicity, reciprocal space representation, which provides a possibility to perform calculations on larger (up to 144×144) clusters than those studied in Ref. 33 and to a large extent eliminates the role of finite-size effects. Moreover, it allows one to obtain unbiased results at low temperature $\beta t = 100$. Further, we investigate stability of filled and half-filled stripes in the t-t'-U model at the doping $x = 1/8$ and show that negative next-neighbor hopping ($t'/t < 0$) favors the latter. We also compare the SB charge and spin density profiles with the ones obtained in the HA. Next, we perform a systematic study of an array of stripes separated by $d = 2, \ldots, 11$ lattice constants which allows us to establish the behavior of the incommensurability ϵ, optimal stripe filling ν, the chemical potential μ, as well as density of states $N(\omega)$ as a function of doping. Finally, we analyze the melting of stripe phases in the overdoped regime $x \geq 0.3$ and show that the spin and charge order disappear simultaneously.

4.1 Spin-rotation-invariant representation of the Hubbard model

In the SB SRI representation of the Hubbard model,

$$H = \sum_{ij,\sigma} t_{ij} c^{\dagger}_{i\sigma} c_{j\sigma} + U \sum_{i} n_{i\uparrow} n_{i\downarrow}, \tag{4.1}$$

one enlarges the Hilbert space of the Hamiltonian (4.1) by introducing auxiliary boson operators: e and d, which act as projection operators on empty and doubly occupied sites, and $p_{\sigma\sigma'}$ boson fields, which accompany single fermions and thus represent projections on singly occupied sites [151],

$$|\sigma\rangle = \sum_{\sigma'} p^{\dagger}_{\sigma\sigma'} f^{\dagger}_{\sigma'} |\mathrm{vac}\rangle, \tag{4.2}$$

where $f^{\dagger}_{\sigma}$ are pseudofermion operators with a spin 1/2 replacing physical fermion operators. Taking into account that the states $|\sigma\rangle$ transform as spinor states, it is obvious that the $p_{\sigma\sigma'}$ boson field must be given by a 2×2 spin matrix operator, which can be represented in terms of its projections onto the Pauli matrices τ_{μ}, including the unit matrix ($\mu = 0$),

$$p^{\dagger}_{\sigma\sigma'} = \frac{1}{2} \sum_{\mu=0}^{3} p^{\dagger}_{\mu} \tau_{\mu,\sigma\sigma'}. \tag{4.3}$$

It follows that the matrix elements of the $p^{\dagger}_{\sigma\sigma'}$ operator satisfy the commutation relation,

$$\left[p_{\sigma_1\sigma_2}, p^{\dagger}_{\sigma_3\sigma_4}\right] = \frac{1}{2} \delta_{\sigma_1\sigma_4} \delta_{\sigma_2\sigma_3}, \tag{4.4}$$

provided the bosons p_{μ} obey $[p_{\mu}, p^{\dagger}_{\nu}] = \delta_{\mu\nu}$. Apart from that, the choice of the $p^{\dagger}_{\sigma\sigma'}$ matrix with the factor 1/2 guarantees normalization of the states $|\sigma\rangle$ to unity, unlike the SRI formalism introduced in Ref. 152 with $\langle\sigma|\sigma\rangle = 2$. Further, since the singly occupied states (4.2) consist of the operator product which is supposed to create a particle with a spin 1/2, the boson fields $p^{\dagger}_{\sigma\sigma'}$ can either form a spin singlet $p^{\dagger}_0$ ($S = 0$), which represents the charge degrees of freedom, or a spin triplet $\mathbf{p}^{\dagger} = (p^{\dagger}_1, p^{\dagger}_2, p^{\dagger}_3)$ ($S = 1$) describing the spin degrees of freedom. Finally, two operators $p^{\dagger}_{\uparrow}$ and $p^{\dagger}_{\downarrow}$ introduced originally in Ref. 141 are the eigenvalues of $p^{\dagger}_{\sigma\sigma'}$ for two spin states.

The main advantage of the SBA is that the electron configurations are controlled by the bosons and one can thus write the Hubbard interaction as a bosonic occupation number operator. In contrast, the operator for the kinetic energy becomes much more involved since the motion of a physical electron changes occupation numbers in the SB space on both lattice sites involved in the hopping process. Hence, one needs to introduce additional operators $z_{\sigma'\sigma}$ in the hopping term of the model (4.1) [151],

$$c_\sigma = \sum_{\sigma'} f_{\sigma'} z_{\sigma'\sigma}, \tag{4.5}$$

$$z_{\sigma'\sigma} = e^\dagger p_{\sigma'\sigma} + \tilde{p}^\dagger_{\sigma'\sigma} d, \tag{4.6}$$

where $\tilde{p}_{\sigma'\sigma}$ is the time reversed operator $p_{\sigma'\sigma}$ with the following transformation properties: $\tilde{p}_0 \equiv \hat{T} p_0 \hat{T}^{-1} = p_0$ and $\tilde{\mathbf{p}} \equiv \hat{T} \mathbf{p} \hat{T}^{-1} = -\mathbf{p}$.

The operator (4.6) describes the sum of the two possible transition channels, either of which may accompany an electron hopping process: (singly occupied site) → (empty site) and (doubly occupied site) → (singly occupied site with a time-reversed spin). Unfortunately, the renormalization of the hopping amplitude (4.6) by the boson fields does not lead to the correct mean-field result, i.e., $\langle \underline{z}_i^\dagger \underline{z}_j \rangle = \underline{\tau}_0$ (hereafter, the underline denotes 2×2 spin matrices) in the noninteracting half-filled limit $U = 0$ with $e^2 = \frac{1}{4}$, $d^2 = \frac{1}{4}$, $p_0^2 = \frac{1}{2}$, and $p = 0$, where p is a modulus of the vector field $\mathbf{p}$. This might be adjusted by making use of the fact that the representation of any operator in terms of slave particles is not unique due to the freedom of choice of additional operator factors whose eigenvalue is unity in the physical subspace. Therefore, the spin matrix operator $\underline{z}$ is modified by the normalization factors in the following way,

$$\underline{z} = e^\dagger \underline{L} M \underline{R} \underline{p} + \underline{\tilde{p}}^\dagger \underline{L} M \underline{R} d, \tag{4.7}$$

with,

$$\begin{aligned} \underline{L} &= \left[(1 - d^\dagger d)\underline{\tau}_0 - 2\underline{p}^\dagger \underline{p}\right]^{-1/2}, \\ \underline{R} &= \left[(1 - e^\dagger e)\underline{\tau}_0 - 2\underline{\tilde{p}}^\dagger \underline{\tilde{p}}\right]^{-1/2}, \\ M &= \left[1 + e^\dagger e + d^\dagger d + \sum_\mu p_\mu^\dagger p_\mu\right]^{1/2}. \end{aligned} \tag{4.8}$$

However, such enlargement of the Hilbert space introduces unphysical states which should be now eliminated so as to recover the original Hilbert space. Therefore, the SB operators have to fulfill the following constraints at each site,

$$e_i^\dagger e_i + d_i^\dagger d_i + \sum_\mu p_{i\mu}^\dagger p_{i\mu} = 1, \tag{4.9}$$

$$2 d_i^\dagger d_i + \sum_\mu p_{i\mu}^\dagger p_{i\mu} = \sum_\sigma f_{i\sigma}^\dagger f_{i\sigma}, \tag{4.10}$$

$$p_{0i}^\dagger \mathbf{p}_i + \mathbf{p}_i^\dagger p_{0i} - i \mathbf{p}_i^\dagger \times \mathbf{p}_i = \sum_{\sigma\sigma'} \boldsymbol{\tau}_{\sigma\sigma'} f_{i\sigma'}^\dagger f_{i\sigma}. \tag{4.11}$$

The constraint (4.9) imposes recovering the correct anticommutation relation for the c operators (4.5). The two additional constraints (4.10) and (4.11) follow from the fact that the number of electrons must match the number of p and d bosons in the physical subspace, i.e., the relation between charge and spin density expressed in terms of pseudofermionic operators f and expressed by using the singlet p_0 and triplet $\mathbf{p}$ components of $\underline{p}$ must be preserved.

In terms of the above SB operators, the Hubbard model (4.1) takes now the form,

$$H_{SB} = \sum_{ij}\sum_{\sigma\sigma'\sigma_1} t_{ij} z^\dagger_{i\sigma_1\sigma} f^\dagger_{i\sigma} f_{j\sigma'} z_{j\sigma'\sigma_1} + U\sum_i d^\dagger_i d_i, \tag{4.12}$$

supplemented by the constraints (4.9)-(4.11), which are enforced by time-dependent Lagrange multipliers $\lambda^{(1)}_i$, $\lambda^{(2)}_{0i}$, and $\boldsymbol{\lambda}^{(2)}_i$. The constrains are conveniently handled in a path integral formulation. The partition function may be written down as a functional integral over coherent states of Fermi and Bose fields ($\beta = 1/k_B T$),

$$Z = Z_b Z_f = \int D[\text{bosons}] D[f, f^\dagger] D[\lambda] e^{-\int_0^\beta d\tau [\mathcal{L}_B(\tau) + \mathcal{L}_F(\tau)]}, \tag{4.13}$$

with the bosonic and fermionic Lagrangians defined by,

$$\begin{aligned}\mathcal{L}_B = \sum_i \Big\{ & e^\dagger_i (\partial_\tau + i\lambda^{(1)}_i) e_i + \sum_\mu p^\dagger_{i\mu} (\partial_\tau + i\lambda^{(1)}_i - i\lambda^{(2)}_{0i}) p_{i\mu} \\ & - \boldsymbol{\lambda}^{(2)}_i (p^\dagger_{0i}\mathbf{p}_i + \mathbf{p}^\dagger_i p_{0i} - i\mathbf{p}^\dagger_i \times \mathbf{p}_i) \\ & + d^\dagger_i (\partial_\tau + i\lambda^{(1)}_i - 2i\lambda^{(2)}_{0i} + U) d_i - i\lambda^{(1)}_i + \mathbf{h}\cdot\mathbf{S}_i \Big\},\end{aligned} \tag{4.14}$$

and,

$$\begin{aligned}\mathcal{L}_F = & \sum_{i,\sigma\sigma'} f^\dagger_{i\sigma} \big[(\partial_\tau - \mu + i\lambda^{(2)}_{0i}) \delta_{\sigma\sigma'} + i\boldsymbol{\lambda}^{(2)}_i \cdot \boldsymbol{\tau}_{\sigma'\sigma} \big] f_{i\sigma'} \\ & + \sum_{ij}\sum_{\sigma\sigma'\sigma_1} t_{ij} z^\dagger_{i\sigma_1\sigma} f^\dagger_{i\sigma} f_{j\sigma'} z_{j\sigma'\sigma_1}.\end{aligned} \tag{4.15}$$

Here, μ is the chemical potential, $\mathbf{h}$ is an external magnetic field, whereas $\mathbf{S}_i$ is the spin operator given by,

$$\mathbf{S}_i = \sum_{\sigma\sigma'\sigma_1} \boldsymbol{\tau}_{\sigma\sigma'} p^\dagger_{i\sigma\sigma_1} p_{i\sigma_1\sigma'} = \frac{1}{2}\big(p^\dagger_{0i}\bar{\mathbf{p}}_i + \bar{\mathbf{p}}^\dagger_i p_{0i} - i\bar{\mathbf{p}}^\dagger_i \times \bar{\mathbf{p}}_i \big), \tag{4.16}$$

with $\bar{\mathbf{p}} = (p_1, -p_2, p_3)$.

However, the partition function (4.13) is still not well defined due to the integration over complex Bose fields, which may cause it to be infinite. A possible remedy is to remove bosonic phases by using the representation with modulus and phase, at the cost of adding gauge terms involving time derivatives of the Bose fields phases [151]. It turns out that, these terms can be absorbed together with the previous Lagrange multipliers into the new constraint fields α_i, β_{0i}, and $\boldsymbol{\beta}_i$.

However, there are only five such fields, so one phase has to remain arbitrary. In what follows the Bose field d_i is left as a complex variable with dynamics. Complex d-field, whose propagator has a pole at $\omega_n = U$ corresponding to the UHB, makes the present approach capable of capturing the physical properties of this band in the large U limit. Further, since the bosons e_i and $p_{i\mu}$ are taken to be real, one can drop out all their time derivatives by imposing the periodic boundary conditions, i.e., $e_i(\beta) = e_i(0)$ and $p_{i\mu}(\beta) = p_{i\mu}(0)$, which eliminate their own dynamics.

The effective bosonic functional integral can be rewritten now as,

$$Z_b = \int D[e, p_0, \mathbf{p}] D[d, d^\dagger] D[\alpha, \beta_0, \boldsymbol{\beta}] e^{-\int\limits_0^\beta d\tau \mathcal{L}_B(\tau)}, \tag{4.17}$$

with,

$$\begin{aligned}\mathcal{L}_B = \sum_i \Big\{ & d_i^\dagger[\partial_\tau + \alpha_i - 2\beta_{0i} + U]d_i + \alpha_i(e_i^2 - 1) \\ & + (\alpha_i - \beta_{0i}) \sum_\mu p_{i\mu}^2 - 2\boldsymbol{\beta}_i \cdot \mathbf{p}_i p_{0i} + \mathbf{h} \cdot \bar{\mathbf{p}}_i p_{0i} \Big\},\end{aligned} \tag{4.18}$$

while the fermionic term takes the form,

$$Z_f = \int D[f, f^\dagger] e^{-\int\limits_0^\beta d\tau \mathcal{L}_F(\tau)}, \tag{4.19}$$

where the corresponding Lagrangian is given by,

$$\begin{aligned}\mathcal{L}_F = & \sum_{i,\sigma\sigma'} f_{i\sigma}^\dagger \big[\big(\partial_\tau - \mu + \beta_{0i}\big)\delta_{\sigma\sigma'} + \boldsymbol{\beta}_i \cdot \boldsymbol{\tau}_{\sigma'\sigma} \big] f_{i\sigma'} \\ & + \sum_{ij} \sum_{\sigma\sigma'\sigma_1} t_{ij} z_{i\sigma_1\sigma}^\dagger f_{i\sigma}^\dagger f_{j\sigma'} z_{j\sigma'\sigma_1}.\end{aligned} \tag{4.20}$$

The five real SB fields e, p_0, and $\mathbf{p}$ are real valued and are integrated like radial parts of complex fields, whereas α, β_0, and $\boldsymbol{\beta}$ are integrated along the imaginary axis.

In order to complete the derivation of the functional integral for the Hubbard model (4.12) one can exactly integrate out the fermionic degrees of freedom, which yields the familiar partition function for a system of noninteracting particles [153],

$$Z_f = \prod_{\mathbf{q}\sigma} \big(1 + e^{-\beta\varepsilon_{\mathbf{q}\sigma}}\big), \tag{4.21}$$

where $\varepsilon_{\mathbf{q}\sigma}$ are quasiparticle energies of the fermionic Lagrangian (4.20), and its grand canonical potential Ω_f,

$$\Omega_f = -k_B T \ln Z_f. \tag{4.22}$$

In the following Section we shall derive the saddle-point solutions that follows from (4.17) and (4.19) and find real values for the boson field d. However, a correct treatment of the fluctuations has to keep track of its phase.

4.2 Slave-boson saddle-point equations

The mean-field solution of the partition functions (4.17) and (4.19) is a good starting point of their loop expansion. In this approximation one replaces the Bose and chemical potential fields by their time-independent averages, i.e., $d_i \equiv \langle d_i^\dagger(\tau)\rangle = \langle d_i(\tau)\rangle$, and so on. Hence, the bosonic Lagrangian becomes,

$$\begin{aligned}\mathcal{L}_b = \sum_i \Big\{ & \alpha_i(e_i^2 + p_{0i}^2 + p_i^2 + d_i^2 - 1) - \beta_{0i}(p_{0i}^2 + p_i^2 + 2d_i^2) \\ & + U_i d_i^2 - 2\boldsymbol{\beta}_i \cdot \mathbf{p}_i p_{0i} + \mathbf{h}\cdot\bar{\mathbf{p}}_i p_{0i}\Big\}. \end{aligned} \tag{4.23}$$

The above expression can be easily simplified by introducing polar coordinates for the amplitudes of boson operators in the following way,

$$\begin{aligned} p_{0i} &= \cos\theta_i, \\ p_i &= \sin\theta_i \cos\phi_i, \\ d_i &= \sin\theta_i \sin\phi_i \cos\psi_i, \\ e_i &= \sin\theta_i \sin\phi_i \sin\psi_i. \end{aligned} \tag{4.24}$$

Such parametrization automatically satisfies the constraint (4.9), so that the resulting bosonic Lagrangian does not include the α-field,

$$\mathcal{L}_b = \sum_i \Big\{ -\beta_{0i}(p_{0i}^2 + p_i^2 + 2d_i^2) + U_i d_i^2 - 2\boldsymbol{\beta}_i \cdot \mathbf{p}_i p_{0i} + \mathbf{h}\cdot\bar{\mathbf{p}}_i p_{0i}\Big\}. \tag{4.25}$$

The SB mean-field free energy,

$$F = \mathcal{L}_b + \Omega_f + \mu N_{el}, \tag{4.26}$$

where N_{el} is the number of particles, follows as,

$$\begin{aligned} F = \sum_i \Big\{ & -\beta_{0i}(p_{0i}^2 + p_i^2 + 2d_i^2) + U_i d_i^2 - 2\boldsymbol{\beta}_i \cdot \mathbf{p}_i p_{0i} + \mathbf{h}\cdot\bar{\mathbf{p}}_i p_{0i}\Big\} \\ & - T\sum_{\mathbf{q}\sigma} \ln\big(1 + e^{-\beta\varepsilon_{\mathbf{q}\sigma}}\big) + \mu N_{el}. \end{aligned} \tag{4.27}$$

The equilibrium values of the classical field amplitudes have to be determined from the saddle-point equations $\nabla F = 0$, where the partial derivatives are taken with respect to β_{0i}, β_i, and $\Psi_i \in \{\theta_i, \phi_i, \psi_i\}$ separately for each inequivalent site i within an elementary unit cell,

$$\frac{\partial F}{\partial \beta_{0i}} = n_i - (p_{0i}^2 + p_i^2 + 2d_i^2), \tag{4.28}$$

$$\frac{\partial F}{\partial \beta_i} = m_i - 2p_{0i}p_i, \tag{4.29}$$

$$\frac{\partial F}{\partial \Psi_i} = \frac{\partial \mathcal{L}_b}{\partial \Psi_i} + \frac{\partial \Omega_f}{\partial \Psi_i}, \tag{4.30}$$

where we have defined the electron density,

$$n_i = \sum_{\mathbf{q}\sigma} f_F(\varepsilon_{\mathbf{q}\sigma}) \frac{\partial \varepsilon_{\mathbf{q}\sigma}}{\partial \beta_{oi}}, \tag{4.31}$$

and the amplitude of the spin density wave,

$$m_i = \sum_{\mathbf{q}\sigma} f_F(\varepsilon_{\mathbf{q}\sigma}) \frac{\partial \varepsilon_{\mathbf{q}\sigma}}{\partial \beta_i}. \tag{4.32}$$

Here,

$$f_F(\varepsilon_{\mathbf{q}\sigma}) = \frac{1}{\exp(\beta\varepsilon_{\mathbf{q}\sigma}) + 1}, \tag{4.33}$$

is the Fermi-Dirac distribution function for the states with energy $\varepsilon_{\mathbf{q}\sigma}$. Each bosonic Lagrangian derivative with respect to the angles Ψ_i in Eq. (4.30) can be easily found by the analytical differentiation of Eq. (4.25), whereas derivatives of the grand canonical potential are computed with Eqs. (4.19) and (4.22) as follows,

$$\begin{aligned} \frac{\partial \Omega_f}{\partial \Psi_i} &= -\frac{k_B T}{Z_f}\frac{\partial Z_f}{\partial \Psi_i} = \sum_{jk}\sum_{\sigma\sigma'\sigma_1} t_{jk} \frac{\partial}{\partial \Psi_i}\left(z_{k\sigma'\sigma_1} z^{\dagger}_{j\sigma_1\sigma}\right)\langle f^{\dagger}_{j\sigma} f_{k\sigma'}\rangle \\ &= \sum_{\delta}\sum_{\sigma\sigma'\sigma_1} t_{i,i+\delta}\left[\left(\frac{\partial z_{i\sigma'\sigma_1}}{\partial \Psi_i}\right) z^{\dagger}_{i+\delta,\sigma_1\sigma}\langle f^{\dagger}_{i+\delta,\sigma} f_{i\sigma'}\rangle + z_{i+\delta,\sigma'\sigma_1}\left(\frac{\partial z^{\dagger}_{i\sigma_1\sigma}}{\partial \Psi_i}\right)\langle f^{\dagger}_{i\sigma} f_{i+\delta,\sigma'}\rangle\right], \end{aligned} \tag{4.34}$$

where δ labels all the neighbors of the site i connected by the hopping $t_{i,i+\delta}$. The last unknown quantity, the chemical potential μ, is determined to satisfy the condition for the total electron density,

$$N_{el} = \sum_{\mathbf{q}\sigma} f_F(\varepsilon_{\mathbf{q}\sigma}). \tag{4.35}$$

4.3 Reciprocal space representation

In order to obtain unbiased results one should carry out calculations on large clusters. This can be accomplished by taking into account periodicity of a stripe phase which allows to cover the entire lattice by small unit cells. Let us consider the fermionic matrix in the momentum representation,

$$\mathcal{H} = \sum_{\mathbf{k}\mathbf{k}'}\sum_{\sigma\sigma'} f^{\dagger}_{\mathbf{k}\sigma} M^{\sigma\sigma'}_{\mathbf{k}\mathbf{k}'} f_{\mathbf{k}'\sigma'}. \tag{4.36}$$

Its elements are found as follows. Each position vector $\mathbf{R}_i$ of an arbitrary atom in a periodic cluster can be decomposed into a sum of periodicity vectors $\mathbf{g}_1$

and $\mathbf{g}_2$, such that $f^{\dagger}_{i+n\mathbf{g}_1+m\mathbf{g}_2} = f^{\dagger}_i$ for each $\{n, m\}$, and a vector $\boldsymbol{\delta}_M$ labeling all inequivalent sites i within the unit cell:

$$\mathbf{R}_i = n\mathbf{g}_1 + m\mathbf{g}_2 + \boldsymbol{\delta}_M. \tag{4.37}$$

Therefore, for the local β_0 term one gets,

$$M^{\sigma\sigma}_{\mathbf{k}\mathbf{k}'}(\beta_0) = \frac{1}{N}\sum_i \beta_{0i} e^{i(\mathbf{k}-\mathbf{k}')\mathbf{R}_i} = \frac{1}{N}\sum_{cells,\boldsymbol{\delta}_M} \beta_{0\boldsymbol{\delta}_M} e^{i(\mathbf{k}-\mathbf{k}')(n\mathbf{g}_1+m\mathbf{g}_2+\boldsymbol{\delta}_M)}. \tag{4.38}$$

Furthermore, any allowed wave vector $\mathbf{k}$ can be decomposed into a sum,

$$\mathbf{k} = \mathbf{K} + \mathbf{G}, \tag{4.39}$$

with a certain vector $\mathbf{G}$ that yields a plane wave with periodicity of a given Bravais lattice by satisfying the following conditions,

$$e^{i\mathbf{G}\mathbf{g}_1} = 1, \qquad e^{i\mathbf{G}\mathbf{g}_2} = 1, \tag{4.40}$$

whereas an appropriate vector $\mathbf{K}$ is chosen to generate a complete set of vectors $\mathbf{k}$. Now, Eq. (4.38) can be rewritten by taking into account Eqs. (4.39) and (4.40),

$$M^{\sigma\sigma}_{\mathbf{k}\mathbf{k}'}(\beta_0) = \frac{1}{N}\sum_{\boldsymbol{\delta}_M} \beta_{0\boldsymbol{\delta}_M} e^{i(\mathbf{K}-\mathbf{K}'+\mathbf{G}-\mathbf{G}')\boldsymbol{\delta}_M} \sum_{cells} e^{i(\mathbf{K}-\mathbf{K}')(n\mathbf{g}_1+m\mathbf{g}_2)}. \tag{4.41}$$

However,

$$\sum_{cells} e^{i(\mathbf{K}-\mathbf{K}')(n\mathbf{g}_1+m\mathbf{g}_2)} = \frac{N}{N_C}\delta_{\mathbf{K}\mathbf{K}'}, \tag{4.42}$$

where N_C is a number of atoms in the unit cell, so that the ratio N/N_C gives the number of unit cells needed to cover a whole cluster with N sites. This reduces the initial matrix $M^{\sigma\sigma}_{\mathbf{k}\mathbf{k}'}(\beta_0)$ down into a block-diagonal one with the blocks,

$$M^{\sigma\sigma}_{\mathbf{G}\mathbf{G}'}(\beta_0) = \frac{1}{N_C}\sum_{\boldsymbol{\delta}_M} e^{i(\mathbf{G}-\mathbf{G}')\boldsymbol{\delta}_M}\beta_{0\boldsymbol{\delta}_M}. \tag{4.43}$$

Analogously, the off-diagonal in spin indices matrix $M^{\sigma\sigma'}_{\mathbf{k}\mathbf{k}'}(\boldsymbol{\beta})$ takes a similar block-diagonal shape,

$$M^{\sigma\sigma'}_{\mathbf{G}\mathbf{G}'}(\boldsymbol{\beta}) = \frac{1}{N_C}\sum_{\boldsymbol{\delta}_M} e^{i(\mathbf{G}-\mathbf{G}')\boldsymbol{\delta}_M}\boldsymbol{\beta}_{\boldsymbol{\delta}_M}\cdot\boldsymbol{\tau}_{\sigma'\sigma}. \tag{4.44}$$

Finally, the kinetic energy term reads,

$$\begin{aligned} T^{\sigma\sigma'}_{\mathbf{k}\mathbf{k}'} &= \frac{1}{N}\sum_{ij,\sigma_1} e^{i\mathbf{k}\mathbf{R}_i} t_{ij} z^{\dagger}_{i\sigma_1\sigma} z_{j\sigma'\sigma_1} e^{-i\mathbf{k}'\mathbf{R}_j} \\ &= \frac{1}{N}\sum_i e^{i(\mathbf{k}-\mathbf{k}')\mathbf{R}_i}\sum_{\boldsymbol{\delta}} e^{-i\mathbf{k}'\boldsymbol{\delta}} t_{i,i+\delta}\left(z_{i+\delta} z^{\dagger}_i\right)^T_{\sigma'\sigma}, \end{aligned} \tag{4.45}$$

and after decompositions (4.37) and (4.39) and subsequent simplifications that follow from Eqs. (4.40) and (4.42) one obtains,

$$
\begin{aligned}
T^{\sigma\sigma'}_{\mathbf{GG'}}(\mathbf{K}) = \frac{1}{N_C} \sum_{\boldsymbol{\delta}_M} & e^{i(\boldsymbol{G}-\boldsymbol{G}')\boldsymbol{\delta}_M} \\
& \times \sum_{\boldsymbol{\delta}} e^{-i(\boldsymbol{K}+\boldsymbol{G}')\boldsymbol{\delta}} t_{\boldsymbol{\delta}_M, \boldsymbol{\delta}_M+\boldsymbol{\delta}} \left(z_{\boldsymbol{\delta}_M+\boldsymbol{\delta}} z^{\dagger}_{\boldsymbol{\delta}_M} \right)^T_{\sigma'\sigma} .
\end{aligned}
\tag{4.46}
$$

Hence, we have reduced the kinetic energy matrix $T^{\sigma\sigma'}_{\mathbf{kk'}}$ into decoupled blocks labeled by vectors $\mathbf{K}$. Due to this transformation, one can split a large $2N \times 2N$ fermionic matrix $M^{\sigma\sigma'}_{\mathbf{kk'}}$, which consists of $M^{\sigma\sigma}_{\mathbf{GG'}}(\beta_0)$, $M^{\sigma\sigma'}_{\mathbf{GG'}}(\boldsymbol{\beta})$, and $T^{\sigma\sigma'}_{\mathbf{kk'}}$ terms, into N/N_C smaller $2N_C \times 2N_C$ matrices (factor two enters owing to the spin degeneracy). This simplification gives a considerable time gain during numerical calculations. Indeed, as the usual workload in a diagonalization algorithm is $\sim N^3$ [154], the number of operation needed for diagonalization of smaller matrices is $\sim \frac{N}{N_C} \cdot N_C^3 = N N_C^2$. This means that the symmetry reduction makes the execution time of a program $(N/N_C)^2$ times more efficient as compared to a straightforward 'brute force' diagonalization of the $N \times N$ matrix.

We finish this Section off by evaluating the local electron and magnetization density,

$$
\langle f^{\dagger}_{i\sigma} f_{i\sigma} \rangle = \sum_{\mathbf{q}} \Psi^{\dagger}_{i\sigma}(\mathbf{q}) \Psi_{i\sigma}(\mathbf{q}) f_F(\epsilon_{\mathbf{q}\sigma}),
\tag{4.47}
$$

$$
\sum_{\sigma\sigma'} \langle f^{\dagger}_{i\sigma} \boldsymbol{\tau}_{\sigma\sigma'} f_{i\sigma'} \rangle = \sum_{\sigma\sigma'} \sum_{\mathbf{q}} \Psi^{\dagger}_{i\sigma}(\mathbf{q}) \boldsymbol{\tau}_{\sigma\sigma'} \Psi_{i\sigma'}(\mathbf{q}) f_F(\epsilon_{\mathbf{q}\sigma}),
\tag{4.48}
$$

where $\varepsilon_{\mathbf{q}\sigma}$ are eigenvalues of the Hamiltonian (4.36) and $\Psi^{\dagger}_{i\sigma}(\mathbf{q})$ are the corresponding real space eigenvectors. In order to, evaluate these averages we introduce first a certain unitary transform,

$$
g_{\mathbf{q}\sigma} = \sum_{\mathbf{k}} \Phi^{\dagger}_{\mathbf{qk}\sigma} f_{\mathbf{k}\sigma},
\tag{4.49}
$$

which diagonalizes the matrix $M^{\sigma\sigma'}_{\mathbf{kk'}}$ so that,

$$
\sum_{\mathbf{kk'}} \sum_{\sigma\sigma'} f^{\dagger}_{\mathbf{k}\sigma} M^{\sigma\sigma'}_{\mathbf{kk'}} f_{\mathbf{k'}\sigma'} = \sum_{\mathbf{q}\sigma} g^{\dagger}_{\mathbf{q}\sigma} \epsilon_{\mathbf{q}\sigma} g_{\mathbf{q}\sigma}.
\tag{4.50}
$$

Now, using the Fourier transform,

$$
f_{\mathbf{k}\sigma} = \frac{1}{\sqrt{N}} \sum_{i} e^{-i\mathbf{kR}_i} f_{i\sigma} = \sum_{i} U_{\mathbf{k}i} f_{i\sigma},
\tag{4.51}
$$

and Eq. (4.49), one can express a real space operator $f_{i\sigma}$ in terms of the Fourier transformed operator $g_{\mathbf{q}\sigma}$,

$$
f_{i\sigma} = \sum_{\mathbf{kq}} U^{\dagger}_{i\mathbf{k}} \Phi_{\mathbf{kq}\sigma} g_{\mathbf{q}\sigma}.
\tag{4.52}
$$

Hence the local electron and magnetization density read,

$$\langle f^\dagger_{i\sigma} f_{i\sigma}\rangle = \sum_{\mathbf{kk'q}} \Phi^\dagger_{\mathbf{qk}\sigma} U_{\mathbf{k}i} U^\dagger_{i\mathbf{k'}} \Phi_{\mathbf{k'q}\sigma} f_F(\varepsilon_{\mathbf{q}\sigma}), \tag{4.53}$$

$$\sum_{\sigma\sigma'} \langle f^\dagger_{i\sigma} \boldsymbol{\tau}_{\sigma\sigma'} f_{i\sigma'}\rangle = \sum_{\sigma\sigma'} \sum_{\mathbf{kk'q}} \Phi^\dagger_{\mathbf{qk}\sigma} U_{\mathbf{k}i} \boldsymbol{\tau}_{\sigma\sigma'} U^\dagger_{i\mathbf{k'}} \Phi_{\mathbf{k'q}\sigma'} f_F(\varepsilon_{\mathbf{q}\sigma}), \tag{4.54}$$

Equivalently, after reduction of the matrix $M^{\sigma\sigma'}_{\mathbf{kk'}}$ into decoupled blocks labeled by $\mathbf{K}$, one obtains,

$$\langle f^\dagger_{i\sigma} f_{i\sigma}\rangle = \sum_{\substack{\mathbf{Kq}\\ \mathbf{GG'}}} \Phi^{\dagger(\mathbf{K})}_{\mathbf{qG}\sigma} U_{\mathbf{K+G},i} U^\dagger_{i,\mathbf{K+G'}} \Phi^{(\mathbf{K})}_{\mathbf{G'q}\sigma} f_F(\varepsilon^{(\mathbf{K})}_{\mathbf{q}\sigma}), \tag{4.55}$$

$$\sum_{\sigma\sigma'} \langle f^\dagger_{i\sigma} \boldsymbol{\tau}_{\sigma\sigma'} f_{i\sigma'}\rangle = \sum_{\sigma\sigma'} \sum_{\substack{\mathbf{Kq}\\ \mathbf{GG'}}} \Phi^{\dagger(\mathbf{K})}_{\mathbf{qG}\sigma} U_{\mathbf{K+G},i} \boldsymbol{\tau}_{\sigma\sigma'} U^\dagger_{i,\mathbf{K+G'}} \Phi^{(\mathbf{K})}_{\mathbf{G'q}\sigma'} f_F(\varepsilon^{(\mathbf{K})}_{\mathbf{q}\sigma}). \tag{4.56}$$

4.4 Stripe unit cells

Here we show how to determine the set of wave vectors $\{\mathbf{G}\}$ for the vertical and diagonal SC stripes, whereas the $\{\mathbf{G}\}$ set for the BC stripes can be found in a similar fashion.

4.4.1 Vertical stripes

Consider as a first example an 8×8 cluster with vertical SC domain walls separated by $d = 4$ lattice spacings as shown in Fig. 4.1(a). The smallest unit cell in this case consists of a row of eight atoms perpendicular to the stripes. One immediately finds two periodicity vectors $\mathbf{g}_1 = \binom{4}{1}$ and $\mathbf{g}_2 = \binom{0}{2}$, which satisfy the condition $f^\dagger_{i+n\mathbf{g}_1+m\mathbf{g}_2} = f^\dagger_i$ and constitute a Bravais lattice. Its reciprocal lattice is characterized by wave vectors $\{\mathbf{G}\}$ satisfying requirements (4.40). In fact one obtains two independent sets of solutions,

$$\mathbf{G}_1 = \frac{2\pi}{8}\begin{pmatrix} 2l_x \\ 0 \end{pmatrix}, \qquad \mathbf{G}_2 = \frac{2\pi}{8}\begin{pmatrix} 2(l_x+1) \\ 4 \end{pmatrix}, \qquad \text{with} \qquad 0 \le l_x \le 3. \tag{4.57}$$

The next step is to find appropriate vectors $\mathbf{K}$ that are necessary to recover in Eq. (4.39) a complete set of the allowed momenta given by,

$$\mathbf{k} = \frac{2\pi}{8}\begin{pmatrix} m_x \\ m_y \end{pmatrix}, \qquad \text{where} \qquad 0 \le m_{x(y)} \le 7. \tag{4.58}$$

Certainly, there is only one required value of the x-component of $\mathbf{K}$ vector, i.e., $K_x = 0$, whereas the number of needed values K_y is given by the ratio of a linear

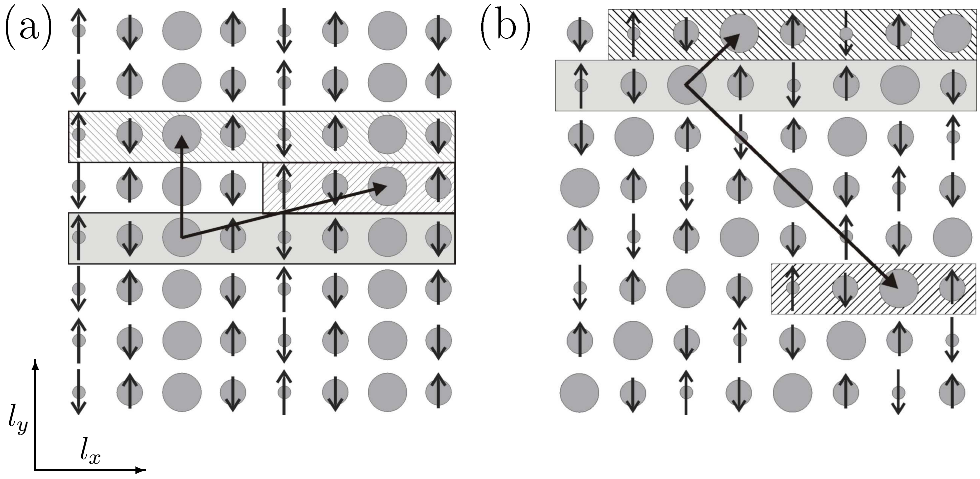

Figure 4.1: (a) Vertical SC stripe phase, its unit cell, and two periodicity vectors $\mathbf{g}_1 = \big(4,1\big)$ and $\mathbf{g}_2 = \big(0,2\big)$. (b) Diagonal SC stripe phase, its unit cell, and two periodicity vectors $\mathbf{g}_1 = \big(1,1\big)$ and $\mathbf{g}_2 = \big(4,-4\big)$.

dimension along the y direction of the cluster and the corresponding size of the unit cell, i.e, one needs eight values. Altogether, one finds,

$$\mathbf{K} = \frac{2\pi}{8}\begin{pmatrix} 0 \\ n_y \end{pmatrix}, \qquad \text{with} \qquad 0 \le n_y \le 7. \tag{4.59}$$

It is easy to verify that the sets (4.57) and (4.59) generate all the allowed momenta $\mathbf{k}$ given by Eq. (4.58).

4.4.2 Diagonal stripes

We shall now discuss how one can take advantage of the periodicity of an analogous 8×8 cluster with a diagonal stripe phase depicted in Fig. 4.1(b). As previously, the smallest unit cell consists of a row of eight atoms along the x-direction. However, the periodicity vectors are now given by $\mathbf{g}_1 = \big(\begin{smallmatrix}1\\1\end{smallmatrix}\big)$ and $\mathbf{g}_2 = \big(\begin{smallmatrix}4\\-4\end{smallmatrix}\big)$. Hence, from Eq. (4.40), one finds the following reciprocal lattice vectors,

$$\mathbf{G}_1 = \begin{pmatrix} 0 \\ 0 \end{pmatrix}, \qquad \mathbf{G}_2 = \frac{2\pi}{8}\begin{pmatrix} l \\ 8-l \end{pmatrix}, \qquad \text{with} \qquad 1 \le l \le 7, \tag{4.60}$$

whereas appropriate vectors $\mathbf{K}$, necessary in Eq. (4.39), are precisely the same as those for the VSC stripe, as both structures have the same unit cell.

4.5 Influence of electron correlations

An important feature of the HA is that it overestimates by far the tendency towards symmetry breaking states since this method utterly ignores electron correlations. Therefore, one should expect that inclusion of the correlation effects modifies considerably the distribution of charge and spin density in a stripe phase, especially around nonmagnetic DWs where the correlation corrections are large.

To illustrate this point, we compare in Fig. 4.2 the local hole $n_{\mathrm{h}}(l_x)$ (3.7) and magnetization $S_\pi(l_x)$ (3.8) density as well as double occupancy $D(l_x)$ (3.16) of the filled VSC (left) and DSC (right) stripe phases found either in the HA (open circles) or SBA (filled circles) in the Hubbard model with $U = 6t$ at $x = 1/8$. The calculations have been carried out on a large 128×128 cluster which allows one to obtain unbiased result at the low temperature $\beta t = 100$. In agreement with the calculations of Ref. 31, we note that the hole density n_h at nonmagnetic DWs is reduced nearly twice in the SBA as compared to the corresponding HA value, regardless of the stripe direction. Such a strong modification follows directly from the fact that the only possibility of double occupancy reduction in the HA is to suppress the electron density locally at the sites with vanishing magnetization (DWs). In contrast, the SBA offers a possibility to optimize the on-site interaction by an additional variational parameter, i.e., the boson field d_i. Indeed, double occupancy D shows a distinct minimum at the DWs leading to a more spread out charge and spin density profiles with respect to the ones found in the HA. In contrast, both approximation yield a narrow *diagonal* stripe revealing its more localized character, as compared to the vertical one, with lower double occupancy D and hence a more favorable average on-site energy which stabilizes the former stripe phase in the strong coupling regime as discussed below.

Remarkably, in contrast to studies within the HA of Chapter 3, the present calculations performed on large clusters yield locally stable half-filled stripes both in the HA and SBA without any necessity of quadrupling of the period along the stripes by an additional on-wall SDW. The obtained HVSC and its diagonal site-centered (HDSC) counterpart stripe structures are shown in Fig. 4.3. Again, one finds a smaller SB charge modulation and a stronger spin polarization of the AF domains in the HA. Note, however, that contrary to the filled case, a narrower charge and spin profile, found in both methods, of the *vertical* stripe with respect to the diagonal one is apparent. Moreover, both approximations indicate that the HVSC structure stronger reduces the double occupancy D. Therefore, based on Figs. 4.2 and 4.3, one can conjecture that there are two possible ground states for doped Hubbard model, in the realistic strong coupling regime, i.e., a filled diagonal stripe phase and a half-filled vertical one. In fact, both structures have been observed in LSCO; the former was found around $x = 0.02$ [52–54], whereas the latter — at a higher $0.06 \leq x \leq 0.125$ doping level [23]. Hence it appears that the filling and orientation of DWs are indeed closely related in the cuprates. In other words, a *half-filled* DWs tend to be aligned vertically/horizontally, whereas

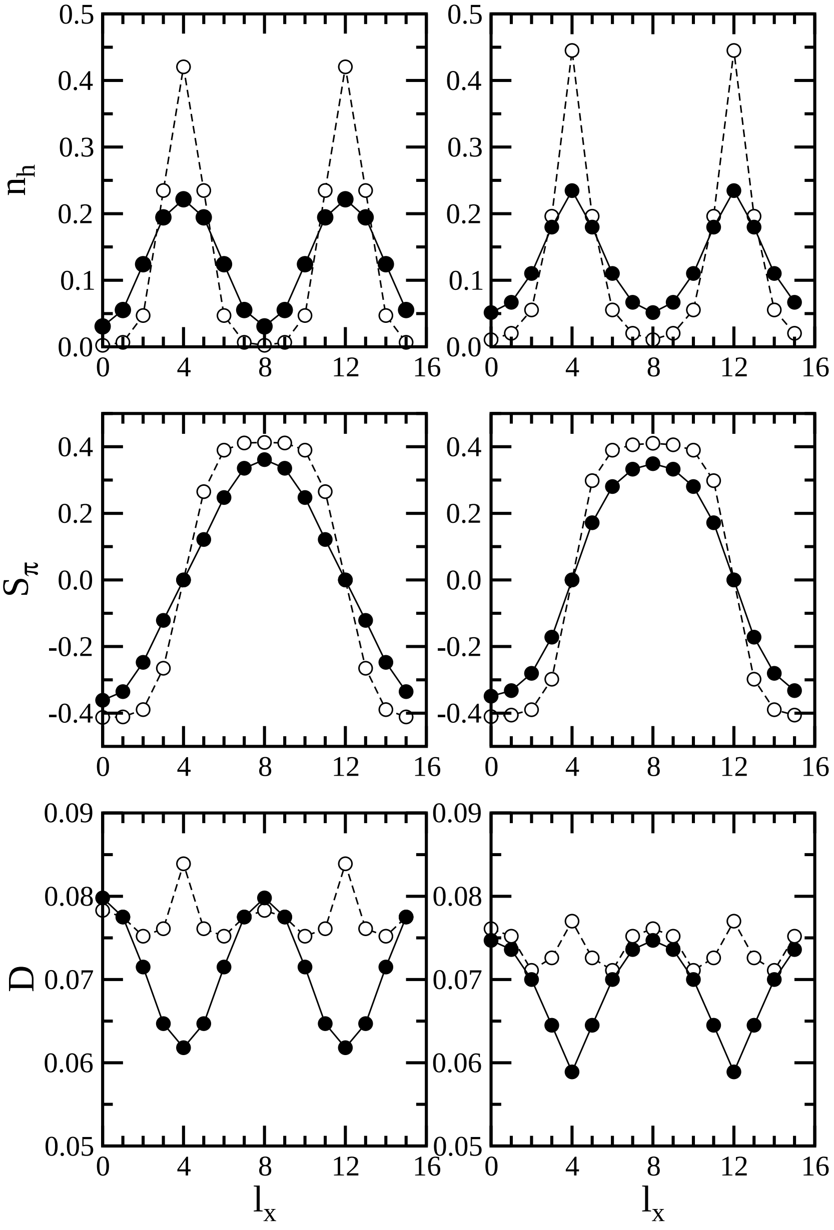

Figure 4.2: Local hole $n_{\mathrm{h}}(l_x)$ (top) and magnetization $S_\pi(l_x)$ (second row) density as well as double occupancy $D(l_x)$ (bottom) of the filled VSC (left) and DSC (right) stripe phases found at temperature $\beta t = 100$ in the Hubbard model on a 128×128 cluster with $U = 6t$ and $x = 1/8$. Open (filled) circles show the results obtained in the HA (SBA), respectively.

filled ones are more stable due to the diagonal arrangement.

This important property is also seen in Table 4.1 showing the Hartree and SB mean-field free energy all four stripe phases, and for completeness, also the energy

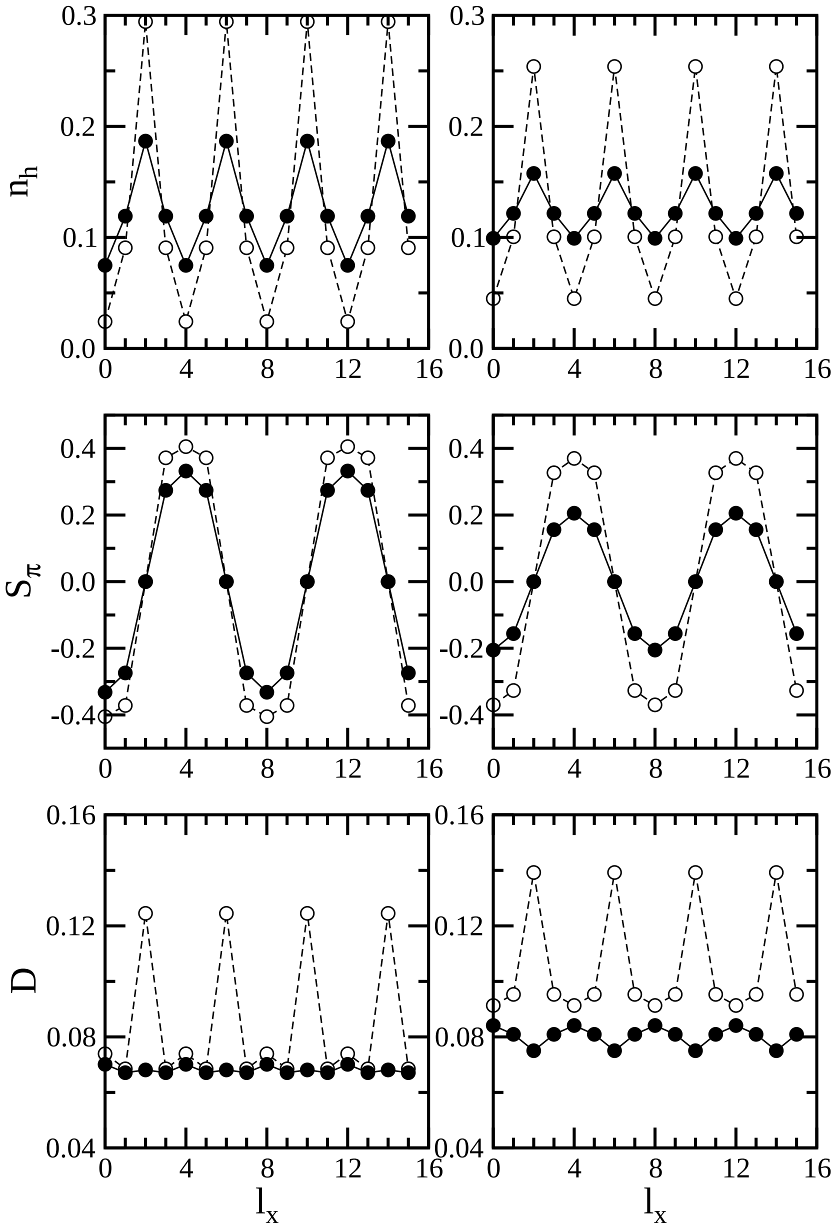

Figure 4.3: The same as in Fig. 4.2 but for the half-filled SC stripes. Open (filled) circles show he results obtained in the HA (SBA), respectively.

of the uniform PM and AF phases, for two representative values of the Coulomb repulsion, i.e., $U/t = 4$ and $U/t = 12$. For clarity, the phases are listed in the increasing energy order from bottom to top. First of all note that the overall order in the weak coupling regime $U/t = 4$ is precisely the same in both methods. Due to electron correlations, in the strong coupling regime $U/t = 12$, a tendency of the HA to promote the AF phase results in the interchanged order of the HVSC and

	HA		SBA	
U/t	phase	F/t	phase	F/t
4	PM	-0.8422	PM	-0.9885
	HDSC	-0.8639	HDSC	—
	HVSC	-0.8832	HVSC	—
	AF	-0.8848	AF	-0.9893
	DSC	-0.9106	DSC	-0.9914
	VSC	-0.9110	VSC	-0.9975
12	PM	0.6890	PM	-0.5040
	HDSC	-0.2183	HDSC	-0.5339
	HVSC	-0.3454	AF	-0.5393
	AF	-0.3675	HVSC	-0.5689
	VSC	-0.4416	VSC	-0.5751
	DSC	-0.4649	DSC	-0.5821

Table 4.1: Comparison of the free energy F per site as obtained for various phases in the Hubbard model from the HA and SBA in the weak (strong) coupling regime $U = 4t$ ($U = 12t$), respectively, at temperature $\beta t = 100$ on a 128×128 cluster with $x = 1/8$.

AF structures as compared to the SBA, in which the HVSC stripe phase is favored over the AF one. More importantly, at $U = 12t$, one does find that the HVSC phase is preferred over the HDSC one, and also, that the filled DSC structure is promoted over the corresponding VSC one.

Let us now compare the density of states $N(\omega)$ obtained within the HA and SBA for the filled VSC and HVSC stripe phases shown in Fig. 4.4. This figure also emphasizes the importance of a proper treatment of electron correlations which modifies the overall shape of $N(\omega)$. Indeed, the width of the Mott-Hubbard gap between the LHB and UHB in the HA, given by $\Delta^{HA} = 2U\langle S^z\rangle$ for a uniform AF phase, is overestimated almost twice as compared to the one obtained in the SBA. As we have already discussed, stripes are characterized by the existence of additional bands within the Mott-Hubbard gap. As the DWs contributing to the mid-gap states are 1D, this part of the Hartree DOS resembles the tight-binding DOS of a 1D chain with peaks at the edges [*cf.* Figs. 4.4(a,b)]. However, more spread out SB charge and spin density profiles, as compared to the Hartree ones, result in a less clear character of the mid-gap segment of $N(\omega)$ [*cf.* Figs. 4.4(c,d)]. We emphasize that both half-filled structures are metallic with the Fermi energy lying inside the mid-gap states and their stability presumably rests on the partially suppressed DOS at the Fermi energy.

An interesting question is which microscopic parameters decide whether a filled diagonal or half-filled vertical stripe phase is more stable. To clarify this point we investigated the competition between the stripe phases in the t-t'-U model.

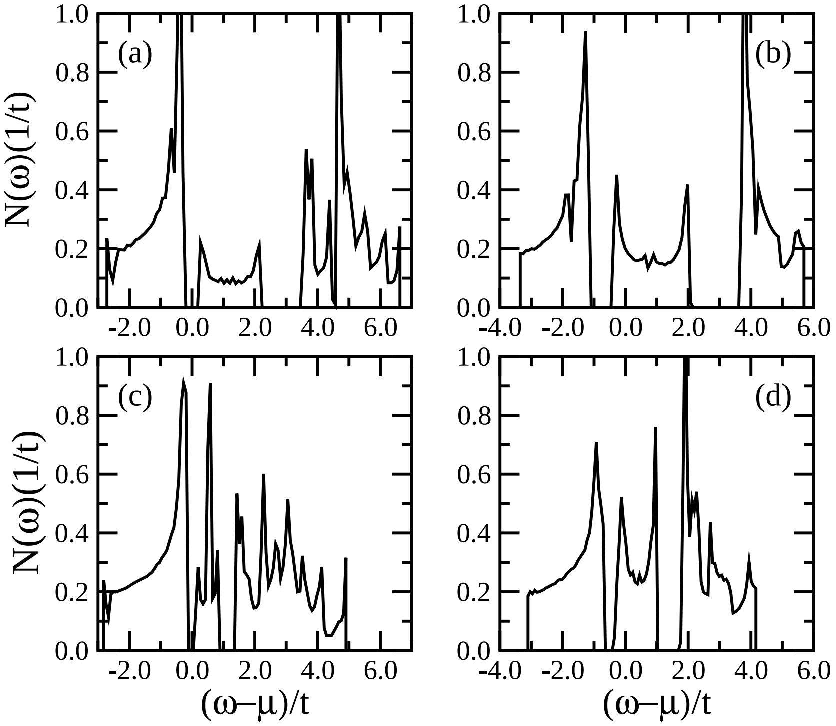

Figure 4.4: Density of states $N(\omega)$ as obtained within the HA (a,b) and SBA (c,d) for the the filled VSC stripe (left), depicted in the left panels of Fig. 4.2, and the HVSC stripe (right), shown in the left panels of Fig. 4.3.

Fig. 4.5 illustrates the effect of increasing $|t'|$ on the free energy F of various phases, as obtained in the HA at temperature $\beta t = 100$ for $x = 1/8$. From Fig. 4.5(a) with $t' = 0$, one finds that the half-filled stripe phase (dashed lines) has significantly higher energy F than the filled one (solid lines), especially in the large U regime, and the ground state consist of either the VSC ($U/t \lesssim 4$) or DSC stripe phases ($U/t > 4$) (*cf.* also Table 4.1) in agreement with the small cluster results discussed in Chapter 3 [*cf.* Fig. 3.5(a)]. Further, increasing $|t'|$ frustrates relatively stronger the AF domains of the VSC structure than the AF domains of a narrower DSC stripe (*cf.* Fig. 4.2) so that the former is already unstable at $t'/t = -0.3$. Simultaneously, the energy difference between the half-filled and filled stripes gradually diminishes. Finally, as shown in Fig. 4.5(c), the HVSC stripe phase becomes the ground state of the system in the regime $U/t \lesssim 4.12$ (*cf.* also Table 4.2). However, increasing U clearly promotes the DSC structure with the number of nonmagnetic DWs lower by a factor of two than in the case of the HVSC one.

Turning now to the analogous results obtained in the SBA, the inclusion of electron correlations improves significantly the free energy of the PM phase with respect to the one found within the HA, as depicted in Fig. 4.6. Therefore, as the

	HA		SBA	
U/t	phase	F/t	phase	F/t
4	VSC	—	VSC	—
	PM	-0.7945	PM	-0.9452
	HDSC	-0.8238	HDSC	—
	AF	-0.8553	AF	-0.9517
	DSC	-0.8667	DSC	-0.9489
	HVSC	-0.8677	HVSC	-0.9540
12	VSC	—	VSC	—
	PM	0.7368	PM	-0.4822
	HDSC	-0.2696	AF	-0.5341
	HVSC	-0.3525	HDSC	-0.5534
	AF	-0.3590	DSC	-0.5655
	DSC	-0.4526	HVSC	-0.5749

Table 4.2: The same as in Table 4.1 but in the t-t'-U model with $t'/t = -0.3$.

average hole density at the half-filled DWs is noticeably smaller than at the filled ones (*cf.* Figs. 4.2 and 4.3), it also helps to stabilize half-filled stripes, because one gains more correlation energy when the nonmagnetic atoms are close to half-filling. Nevertheless, the SB ground state of the Hubbard model ($t' = 0$) consists solely of filled stripes in the entire investigated regime $4 \leq U/t \leq 14$, as shown in Fig. 4.6(a). Interestingly, one recovers here the crossover from vertical to diagonal stripes upon increasing on-site repulsion U, shifted, however, towards a higher value $U/t \simeq 6$ than predicted by the HA. Another similarity with the Hartree results is that increasing $|t'|$ reduces the stability of the VSC stripe phase which becomes unstable already at $t/t = -0.15$ below $U/t \simeq 7$ (*cf.* Fig. 4.6(b). Eventually, further increase of $|t'|$ yields the HVSC stripe phase as the ground state in the wide $4 \leq U/t \leq 14$ regime as illustrated in Fig. 4.6(c). Moreover, from the curvature of the free energies in HDSC and DSC stripe phases, one can expect that the half-filled diagonal stripe phase also takes over the filled DSC stripe phase in the strongly correlated $U/t > 14$ regime. Values of the free energy, found in t-t'-U model with $U/t = 4$ and $U/t = 12$ as well as with $t'/t = -0.3$, are reported in Table 4.2. Once again, one finds that the overall order of listed phases is exactly the same in both methods in the weak coupling regime $U/t = 4$. One also recovers a strong tendency of the HA to promote the AF phase which becomes more stable than both types of the half-filled stripe phase in the strongly correlated regime $U/t \gtrsim 11.5$, a situation which is avoided in the SBA.

The explanation of the enhanced stability of the HVSC stripe with respect to the DSC structure, upon increasing $|t'|$ follows to some extent from Tables 4.3 and 4.4, in which we show local hole $\langle n_{\mathrm{h}i} \rangle$ (3.5) and magnetization $\langle S_i^z \rangle$ (3.6) density as well as double occupancy $D_i = \langle n_{i\uparrow} n_{i\downarrow} \rangle$ of the DSC (Table 4.3) and HVSC (Ta-

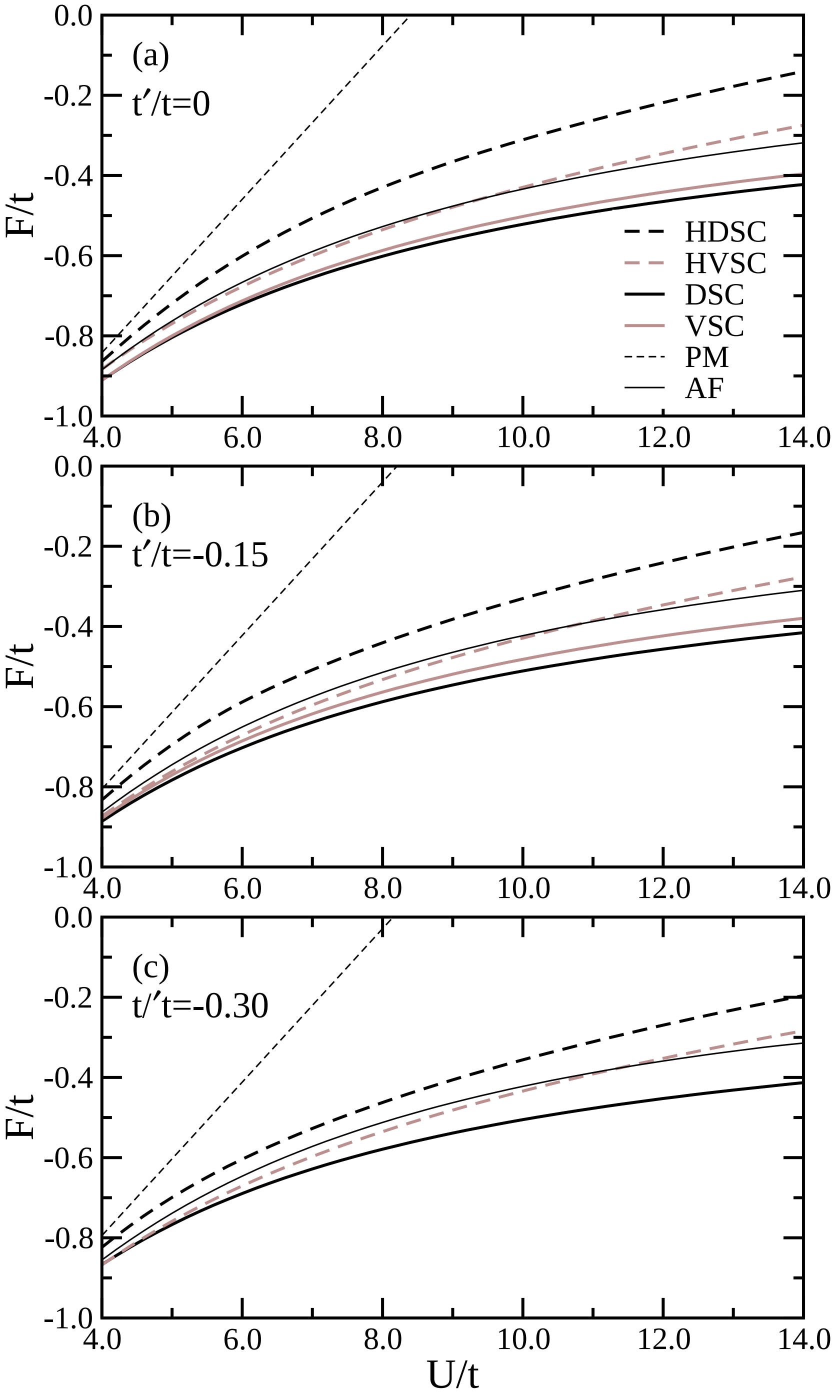

Figure 4.5: Free energy F of various phases per site as a function of U, obtained in the HA at temperature $\beta t = 100$ for the t-t'-U model on a 128×128 cluster with $x = 1/8$ and for: (a) $t' = 0$, (b) $t' = -0.15t$, and (c) $t' = -0.3t$.

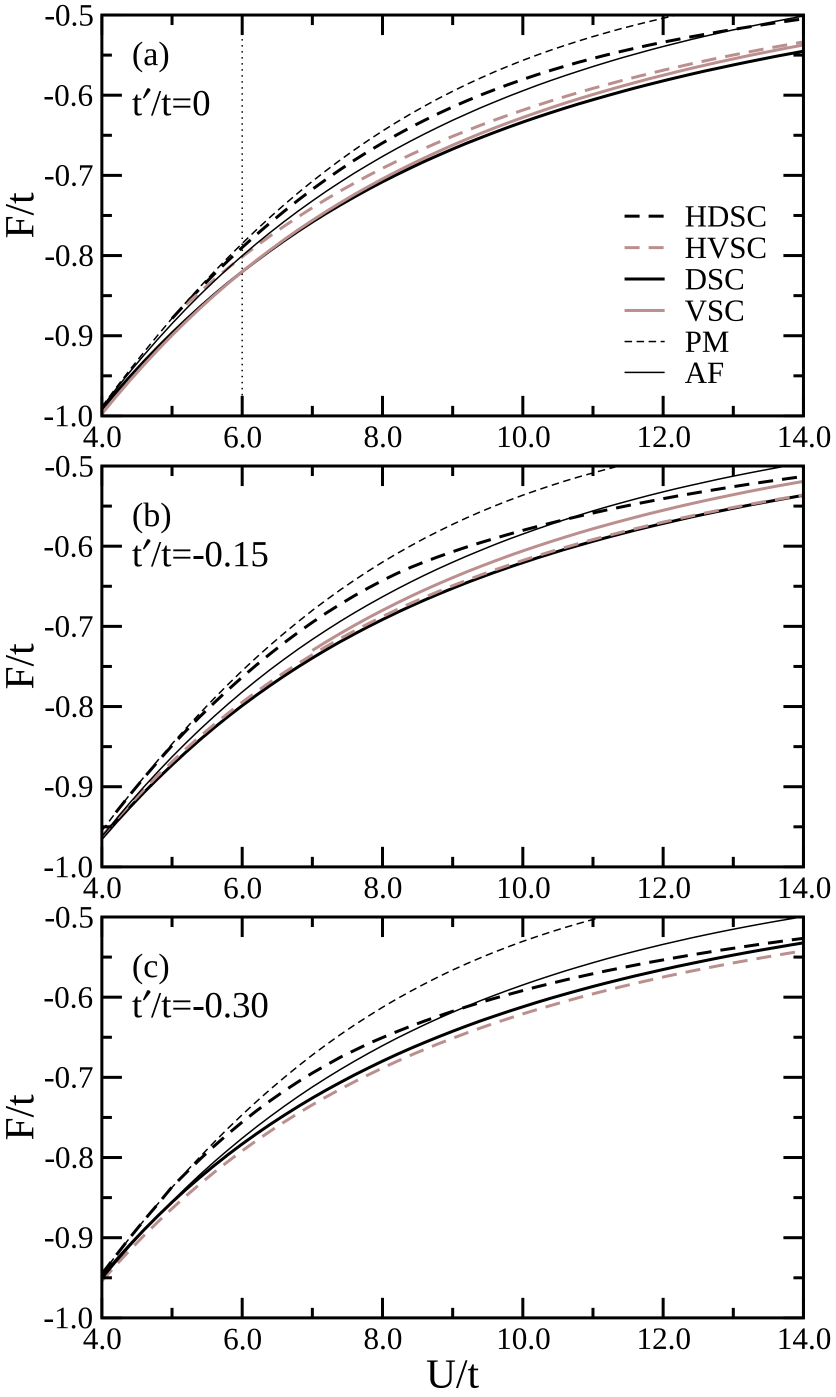

Figure 4.6: The same as in Fig. 4.5 but in the SBA. Thin dotted line in panel (a) indicates a crossover from the VSC to DSC stripe phase.

ble 4.4) stripe phases found in the t-t'-U model with $t' = 0$ and $t'/t = -0.3$. As we have already observed in Chapter 3, a negative ($t'/t < 0$) next-neighbor hopping

	i	1	2	3	4	5
	$\langle n_{\mathrm{h}i}\rangle$	0.445	0.196	0.055	0.020	0.011
HA		(0.471)	(0.194)	(0.052)	(0.014)	(0.008)
	$\langle S_i^z\rangle$	0.000	0.298	0.390	0.406	0.410
		(0.000)	(0.318)	(0.399)	(0.410)	(0.412)
	D_i	0.077	0.073	0.071	0.075	0.076
		(0.070)	(0.061)	(0.065)	(0.075)	(0.076)
	$\langle n_{\mathrm{h}i}\rangle$	0.235	0.180	0.110	0.067	0.051
SBA		(0.236)	(0.176)	(0.115)	(0.065)	(0.052)
	$\langle S_i^z\rangle$	0.000	0.172	0.280	0.332	0.349
		(0.000)	(0.200)	(0.287)	(0.342)	(0.355)
	D_i	0.059	0.064	0.070	0.074	0.075
		(0.053)	(0.059)	(0.065)	(0.070)	(0.072)

Table 4.3: Local hole $\langle n_{\mathrm{h}i}\rangle$ and magnetization $\langle S_i^z\rangle$ density as well as average double occupancy D_i per site in the DSC stripe phase, given for inequivalent sites with decreasing hole density in the x-direction, as found either in the HA or SBA, at temperature $\beta t = 100$ in the Hubbard model on a 128×128 cluster with $U = 6t$ and $x = 1/8$. The values given in parenthesis are for the t-t'-U model with $t'/t = -0.3$.

	i	1	2	3
	$\langle n_{\mathrm{h}i}\rangle$	0.294	0.091	0.024
HA		(0.293)	(0.091)	(0.025)
	$\langle S_i^z\rangle$	0.000	0.372	0.405
		(0.000)	(0.381)	(0.407)
	D_i	0.124	0.068	0.074
		(0.125)	(0.062)	(0.071)
	$\langle n_{\mathrm{h}i}\rangle$	0.187	0.119	0.075
SBA		(0.185)	(0.119)	(0.077)
	$\langle S_i^z\rangle$	0.000	0.274	0.332
		(0.000)	(0.290)	(0.344)
	D_i	0.068	0.067	0.070
		(0.067)	(0.062)	(0.064)

Table 4.4: The same as in Table 4.3 but for the HVSC stripe phase.

yields a positive kinetic energy contribution and is best optimized in a phase with the filled stripe by expelling the holes from the AF domains, stronger reduction of double occupancy, and consequently, by a larger spin polarization of the AF regions between stripes. All these features are clearly seen in Table 4.3. By con-

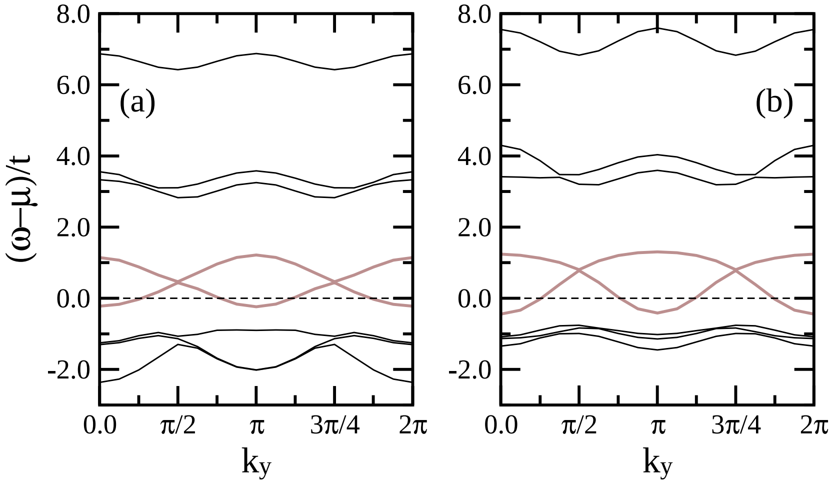

Figure 4.7: SB band structure of the HVSC stripe phase as a function of parallel momentum k_y, calculated from the unit cell shown in Fig. 4.1(a) at temperature $\beta t = 50$ in the t-t'-U model on a 8×16 cluster with $U/t = 12$ and: (a) $t' = 0$ and (b) $t'/t = -0.3$. Black (gray) line corresponds to the bulk (mid-gap) bands, respectively, whereas the dashed line indicates the Fermi level.

trast, even though the half-filled stripe phase also reduces double occupancy and develops strong polarization of the AF domains upon increasing $|t'|$, the average hole density within the AF domains remains constant or even it is slightly enhanced as illustrated in Table 4.4. This means that such a configuration provides a possibility to gain the kinetic energy associated with t' due to the mechanism known for the HVSC stripe phase with a period quadrupling [*cf.* Fig. 3.18(a)]. Indeed, in agreement with Ref. 33, Fig. 4.7 shows that negative t' leads to a distinct broadening of the partially filled mid-gap band and consequently to a shift of this state to lower energy. Conversely, the energy gain due to such a modification of the band structure is not possible in the case of filled stripes as their mid-gap states are entirely *unoccupied* [*cf.* Fig. 3.15(a)]. This clarifies the puzzling role of t' in promoting partially filled DWs.

4.6 Doping dependence of the stripe ground state

In the preceding Section we have discussed the competition between two idealized stripe phases, i.e., pure half-filled and entirely filled structure. However, the true ground state could correspond to neither one of those special cases as the optimal filling might vary with doping. Moreover, one would like to know whether the SC or BC stripes are preferred in particular doping regimes.

With the goal of elucidating these points we have performed extensive SB studies involving vertical SC (BC) stripes with the size of the AF domains varying

d	SC stripes	BC stripes
2	128×128	—
3	144×144	144×144
4	128×128	128×128
5	140×140	140×140
6	120×120	120×120
7	140×140	140×140
8	128×128	128×128
9	144×144	144×144
10	120×120	120×120
11	132×132	132×132

Table 4.5: Cluster size used in calculations for both SC and BC stripes separated by a different distance d in units of the lattice constant. BC stripes with $d = 2$ do not exist.

from $d = 2$ ($d = 3$) up to 11 lattice constants, respectively. Note that in the case of BC stripes, there is no BC configuration with $d = 2$. Calculations were carried out on a squared cluster with the linear dimension along the x direction chosen always as an *even* multiplicity of the elementary unit cell dimension. The cluster size used in calculations for a given distance d is listed explicitly in Table 4.5. In both structures, the largest $d = 11$ corresponds to a unit cell with 22 atoms. On the one hand, unit cell of the SC stripes consists of two nonmagnetic DWs and two AF domains containing $n_{\rm AF}^{\rm SC} = d - 1$ atoms each. This yields a total number of atoms,

$$L_{\rm SC} = 2\big(n_{\rm AF}^{\rm SC} + 1\big) = 2d. \tag{4.61}$$

On the other hand, unit cell of the BC stripes consists of two DWs made out of pairs of atoms with FM spin polarization and also two AF domains containing $n_{\rm AF}^{\rm BC} = d - 2$ atoms each. This results in a total number of atoms,

$$L_{\rm BC} = 2\big(n_{\rm AF}^{\rm BC} + 2\big) = 2d. \tag{4.62}$$

The same length of the magnetic unit cell for a fixed d makes both structures practically indistinguishable in neutron diffraction experiments. We believe that such large systems, as those reported in Table 4.5, suppress the finite size effects and allow one to obtain a realistic comparison of the free energies of structures with a different length of the unit cell. In the numerical studies, we have chosen $U/t = 12$, which gives the ratio of $J/t = 1/3$ with $J = 4t^2/U$, being a value representative for LSCO [130].

In Fig. 4.8, we show the SB free energy gain of the VSC stripe phase with respect to the AF phase δF_{AF} as a function of doping x found in the t-t'-U model for representative values of the next-neighbor hopping, i.e., $t' = 0$, $t' = -0.15t$,

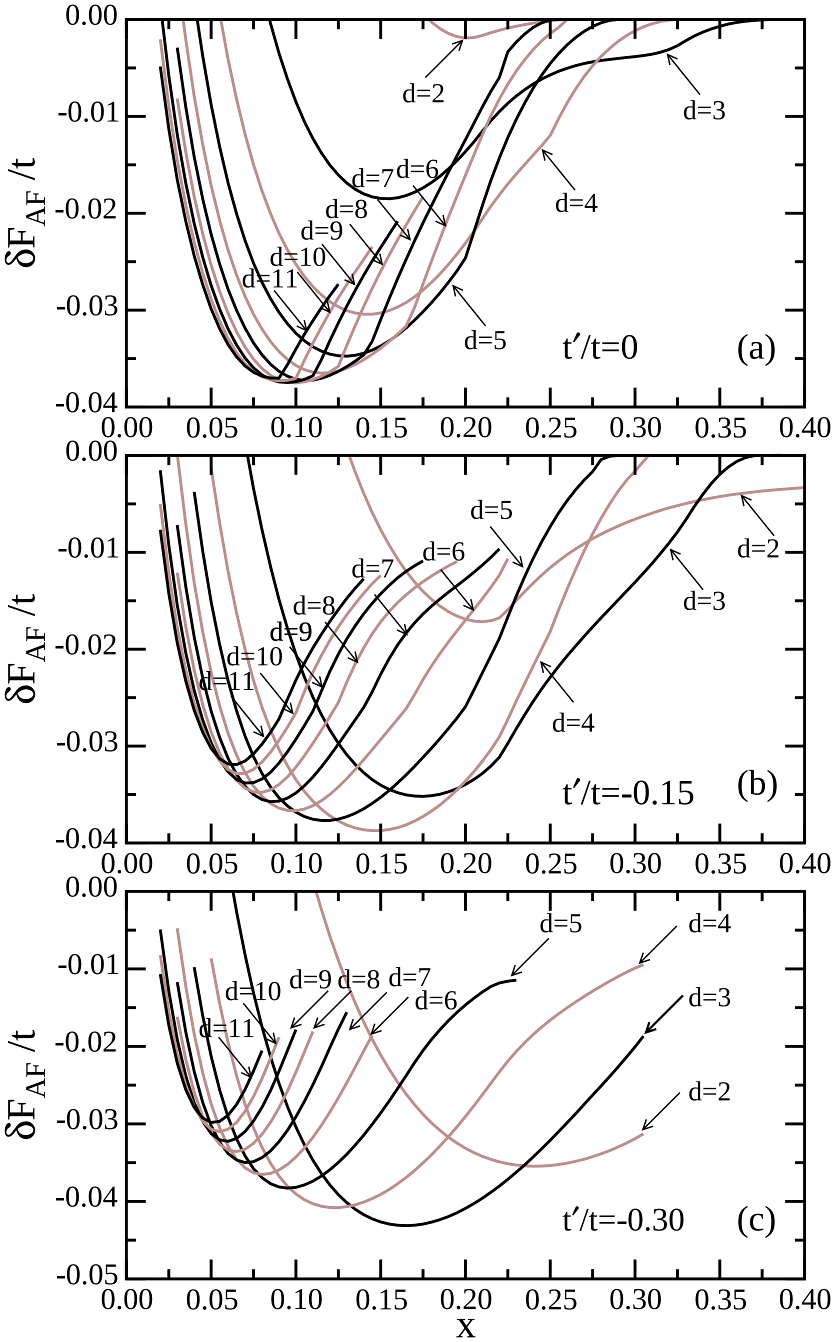

Figure 4.8: SB free energy gain of the VSC stripe phases with respect to the AF phase δF_{AF} as a function of doping x, as obtained at temperature $\beta t = 100$ for the t-t'-U model with $U = 12t$ and: (a) $t' = 0$, (b) $t' = -0.15t$, and (c) $t' = -0.3t$. Stripes are separated by $d = 2, \ldots, 11$ lattice constants.

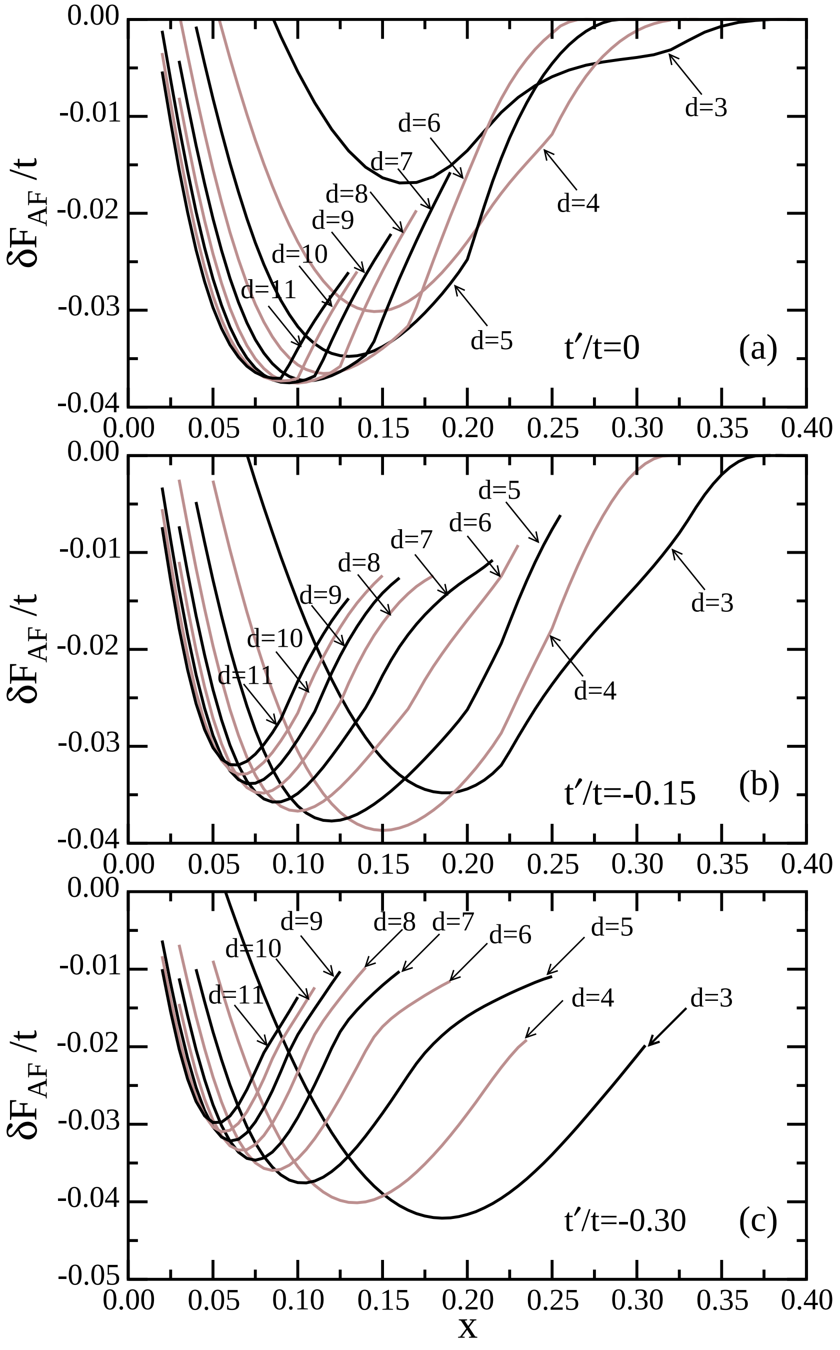

Figure 4.9: The same as in Fig. 4.8 but for the VBC stripes.

and $t' = -0.3t$. Quite general, one observes that a curve with the largest $d = 11$, appears at the lowest values of x and upon further doping curves with smaller d systematically cross the ones with larger d, meaning that stripes with smaller periodicity become the lowest energy solutions. For $t' = 0$, this effects continues

	VSC		VBC	
x	d	F/t	d	F/t
0.050	11	−0.4263	11	−0.4263
0.055	10	−0.4360	10	−0.4359
0.060	9	−0.4456	9	−0.4455
0.070	8	−0.4649	8	−0.4648
0.080	7	−0.4841	7	−0.4840
0.090	6	−0.5034	6	−0.5032
0.100	5	−0.5225	6	−0.5224
0.120	5	−0.5607	5	−0.5607
0.140	4	−0.5985	4	−0.5983
0.160	4	−0.6342	4	−0.6342
0.180	4	−0.6671	4	−0.6670
0.200	3	−0.6978	3	−0.6983
0.250	3	−0.7682	3	−0.7689
0.300	3	−0.8242	3	−0.8245
0.350	2	−0.8627	3	−0.8605

Table 4.6: Comparison of the SB ground state free energy F for the VSC and VBC stripes as found in the t-t'-U model with $U = 12t$ and $t' = -0.15t$.

until the $d = 3$ stripe sets in, as the $d = 2$ one is, for the present value of U, a highly-excited state and never corresponds to the ground state. By contrast, finite t' results in a deeper minimum of the $d = 2$ curve and stabilizes such a phase with with a single atom in the AF domains in the overdoped regime $x \geq 0.34$ ($x \geq 0.23$) for $t'/t = -0.15$ ($t'/t = -0.30$), respectively. We shall, however, not pursue here this effect as the properties and mechanism leading to formation of the $d = 2$ stripe is discussed in the next Section. Next, except for the smallest $d \leq 3$ cases, increasing $|t'|$ shifts the free energy minima towards lower doping level which should affect the filling of the DWs and the charge distribution in the stripe ground state.

Similar tendency to promote stripes with larger (smaller) unit cells at lower (higher) x, respectively, as well as to shift the minima of F to lower doping upon increasing $|t'|$, is observed for the VBC stripes, as shown in Fig. 4.9, and seemingly it is a robust feature of both structures. Remarkably, for $t'/t = -0.15$, a value very close to the LSCO model parameter, i.e., $t'/t = -0.1$ [140], one finds for both the SC and BC phase, that the most stable stripes are separated by $d = 4$ lattice spacings a sizeable doping range above $x \simeq 1/8$, in agreement with neutron scattering experiment [23] and with theory [130] for LSCO.

In Table 4.6 we report the SB ground state free energy F for both types of stripes as found for $U = 12t$ and $t' = -0.15t$. Unfortunately, based on the present studies, one cannot reach any unambiguous conclusion concerning the competition

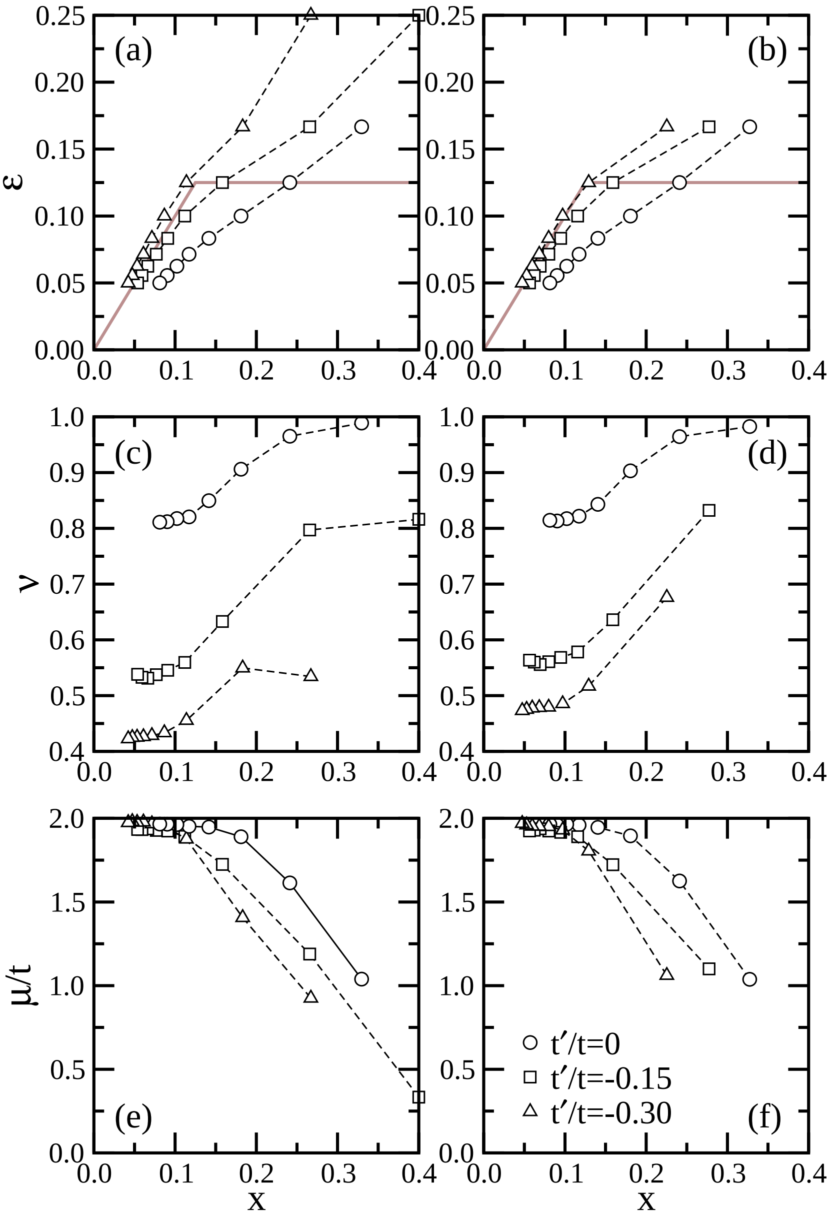

Figure 4.10: Doping dependence of: (a,b) magnetic incommensurability ϵ, (c,d) stripe filling ν, and (e,f) chemical potential μ for the VSC (left) and VBC (right) stripe ground state deduced from Figs. 4.8 and 4.9. Gray solid line in panels (a,b) shows the experimental behavior of ϵ in LSCO [23].

between the SC and BC stripes. Even though the SC stripes appear to be more favorable in the doping regime $x \leq 0.18$, in agreement with DMFT results [130] as well as with SB findings obtained on small 16×16 clusters, the energy difference between the best SC and BC configuration does not exceed $-0.0002t$, being comparable to the accuracy of the calculations. Therefore, it seems that quantum fluctuations might play a crucial role and either stabilize one of two possible structures or even lead to dynamical stripes for certain parameters. Moreover, a detailed analysis of a hole propagation inside the BC DWs, with the filling slightly below 1/2, shows that such a spin background yields larger kinetic energy gain than narrower SC DWs [155]. This gain becomes more important especially at larger doping levels $x \simeq 1/8$ when the distances between stripes are small. Interestingly, doping above $x = 0.18$ stabilizes the $d = 3$ BC stripes and the energy difference reaches its maximum 0.0007t at $x = 1/4$, then it gradually decreases, and finally, the $d = 2$ SC structure becomes the lowest energy configuration, as there is no such a BC counterpart (*cf.* Table 4.6).

The presence of IC spin fluctuations $\mathbf{Q}_s = \pi(1 \pm 2\epsilon, 1)$ and $\mathbf{Q}_s = \pi(1, 1 \pm 2\epsilon)$ consistent with stripe order in the CuO$_2$ planes of LSCO and Nd-LSCO is by now well accepted [13, 18–20, 23]. Remarkably, the incommensurability $\epsilon = 1/2d$ varies linearly with doping $\epsilon = x$ in the underdoped regime of $x < 1/8$ meaning a fixed stripe filling $\nu = 1/2$. By contrast, beyond $x = 1/8$, one finds in experiment a lock-in effect with $\epsilon = 1/8$, corresponding to a stripe phase with a charge (magnetic) unit cell consisting of four (eight) sites, and the AF domains with three atoms along the x direction. This should be compared with our findings concerning the behavior of ϵ and the optimal stripe filling,

$$\nu = \frac{N_{\rm h}}{N_y N_{\rm DW}}, \tag{4.63}$$

upon increasing doping x for different values of t', in both vertical SC and BC phases, are shown in Fig. 4.10(a-d). In Eq. (4.63), $N_{\rm h}$ is the hole excess compared to half-filling, whereas N_y denotes the length in the y direction of the cluster with $N_{\rm DW}$ domain walls. The points in Fig. 4.10 correspond to the middle of stability region of the lowest energy configuration. Such a choice guarantees that, at this particular doping level, a considered stripe phase with a given periodicity d would be indeed realized at least in the vast majority of the system.

Comparing Fig. 4.10 with the experimental data in LSCO, one finds that phenomenon of the half-filled $d = 4$ stripes at $x = 1/8$ requires, in agreement with the previous SB studies [33], a finite next-neighbor hopping $t'/t < -0.15$. Further, for $t'/t < -0.15$, present calculations give almost linear dependence $\epsilon = x$ for $x \lesssim 1/8$ and may be considered as reproducing a lock-in effect in a sizeable doping range above $x \simeq 1/8$ until the $d = 3$ stripes do not set in. It is worth mentioning here that stable $d = 3$ stripes with $\epsilon = 1/6 \simeq 0.17$ have also been found in the SB studies of the three-band model in the doping regime $x > 0.225$ [116]. Moreover, these studies have also revealed the trend to suppress ν upon increasing oxygen-oxygen hopping t_{pp}, imitated in the effective single-band model by t'. Remarkably, in the regime where ϵ follows linearly x, an increasing density of stripes allows the system to maintain fixed ν and its value strongly depends on t'. This, in turn, pins the chemical potential μ, as shown in Fig. 4.10(e,f). In fact, such a suppression has

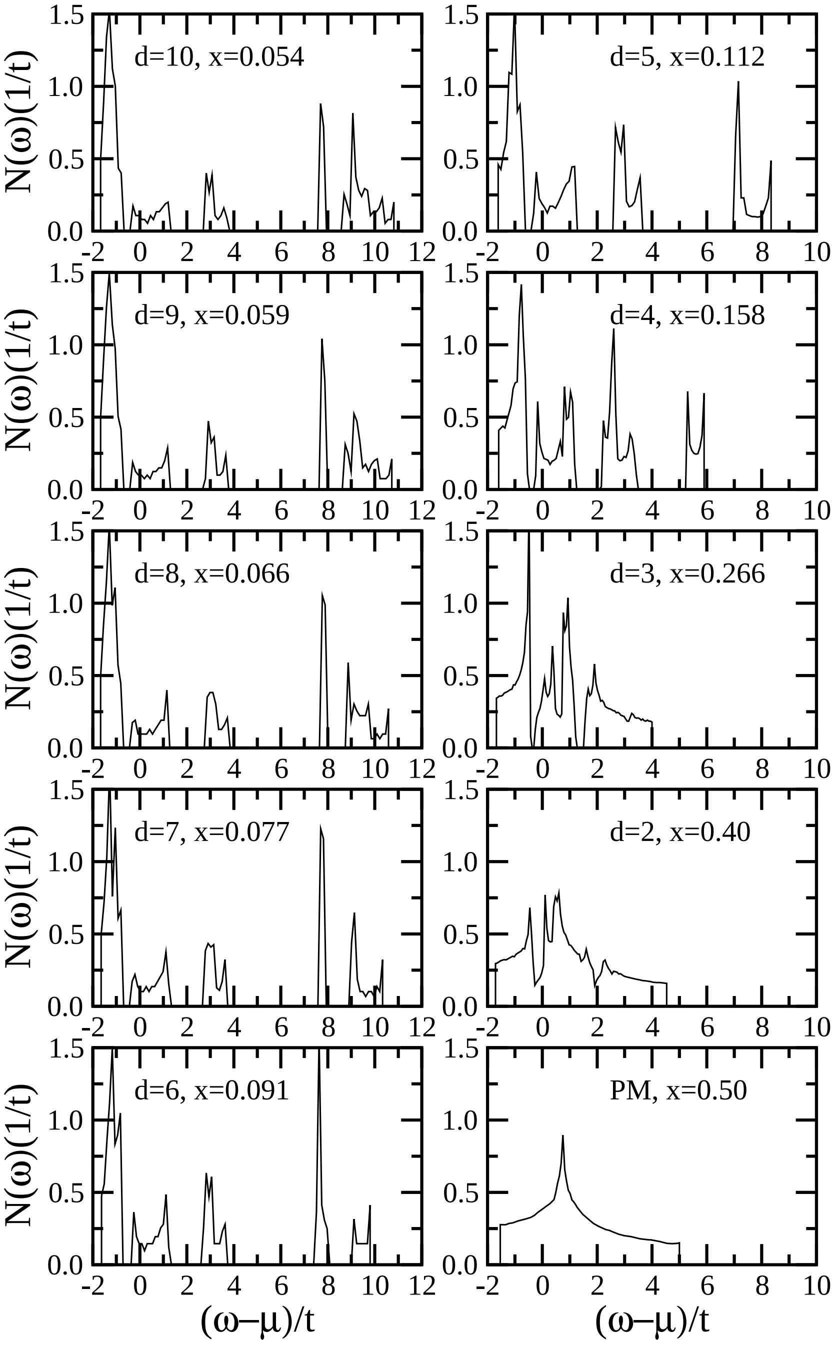

Figure 4.11: Doping dependence of the density of states $N(\omega)$ for the VSC stripe ground state, deduced from Fig. 4.8(b), of the t-t'-U model with $U = 12t$ and $t' = -0.15t$. Bottom right panel shows the result obtained for the same parameters for the PM ground state at x=0.5.

been experimentally observed in LSCO in Ref. 80 [*cf.* Fig. 2.6(b)]. Unfortunately, for $t'/t = -0.15$, the established shift of the chemical potential $\Delta\mu$ in the regime $x > 0.15$ exceeds the experimental value $\simeq -1.5$ eV/hole by a factor close to 2. Indeed, the effective hopping $t = 0.62$ eV, which follows from $t = t_{pd}^2/\Delta$, with Cu-O hopping $t_{pd} = 1.47$ eV and charge transfer energy $\Delta = 3.5$ eV [156], yields $\Delta\mu \simeq -3.1$ (-3.3) eV/hole for the SC (BC) stripes, respectively.

Our approach also allows one to investigate evolution of the density of states $N(\omega)$ as a function of doping, depicted in Fig. 4.11, for the VSC stripe ground state. The analysis of $N(\omega)$ reveals a systematic transfer of spectral weight from the UHB into the LHB upon doping, in agreement with strong-coupling perturbation theory for the Hubbard model [157], as well as into the mid-gap bands which emerge and grow when the stripe order develops. Next, in the whole regime of doping where the stripes are stable, i.e., below $x \lesssim 0.3$, one observes that the mid-gap states are clearly separated from both the LHB and UHB by real gaps. In contrast, the gaps are gradually filled up with the spectral weight when the $d = 2$ melt, so that at $x = 0.5$ one recovers a well-know density of states that resembles a simple tight-binding DOS.

4.7 Melting of the stripe phases

As we have pointed out in Introduction, two main scenarios for a driving mechanism of the stripe phase have been proposed [10]. In the first one stripes arise from the Fermi surface instability with the spin driven transition [5–9]; then spin and charge order simultaneously, or charge order follows spin order. The second scenario comes from Coulomb-frustrated phase separation suggesting that stripe formation is commonly charge driven, and the charge order sets in first when the temperature is lowered. However, SB studies of the 2D t-t'-U Hubbard model showed that the spin susceptibility diverges while the charge susceptibility does not [143], supporting the former scenario. Therefore, the microscopic origin of the stripe instability in real systems remains unclear.

Here, we investigate the mechanism leading to phase separation and the melting of vertical BC and SC stripes separated by $d \leq 3$ in the overdoped regime $x \geq 0.3$ of the 2D t-t'-U Hubbard model. For the model parameters for LSCO: $U/t = 12$ and $t'/t = -0.15$, one obtains that the most stable SC DWs are separated by $d = 3$ for $0.2 \leqslant x \leqslant 0.34$. As shown in Fig. 4.12(a), increasing doping stabilizes finally the SC stripes with a single atom in the AF domains. In contrast, for the BC stripes above $x = 0.19$, the size of the AF domains remains fixed at $d = 3$, as the BC configuration with $d = 2$ does no exist.

In Fig. 4.12(a) we show the energy gain of the stripe phases with respect to the PM phase δF_{PM}. Remarkably, the difference in energy between the best SC and BC stripes is smaller than both the accuracy of the calculations, and the resolution of Fig. 4.12(a), suggesting that quantum fluctuations might be impor-

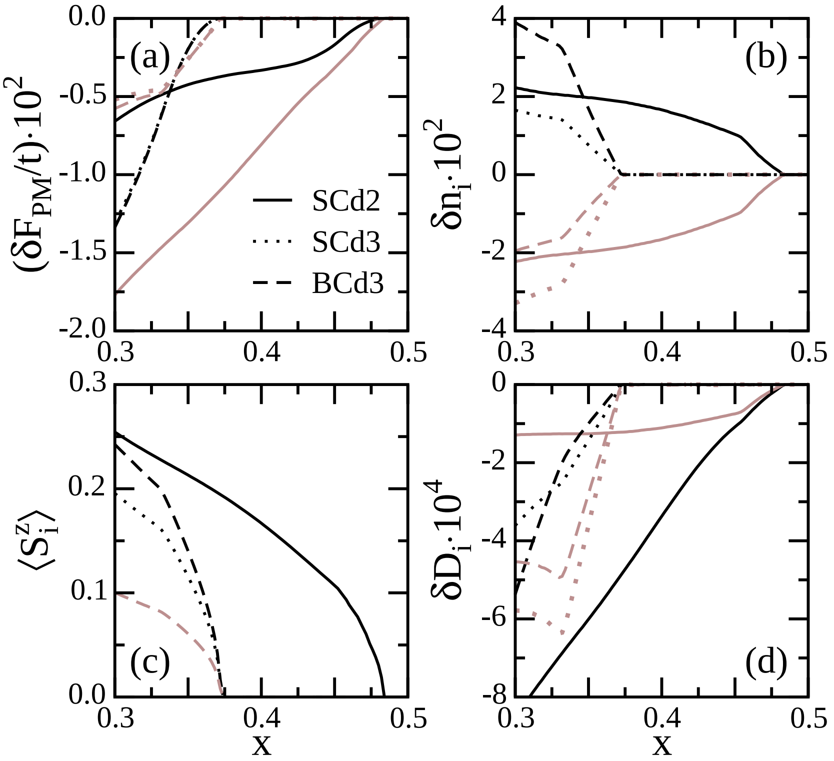

Figure 4.12: Melting of vertical BC and SC with increasing doping x at temperature $\beta t = 100$: (a) the free energy δF_{PM} (black line) and interaction (grey line) energy gain in the stripe phases; (b) local charge densities δn_i relative to their average values; (c) amplitude of local magnetization $\langle S_i^z \rangle$; (d) double occupancies δD_i relative to the values in the PM phase (scaled by a factor $\frac{1}{3}$ for the $d = 2$ stripe). In panels (b)-(d) the black (gray) curves correspond to the strongly (weakly) polarized sites, respectively.

tant. We characterize the melting of stripes by their SB local averages: density $n_i = \sum_\sigma \langle n_{i\sigma} \rangle$, amplitude of the magnetization $\langle S_i^z \rangle$, and double occupancies D_i.

In the $d = 2$ SC stripe, reported here for the first time, the two $\delta n_i(x)$ curves are symmetrical in Fig. 4.12(b). In contrast, in the $d = 3$ BC stripe there are two sites with weak magnetic moments per one strongly polarized site. We note that, unlike in the SC phase, the variation in density is largest on the strongly polarized sites in the BC phase. The magnetic moments $\langle S_i^z \rangle$ vanish for both types $d = 3$ stripes at the same doping $x = 0.375$ [*cf.* Fig. 4.12(c)], suggesting that they originate from the same instability.

The microscopic mechanism stabilizing the $d = 2$ SC stripes appears to differ markedly from the one stabilizing the $d = 3$ ones [111]. Indeed, for stripes separated by $d = 2$, the reduction of double occupancy is strongest on the magnetic sites, as shown in Fig. 4.12(d), and the corresponding reduction of interaction energy exceeds the gain of free energy [*cf.* Fig. 4.12(a)]. Thus the mechanism leading to the formation of the $d = 2$ stripe is primarily local, making use of two complementary effects helping to reduce double occupancy: finite magnetization at magnetic sites and reduced electron density at nonmagnetic ones. Even though the kinetic energy is partially lost in such a state, the gain in the interaction energy overcompensates this loss, stabilizing this order in a wide doping range $x \leqslant 0.485$.

In contrast, for $d = 3$ stripes, both contributions to the free energy are substantially decreased while the stripe order starts to melt already at $x < 0.3$ mainly by a stronger reduction of double occupancies in DWs than within AF domains leading to gradually disappearing magnetic moments upon doping. Therefore, both potential and kinetic energy (including the superexchange) cooperate to stabilize the stripe phase with $d > 2$.

In fact, for both types of $d = 3$ stripes, the mechanism is doping dependent; in the small magnetization regime, the interaction energy plays the leading role, whereas under a further decrease of hole density, this gain nearly saturates (at $x \simeq 0.33$), and the gain in the kinetic energy starts to dominate. Moreover, it is only slightly larger for the SC stripe phase as compared to the BC one, and therefore it is easily compensated, mainly by the presence of finite magnetic moments at the BC DWs. As a common feature, the spin and charge order *disappear* simultaneously at the critical doping. Therefore, in the absence of longer ranged Coulomb interaction the charge order is always accompanied by the spin order. This gives further support to the first of he discussed scenarios that the stripe order is a common charge-and-spin instability.

Summarizing, we have investigated the microscopic mechanisms responsible for the formation of the vertical BC and SC stripe phases with $d \leq 3$. Interestingly, we have found that both phases remain nearly degenerate, and *spin and charge* order vanish simultaneously when the stripes melt, demonstrating a cooperative character of the stripe order.

Chapter 5

Systems with orbital degeneracy

The Hubbard model has been employed for a long time as a standard model for metallic ferromagnetism of itinerant electrons [158, 159] and localization [160]. However, it turns out that this model on the hypercubic lattice does not easily yield ferromagnetism and some additional features are necessary to stabilize a FM phase if one goes beyond the HF approximation. For example, Nagaoka established that in the limit of infinite Coulomb interaction U, a single hole doped into a half-filled system leads to the FM ground state [161]. Ferromagnetism may be also promoted by a particular lattice or band structure. Lieb first showed that a half-filled flat band induces a net magnetization [162]. Furthermore, Hirsch and others have focused on the effect of additional off-diagonal matrix elements of the Coulomb interaction [163–165].

A major step towards understanding the physics of real ferromagnets, e.g., transition metals Fe, Co, and Ni was the suggestion that orbital degeneracy might play a crucial role. It was first pointed out by Slater, Statz, and Koster [166] and then stressed by van Vleck [167] that in the presence of degenerate orbitals, Hund's coupling J_H favors local triplet spin configurations of two electrons occupying different orbitals. Roth [168] examined the doubly degenerate model in the three-dimensional quarter-filling case with one electron per site. She found that the ground state is a spin triplet and orbital singlet, i.e., the system forms an orbital superlattice structure in which two sublattices are occupied by electrons of different orbitals. Taking into account the connection between staggered orbital order and spin ferromagnetism, Kugel and Khomskii [169] derived an effective strong coupling Hamiltonian with coupled spin and orbital degrees of freedom, extended further by Cyrot and Lyon-Caen [170], who included the effect of on-site pair hopping, and by Inagaki [171]. These seminal papers started a new field — spin-orbital physics in correlated transition metal oxides [2].

While systems of higher dimensionality are clearly the ones of most interest recently [172–180], significant insight into the complementary behavior of both degrees of freedom was obtained in a 1D model. Indeed, many of essential features of such 1D systems were established by QMC simulations [181], ED studies [182–

184], and DMRG method [185]. Finally, quite an interesting result was obtained in the classical spin limit which gives an orbital valence bond ground state, in which each bond is an orbital singlet and spin triplet, whereas the spin on neighboring bonds interact antiferromagnetically [186].

However, in all above studies a theoretically simplified model, the orbital degenerate Hubbard model in which two equivalent orbitals that are not mixed by the hopping. In contrast, the orbital flavor for the e_g electrons is not conserved, and this is likely to lead to partial orbital polarization which is expected to modify the magnetic instabilities. Therefore, in Section 5.1 we introduce a *realistic model* with the e_g electrons and in Section 5.2 we verify if the phenomenon of a complementary behavior of the spin and orbital flavors is also a characteristic feature of this particular case by solving exactly a two-site system at quarter-filling. Next, in Section 5.3, we determine a phase diagram of the model in the HA and compare the mean-field results with the ED solutions. In particular, we address the occurrence of orbitally polarized states due to the inequivalent orbitals, and their interplay with FM and AF spin order. We also discuss the role played by Hund's exchange coupling J_H and by the crystal field orbital splitting E_z in stabilizing one of the competing phases.

The magnetic and orbital instabilities within the e_g band become especially relevant in the context of doped nickelates LSNO and LNO, where interesting novel phases including the stripe order were discovered [14]. Therefore, in Section 5.4, we shall investigate behavior of the incommensurability ϵ, optimal stripe filling ν, and the chemical potential μ in the stripe ground state, similarly as we have done in Chapter 4 within a single-band Hubbard model for the cuprates. For this purpose we use the HA known to provide, when applied to a four-band Peierls-Hubbard model, a good description of the stripe phase in the nickelates [101, 102] and show that the filled diagonal BC stripes observed in the nickelates appear naturally within the effective model for the e_g electrons, whereas a simplified equivalent band model, i.e., DDH model, yields half-filled DWs and appears to be insufficient to reproduce the experimental data.

5.1 Hamiltonian for e_g electrons

Even though doped nickelate LSNO is isostructural with the cuprate counterpart LSCO, its electronic degrees of freedom are more complicated. In fact, a realistic Hamiltonian for LSNO must contain, besides the $|x^2-y^2\rangle$ orbital states included in the cuprate oxide models, also the $|3z^2-r^2\rangle$ orbital states, so as to account for the actual filling with two holes and for the high spin state ($S=1$) in the stoichiometric compound. Such a model of interacting e_g electrons in a 2D (a,b) plane may be written as follows,

$$\mathcal{H} = H_{kin} + H_{int} + H_{cf}, \tag{5.1}$$

with two orbital flavors: $|x\rangle \sim |x^2-y^2\rangle$ and $|z\rangle \sim |3z^2-r^2\rangle$ forming a basis in the orbital space. The kinetic energy is described by

$$H_{kin} = \sum_{\langle ij\rangle}\sum_{\alpha\beta\sigma} t_{ij}^{\alpha\beta} c_{i\alpha\sigma}^{\dagger} c_{j\beta\sigma}, \qquad t_{ij}^{\alpha\beta} = -\frac{t}{4}\begin{pmatrix} 3 & \pm\sqrt{3} \\ \pm\sqrt{3} & 1 \end{pmatrix}, \tag{5.2}$$

where t stands for an effective $(dd\sigma)$ hopping matrix element due to the hybridization with oxygen orbitals on Ni$-$O$-$Ni bonds, and the off-diagonal hopping t_{ij}^{xz} along a and b axis depends on the phase of the $|x\rangle$ orbital along the considered cubic direction. The electron-electron interactions are described by the on-site terms, which we write in the following form,

$$\begin{aligned} H_{int} = {} & U\sum_i \big(n_{ix\uparrow}n_{ix\downarrow} + n_{iz\uparrow}n_{iz\downarrow}\big) + \big(U - \tfrac{5}{2}J_H\big)\sum_i n_{ix}n_{iz} \\ & - 2J_H\sum_i \mathbf{S}_{ix}\cdot\mathbf{S}_{iz} + J_H\sum_i \big(c_{ix\uparrow}^{\dagger}c_{ix\downarrow}^{\dagger}c_{iz\downarrow}c_{iz\uparrow} + c_{iz\uparrow}^{\dagger}c_{iz\downarrow}^{\dagger}c_{ix\downarrow}c_{ix\uparrow}\big), \end{aligned} \tag{5.3}$$

where U and J_H stand for the intraorbital Coulomb and Hund's exchange elements, whereas $n_{i\alpha} = \sum_\sigma n_{i\alpha\sigma}$ for $\alpha = (x,z)$. The interactions H_{int} are rotationally invariant both in the spin and in the orbital space [187]. The last term H_{cf} describes the uniform crystal-field splitting between $|x\rangle$ and $|z\rangle$ orbitals along the c axis,

$$H_{cf} = \tfrac{1}{2}E_0\sum_{i\sigma}(n_{ix\sigma} - n_{iz\sigma}). \tag{5.4}$$

The reason of splitting between the e_g orbitals is the tetragonal Jahn-Teller distortion of the NiO$_6$ octahedron. In La$_2$NiO$_4$, however, the octahedron, with the Ni$-$O$-$Ni bond lengths to be 1.95 (2.26) Å in-plane (out-of-plane) [189], respectively, is much less distorted as compared with 1.89 and 2.43 Å for La$_2$CuO$_4$ [190], which reflects the difference in electron filling. In what follows we consider only a realistic positive E_0 favoring, due to elongated octahedra, the $|z\rangle$-occupancy over the $|x\rangle$-occupancy by the e_g electrons in doped compounds.

5.2 Exact solution of the two-site cluster

First, in order to understand better the electronic structure and intersite correlations, we solve exactly in this section the two-site molecule with either e_g or t_{2g} orbitals at quarter-filling. Although it is straightforward to solve the present problem numerically, it is instructive to find the solution analytically. Along this process several important aspects will be clarified.

For the 1D model it is most convenient to consider a chain with a basis consisting of a directional orbital along the chain $|\zeta\rangle$ and a planar orbital $|\xi\rangle$ orthogonal to the bond direction [188]. Pairs of such orthogonal orbitals forming a new basis

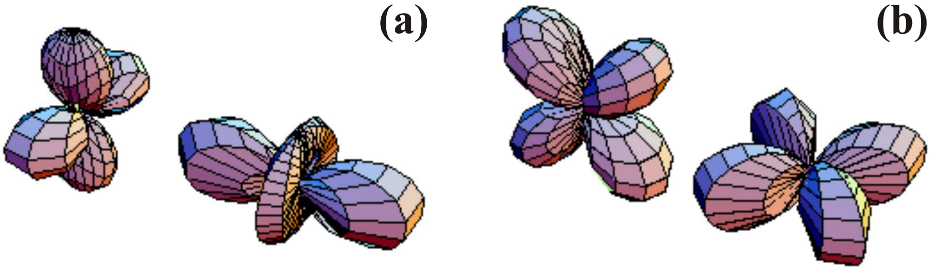

Figure 5.1: Pairs of orthogonal orbitals $\{|\zeta\rangle, |\xi\rangle\}$ aligned along the a axis. (a) e_g orbitals; (b) t_{2g} orbitals.

might be obtained by the following transformation of the original orbital basis $\{|x\rangle, |z\rangle\}$,

$$\begin{pmatrix} |\zeta\rangle \\ |\xi\rangle \end{pmatrix} = \begin{pmatrix} \cos\frac{\theta}{2} & \sin\frac{\theta}{2} \\ -\sin\frac{\theta}{2} & \cos\frac{\theta}{2} \end{pmatrix} \begin{pmatrix} |z\rangle \\ |x\rangle \end{pmatrix}, \tag{5.5}$$

with the angle $\theta = \pm\frac{2\pi}{3}$ depending on whether one considers the chain along a or b axis. Explicitly, we obtain,

$$|\zeta\rangle = \tfrac{1}{2}\big(|z\rangle \pm \sqrt{3}|x\rangle\big), \qquad |\xi\rangle = \tfrac{1}{2}\big(\mp\sqrt{3}|z\rangle + |x\rangle\big), \tag{5.6}$$

i.e., the directional $|\zeta\rangle \sim |3x^2 - r^2\rangle$ or $|\zeta\rangle \sim |3y^2 - r^2\rangle$ orbital along the chain consists of predominantly $|x\rangle$ contribution, whereas the orthogonal $|\xi\rangle \sim |y^2 - z^2\rangle$ or $|\xi\rangle \sim |z^2 - x^2\rangle$ has a larger amplitude of $|z\rangle$ than $|x\rangle$ orbital. The above rotation leads to a simple hopping matrix,

$$t_{e_g}^{\zeta\xi} = -t\begin{pmatrix} 1 & 0 \\ 0 & 0 \end{pmatrix}, \tag{5.7}$$

allowing only for intersite transitions between the directional $|\zeta\rangle$ orbitals. We compare this case with a frequently studied diagonal-hopping model, i.e., with the DDH model. Assuming again two orbitals in the 1D case it describes the dynamics of two active t_{2g} orbitals, e.g. for a chain along x axis, $|\zeta\rangle \sim |xz\rangle$ and $|\xi\rangle \sim |xy\rangle$, so that,

$$t_{t_{2g}}^{\zeta\xi} = -t\begin{pmatrix} 1 & 0 \\ 0 & 1 \end{pmatrix}. \tag{5.8}$$

Pairs of orthogonal orbitals $\{|\zeta\rangle, |\xi\rangle\}$ used in both models are presented in Fig. 5.1.

As we are interested in the crystal field acting along the c axis perpendicular to the chain, we need to rotate the field (5.4) by the same angle $\theta = \pm\frac{2\pi}{3}$. Making an inverse transformation to (5.5) and expressing orbital projection operators on $|x\rangle$ and $|z\rangle$ orbital,

$$n_{ix\sigma} = |x_{i\sigma}\rangle\langle x_{i\sigma}|, \qquad n_{iz\sigma} = |z_{i\sigma}\rangle\langle z_{i\sigma}|, \tag{5.9}$$

in terms of new fermion operators $c^\dagger_{i\zeta(\xi)\sigma}$, which create an electron at $|\zeta\rangle$ ($|\xi\rangle$) orbital, respectively, the crystal field term (5.4) takes the form,

$$H_{cf} = \tfrac{1}{2}E_0\sum_{i\sigma}\big[\cos\theta(c^\dagger_{i\xi\sigma}c_{i\xi\sigma} - c^\dagger_{i\zeta\sigma}c_{i\zeta\sigma}) + \sin\theta(c^\dagger_{i\xi\sigma}c_{i\zeta\sigma} + c^\dagger_{i\zeta\sigma}c_{i\xi\sigma})\big]. \tag{5.10}$$

Note that $\cos\theta$ is negative so the field (5.10) favors the $|\xi\rangle$-occupancy over the $|\zeta\rangle$-occupancy, as it should.

Let us now define the total spin operator $\mathbf{S} = \sum_i \mathbf{S}_i$ with the spin components defined in the usual way,

$$\mathbf{S}_i = (\mathcal{S}^+_i, \mathcal{S}^-_i, \mathcal{S}^z_i) = \Big\{\sum_\alpha c^\dagger_{i\alpha\uparrow}c_{i\alpha\downarrow}, \sum_\alpha c^\dagger_{i\alpha\downarrow}c_{i\alpha\uparrow}, \tfrac{1}{2}\sum_\alpha(n_{i\alpha\uparrow} - n_{i\alpha\downarrow})\Big\}, \tag{5.11}$$

where the summations run over both orbitals $\alpha = \{\zeta, \xi\}$. The Hamiltonian (5.1) commutes both with the square and z-component of the total spin operator,

$$[\mathbf{S}^2, \mathcal{H}] = [\mathcal{S}^z, \mathcal{H}] = 0. \tag{5.12}$$

This implies that it is possible to find simultaneous eigenstates of these operators and the Hamiltonian $\mathcal{H}$. Therefore, they are good quantum numbers and label the eigenstates. Likewise, we introduce the total orbital pseudospin operator $\mathbf{T} = \sum_i \mathbf{T}_i$ where the three components of pseudospin are given by,

$$\mathbf{T}_i = (\mathcal{T}^+_i, \mathcal{T}^-_i, \mathcal{T}^\zeta_i) = \Big\{\sum_\sigma c^\dagger_{i\xi\sigma}c_{i\zeta\sigma}, \sum_\sigma c^\dagger_{i\zeta\sigma}c_{i\xi\sigma}, \tfrac{1}{2}\sum_\sigma(n_{i\xi\sigma} - n_{i\zeta\sigma})\Big\}. \tag{5.13}$$

In order to distinguish perpendicular to a chain c axis from the other axes along which one can consider the chain, we have labeled the third component of the pseudospin with the ζ index. Note however that in contrast to the spin operator, the ζ-component of the pseudospin operator $\mathcal{T}^\zeta_i$ does not commute with the Hamiltonian (5.1) which mix states with different values of this observable. Nevertheless, we will use its eigenvalues together with the z-component of $\mathbf{S}$ to specify multiparticle states in terms of which we write the Hamiltonian. To count available configurations, we apply elementary statistics which gives for a N_d-fold orbitally degenerate band system with N sites and N_e electrons,

$$L = \binom{2N\cdot N_d}{N_e}, \tag{5.14}$$

atomic configurations forming a basis. Hence in our two-site chain with two bands, the basis consists of $L = 28$ states altogether. Among them, there are,

$$L_\pm = 2\binom{N\cdot N_d}{N_e} = 12, \tag{5.15}$$

states in the subspace with $S^z = \pm 1$, whereas,

$$L_0 = \begin{pmatrix} N \cdot N_d \\ N_\sigma \end{pmatrix}^2 = 16, \tag{5.16}$$

states span the $S^z = 0$ subspace, with $N_\sigma = N_e/2$ being the number of electrons with a given spin σ. Notice that by accident, the number of states with $S^z = 0$ is precisely the same as the number of low energy singly occupied states,

$$L_S = (2 \cdot N_d)^N = 16. \tag{5.17}$$

It is straightforward to construct explicitly all the states, starting with the $S^z = 1$ subspace. There are two states with $T^\zeta = \pm 1$,

$$|\Psi_{\zeta\uparrow}\rangle = c^\dagger_{1\zeta\uparrow} c^\dagger_{2\zeta\uparrow}|0\rangle, \qquad |\Psi_{\xi\uparrow}\rangle = c^\dagger_{1\xi\uparrow} c^\dagger_{2\xi\uparrow}|0\rangle, \tag{5.18}$$

and four with $T^\zeta = 0$,

$$|\Psi^{\pm}_{1\uparrow}\rangle = \tfrac{1}{\sqrt{2}}\big(c^\dagger_{1\xi\uparrow} c^\dagger_{2\zeta\uparrow} \pm c^\dagger_{1\zeta\uparrow} c^\dagger_{2\xi\uparrow}\big)|0\rangle, \tag{5.19}$$

$$|\Psi^{\pm}_{2\uparrow}\rangle = \tfrac{1}{\sqrt{2}}\big(c^\dagger_{1\xi\uparrow} c^\dagger_{1\zeta\uparrow} \pm c^\dagger_{2\xi\uparrow} c^\dagger_{2\zeta\uparrow}\big)|0\rangle. \tag{5.20}$$

In the high spin subspace $S^z = \pm 1$, the Hamiltonian (5.1) with the field given by Eq. (5.10) is decomposed into a 4×4 matrix,

$$H_1 = \sum_\sigma \big(\langle\Psi_{\xi\sigma}|, \langle\Psi_{\zeta\sigma}|, \langle\Psi^+_{1\sigma}|, \langle\Psi^-_{2\sigma}|\big) \times \begin{pmatrix} E_c & 0 & \sqrt{2}E_s & 0 \\ 0 & -E_c & \sqrt{2}E_s & 0 \\ \sqrt{2}E_s & \sqrt{2}E_s & 0 & t_- \\ 0 & 0 & t_- & U_3 \end{pmatrix} \begin{pmatrix} |\Psi_{\xi\sigma}\rangle \\ |\Psi_{\zeta\sigma}\rangle \\ |\Psi^+_{1\sigma}\rangle \\ |\Psi^-_{2\sigma}\rangle \end{pmatrix}, \tag{5.21}$$

and a 2×2 matrix,

$$H_2 = \sum_\sigma \big(\langle\Psi^-_{1\sigma}|, \langle\Psi^+_{2\sigma}|\big) \begin{pmatrix} 0 & t_+ \\ t_+ & U_3 \end{pmatrix} \begin{pmatrix} |\Psi^-_{1\sigma}\rangle \\ |\Psi^+_{2\sigma}\rangle \end{pmatrix}. \tag{5.22}$$

Here we have introduced the effective hopping amplitudes $t_\pm = t_{\zeta\zeta} \pm t_{\xi\xi}$. Their explicit values depend on the pseudospin symmetry. For the e_g model with the immobile $|\xi\rangle$ pseudospin one obtains $t_+ = t_- = t$, whereas for the t_{2g} one with the equivalent bands one has $t_+ = 2t$ and $t_- = 0$. Further, $U_3 = U - 3J_H$ is the on-site interorbital Coulomb interaction of two parallel spins (triplet state). Finally, $E_c = E_0 \cos\theta$ and $E_s = \frac{E_0}{2}\sin\theta$ are the diagonal and off-diagonal matrix elements of the crystal field term. Twice larger amplitude of the former $\propto \pm\sum_{i\sigma} n_{i\alpha\sigma}$ is due to the fact that applied on the $|\Psi_{\alpha\sigma}\rangle$ state, consisting of both electrons with the α pseudospin flavor, yields a factor 2. Additionally, $\sqrt{2}$ in the Hamiltonian matrix (5.21) is owing to different normalization factors of the $|\Psi_{\alpha\sigma}\rangle$ and $|\Psi^+_{1\sigma}\rangle$ states.

In the absence of a finite crystal field, the $|\Psi_{\alpha\sigma}\rangle$ triplets with $T^\zeta = \pm 1$, become fully localized and degenerate with eigenenergy $E_T^{\pm} = 0$, being common for both models. The other four eigenenergies might be written in a compact expression,

$$E_{T_\pm}(t_\pm) = \tfrac{1}{2}\Big(U - 3J_H \pm \sqrt{(U-3J_H)^2 + 4t_\pm^2}\Big). \tag{5.23}$$

Now we are left with the $S^z = 0$ subspace consisting of eight states with $T^\zeta = \pm 1$,

$$|\Phi_1^\pm\rangle = \tfrac{1}{\sqrt{2}}\big(c_{1\zeta\uparrow}^\dagger c_{2\zeta\downarrow}^\dagger \pm c_{1\zeta\downarrow}^\dagger c_{2\zeta\uparrow}^\dagger\big)|0\rangle, \tag{5.24}$$
$$|\Phi_2^\pm\rangle = \tfrac{1}{\sqrt{2}}\big(c_{1\zeta\uparrow}^\dagger c_{1\zeta\downarrow}^\dagger \pm c_{2\zeta\uparrow}^\dagger c_{2\zeta\downarrow}^\dagger\big)|0\rangle, \tag{5.25}$$
$$|\Phi_3^\pm\rangle = \tfrac{1}{\sqrt{2}}\big(c_{1\xi\uparrow}^\dagger c_{1\xi\downarrow}^\dagger \pm c_{2\xi\uparrow}^\dagger c_{2\xi\downarrow}^\dagger\big)|0\rangle, \tag{5.26}$$
$$|\Phi_4^\pm\rangle = \tfrac{1}{\sqrt{2}}\big(c_{1\xi\uparrow}^\dagger c_{2\xi\downarrow}^\dagger \pm c_{1\xi\downarrow}^\dagger c_{2\xi\uparrow}^\dagger\big)|0\rangle, \tag{5.27}$$

and eight with $T^\zeta = 0$,

$$|\Phi_5^\pm\rangle = \tfrac{1}{\sqrt{2}}\big(c_{1\xi\uparrow}^\dagger c_{1\zeta\downarrow}^\dagger \pm c_{2\xi\uparrow}^\dagger c_{2\zeta\downarrow}^\dagger\big)|0\rangle, \tag{5.28}$$
$$|\Phi_6^\pm\rangle = \tfrac{1}{\sqrt{2}}\big(c_{1\xi\uparrow}^\dagger c_{2\zeta\downarrow}^\dagger \pm c_{1\zeta\downarrow}^\dagger c_{2\xi\uparrow}^\dagger\big)|0\rangle, \tag{5.29}$$
$$|\Phi_7^\pm\rangle = \tfrac{1}{\sqrt{2}}\big(c_{1\xi\downarrow}^\dagger c_{1\zeta\uparrow}^\dagger \pm c_{2\xi\downarrow}^\dagger c_{2\zeta\uparrow}^\dagger\big)|0\rangle, \tag{5.30}$$
$$|\Phi_8^\pm\rangle = \tfrac{1}{\sqrt{2}}\big(c_{1\xi\downarrow}^\dagger c_{2\zeta\uparrow}^\dagger \pm c_{1\zeta\uparrow}^\dagger c_{2\xi\downarrow}^\dagger\big)|0\rangle. \tag{5.31}$$

In terms of these states, the following Hamiltonian matrices are found:

$$\begin{aligned} H_3 = &\big(\langle\Phi_1^-|, \langle\Phi_2^+|, \langle\Phi_3^+|, \langle\Phi_4^-|, \langle\Phi_5^+|, \langle\Phi_6^-|, \langle\Phi_7^+|, \langle\Phi_8^-|\big) \\ &\times \begin{pmatrix} -E_c & 2t_{\zeta\zeta} & 0 & 0 & 0 & E_s & 0 & -E_s \\ 2t_{\zeta\zeta} & U-E_c & J_H & 0 & E_s & 0 & -E_s & 0 \\ 0 & J_H & U+E_c & 2t_{\xi\xi} & E_s & 0 & -E_s & 0 \\ 0 & 0 & 2t_{\xi\xi} & E_c & 0 & E_s & 0 & -E_s \\ 0 & E_s & E_s & 0 & U_2 & t_+ & -J_H & 0 \\ E_s & 0 & 0 & E_s & t_+ & 0 & 0 & 0 \\ 0 & -E_s & -E_s & 0 & -J_H & 0 & U_2 & t_+ \\ -E_s & 0 & 0 & -E_s & 0 & 0 & t_+ & 0 \end{pmatrix} \begin{pmatrix} |\Phi_1^-\rangle \\ |\Phi_2^+\rangle \\ |\Phi_3^+\rangle \\ |\Phi_4^-\rangle \\ |\Phi_5^+\rangle \\ |\Phi_6^-\rangle \\ |\Phi_7^+\rangle \\ |\Phi_8^-\rangle \end{pmatrix}, \end{aligned} \tag{5.32}$$

and,

$$\begin{aligned} H_4 = &\big(\langle\Phi_1^+|, \langle\Phi_2^-|, \langle\Phi_3^-|, \langle\Phi_4^+|, \langle\Phi_5^-|, \langle\Phi_6^+|, \langle\Phi_7^-|, \langle\Phi_8^+|\big) \\ &\times \begin{pmatrix} -E_c & 0 & 0 & 0 & 0 & E_s & 0 & E_s \\ 0 & U-E_c & J_H & 0 & E_s & 0 & -E_s & 0 \\ 0 & J_H & U+E_c & 0 & E_s & 0 & -E_s & 0 \\ 0 & 0 & 0 & E_c & 0 & E_s & 0 & E_s \\ 0 & E_s & E_s & 0 & U_2 & t_- & -J_H & 0 \\ E_s & 0 & 0 & E_s & t_- & 0 & 0 & 0 \\ 0 & -E_s & -E_s & 0 & -J_H & 0 & U_2 & t_- \\ E_s & 0 & 0 & E_s & 0 & 0 & t_- & 0 \end{pmatrix} \begin{pmatrix} |\Phi_1^+\rangle \\ |\Phi_2^-\rangle \\ |\Phi_3^-\rangle \\ |\Phi_4^+\rangle \\ |\Phi_5^-\rangle \\ |\Phi_6^+\rangle \\ |\Phi_7^-\rangle \\ |\Phi_8^+\rangle \end{pmatrix}, \end{aligned} \tag{5.33}$$

with $U_2 = U - 2J_H$, being the on-site interorbital Coulomb interaction of two antiparallel spins. In the present subspace both singlets and triplets are represented. However, by assuming $E_0 = 0$ which decouples the $T^\zeta = \pm 1$ states from the $T^\zeta = 0$ ones in matrices (5.32) and (5.33), we can readily identify them.

Let us consider first a model with two t_{2g} orbitals. Note that this problem is different from three t_{2g} orbitals and, consequently, the excitation energies will not be the same. In this case, both block diagonal sectors of the matrix (5.32) can be trivially diagonalized with six eigenvalues corresponding to singlets and with other two corresponding to triplet components. Explicitly, we obtain the two doubly degenerate singlets with energies,

$$E_{S_\pm}^{t_{2g}}(U - J_H) = \tfrac{1}{2}\Big(U - J_H \pm \sqrt{(U - J_H)^2 + 16t^2}\Big), \tag{5.34}$$

and the other two singlets with energies,

$$E_{S_\pm}^{t_{2g}}(U + J_H) = \tfrac{1}{2}\Big(U + J_H \pm \sqrt{(U + J_H)^2 + 16t^2}\Big), \tag{5.35}$$

whereas the two remaining states belong to the triplet subspace,

$$E_{T_\pm}^{t_{2g}}(t_+) = \tfrac{1}{2}\Big(U - 3J_H \pm \sqrt{(U - 3J_H)^2 + 16t^2}\Big). \tag{5.36}$$

The eigenvalues of the matrix (5.33) are (with the degeneracy given in parenthesis),

$$0\ (4), \qquad U - 3J_H, \qquad U - J_H\ (2), \qquad U + J_H. \tag{5.37}$$

Eliminating the ones which are not degenerate with the previously found $S^z = \pm 1$ levels, yields three other singlets. They are:

$$E_{S_-}^{t_{2g}} = U - J_H\ (2), \qquad E_{S_+}^{t_{2g}} = U + J_H. \tag{5.38}$$

Further, two of the eigenvalues zero correspond to the Hamiltonian eigenstates $|\Phi_1^+\rangle$ and $|\Phi_4^+\rangle$ and together with the $|\Psi_{\alpha\sigma}\rangle$ eigenstates, they form two $E_T^\pm$ triplets. Next, we notice other two eigenstates $|\Phi_6^+\rangle$ and $|\Phi_8^+\rangle$ of the matrix (5.33), with the interchanged $\uparrow$- and $\downarrow$-spins, both with eigenvalue zero. However, applying the spin lowering operator $\mathcal{S}^- = \sum_{i\alpha} c_{i\alpha\downarrow}^\dagger c_{i\alpha\uparrow}$ to the high-spin eigenstate $|\Psi_{1\sigma}^+\rangle$ with eigenenergy $E_{T_-}^{t_{2g}}(t_-) = 0$, gives a superposition of both states. Therefore, the $|\Phi_6^+\rangle$ and $|\Phi_8^+\rangle$ states should be combined into a new eigenstate,

$$|\Phi_{68}^+\rangle = \tfrac{1}{\sqrt{2}}\Big(|\Phi_6^+\rangle + |\Phi_8^+\rangle\Big), \tag{5.39}$$

which is ascribed to the $E_{T_-}^{t_{2g}}(t_-) = 0$ triplet, whereas its counterpart,

$$|\Phi_{68}^-\rangle = \tfrac{1}{\sqrt{2}}\Big(|\Phi_6^+\rangle - |\Phi_8^+\rangle\Big), \tag{5.40}$$

corresponds to another singlet state. Finally, we identify the last remaining state in Eq. (5.37) as a component of the $E_{T_+}^{t_{2g}}(t_-) = U - 3J_H$ triplet.

Turning now to the e_g orbital model and recollecting the immobile $|\xi\rangle$ orbital flavor, we notice in the matrix (5.32) one entirely decoupled $T^\zeta = 1$ singlet $|\Phi_4^-\rangle$ with the energy $E_S^{e_g} = 0$. The singlet $|\Phi_4^-\rangle$ is accidently degenerated with the eigenstates $|\Phi_1^+\rangle$ and $|\Phi_4^+\rangle$ of the matrix (5.33). They constitute together with the $|\Psi_{\alpha\sigma}\rangle$ eigenstates two $E_T^\pm$ triplets, already seen in the t_{2g} model. The second similarity between the models are two singlets from diagonalization of a 2×2 sector with the $|\Phi_2^-\rangle$ and $|\Phi_3^-\rangle$ states, having the energies $E_{S_\pm}^{e_g} = U \pm J_H$.

Next, recalling that for the e_g orbitals $t_\pm = t$, there are two identical 4×4 subspace spanned by the $T^\zeta = 0$ states of both matrices (5.32) and (5.33). They yield two doubly degenerated singlets,

$$E_{S_\pm}^{e_g}(U - J_H) = \tfrac{1}{2}\Big(U - J_H \pm \sqrt{(U - J_H)^2 + 4t^2}\Big), \tag{5.41}$$

whereas other eigenstates form, together with the $S_z = \pm 1$ states, two triplets,

$$E_{T_\pm}^{e_g} = \tfrac{1}{2}\Big(U - 3J_H \pm \sqrt{(U - 3J_H)^2 + 4t^2}\Big), \tag{5.42}$$

being again doubly degenerate. Finally, we are left with a submatrix in terms of the $|\Phi_1^-\rangle$, $|\Phi_2^+\rangle$, and $|\Phi_3^+\rangle$ states. Determining of its eigenvalues involves solving a cubic equation and does not lead to a simple expression. However, in order to find out an approximate lowest energy state, one can leave out highly energetic pair-hopping processes, which require an empty and a double-occupied orbital to take place. Such configurations should be strongly suppressed by the intraorbital Coulomb repulsion U. It completely decouples the $|\Phi_3^+\rangle$ state and working with the 2×2 matrix gives the following eigenvalues,

$$E_{S_\pm}^{e_g}(U) = \tfrac{1}{2}\Big(U \pm \sqrt{U^2 + 16t^2}\Big). \tag{5.43}$$

To get an insight into a competition between tendency towards the AF and FM ground state, let us discuss the lowest energy eigenstates in the strong coupling limit. As it was expected, in both systems the lowest energy spin triplet is supported by a pseudospin singlet. However, recalling twice larger effective hopping amplitude t_+ of the t_{2g} system, its lowest-lying triplet levels should have significantly lower energy than those of the corresponding triplet of the e_g model. Indeed, in the case of strong on-site interorbital repulsion $(U - 3J_H \gg t)$, the square root in Eq. (5.23) can be expanded to second order yielding the excitation energy $-t_+^2/(U - 3J_H)$. Thus, the lowest high-spin excitation energy in the e_g subspace $E_{T_0}^{e_g}$ and the corresponding one in the t_{2g} subspace $E_{T_0}^{t_{2g}}$ are,

$$E_{T_0}^{e_g} = -\frac{t^2}{U - 3J_H}, \qquad E_{T_0}^{t_{2g}} = -\frac{4t^2}{U - 3J_H}. \tag{5.44}$$

$J_H = 0$			$J_H = U/8$			$J_H = U/4$		
E_n/t	S_n	T_n^ζ	E_n/t	S_n	T_n^ζ	E_n/t	S_n	T_n^ζ
-0.4721	1	0	-0.7016	1	0	-1.2361	1	0
	0	±1	-0.5311	0	0	-0.6056	0	0
	0	0		0	0		0	0
0.0000	1	±1	-0.4244	0	0	-0.3852	0	0
	1	0	0.0000	1	±1	0.0000	1	±1
	0	0		1	0		1	0
8.0000	1	0		0	0		0	0
	0	±1	5.0000	1	0	2.0000	1	0
	0	0	5.7016	1	0	3.2361	1	0
8.4721	1	0	7.0000	0	0	6.0000	0	0
	0	±1		0	0		0	0
	0	0	7.5311	0	0	6.6056	0	0
				0	0		0	0
			9.0000	0	0	10.0000	0	0
			9.4244	0	0	10.3852	0	0

Table 5.1: Eigenenergies of the model (5.1) with the t_{2g} orbitals in the strong coupling regime $U = 8t$. The eigenstates are specified by the total spin S_n and the expectation values of the ζ-component of the total pseudospin $\mathcal{T}^\zeta$. Triplet states with $S_n = 1$ contain three components $S_n^z = \pm1, 0$.

Note however that finite J_H could reduce significantly the value of the interorbital repulsion $U - 3J_H$, so that it would no longer be much larger than t. As a consequence, corrections to the above result of the second order expansion are expected in this case.

Analogously, in order to find out the lowermost low-spin excitations for both models one can expand the square root in Eqs. (5.34) and (5.43). They are,

$$E_{S_0}^{e_g} = -\frac{4t^2}{U}, \qquad E_{S_0}^{t_{2g}} = -\frac{4t^2}{U - J_H}. \tag{5.45}$$

Comparison of (5.45) with the lowest high-spin excitations (5.44) allows to draw interesting conclusions about conditions for ferromagnetism. It is apparent that $E_{S_0}^{t_{2g}}$ and $E_{T_0}^{t_{2g}}$ are degenerate for $J_H = 0$. However, even infinitesimally small $J_H > 0$ lifts this degeneracy and might give rise to spin ferromagnetism combined with the AF pseudospin correlations. On the contrary, we expect the singlet state with energy $E_{S_0}^{e_g}$ to be the ground state of the e_g shell model until $J_H < U/4$. Therefore, Hund's rule coupling J_H is a driving force of the FM solution in both models but it is decisively more efficient when both orbital pseudospins are mobile.

The eigenenergy spectra obtained from the ED of the Hamiltonian (5.1) with the t_{2g} (e_g) orbitals in the strong coupling regime $U = 8t$ for a few values of J_H

$J_H = 0$			$J_H = U/8$			$J_H = U/4$		
E_n/t	S_n	T_n^ζ	E_n/t	S_n	T_n^ζ	E_n/t	S_n	T_n^ζ
-0.4721	0	-1	-0.4784	0	-0.9985	-0.4983	0	-0.9935
-0.1231	1	0	-0.1926	1	0.0000	-0.4142	1	0.0000
	1	0		1	0.0000		1	0.0000
	0	0	-0.1401	0	0.0000	-0.1623	0	0.0000
	0	0		0	0.0000		0	0.0000
0.0000	1	±1	0.0000	1	±1.0000	0.0000	1	±1.0000
	0	1		0	1.0000		0	1.0000
8.0000	0	±1	5.1926	1	0.0000	2.4142	1	0.0000
	0	1		1	0.0000		1	0.0000
8.1231	1	0	7.0000	0	0.0000	6.0000	0	0.0000
	1	0	7.1401	0	0.0000	6.1623	0	0.0000
	0	0		0	0.0000		0	0.0000
	0	0	7.2388	0	0.2318	6.2927	0	0.1097
8.4721	0	-1	9.0000	0	0.0000	10.0000	0	0.0000
			9.2396	0	-0.2333	10.2056	0	-0.1162

Table 5.2: The same as in Table 5.1 but with the e_g orbitals.

are gathered in Table 5.1 (5.2), respectively. We have specified them in terms of the total spin S_n. Two electrons can built a state with the total spin either $S_n = 0$ or $S_n = 1$. In the latter case, the z-component takes values $S_n^z = \pm1, 0$. Another value used for the classification of states is the ζ-component of the total pseudospin operator. However, it is not a good quantum number being modified by the pair-hopping processes from one orbital to the other. Indeed, in matrix (5.32), a sector consisting of $|\Phi_1^-\rangle$ and $|\Phi_2^+\rangle$ states, carrying the $T^\zeta = -1$ pseudospin flavor, is coupled to the one in terms of $|\Phi_3^+\rangle$ and $|\Phi_4^-\rangle$ states, carrying the opposite $T^\zeta = 1$ flavor. Similarly, sectors with different pseudospin flavors are mixed in matrix (5.33). Thus, one has to determine the expectation values of $\mathcal{T}^\zeta$ by a direct calculation in the Hamiltonian eigenstates.

Looking at these values one sees that in contrast to the e_g case, all the components of a given t_{2g} pseudospin triplet remain degenerate, even for finite J_H. We also note full or at least partial quenching of the pseudospin. More precisely, there are six eigenstates with the fully suppressed orbital flavor in the case of the t_{2g} model, whereas only two eigenstates of the e_g model become pseudospinless upon finite J_H. Recalling the two singlets with energy $E_{S_\pm} = U \pm J_H$, common for both models, we readily identify these two pseudospinless eigenstates as a symmetric and antysymmetric linear combination of $|\Phi_2^-\rangle$ and $|\Phi_3^-\rangle$ states carrying the opposite pseudospin flavors. Analogously, the other two with $T^\zeta = -1$ and two with with $T^\zeta = 1$ pseudospin triplet components, turning (due to finite J_H) into doubly degenerate pseudospin singlets with energies $E_{S_\pm}^{t_{2g}}(U - J_H)$, are ascribed to the two identical, T^{ζ}, sectors in terms of $\{|\Phi_1^-\rangle, |\Phi_2^+\rangle\}$ and $\{|\Phi_3^+\rangle, |\Phi_4^-\rangle\}$ being coupled by J_H. These two sectors are characterized by the opposite values of T^{ζ}.

In contrast, $|\Phi_4^-\rangle$ is the eigenstate $E_S^{e_g} = 0$ of the e_g model so its pseudospin $T_{\zeta} = 1$ is conserved regardless of J_H. Therefore, due to inequivalent number of states with the opposite value of T^{ζ} forming the submatrix $\{|\Phi_1^-\rangle, |\Phi_2^+\rangle, |\Phi_3^+\rangle\}$, its eigenstates have partially quenched pseudospin. Of course, regardless of the pseudospin symmetry, pseudospin quenching obeys a constraint,

$$\sum_n T_n^{\zeta} = 0, \tag{5.46}$$

where the sum runs over the eigenstates.

Remarkably, even for unrealistically large $J_H = U/4$, the e_g ground state is a singlet with the occupied mobile pseudospin $|\zeta\rangle$ orbitals (*cf.* Table 5.2) contradicting our predictions from the strong coupling regime. It is apparently because the approximate low-spin state energy $E_{S_0}^{e_g} = -4t^2/U$ overestimates the tendency towards ferromagnetism (high-spin state) as we have left out the pair-hopping processes. We shall see later on that the pair-hopping of the e_g electrons remain important even for large $U/t = 20$. Nevertheless, it is evident that increasing J_H diminishes the difference between the lowest singlet and the two excited triplets.

On the contrary, the ground state of the t_{2g} model with finite J_H is a spin triplet accompanied by a pseudospin singlet (*cf.* Table 5.1). Notice however that its energy $E_{T_-}^{t_{2g}}(t_+) = -1.2361t$ obtained for $J_H = U/4$ differs vastly from the lowermost roughly estimated high-spin excitation $E_{T_0}^{t_{2g}} = -2t$ (5.44). The reason of this discrepancy is certainly the fact that the second order perturbation theory is controlled by $t^2/(U - 3J_H)$ being of order $\mathcal{O}(t)$ here. Therefore, it can be used only for qualitative arguments in this regime, while it works much better for smaller $J_H = U/8$, yielding $E_{T_0}^{t_{2g}} = -0.8t$, much closer to the ED energy $E_{T_-}^{t_{2g}}(t_+) = -0.7016t$.

Now we shall discuss the influence of the crystal field (5.10). Except for the Hamiltonian matrix (5.22) yielding the eigenvalues $E_{T_{\pm}}(t_+)$ (5.23), the form of the other matrices for this calculation is considerably more complicated due to additional coupling of states with different T^{ζ}. In general, it is not possible to obtain analytic expressions for eigenvalues and one has to resort to a numerical diagonalization. However, due to the equivalent hopping amplitudes, the eigenvalues of the t_{2g} model should be independent of the rotation angle θ, i.e., one has to get the same energy spectrum for a field (5.10) with finite θ, as well as for a diagonal in pseudospin field of the form $E_0\mathcal{T}^{\zeta}$. It acts along the chain and corresponds to $\theta = 0$ in Eq. (5.10). Applying the latter immediately leads to a diagonal form of the matrix (5.21) with the eigenvalues: 0, $\pm E_0$ and $U - 3J_H$. Obviously, $U - 3J_H$ is also eigenvalue of the matrix with finite θ, whereas the others can be found by analytical diagonalization. They are,

$$\lambda_0 = 0, \qquad \lambda_{\pm} = \pm\sqrt{E_c^2 + 4E_s^2}. \tag{5.47}$$

Accordingly, substituting $E_c = E_0 \cos\theta$ and $E_s = \frac{E_0}{2}\sin\theta$ one recovers the previously found eigenvalues $\pm E_0$. We immediately recognize the corresponding eigenstates. They constitute two degenerate spin triplets at energy $E_0 = 0$ with the opposite pseudospin flavors $T^\zeta = \pm 1$ (*cf.* Table 5.1).

Numerical values of the calculation with $E_0 = 2t$ and $\theta = \pm\frac{2\pi}{3}$ are listed in Table 5.3. Although the energy spectrum of the t_{2g} model indeed does not depend on the field direction, expectation values of $\mathcal{T}^\zeta$ in the Hamiltonian eigenstates certainly do, as a finite rotation angle θ enables mixing of states with different values of $\mathcal{T}^\zeta$. As a consequence, the initial pseudospin $T^\zeta = \pm 1$ of spin triplets with the energy $\pm E_0$ is reduced up to $T^\zeta = \pm 0.5$ by the field with $\theta = \pm\frac{2\pi}{3}$, whereas it is conserved when $\theta = 0$.

Contrary to the $E_0 = 0$ case with a spin triplet and pseudospin singlet as the t_{2g} ground state, provided $J_H > 0$, finite positive E_0 suppresses the AF pseudospin correlations and stabilizes a spin singlet with the positive value of $T^\zeta \simeq 0.5$. On the other hand, the effect of the crystal field on the e_g ground state is just the opposite. Namely, by lifting the degeneracy of pseudospin flavors it promotes the immobile $|\xi\rangle$ one. Consequently, there is not that much kinetic energy to be gained and the Coulomb interactions start to be crucial. However, they are noticeably better optimized by a FM phase. Indeed, from Table 5.3 one sees a strong competition between the lowest singlet and triplet, both with positive but still smaller than in the t_{2g} case value of $T^\zeta \simeq 0.45$. However, it becomes energetically advantageous to have the triplet as a ground state for large $J_H = U/4$. In spite of the complicated form of pseudospin mixing by the crystal field, we have noticed that the pseudospin quenching satisfies again the condition (5.46) in both systems.

Having numerically determined all the eigenstates $|\phi_n\rangle$ and the corresponding eigenvalues E_n of the Hamiltonian (5.1), we can evaluate the partition function,

$$Z = \sum_n \exp(-\beta E_n), \tag{5.48}$$

from which thermodynamic properties of both systems can be inferred in the entire parameter range. Thermodynamics of a twofold degenerate Hubbard model with equivalent bands was studied in Ref. 182. For example, the internal energy U is given by the expectation value of the energy $\langle E\rangle$,

$$U = \langle E\rangle = \frac{1}{Z}\sum_n \langle\phi_n|\mathcal{H}|\phi_n\rangle \exp(-\beta E_n) = \frac{1}{Z}\sum_n E_n \exp(-\beta E_n), \tag{5.49}$$

This can also be written in terms of a derivative of the partition function,

$$U = -\frac{1}{Z}\frac{\partial Z}{\partial\beta} = -\frac{\partial \ln Z}{\partial\beta}. \tag{5.50}$$

Further, the specific heat is defined as a derivative of the internal energy,

$$C = \frac{\partial U}{\partial T} = -k_B\beta^2\frac{\partial U}{\partial\beta} = k_B\beta^2\frac{\partial^2 \ln Z}{\partial\beta^2}. \tag{5.51}$$

e_g orbitals						t_{2g} orbitals					
$J_H = U/8$			$J_H = U/4$			$J_H = U/8$			$J_H = U/4$		
E_n/t	S_n	T_n^ζ	E_n/t	S_n	T_n^ζ	E_n/t	S_n	T_n^ζ	E_n/t	S_n	T_n^ζ
−2.0786	0	0.4229	−2.0965	1	0.4429	−2.4767	0	0.4995	−2.4910	0	0.4980
−2.0548	1	0.4695	−2.0852	0	0.4179	−2.0000	1	0.5000	−2.0000	1	0.5000
−0.2286	0	−0.0348	−0.4142	1	0.0000	−0.7016	1	0.0000	−1.2361	1	0.0000
−0.1926	1	0.0000	−0.2410	0	−0.0305	−0.5311	0	0.0000	−0.6056	0	0.0000
−0.1468	0	0.0002	−0.1703	0	0.0003	0.0000	1	0.0000	0.0000	1	0.0000
−0.0494	1	0.0734	−0.1169	1	0.1658		0	0.0000		0	0.0000
1.6727	0	−0.3841	1.5089	1	−0.4969	1.5183	0	−0.4977	1.4876	0	−0.4899
1.8878	1	−0.5409	1.6340	0	−0.3713	2.0000	1	−0.5000	2.0000	1	−0.5000
5.1926	1	0.0000	2.4142	1	0.0000	5.0000	1	0.0000		1	0.0000
5.2165	1	−0.0020	2.7045	1	−0.1118	5.7016	1	0.0000	3.2361	1	0.0000
5.8526	0	0.4929	5.2848	0	0.4140	5.7639	0	0.4472	5.1716	0	0.3536
5.8564	0	0.4885	5.3156	0	0.3627	6.2695	0	0.4498	5.7610	0	0.3539
7.0374	0	−0.0538	6.0468	0	−0.0631	7.0000	0	0.0000	6.0000	0	0.0000
7.2305	0	0.0461	6.2702	0	0.0517	7.5311	0	0.0000	6.6056	0	0.0000
10.2567	0	−0.4394	10.8387	0	−0.3512	10.2361	0	−0.4472	10.8284	0	−0.3536
10.5476	0	−0.5385	11.1064	0	−0.4305	10.6890	0	−0.4516	11.2424	0	−0.3620

Table 5.3: Eigenenergies of the model (5.1) with either the e_g or t_{2g} orbitals in the strong coupling regime $U = 8t$ with the finite crystal field $E_0 = 2t$ acting perpendicular to the chain.

Finally, the second derivative of $\ln Z$ with respect to β gives,

$$\frac{\partial^2 \ln Z}{\partial \beta^2} = \frac{1}{Z}\frac{\partial^2 Z}{\partial \beta^2} - \left(\frac{1}{Z}\frac{\partial Z}{\partial \beta}\right)^2 = \langle E^2 \rangle - \langle E \rangle^2. \tag{5.52}$$

which is the mean square deviation $\langle \delta E \rangle^2$ of individual, instantaneous measurement of the internal energy E away from the mean value $\langle E \rangle$,

$$\langle \delta E \rangle^2 = \langle (E - \langle E \rangle)^2 \rangle. \tag{5.53}$$

Using Eq. (5.52) to eliminate the second derivative in the specific heat (5.51), we can relate the size of spontaneous fluctuations $\langle \delta E \rangle^2$ to the rate at which energy will change due to temperature alterations,

$$C = \frac{\langle E^2 \rangle - \langle E \rangle^2}{k_B T^2}. \tag{5.54}$$

Note that the fluctuations of thermodynamic variables determine in general the system properties and similar equations to Eq. (5.54) may be derived. Indeed, each parameter of a system that we fix has a conjugate variable which represents the response of the system to the perturbation of this parameter. For example, the effect of an external magnetic field h^z on a magnet can be accounted for by a magnetic energy term in a Hamiltonian of the form $-\gamma h^z \mathcal{S}^z$, where $\mathcal{S}^z$ is the z-component of the total spin $\mathbf{S}$, and γ is the gyromagnetic factor. Since $E_n = E_n(h^z)$ now, we can write the expectation value $\langle S^z \rangle = \frac{1}{Z}\sum_n S^z_n \exp(-\beta E_n)$ in terms of a derivative of the partition function,

$$\langle S^z \rangle = \frac{1}{\gamma \beta Z}\frac{\partial Z}{\partial h^z} = \frac{1}{\gamma \beta}\frac{\partial \ln Z}{\partial h^z}. \tag{5.55}$$

Here, S^z_n is the value of $\mathcal{S}^z$ in the state $|\phi_n\rangle$. Another derivative of $\ln Z$ with respect to h^z produces again a factor of S^z_n in the sum over states and one finds, in a direct parallel with Eq. (5.52),

$$\frac{\partial^2 \ln Z}{\partial (h^z)^2} = \frac{1}{Z}\frac{\partial^2 Z}{\partial (h^z)^2} - \left(\frac{1}{Z}\frac{\partial Z}{\partial h^z}\right)^2 = \beta^2\gamma^2\Big(\langle (S^z)^2 \rangle - \langle S^z \rangle^2\Big), \tag{5.56}$$

which one recognizes as the mean square fluctuations of $\mathcal{S}^z$. Moreover, the spin susceptibility χ_s, which measures the strength of the response of $\mathcal{S}^z$ to changes in h^z, is proportional to $\frac{\partial \langle S^z \rangle}{\partial h^z}$. It follows that,

$$\chi_s = \gamma^2 \frac{\langle (S^z)^2 \rangle - \langle S^z \rangle^2}{k_B T}, \tag{5.57}$$

i.e., the spin susceptibility depends on fluctuations of $\mathcal{S}^z$.

This is a useful identity in statistical mechanics for calculating thermal fluctuations of a physical quantity, even if no appropriate field coupling to that quantity appears in the Hamiltonian [191]. We simply make up a fictitious field which couples to our quantity which allows us to calculate fluctuations of the quantity we are interested in, and finally we set the field to zero making the fictitious field vanish from the Hamiltonian again. Let us suppose now that a finite crystal field acts along the chain. The conjugated variable to this field is the ζ-component of the total pseudospin operator $\mathcal{T}^\zeta$, and the two are linked via a term in the Hamiltonian $E_0\mathcal{T}^\zeta$. Thus, the corresponding pseudospin (orbital) susceptibility χ_t is equal to,

$$\chi_t = \frac{\langle (\mathcal{T}^\zeta)^2\rangle - \langle \mathcal{T}^\zeta\rangle^2}{k_B T}. \tag{5.58}$$

Knowing the partition function (5.48), we can also write an expression for the free energy of the system,

$$F = -k_B T \ln Z. \tag{5.59}$$

Finally, having found F one may calculate the entropy S, which measures the amount of disorder in the system,

$$S = -\left(\frac{\partial F}{\partial T}\right)_{V,N} \tag{5.60}$$

We have thus shown that the knowledge of Z allows to evaluate all the important thermodynamic quantities. Let us now discuss their temperature dependence.

Magnetic nature of the ground state is best described by considering the on-site $\langle \mathbf{S}_i^2\rangle$ and intersite $\langle \mathbf{S}_1\cdot\mathbf{S}_2\rangle$ spin-spin correlation functions. Analogously, we shall determine the on-site $\langle \mathbf{T}_i^2\rangle$ and intersite $\langle \mathbf{T}_1\cdot\mathbf{T}_2\rangle$ pseudospin correlation functions yielding information about an orbital state together with orbital correlations between neighboring sites. In Fig. 5.2 we present temperature dependence of the spin (solid line) and pseudospin (dashed line) correlation functions, both susceptibilities and the specific heat of the model with either e_g (left panels) or t_{2g} orbitals (right panels). We have set Hund's exchange coupling to be $J_H/U = 1/8$ (gray line) and $J_H/U = 1/4$ (black line).

Consider first the e_g system. At low temperature, one expects to have the charge localization due to the strong coupling regime $U = 8t$. Indeed, the local spin moment $\langle \mathbf{S}_i^2\rangle$ reaches virtually the magnitude $S(S+1) = 3/4$ of the spin $S = 1/2$, regardless of $J_H > 0$. A rise of $\langle \mathbf{S}_i^2\rangle$ upon increasing temperature is possible due to excitations to triplet states. They are stabilized by Hund's interaction and form local high-spin configurations. Consequently, the rise of $\langle \mathbf{S}_i^2\rangle$ is larger for stronger $J_H = U/4$. Next, the intersite spin-spin correlation function $\langle \mathbf{S}_1\cdot\mathbf{S}_2\rangle$ indicates the AF nature of the ground state, whereas the corresponding pseudospin function $\langle \mathbf{T}_1\cdot\mathbf{T}_2\rangle$ illustrates the FM pseudospin correlations. The opposite behavior of $\langle \mathbf{S}_1\cdot\mathbf{S}_2\rangle$ and $\langle \mathbf{T}_1\cdot\mathbf{T}_2\rangle$ is also well seen in both susceptibilities. Upon taking the logarithm of χ_t we find that it is of the Curie-Weiss type with linear segments in the low and high temperature regions. The displacement of these two segments does not appear when $J_H = 0$. Accordingly, it is presumably related to partial

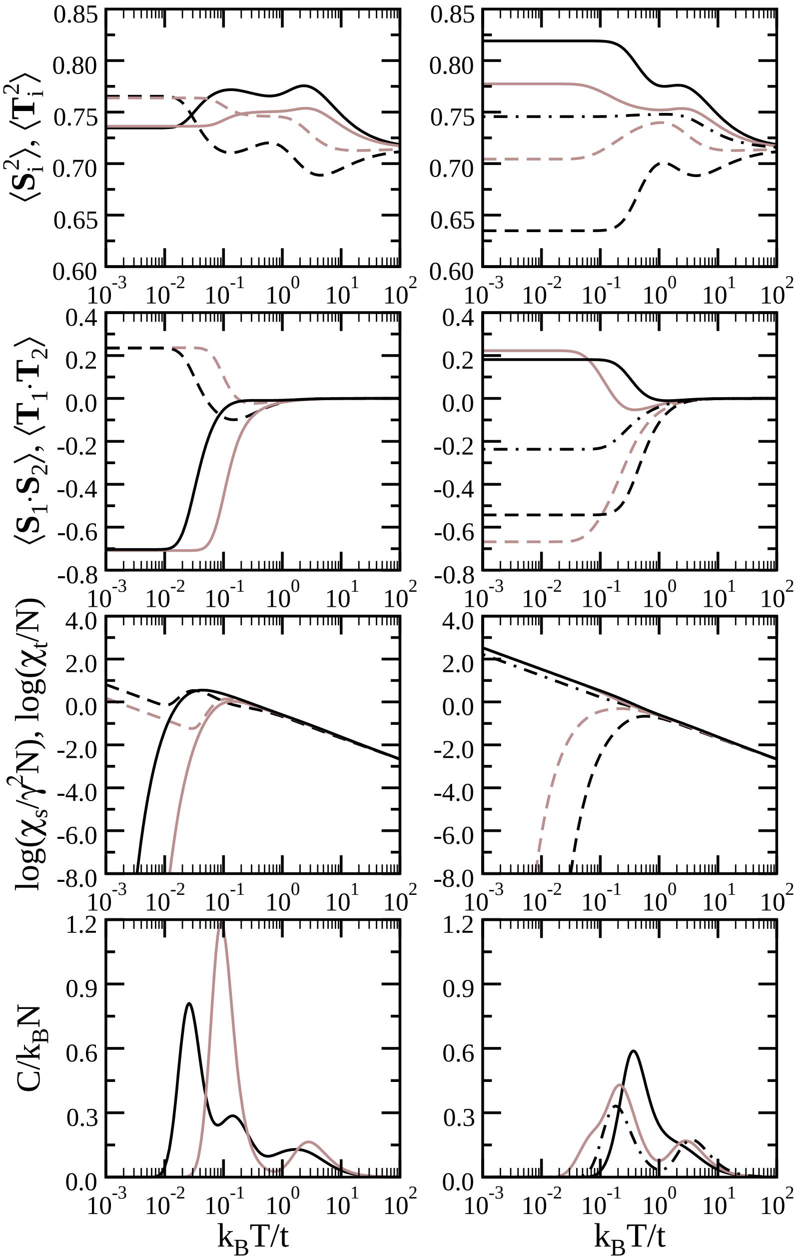

Figure 5.2: Temperature dependence of: local spin $\langle \mathbf{S}_i^2 \rangle$ and pseudospin $\langle \mathbf{T}_i^2 \rangle$ moments (top); spin $\langle \mathbf{S}_1 \cdot \mathbf{S}_2 \rangle$ and pseudospin $\langle \mathbf{T}_1 \cdot \mathbf{T}_2 \rangle$ correlation functions (second row); spin $\log(\frac{\chi_s}{\gamma^2 N})$ and pseudospin $\log(\frac{\chi_t}{N})$ susceptibilities (third row), and the specific heat $\frac{C}{k_B N}$ (bottom) of the model with either the e_g (left panels) or t_{2g} orbitals (right panels). Parameters: $U = 8t$, $J_H = U/8$ (gray line), $J_H = U/4$ (black line) and $E_0 = 0$. Solid (dashed) line (rows 1-3) refers to spin (pseudospin), respectively, and the dot-dashed line (right panels) shows the results for $J_H = 0$.

quenching of T^ζ due to pair-hopping processes. In contrast, χ_s shows a typical AF behavior with a characteristic cusp at the critical temperature $T_c(e_g)$. Obviously, the AF array that sets in has zero net magnetic moment at the temperature below $T_c(e_g)$ and that is the reason of the observed cusp in χ_s. Moreover, the particular kink in the curve χ_s versus T coincides with the low temperature peak of the specific heat. Comparing position of the peaks corresponding to $J_H = U/8$ and $J_H = U/4$, one finds that increasing J_H reduces $T_c(e_g)$. Note, however, that for $J_H = U/4$ the low temperature peak in the specific heat splits into two. The first one corresponds to a transition from the ground state to the first two excited triplet states with the excitation energy $\Delta E_1/t = 0.0841$, whereas the second one appears due to excitations into higher levels with the excitation energy $\Delta E_2/t = 0.336$ and $\Delta E_3/t = 0.498$. In contrast, when $J_H = U/8$, the excitation energy into the first excited state is much larger $\Delta E_1'/t = 0.286$, whereas the other excitation energies are nearly unaltered: $\Delta E_2'/t = 0.338$ and $\Delta E_3'/t = 0.478$. This results in a single broad low temperature peak. Finally, high temperature peaks occur due to the thermal excitations which create double occupancies and lead to charge delocalization, well seen in the suppression of $\langle \mathbf{S}_i^2 \rangle$.

On the contrary, in the t_{2g} model, except for $J_H = 0$ when the intersite spin and pseudospin correlation functions overlap and are negative, positive $\langle \mathbf{S}_1 \cdot \mathbf{S}_2 \rangle$ demonstrates the FM nature of the ground state supported by the pseudospin singlet with negative $\langle \mathbf{T}_1 \cdot \mathbf{T}_2 \rangle$. Thereby, χ_s is of the Curie-Weiss type, whereas χ_t displays the AF kink at the critical temperature $T_c(t_{2g})$. Unlike the e_g case, increasing J_H shifts $T_c(t_{2g})$ towards higher temperatures. As a result, the critical temperatures of both systems differ substantially, especially in the large $J_H = U/4$ regime. Indeed, from the position of the low temperature peak of the specific heat in Fig. 5.2, one can read off that $k_B T_c(e_g) = 0.025t$, whereas $k_B T_c(t_{2g}) = 0.35t$. Origin of this marked difference is certainly the fact that increasing J_H diminishes (enlarges) the gap between the spin singlet (triplet) ground state and the first excited triplet (singlet) of the e_g (t_{2g}) system, respectively (*cf.* Tables 5.1 and 5.2).

Different energy spectra of the e_g and t_{2g} systems result in quite different temperature evolution of the entropy S, as shown in Fig. 5.3. In the former case, with a spin singlet as the ground state, vanishingly small S corresponds to a state of perfect order in the system in the low T limit. Basically, the overall evolution of the curves in Fig. 5.3(a) is very much the same, i.e., the entropy rises rapidly around $T_c(e_g)$ corresponding to the low temperature peak in the specific heat and approaches the limiting value $S = k_B \ln 28$, meaning that the energy of the system tends to a constant value as all the microscopic states are equally probable. However, a detailed behavior of S is J_H dependent. In a small Hund's exchange $J_H \leq U/8$ regime, where $L_S = 16$ singly occupied states are clearly separated from doubly occupied states, S possesses a point of inflection $S = k_B \ln 16$ at $k_B T \simeq t$, which follows from a vanishing character of the specific heat. In contrast, in the large $J_H = U/4$ regime favoring spin triplets, the gap between singly and

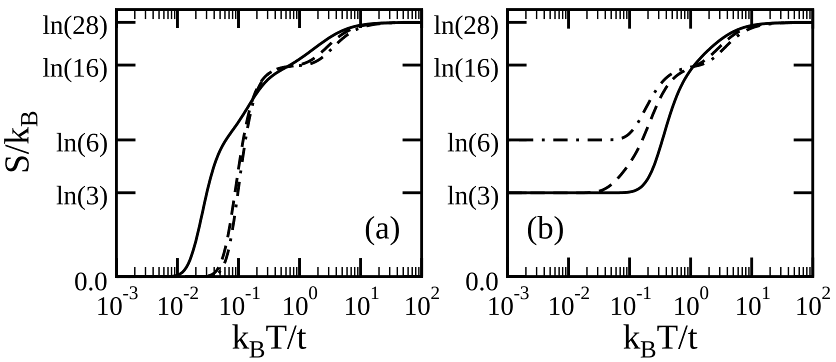

Figure 5.3: Temperature dependency of the entropy S: (a) e_g orbitals; (b) t_{2g} orbitals. Solid, dashed, and dot-dashed line corresponds to $J_H = U/4$, $J_H = U/8$, $J_H = 0$, respectively.

doubly occupied states is smaller and the corresponding point of inflection is less transparent.

In fact, the limiting value $S = k_B \ln 28$ results from the calculation performed in the canonical ensemble with a fixed number of electrons. However, in the grand canonical ensemble at high temperature, entropy would be further modified by three- and four-electron states. Indeed, entropy shall approach the limiting value $S' = 2k_B \ln 16$, as the total number of possible configurations in a doubly degenerate model with two sites, which includes such high energy states is given by,

$$L' = 4^{N_d \cdot N} = 16^2. \tag{5.61}$$

Turning to Fig. 5.3(b), which depicts the evolution of S in the t_{2g} system, one can notice that in the low temperature limit the entropy approaches either the value $k_B \ln 3$ for both $J_H = U/8$ and $J_H = U/4$ or $k_B \ln 6$ when $J_H = 0$. The explanation is contained in Table 5.1. For $J_H = 0$, the ground state corresponds to six degenerate states — three of them constitute a spin triplet, whereas the others are singlets. However, any finite $J_H > 0$ splits up these states and leads to the triplet ground state with the entropy $S = k_B \ln 3$. As in the e_g case, S has a clear point of inflection only in the small $J_H \leq U/8$ regime.

The situation is quite different in the case of a finite crystal field $E_0 = 2t$, shown in Fig. 5.4. The low temperature ground state of the e_g system depends on the value of J_H, being AF (negative $\langle \mathbf{S}_1 \cdot \mathbf{S}_2 \rangle$) for $J_H = U/8$ and FM (positive $\langle \mathbf{S}_1 \cdot \mathbf{S}_2 \rangle$) for $J_H = U/4$, whereas $\langle \mathbf{T}_1 \cdot \mathbf{T}_2 \rangle$ is positive and almost insensitive to J_H. This is reflected by the Curie-Weiss type of χ_s obtained for $J_H = U/4$ and both χ_t in contrast to the AF behavior of χ_s corresponding to $J_H = U/8$. The position of the high temperature peak of the specific heat at the temperature $k_B T \simeq t$ is almost the same as the position of the strong anomalies of both on-site correlation functions. The rise (fall) of $\langle \mathbf{S}_i^2 \rangle$ ($\langle \mathbf{T}_i^2 \rangle$), respectively, upon increasing temperature

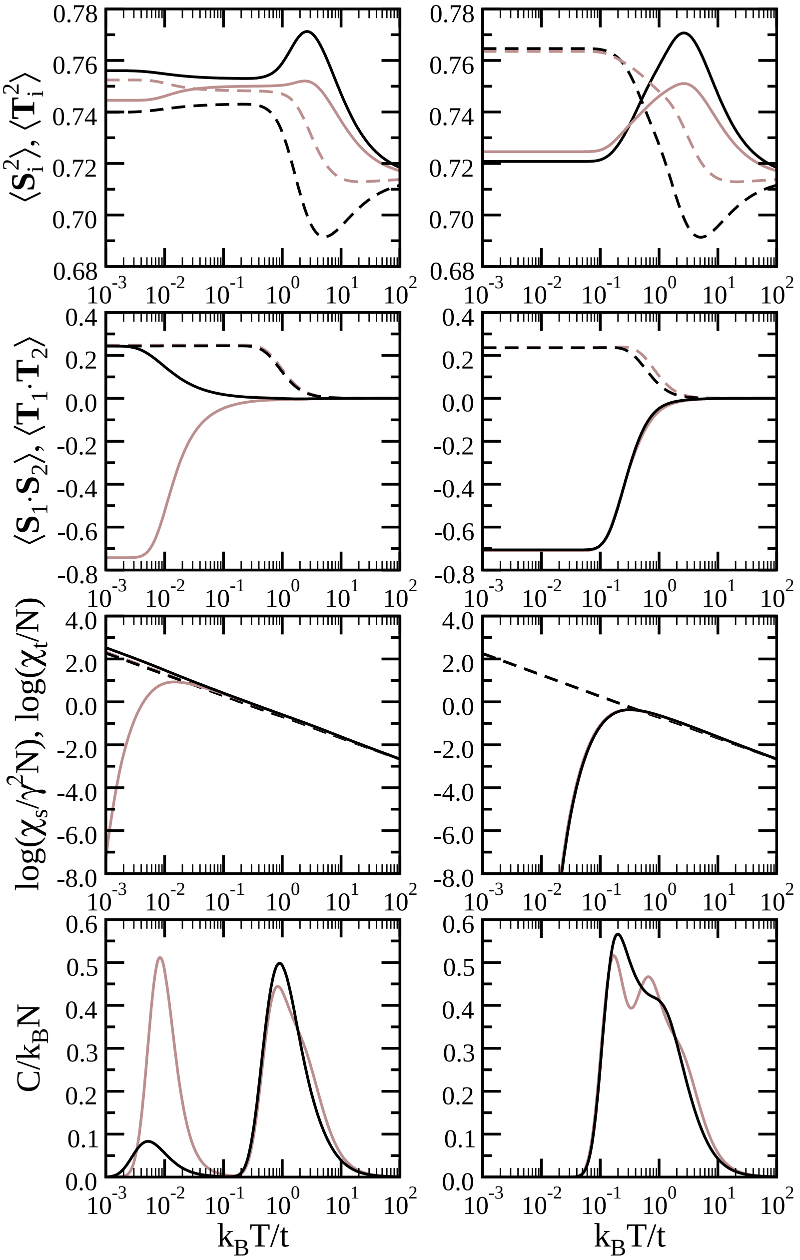

Figure 5.4: The same as in Fig. 5.2 but with the finite crystal field $E_0 = 2t$.

is mainly associated to the transitions from the low energy states to the excited triplet with the opposite to the ground state pseudospin $T^\zeta \simeq -0.5$ (*cf.* Table 5.3).

A finite crystal field affects drastically the behavior of the t_{2g} correlation functions as well. At low temperature negative $\langle \mathbf{S}_1 \cdot \mathbf{S}_2 \rangle$ reveals the AF coupling between spins, whereas positive $\langle \mathbf{T}_1 \cdot \mathbf{T}_2 \rangle$ indicates the FM pseudospin correlations, regardless of J_H. Again this is reflected by the Curie-Weiss behavior of χ_t

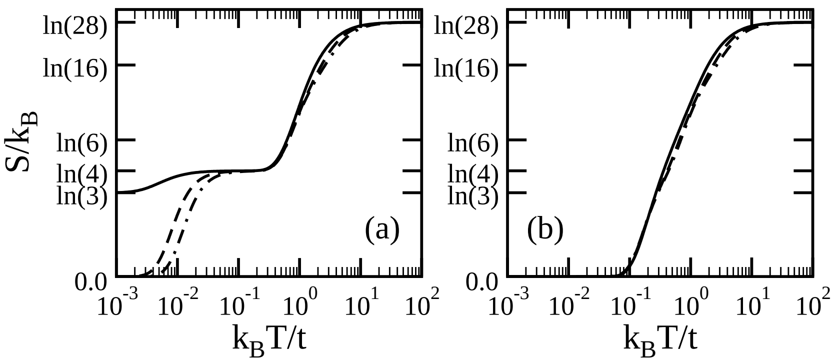

Figure 5.5: The same as in Fig. 5.3 but with the finite crystal field $E_0 = 2t$.

and by the AF character of χ_s. Instead of the high and low temperature peaks of the specific heat we observe two slightly parted peaks for $J_H = U/8$ which merge into a wide one for $J_H = U/4$. Analogously to the e_g case, the rise (fall) of $\langle \mathbf{S}_i^2 \rangle$ ($\langle \mathbf{T}_i^2 \rangle$) upon increasing temperature is related to the transitions from the low energy states to the excited triplet with $T^\zeta \simeq -0.5$ (*cf.* Table 5.3).

In addition, finite crystal field also modifies the temperature evolution of the entropy, illustrated in Figs. 5.5(a) (e_g orbitals) and 5.5(b) (t_{2g} orbitals). Depending on J_H, the low temperature entropy S of the e_g system either vanishes ($J_H \leq U/8$) or approaches the value $k_B \ln 3$ ($J_H = U/4$). Certainly, the latter corresponds to a spin triplet as the ground state. Nevertheless, owing to the vanishing specific heat, all the curves in Fig. 5.5(a) have a point of inflection $S = k_B \ln 4$ at $k_BT \simeq 0.1t$. Note that in contrast to the case without a crystal field, there is no such a point when $S = k_B \ln 16$. Namely, by promoting one pseudospin over the other, a finite crystal field markedly lowers the states with double occupancies, hence an analogous gap between the singly and doubly occupied states vanishes.

Finally, as shown in Fig. 5.5(b), the entropy of the t_{2g} system is almost independent of J_H. We note that S is entirely suppressed at low T due to a spin singlet ground state; it rises rapidly at $k_BT \simeq 0.1t$, and approaches eventually the limiting value $S = k_B \ln 28$, not having any point of inflection. Such a behavior is a direct consequence of a broad single peak in the specific heat.

Another interesting aspect of the present model is the role of local quantum fluctuations due to the orbital-flip term. These processes significantly increase the size of the Hilbert space and are often neglected [182, 184]. In order to examine the effects of such terms we consider the following limits of the full quantum Hamiltonian (5.1): classical one (only the Ising part $\mathbf{S}_{i\alpha} = S^z_{i\alpha}$ of Hund's exchange coupling is taken into account and we also leave out the pair-hopping processes from one orbital to the other), quantum spin only (no orbital-flip term), and finally quantum pseudospin only (no spin-flip term). The corresponding intersite spin correlation functions $\langle \mathbf{S}_1 \cdot \mathbf{S}_2 \rangle$ obtained without the crystal field are plotted as functions of the Stoner parameter $U + J_H$ in Fig. 5.6(a). Note that $\langle \mathbf{S}_1 \cdot \mathbf{S}_2 \rangle$

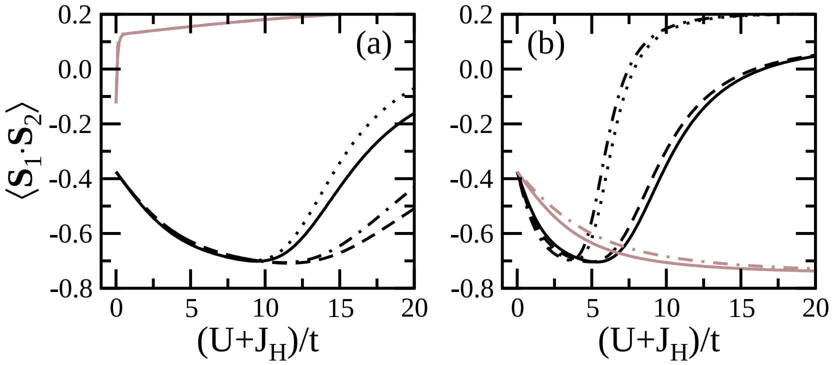

Figure 5.6: Intersite spin correlation functions $\langle \mathbf{S}_1 \cdot \mathbf{S}_2 \rangle$ of the model with either t_{2g} (gray lines) or e_g orbitals (black lines) as functions of the Stoner parameter $U + J_H$ with $J_H = U/4$ at temperature $\beta t = 100$ for: (a) $E_0 = 0$, and (b) $E_0 = 2t$. Solid (dot-dashed) lines, show the results of the entirely classical (quantum) model, whereas dotted (dashed) lines of the quantum spin (pseudospin) only limit, respectively.

is finite and negative even in the noninteracting $U = 0$ limit due to the Pauli principle.

It turns out that either spin or pseudospin fluctuations almost do not affect $\langle \mathbf{S}_1 \cdot \mathbf{S}_2 \rangle$ of the classical model with the t_{2g} orbitals (gray solid lines) and all the correlation functions overlap. On the contrary, in the e_g orbital model (black lines), $\langle \mathbf{S}_1 \cdot \mathbf{S}_2 \rangle$ of the classical model (solid line) differs noticeably from the one obtained in the full quantum model (dot-dashed line). More precisely, spin fluctuations (dotted line) suppress the AF spin correlations, whereas the pseudospin dynamics (dashed line) supports negative $\langle \mathbf{S}_1 \cdot \mathbf{S}_2 \rangle$.

The explanation is provided by the eigenenergies of the matrix H_3 (5.32), yielding the lowest energy states in the $S^z = 0$ subspace. In the case of the t_{2g} model they might be written in a generic form,

$$E(H_3) = \tfrac{1}{2}\left(\tilde{U} \pm J_H \pm \sqrt{(\tilde{U} \pm J_H)^2 + 16t^2}\right), \tag{5.62}$$

with $\tilde{U} = \{U, U_2\}$. The corresponding second order perturbation excitations $E_1^{\pm}$ ($E_2^{\pm}$) including the spin (pseudospin) dynamics, respectively, are,

$$E_1^{\pm} = -\frac{4t^2}{U_2 \pm J_H}, \qquad E_2^{\pm} = -\frac{4t^2}{U \pm J_H}. \tag{5.63}$$

Recalling the lowest energy high- (5.44) and low-spin excitations (5.45) of the t_{2g} model, one finds that E_1^- corresponds to the $S_z = 0$ triplet component, whereas E_1^+ to the singlet one. Therefore, spin dynamics splits up the above levels and by pushing upwards the latter favors ferromagnetism, whereas pseudospin dynamics

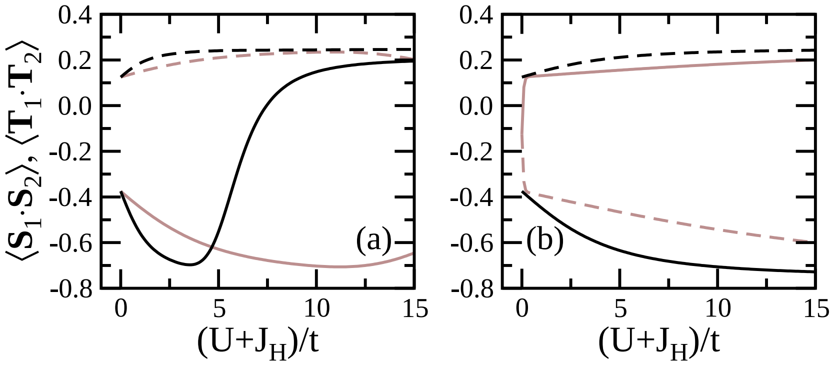

Figure 5.7: Intersite correlation functions: spin $\langle \mathbf{S}_1 \cdot \mathbf{S}_2 \rangle$ (solid line) and pseudospin $\langle \mathbf{T}_1 \cdot \mathbf{T}_2 \rangle$ (dashed line) as functions of the Stoner parameter $U + J_H$ with $J_H = U/4$ at temperature $\beta t = 100$ for: (a) e_g orbitals, and (b) t_{2g} orbitals. Parameters: $E_0 = 0$ (gray line) and $E_0 = 2t$ (black line).

should clearly stabilize antiferromagnetism. However, due to a large energy gap between the triplet ground state and the first excited singlets (*cf.* Table 5.1), fluctuations do not affect at all the value of $\langle \mathbf{S}_1 \cdot \mathbf{S}_2 \rangle$ for the classical t_{2g} model. In contrast, there is a strong competition between the lowest-lying singlet and the two excited triplets in the e_g model (*cf.* Table 5.2) and consequently one cannot neglect fluctuations which modify substantially a spin correlation function of the classical model, displayed in Fig. 5.6(a). However, the antiferromagnetism supporting feature of the orbital-flip term is strongly suppressed by finite crystal field $E_0 = 2t$ [*cf.* Fig. 5.6(b)], as pair-hopping processes between different orbitals involve now an additional energy. Nevertheless, $\langle \mathbf{S}_1 \cdot \mathbf{S}_2 \rangle$ of the classical and quantum e_g model differs vastly owing to the spin-flip term. Finally, fluctuations only slightly suppress the spin correlation function of the classical t_{2g} model with $E_0 = 2t$. Thereby, for the sake of clarity we show only $\langle \mathbf{S}_1 \cdot \mathbf{S}_2 \rangle$ of the classical and full quantum model.

In Fig. 5.7 we present a comparison of intersite spin $\langle \mathbf{S}_1 \cdot \mathbf{S}_2 \rangle$ (solid line) and pseudospin $\langle \mathbf{T}_1 \cdot \mathbf{T}_2 \rangle$ (dashed line) correlation functions for e_g system [*cf.* Fig. 5.7(a)] and for t_{2g} system [*cf.* Fig. 5.7(b)] as a function of $U + J_H$. The e_g results illustrate the AF correlations between spins in the weak coupling regime $U + J_H \leqslant 7.5t$. However, further increase of the interaction strength in the presence of the finite crystal field changes gradually the AF coupling into a FM one, with the preferred immobile $|\xi\rangle$ pseudospin, whereas $\langle \mathbf{T}_1 \cdot \mathbf{T}_2 \rangle$ is only slightly affected by the field.

As we expected, in the absence of a finite crystal field the ground state of the t_{2g} system with a finite interaction is a spin triplet (positive $\langle \mathbf{S}_1 \cdot \mathbf{S}_2 \rangle$) and a pseudospin singlet (negative $\langle \mathbf{T}_1 \cdot \mathbf{T}_2 \rangle$). The situation is changed drastically by a finite crystal field. The resulting $\langle \mathbf{S}_1 \cdot \mathbf{S}_2 \rangle$ is then negative revealing the

AF nature of the ground state, whereas positive $\langle \mathbf{T}_1 \cdot \mathbf{T}_2 \rangle$ shows that the AF pseudospin correlations are suppressed. In the following Section we shall compare these results with the one obtained in the HA.

5.3 Instabilities of the e_g model

While several features are generic in the models with two [172–174, 177–179] or more [175, 176, 180] orbitals per ion, and occur already when diagonal hopping is assumed, we note that these models are closer to the behavior of t_{2g} electrons — strong interactions between them might explain a FM instability in ruthenates [28]. Here we are interested in the magnetic and orbital order for interacting e_g electrons. It is known that strong quantum fluctuations may lead in the regime of large intraorbital Coulomb interaction U to qualitatively new behavior in a Mott insulator with three e_g electrons per site [192], but the competition between various magnetic and orbital instabilities was little explored in the weak coupling regime. Therefore, in this Section we determine a phase diagram of the e_g electrons within the HA, searching for phases which are both orbitally and magnetically polarized. In order to obtain a transparent description of such phases, it is convenient to rewrite the Hamiltonian (5.3) by introducing the following operators [193]:

$$n_i = \sum_{\alpha\sigma} n_{i\alpha\sigma}, \tag{5.64}$$

$$m_i = \sum_{\alpha\sigma} \lambda_\sigma n_{i\alpha\sigma}, \qquad o_i = \sum_{\alpha\sigma} \lambda_\alpha n_{i\alpha\sigma}, \qquad p_i = \sum_{\alpha\sigma} \lambda_\alpha \lambda_\sigma n_{i\alpha\sigma}, \tag{5.65}$$

$$f_{i\sigma} = \sum_{\alpha\beta} c^\dagger_{i\alpha\sigma} \tau^x_{\alpha\beta} c_{i\beta\sigma}, \tag{5.66}$$

with $\lambda_\sigma = \pm 1$ for $\sigma = \uparrow (\downarrow)$ spin and $\lambda_\alpha = \pm 1$ for $\alpha = x(z)$ orbital, and τ^x being the Pauli matrix. These operators correspond to: the total density, the total magnetization, the orbital polarization, the magnetic orbital polarization, and the on-site orbital flip, respectively. The Coulomb interaction term H_{int} (5.3) can be then written as:

$$\begin{aligned} H_{int} &= \tfrac{1}{8} \sum_i \left[(3U - 5J_H) n_i^2 - (U + J_H) m_i^2 - (U - 5J_H) o_i^2 - (U - J_H) p_i^2 \right] \\ &+ J_H \sum_i f_{i\uparrow} f_{i\downarrow}. \end{aligned} \tag{5.67}$$

The order parameters introduced in Eqs. (5.65): m_i, o_i, and p_i, used next to minimize the ground state energy, provide a complete description of the ground state at finite doping. We emphasize that they also reveal the dominating role of the kinetic energy of doped holes over the superexchange energy. Namely, large electron filling of $|z\rangle$ orbitals, contributing to a narrow band, optimizes the kinetic energy of holes in magnetically polarized and partly filled $|x\rangle$ orbitals, contributing to a wide band. On the contrary, the superexchange $\propto J = 4(t^{\alpha\alpha})^2/U$ at large U suggests that the system would better optimize the magnetic energy when the orbitals with larger hopping elements t^{xx} were closer to half filling. This, however, cannot happen as the loss of the kinetic energy is too large. We show below that the complex interplay between all the degrees of freedom of the model (5.1) results in rather peculiar doping dependence of the order parameters (5.65), and thus leads to highly nontrivial and rich phase diagrams.

We investigate the stability of possible phases with either uniform or staggered magnetic order in the HA by expressing the local operators (5.64) and (5.65) by their mean-field averages,

$$\gamma_i^2 \simeq 2\gamma_i\langle\gamma_i\rangle - \langle\gamma_i\rangle^2. \tag{5.68}$$

In order to establish unbiased results, the calculations are carried out on a large 128×128 cluster, using periodic boundary conditions at low temperature $\beta t = 100$. For simplicity, throughout the present analysis we assume consistently $\langle f_{i\sigma}\rangle = 0$.

5.3.1 Magnetic order and orbital polarization

As shown in Figs. 5.8(b) and 5.8(e), in the PM state at $E_z = 0$, with $\langle m\rangle = \langle p\rangle = 0$, a higher electron density is found in $|x\rangle$ orbitals ($\langle o\rangle > 0$), as then the kinetic energy is lowered, except for $x = 0$. This state is our reference state for possible magnetic instabilities.

We now proceed with the discussion of the magnetic order and orbital polarization for two characteristic values of the Stoner parameter,

$$I \equiv U + J_H, \tag{5.69}$$

i.e., intermediate coupling $I = 4t$, and strong coupling $I = 8t$, being smaller and larger than the bandwidth $W = 6t$, respectively. Let us begin with the FM phase. In Fig. 5.8(a) we show the magnetization $\langle m\rangle$ as a function of doping x for the ratio $J_H/U = 0.25$ which is representative for the strong Hund's exchange coupling regime. In this case the interaction in the o-channel is *repulsive*. As depicted in Fig. 5.8, several FM phases then occur.

Consider first the intermediate interaction strength $I = 4t$ shown in Figs. 5.8(a-c), where one finds two disconnected FM states: one for $0 \le x < 1$, and the second one for $x \simeq 1.5$. The latter corresponds to a van Hove singularity in the density of states. Since it is predominantly related to the $|x\rangle$ orbital, both the orbital polarization $\langle o\rangle$ [*cf.* Fig. 5.8(b)] and the magnetic polarization $\langle p\rangle$ [*cf.* Fig. 5.8(c)] are positive in this doping regime. In contrast, for $0 \le x < 1$ the total energy is minimized when a higher electron density is found in the $|z\rangle$ orbital, where also larger magnetic moments are formed. Such anisotropic filling of e_g orbitals follows from a large difference between the t^{xx} and t^{zz} hopping elements [194]. Note that the orbital polarization is here opposite to that in the reference PM state.

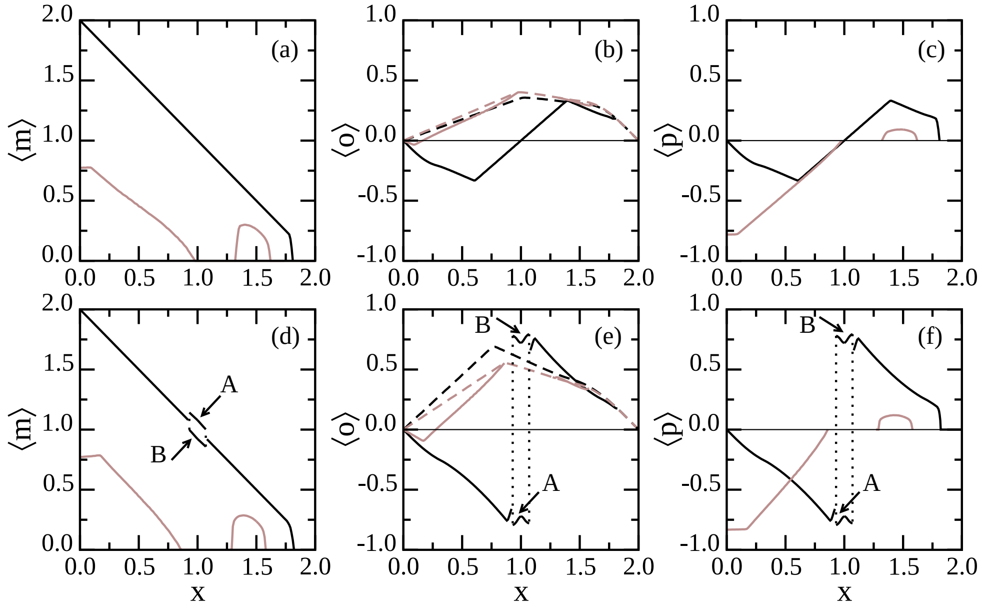

Figure 5.8: Order parameters: magnetization $\langle m\rangle$, orbital polarization $\langle o\rangle$, and magnetic polarization $\langle p\rangle$ in the FM phase as a function of doping x for: (a-c) $J_H = 0.25U$ and (d-f) $J_H = 0.15U$, and for two values of the Stoner parameter: $U + J_H = 8t$ (black solid line) and $U + J_H = 4t$ (gray solid line). A and B refer to two sublattices in the orbital ordered state for $x \simeq 1$. The orbital polarization in the reference PM states is shown by dashed line.

The above peculiar behavior disappears gradually when the interaction strength is enhanced to $I = 8t$ and both $\langle o\rangle$ and $\langle p\rangle$ tend to saturate to the optimal value, being positive (negative) for $x < 1$ ($x > 1$), leaving the $|z\rangle$ orbital almost fully polarized. Here the magnetic instability, with the largest effective interaction term $U + J_H$, dominates and the magnetization barely deviates from its saturation value $2 - x$, except for the low electron density $x > 1.8$. In this case doping of the half-filled FM state first leads to holes introduced into the $|x\rangle$ orbitals, leaving the center of the narrower band, with predominantly $|z\rangle$ orbital character, below the former broader one. Therefore, in this situation the formation of local magnetic moments optimizes the energy. They are naturally associated with the $|z\rangle$ orbitals since they contribute to the narrower band.

When Hund's exchange coupling J_H is reduced, the interaction in the o-channel becomes *attractive*. As a result, for large $I = 8t$, both $\langle o\rangle$ and $\langle p\rangle$ nearly saturate to the ideal behaviors $-x$ for $x < 1$ and $2 - x$ for $x > 1$. Therefore, a transition between these two solutions would be first order, and one observes a jump at $x \simeq 1$. However, as shown in Figs. 5.8(d-f), the two-sublattice orbital order sets in in this crossover regime in the form of a FM$_{xz}$ state. This state has opposite orbital polarization $\langle o\rangle_A \simeq -0.8$ and $\langle o\rangle_B \simeq 0.8$ on both sublattices [*cf.* Fig. 5.8(e)].

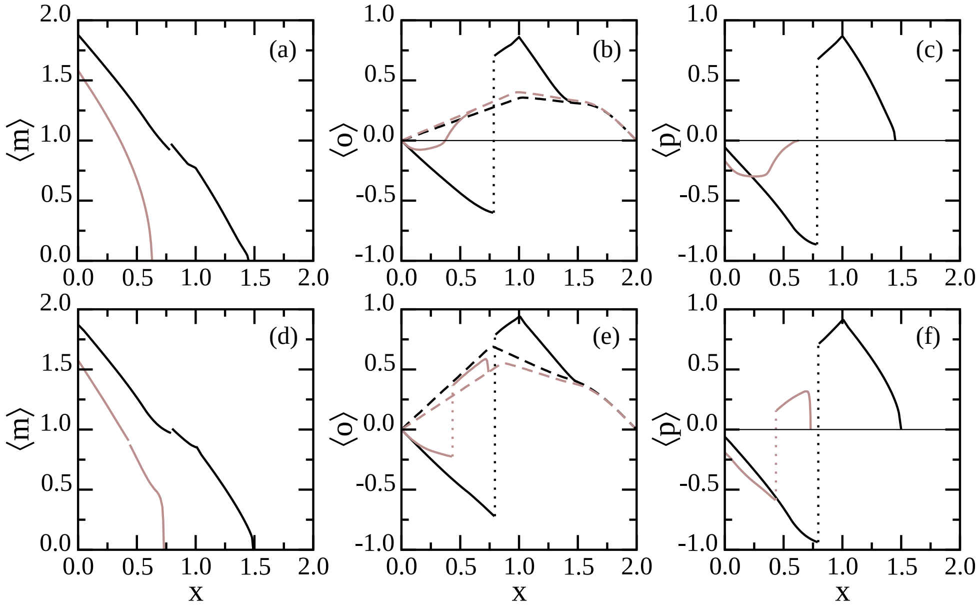

Figure 5.9: Order parameters as in Fig. 5.8 but for the AF phase.

While the total density $\langle n\rangle_A$ is somewhat higher than $\langle n\rangle_B$ due to inequivalent e_g orbitals, also $\langle m\rangle_A > \langle m\rangle_B$. For large doping $x > 1$ the electrons occupy mainly the $|x\rangle$ orbitals, and the small occupancy of $|z\rangle$ orbital results solely from the interorbital hopping term $\propto t_{xz}$. Indeed, at $x \simeq 1.3$ one finds appreciable orbital polarization, with $|x\rangle$ orbitals occupied and almost empty $|z\rangle$ orbitals, the situation encountered in $La_{1-x}Sr_{1+x}MnO_4$ manganites [195]. In all FM phases found at $J_H = 0.15U$ the total magnetization is close to saturation. When U is reduced, one gradually recovers the behavior obtained for large J_H/U.

We now turn to the AF phase, expected as a ground state near half filling ($x = 0$). The order parameters are illustrated in Fig. 5.9 for the same parameter values as considered above for the FM case. For $I = 8t$ and $J_H/U = 0.25$ the mean-field equations possess two competing solutions [*cf.* Figs. 5.9(a-c)]. The first one, which can be continued to weak coupling, is characterized by negative values of orbital $\langle o\rangle$ and magnetic $\langle p\rangle$ polarizations. Namely, the higher electron density is found within the $|z\rangle$ orbitals, and these orbitals carry the magnetic moment. More precisely, introducing holes in the half-filled insulating AF state mostly affects the band with $|x\rangle$ orbital character, leaving the magnetic moments within the more localized $|z\rangle$ orbitals almost saturated. This solution extends to large doping $x \simeq 1$. In contrast, the second solution rather stems from the behavior expected for low density: the electrons first occupy the broader band with $|x\rangle$ orbital character until quarter filling ($x = 1$) is reached, and next they gradually occupy the other band, with $|z\rangle$ orbital character. However, since the interaction in the o-channel is *repulsive* and since both bands are coupled, the

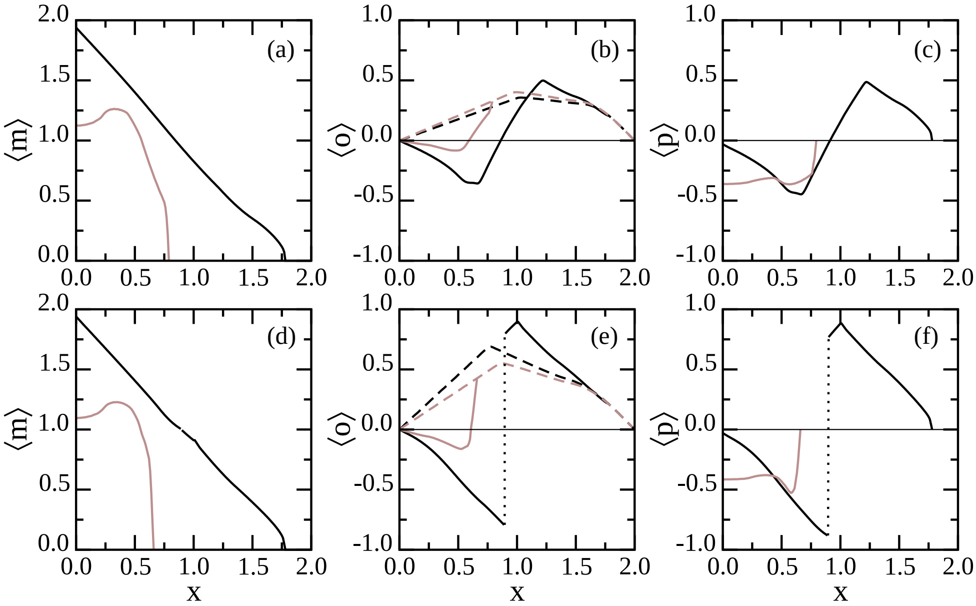

Figure 5.10: Order parameters as in Fig. 5.8 but for the C-AF phase.

orbital polarization $\langle o\rangle$ and the magnetic polarization $\langle p\rangle$ are reduced from their maximal values which would be reached for decoupled orbitals. These two trends from $x = 0$ and $x = 2$ contradict each other, and therefore an abrupt (first order) transition between both solutions is observed at $x \simeq 0.7$, as shown in Figs. 5.9(b-c).

Reducing J_H barely affects the above findings for strong coupling $I = 8t$ [*cf.* Fig. 5.9(d-f)]. While the magnetization $\langle m\rangle$ is almost unchanged, the first order transition between two differently polarized states is more pronounced, as the values of the orbital polarization and the magnetic polarization are enhanced. When reducing U the location of the first order phase transition shifts towards smaller doping, while all order parameters are suppressed. At the same time the critical doping locating the second order phase transition is reduced by a weaker Coulomb interaction U but is enhanced by a weaker Hund's exchange coupling J_H. When seeking for other phases one may expect that two-sublattice FM solutions can smoothly interpolate between the FM and AF states. Such solutions never turned out to be the ground state in this study (up to $I = 8t$).

A competition between the FM and AF order in the present model of e_g band may lead to a superposition of the two phases in a form of C-AF phase, where the magnetic moments are FM along one direction and staggered in the other (orthogonal) one. According to recent numerical simulations [196], a coexistence of FM and AF bonds is indeed expected for $x \simeq 0.5$. Unlike in the AF phase, the order parameters are continuous functions of doping for $J_H/U = 0.25$, as can be seen in Figs. 5.10(a-c). This behavior is similar to that of the FM case [*cf.* Fig. 5.8]. Its origin can be attributed to the orbital polarization which is substantially stronger

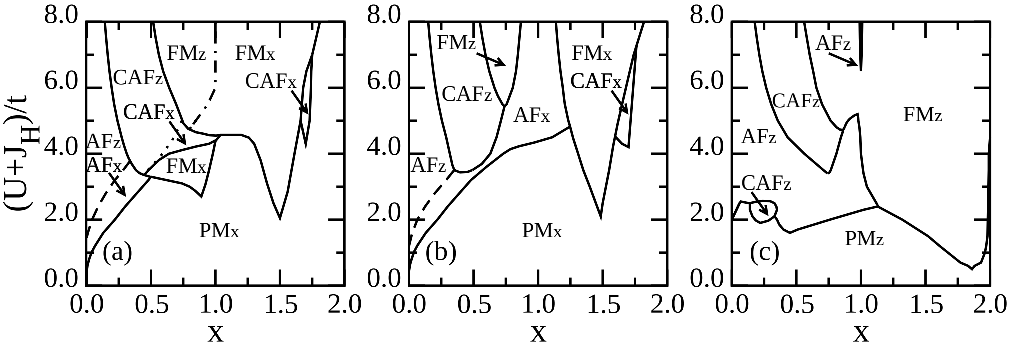

Figure 5.11: Phase diagrams of the e_g orbital model (5.1) as functions of the Stoner parameter $U + J_H$ and hole doping $x = 2 - n$, with: (a) $J_H = 0.25U$, and (b) $J_H = 0.15U$. Panel (c) shows the stable phases for finite crystal field splitting $E_z = 2t$ and $J_H = 0.25U$. Transitions from the PM phase to magnetic phases are second order. The remaining solid lines denote first order transitions while the dashed, dotted, and dashed-dotted lines indicate second order transitions.

in the AF case to the extent that is exceeds a certain threshold above which no smooth solution can interpolate between the small and large doping regimes. For $x \simeq 0.5$ the magnetic moment $\langle m \rangle$ is carried by the $|z\rangle$ orbital for large U, while $\langle m \rangle$ decreases and $\langle o \rangle$ changes sign for small U.

When reducing J_H/U, the orbital polarization is enhanced and a first order transition appears for $I = 8t$, as illustrated in Figs. 5.10(d-f). In this case both the orbital polarization and the magnetic moment are predominantly carried by the stronger correlated $|z\rangle$ orbital (with a weaker hopping and thus larger ratio U/t^{zz} than U/t^{xx}) in the physically relevant doping range centered around $x = 0.5$.

5.3.2 Magnetic phase diagrams

Our main findings are summarized in the phase diagrams in Fig. 5.11. As shown in Fig. 5.11(a), the doped PM phase for $J_H/U = 0.25$ is characterized by a positive orbital polarization, therefore denoted PMx. It is unstable towards AFx phase for small doping up to $x \simeq 0.5$, towards C-AFx phase for $1 \leq x \leq 1.02$ and for $1.65 \leq x \leq 1.75$, and towards FMx phase otherwise. In particular, for $x = 1$ the FMx, C-AFx, orbitally unpolarized FM and (for $I > 16t$) the alternating FMxz phases appear successively with increasing interaction strength I. The C-AF phases are found for $x \simeq 0.5$ at $I > 4t$, and also in a small range around $x \simeq 7/4$.

When reducing J_H/U, the main difference appears for $x \simeq 1$, as illustrated in Fig. 5.11(b). Here the PMx phase is unstable towards an AFx phase which itself is robust and remains stable up to strong coupling. This seemingly peculiar behavior can be better understood by recalling the results obtained from the ED

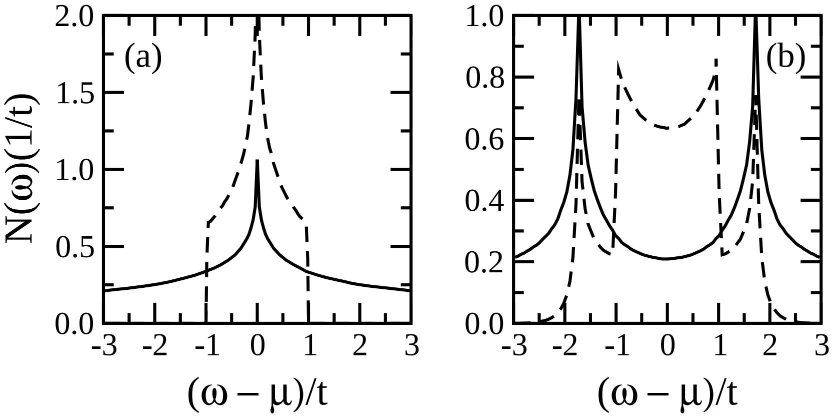

Figure 5.12: Tight binding density of states $N_\alpha(\omega)$, projected on the orbital $|x\rangle$ (solid line) and $|z\rangle$ (dashed line) of the Hamiltonian (5.2) at $x = 0$ with: (a) diagonal hopping elements $t_{ij}^{\alpha\beta}\delta_{\alpha\beta}$, and (b) all the hopping elements $t_{ij}^{\alpha\beta}$.

of a two-site cluster. Namely, even though ED of the full Hamiltonian (5.1) gives a singlet ground state also for $J_H = U/4$, (*cf.* Table 5.2), one finds in the large U expansion, by leaving out the orbital-flip term as in the present approximation, the ground state to be AFx, with the energy $E_{S_0}^{e_g} = -4t^2/U$ for $J_H < U/4$, and FMxz, with $E_{T_0}^{e_g} = -t^2/(U - 3J_H)$, for larger J_H, in qualitative agreement with our mean-field calculation.

Let us finally mention that the tight-binding Hamiltonian (5.2) is known to have a van Hove singularity at $\mu = \sqrt{3}t$ corresponding to $x = 1.5$. Indeed, in Fig 5.12, we show the density of states,

$$N_\alpha(\omega) = \frac{1}{N}\sum_{\mathbf{k}}\sum_{i\sigma}|\Psi_{i\alpha\sigma}(\mathbf{k})|^2\delta(\omega - \varepsilon_{\mathbf{k}\sigma}), \tag{5.70}$$

projected either on the orbital $|x\rangle$ or $|z\rangle$. Here, $\Psi_{i\alpha\sigma}(\mathbf{k})$ are the eigenvectors associated with eigenvalues $\varepsilon_{\mathbf{k}\sigma}$. One clearly observes that the off-diagonal hopping element $t_{ij}^{\alpha\beta} = \pm\sqrt{3}t/4$ modifies substantially $N_\alpha(\omega)$ by shifting the van Hove singularity from $\mu = 0$ [*cf.* Fig 5.12(a)] towards $\mu = \sqrt{3}t$ [*cf.* Fig 5.12(b)]. Therefore, at $x = 1.5$, one would expect a FM instability for arbitrary weak coupling at zero temperature. This particular instability, however, turns out to be unusually strongly temperature dependent. As a result, the corresponding critical value of the Stoner parameter I is finite at temperature $T > 0$, and reaches a value close to $W/3$ (Fig. 5.11) at $T = W/600$ used in this work.

5.3.3 Consequences of the crystal field splitting

A complete investigation of the phase diagrams at finite crystal field splitting E_z would be quite involved. Such a study would be worthwhile if motivated by real compounds and is left for future work; here we only show qualitatively what happens for selected values. At $E_z = 0$ the majority of stable magnetic solutions is characterized by a positive orbital polarization, a tendency expected for a 2D model of e_g electrons [195], which would certainly be enhanced by a negative crystal field E_z. We therefore limit our present discussion to the influence of a positive E_z, in order to investigate a competition between the kinetic energy, which is lower when the broad band with predominantly $|x\rangle$ orbital character is closer to half filling, and the potential energy at finite E_z. Furthermore, we restrict ourselves to the strong Hund's exchange coupling regime of $J_H = 0.25U$.

As shown in Fig. 5.11(c), the orbital polarization of the PM phase is changed to negative (PMz phase) already for moderate $E_z = 2t$. As a result, the magnetic moment and the orbital polarization are carried by the same orbital in all phases, and the magnetic instabilities are achieved for lower values of $I = U + J_H$. Another consequence of finite $E_z > 0$ is the observed shift of the van Hove singularity to larger doping, strongly enhancing the tendency towards ferromagnetism in the low density regime.

In addition, the competition between FM and AF phases at quarter filling ($x = 1$) remains quite spectacular: even though ED studies of the two-site molecule in the classical limit yield negative $\langle \mathbf{S}_1 \cdot \mathbf{S}_2 \rangle$, suggesting the AF nature of the ground state in the entire coupling regime up to $I = 15t$ [*cf.* Fig 5.7(b)], in the HA, FM phase takes over in an intermediate coupling regime $5.15t < I < 6.5t$. We conclude therefore that the Hartree approach slightly overestimates the tendency towards ferromagnetism in this narrow region as the energy difference does not exceed 0.002t at $I = 6t$. In contrast, we have found that the HA predicts a stable FM phase in the large U regime with a crossover at $I = 16t$, in agreement with the ED studies.

In summary, we have determined the phase diagram of e_g electrons on the square lattice within the HA. The occurrence of antiferromagnetism in the vicinity of half filling, followed by C-AF phase at $x \simeq 0.5$, as well as FM phases for $x \simeq 0.75$ and $x \simeq 1.5$, are robust features of this model. Note that the regions of stability of the AF and C-AF phases with respect to the FM one would still be somewhat extended due to quantum corrections [197]. In particular, it should be stressed out that while the orbital polarization systematically appears in all phases, the orbital carrying the magnetic moment does not necessarily coincide with the one carrying higher electron density, leading to a particularly interesting interplay between magnetic and orbital degrees of freedom.

5.4 Stripe phases

So far we have focused on structures with up to two atoms in the unit cell. However, neutron diffraction experiments on nickelates point to the existence of filled stripe phases with DWs running diagonally across the NiO$_2$ planes [14, 15, 24–

d	$L\times L$	d	$L\times L$
3	72×72	8	64×64
4	80×80	9	72×72
5	80×80	10	80×80
6	72×72	11	88×88
7	84×84		

Table 5.4: Cluster sizes used in the calculations for the BC stripes separated by a different distance d in units of the lattice constant.

29]. They were also obtained in the theory using either the HF approximation applied to a charge transfer model, in which both the nickel and oxygen degrees of freedom are explicitely taken into account [101, 102, 113], or by the ED of finite clusters within the effective two-band model (5.1) extended by the coupling of e_g electrons to the lattice [196]. However, due to a large number of basis states, the latter calculation has solely been done for an eight site cluster allowing only for searching stripe phases with a small unit cell observed experimentally at high doping levels $x = 1/3$ and $x = 1/2$. In contrast, the HA allows one to investigate DWs structures with larger unit cells and hence it should provide an answer to the important question whether the description of NiO_2 planes by the simplified e_g model (5.1) yields results consistent with the charge transfer model predictions [101, 102, 113]. An important aspect of these studies, as compared to the pioneering work on the cuprates, where the relevant models yield DWs with *nonmagnetic* Cu^{3+} ions [5–9], is that DWs in the nickelates are formed of Ni^{3+} ions carrying a *finite* spin $S = 1/2$ leading to a FM arrangement along DWs. Moreover, in the preceding Section, we have obtained phase diagrams showing, in the regime away from half-filling, a clear tendency to ferromagnetism for $J_H = U/4$, or at least to the C-AF phase for $J_H = 0.15U$ (*cf.* Fig. 5.11). Therefore, in what follows we investigate the properties of BC stripes made out of pairs of atoms with a FM spin polarization within the model Hamiltonian (5.1) in the wide doping regime $0.05 \leq x \leq 0.4$.

In order to obtain unbiased results, we performed calculations on large clusters and used a reciprocal space HA, based on the smallest unit cell choice, similar to the one introduced in Chapter 4. As previously, we worked on squared clusters with the linear dimension along the x direction chosen as previously as an *even* multiplicity of the elementary unit cell dimension. However, due to orbital degeneracy we solved the mean-field equations on smaller clusters as compared to the ones used for a single-band Hubbard model (*cf.* Tables 4.5 and 5.4).

To ensure that the model (5.1) is indeed relevant for the nickelates, it is necessary to adopt appropriate values of parameters U, J_H, and E_z. Therefore, taking into account that LSNO is a charge-transfer insulator with the charge-transfer energy Δ nearly the same as that of NiO, as concluded upon x-ray-absorption

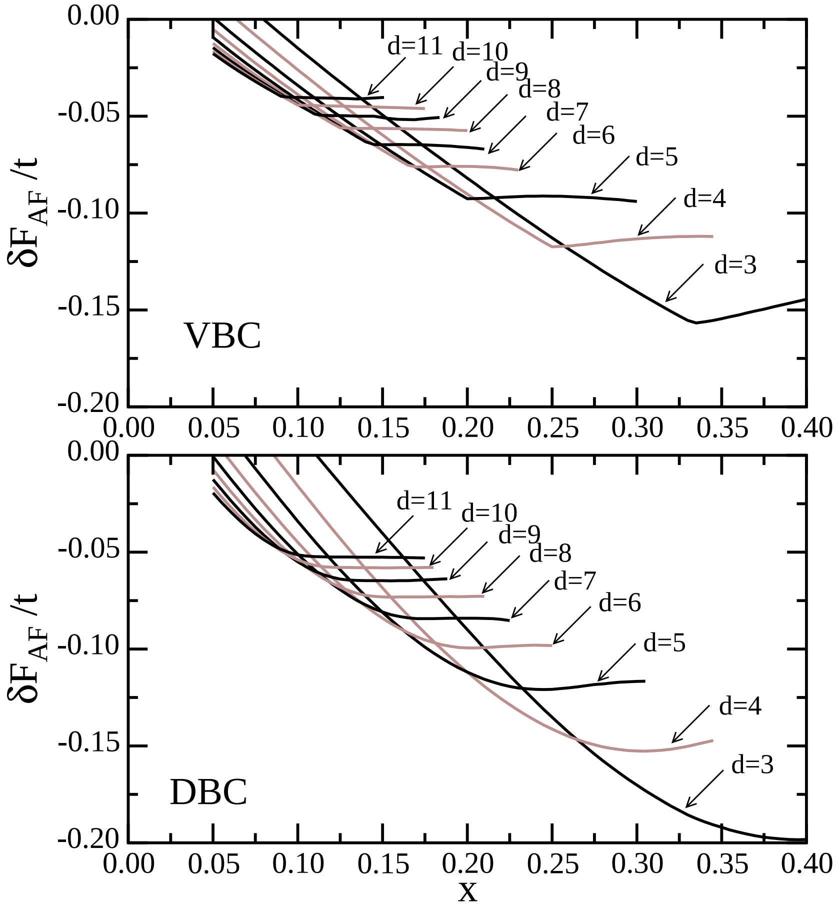

Figure 5.13: Free energy gain of the VBC (top) and DBC (bottom) stripe phases with respect to the AF phase δF_{AF} as a function of doping x, as obtained at temperature $\beta t = 100$ for the e_g model with $U = 8t$, $J_H = 1.5t$, and $E_z = 0$. Stripes are separated by $d = 3, \ldots, 11$ lattice constants.

(XAS) measurements [198] as well as on XPS and bremsstrahlung-isochromat spectroscopy (BIS) studies [199] of the electronic structure of LSNO, the parameters are taken as in the self-consistent Born calculations reproducing quite well photoemission spectra of NiO [200]. More precisely, owing to the fact that our approximation utterly ignores electron correlations we replace the strong on-site Coulomb repulsion in LSNO by a smaller value of the charge-transfer energy Δ of NiO, i.e., we set $U = \Delta = 5$ eV. Next, as the in-plane Ni$-$O$-$Ni bond length in La_2NiO_4 of 1.95 Å[189] is very much the same as compared with 1.89 Å for La_2CuO_4 [190], we set hopping t_{pd} between the p_σ orbitals and $|x\rangle \sim |x^2 - y^2\rangle$ orbitals to be as in LSCO, i.e., $t_{pd} = 1.47$ eV [156]. This in turn yields an effective in-plane Ni-Ni hopping $t^{xx} = 0.43$ eV. However, it is more convenient to take as the energy unit t an effective $(dd\sigma)$ hopping element connecting two $|z\rangle \sim |3z^2 - r^2\rangle$ or-

	VBC		DBC	
x	d	F/t	d	F/t
0.05	11	2.8811	11	2.8794
0.06	11	2.8376	11	2.8326
0.07	11	2.7946	11	2.7870
0.08	11	2.7519	11	2.7430
0.09	10	2.7099	10	2.7001
0.10	10	2.6677	9	2.6570
0.11	9	2.6258	8	2.6140
0.12	8	2.5839	7	2.5712
0.14	7	2.5001	6	2.4853
0.16	6	2.4162	6	2.3997
0.18	5	2.3329	5	2.3130
0.20	5	2.2485	4	2.2291
0.25	4	2.0394	4	2.0155
0.30	3	1.8325	3	1.8029
0.40	3	1.4619	3	1.4081

Table 5.5: Comparison of the ground state free energy F for the VBC and DBC stripe phases as found in the e_g model with $U = 8t$, $J_H = 1.5t$ and $E_z = 0$.

bitals along the c-axis, related to t^{xx} via the Slater-Koster relation $t = 4t^{xx}/3 \simeq 0.6$ eV, so that $U \simeq 8t$. Next, the value of Hund's exchange between t_{2g} electrons in NiO $J'_H = 0.8$ eV [200], is associated with J_H for e_g electrons through a simple relation,

$$J_H = J'_H + B, \tag{5.71}$$

where B stands for the Racah parameter [201]. Taking into account that $B \simeq 0.13$ eV for NiO$_2$ [202], one finds $J_H = 0.93$ eV, i.e., $J_H \simeq 1.5t$. Indeed, it has been shown that $J_H = 1$ eV reproduces the experimental band gap and the magnetic moment of La$_2$NiO$_4$ [203]. Finally, band structure calculations in the local density approximation predict the crystal field splitting between e_g orbitals to be 0.5 eV [204]. On the other hand, XAS spectra reveal a larger splitting of 0.7 eV [205], a value also deduced from the optical spectroscopy [103]. Altogether, we set $E_z = t = 0.6$ eV as a realistic value of the crystal field splitting in the nickelates.

We proceed now to discuss our key qualitative results obtained for increasing doping. Fig. 5.13 shows free energy gain of the VBC and DBC stripe phases with respect to the AF phase δF_{AF} as a function of doping x, as obtained at temperature $\beta t = 100$ for the e_g model (5.1) with $U = 8t$, $J_H = 1.5t$, and $E_z = 0$. Analogously to the single-band findings, Fig. 5.13 gives a clear demonstration of the tendency to a gradual formation of stripe phases with smaller unit cells upon increasing doping. Another important observation is that, in agreement with the results of multiband models for nickelates [101, 113], for a given fixed doping diagonal

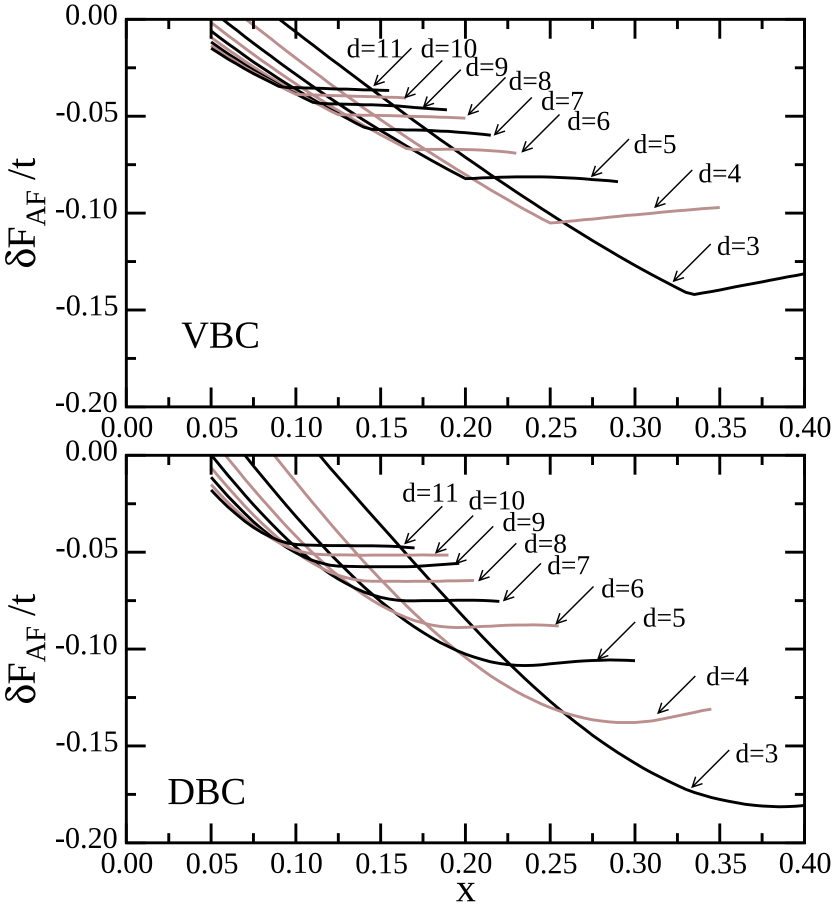

Figure 5.14: The same as in Fig. 5.13 but with finite crystal field splitting $E_z = t$.

structures are significantly lower in energy than vertical ones, especially in large doping regime $x = 0.4$. The robust stability of the DBC stripe phase with respect to the VBC one is illustrated more transparently in Table 5.5, where we compare the ground state free energy F for both structures. Note that a similar variation of the optimal distance between DWs d suggests the same optimal stripe filling.

A further qualitative point concerns the influence of a finite crystal splitting between the $|x\rangle$ and $|z\rangle$ orbitals on stability of DW structures. As depicted in Fig. 5.14, realistic value $E_z = t$ seems not to promote noticeably any stripe phases and one recovers DBC stripes as the ground state. We conclude therefore that it is not E_z that is responsible for a different orientation of DWs in nickelates and cuprates. Later on we shall see that finite E_z has also only a little visible effect on optimal stripe filling. However, a reduced stability of both stripe phases with respect to the uniform AF phase appears to be rather puzzling at first sight. One finds that realistic positive E_z promotes $|z\rangle$ orbitals with a narrow band which suppresses substantially the AF superexchange gain $\propto J = 4(t^{zz})^2/U$. Moreover, larger filling of the $|z\rangle$ orbitals means that holes are predominately doped into the $|x\rangle$ orbitals. Hence, one would expect that such charge redistribution strongly increases the kinetic energy gain due to a wider band formed by holes, propagating especially easily along DWs where the AF order is partially suppressed. Nevertheless, this gain is apparently easily overcompensated by the kinetic energy loss due to hopping perpendicular to the stripes. On the one hand, our studies of the BC stripe phases within the single-band Hubbard model have shown that the largest kinetic energy gain is released on the bonds connecting pairs of ferromagnetically coupled atoms located in the DWs (*cf.* Fig. 3.4). On the other hand, in the e_g model, FM order of the DW spins is substantially stabilized by the off-diagonal hopping t^{xz} yielding low-energy excitations of the FM superexchange $\propto J_{FM} = 4(t^{xz})^2/(U - 3J_H)$. However, when one orbital is sufficiently favored by finite crystal field over the other one, these low-energy processes are practically blocked, explaining enhanced stability of the AF order with respect to the BC solutions (*cf.* Figs. 5.13 and 5.14).

Let us now pause for a moment to remind the main experimental data concerning stripe phases in nickelates. The stripe order in LSNO is characterized by both charge $\mathbf{Q}_c = \pm\pi(2\epsilon, 2\epsilon)$ and spin $\mathbf{Q}_s = \pi(1 \pm \epsilon, 1 \pm \epsilon)$ IC wave vectors along the diagonal, with respect to the Ni-O bond, direction, with the incommensurability ϵ, corresponding to the inverse of the distance d between DWs, i.e., $\epsilon = 1/d$ [14, 15, 24–29]. Further, ϵ varies continously upon doping x following the linear relation $\epsilon = x$ in the wide doping regime $x \leq 1/3$ and than it gradually saturates with the value $\epsilon \simeq 0.44$ [29]. Such behavior of ϵ indicates a fixed hole density of one hole/Ni ion and it is consistent with the HF predictions both in the single- and multiband models [5–9, 101, 102, 113]. Finally, a fixed hole density along DWs results in the pinning of the chemical potential μ for $x \leq 1/3$, whereas a large ($\simeq 1$ eV/hole) downward shift appears in the higher doping regime [110].

Our theoretical findings concerning the properties of BC stripe phases are summarized in Fig. 5.15 showing the doping dependence of the incommensurability ϵ, stripe filling ν, and chemical potential μ for both the VBC (left) and DBC (right) stripe ground state deduced from Figs. 5.13 and 5.14. Here, by analogy with Fig. 4.10 illustrating doping dependence of ϵ, ν, and μ in the model for cuprates, the points correspond to the middle of stability region of a given type of the ground state. The only exception is the $d = 3$ case, in which ϵ, ν, and μ, are plotted for the minimum of the free energy.

In agreement with the experimental data for LSNO, indicated here by a gray solid line in panels (a,b), one observes that ϵ follows the law $\epsilon \simeq x$ up to $x \simeq 0.2$ and then it tends to saturate with the highest possible value for the BC stripe phase, i.e., $\epsilon = 1/3$, as there are no BC stripe phases in which DWs are separated by $d = 2$ lattice spacings. Further, in the regime where ϵ follows linearly x, decreasing stripe periodicity allows the system to maintain nearly fixed ν [*cf.* Fig. 5.15(c,d)] pinning simultaneously the chemical potential μ, as shown in Fig. 5.15(e,f). Remarkably, the ground state of both the VBC and DBC stripe phases is characterized by the

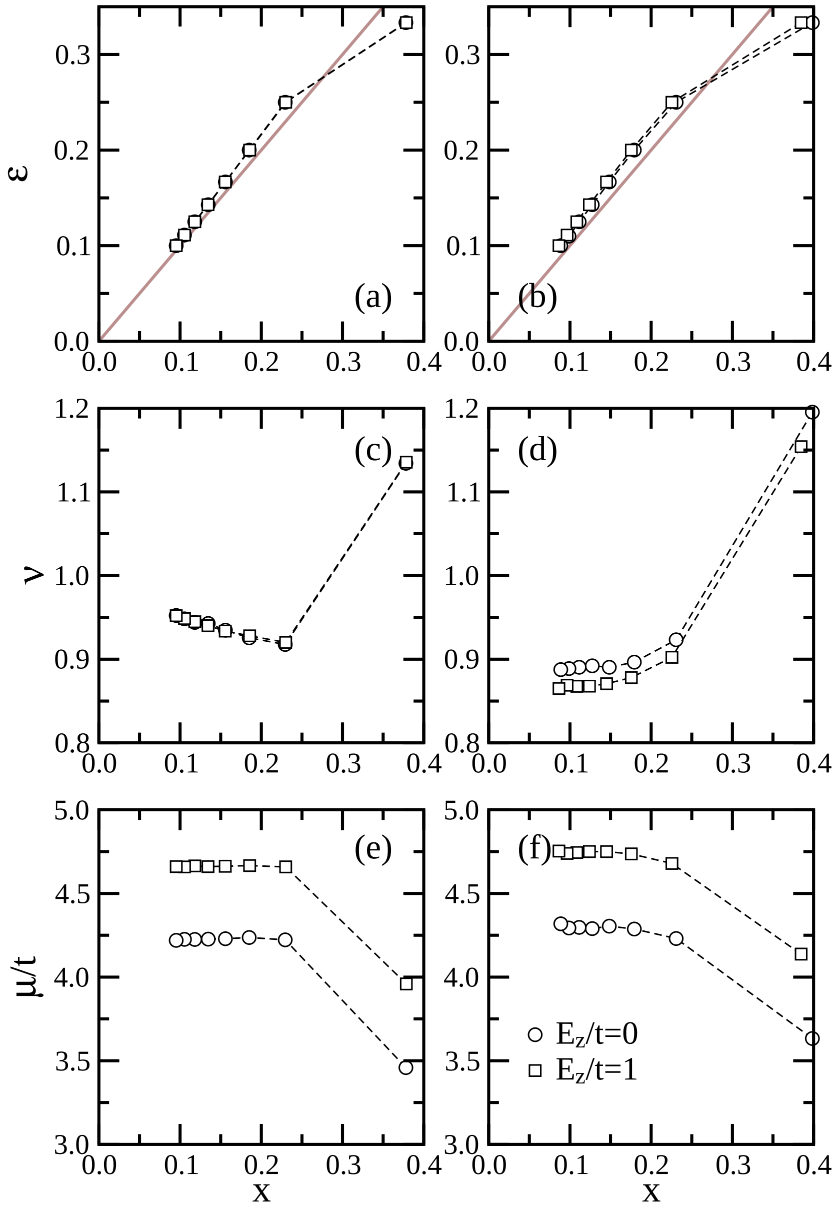

Figure 5.15: Doping dependence of: (a,b) magnetic incommensurability ϵ, (c,d) stripe filling ν, and (e,f) chemical potential μ for the VBC (left) and DBC (right) stripe ground state deduced from Figs. 5.13 and 5.14. Gray solid line in panels (a,b) shows the experimental behavior of ϵ in LSNO [29].

optimal filling 0.9 hole/Ni, very close to the experimental value one hole/Ni ion, and the optimal filling remains almost unaltered in the model with a finite crystal field $E_z = t$.

Regarding the chemical potential shift $\Delta\mu$ in the doping regime $x > 0.2$, one finds that, as in the calculations for the cuprates, it exceeds the experimental

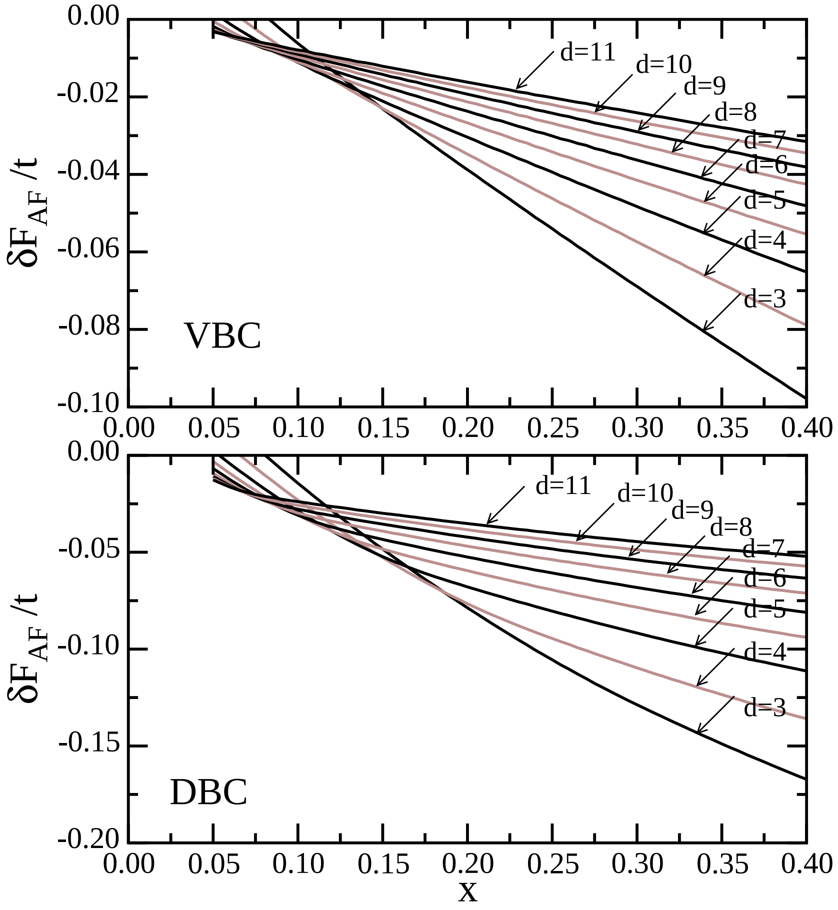

Figure 5.16: Free energy gain of the VBC (top) and DBC (bottom) stripe phases with respect to the AF phase δF_{AF} as a function of doping x, as obtained at the temperature $\beta t = 100$ for the DDH model with $U = 8t$, $J_H = 1.5t$, and $E_z = 0$.

value $\simeq -1$ eV/hole [*cf.* Fig. 2.9(d)] by a factor of 2. Indeed, assuming the effective hopping $t = 0.6$ eV, one obtains $\Delta\mu \simeq -2.2$ (-2.1) eV/hole for $E_z = 0$ $(E_z = t)$, respectively. Therefore, we conclude that either one needs to carry out calculations within more realistic multiband models with oxygen atoms, or the value of the effective hopping is a decreasing function of doping x, which could be ascribed to an increasing disorder in the system.

We proceed now to figure out whether the established results concerning the ground state with the DBC stripe phase as well as doping dependence of ϵ and ν, appear solely in the realistic e_g model or if they are also a common feature of the DDH model with a simplified hopping matrix $t^{\alpha\beta} = -(t/2)\delta_{\alpha\beta}$. Note, that the average bandwidth of the e_g and DDH models is the same, which ensures that for a given U, electrons in both models are approximately equally correlated. Here, we shall set the same value of parameters as we have chosen for the e_g model, i.e.,

	VBC		DBC	
x	d	F/t	d	F/t
0.050	11	3.1095	11	3.1000
0.055	10	3.0912	11	3.0804
0.060	9	3.0729	11	3.0610
0.065	8	3.0547	10	3.0417
0.070	8	3.0364	9	3.0225
0.080	8	3.0001	8	2.9839
0.090	7	2.9636	7	2.9454
0.100	6	2.9269	7	2.9070
0.110	5	2.8902	6	2.8683
0.120	4	2.8538	5	2.8301
0.140	4	2.7807	5	2.7530
0.160	3	2.7077	4	2.6760
0.180	3	2.6347	4	2.5996
0.200	3	2.5626	3	2.5227
0.300	3	2.2129	3	2.1531
0.400	3	1.8809	3	1.8116

Table 5.6: Comparison of the ground state free energy F per site for the VBC and DBC stripe phases as found in the DDH model with $U = 8t$, $J_H = 1.5t$, and $E_z = 0$.

$U = 8t$, $J_H = 1.5t$, and we consider only the $E_z = 0$ case. In addition, we restrict ourselves, due to equivalence of the bands, to the subspace with $\langle o\rangle = \langle p\rangle = 0$.

Fig. 5.16 shows free energy gain of the VBC and DBC stripe phases with respect to the AF phase δF_{AF} as a function of doping x, as obtained at temperature $\beta t = 100$ for the DDH model. First of all, for a fixed doping diagonal structures are again significantly lower in energy than vertical ones (*cf.* also Table 5.6). Moreover, also in this case, we recover here a tendency to gradual crossover towards stripe phases with smaller unit cells upon increasing doping, Note, however, that in contrast to the predictions made within the e_g model, structures with vertical (diagonal) DWs separated by a distance $d \geq 5$ are the lowest energy solutions only in a narrow doping region $x \lesssim 0.12$ ($x \lesssim 0.15$), respectively. Hence, in the DDH model, one observes a fast variation of the optimal distance d which should result in a small optimal stripe filling. Indeed, as depicted in Fig. 5.17, a linear in x segment of the incommensurability ϵ, exceeds the experimental value in LSNO roughly by a factor 2 (1.5) in the case of the VBC (DBC) stripe phase, respectively. Consequently, the optimal stripe filling in the former case is substantially reduced down to $\nu \simeq 0.55$ and in the latter case — down to $\nu \simeq 0.65$ [*cf.* Fig. 5.17(c,d)]. Finally, one finds that the chemical potential in the VBC stripe phase is released already at $x \simeq 0.14$ and at slightly larger doping $x \simeq 0.16$ in the DBC one.

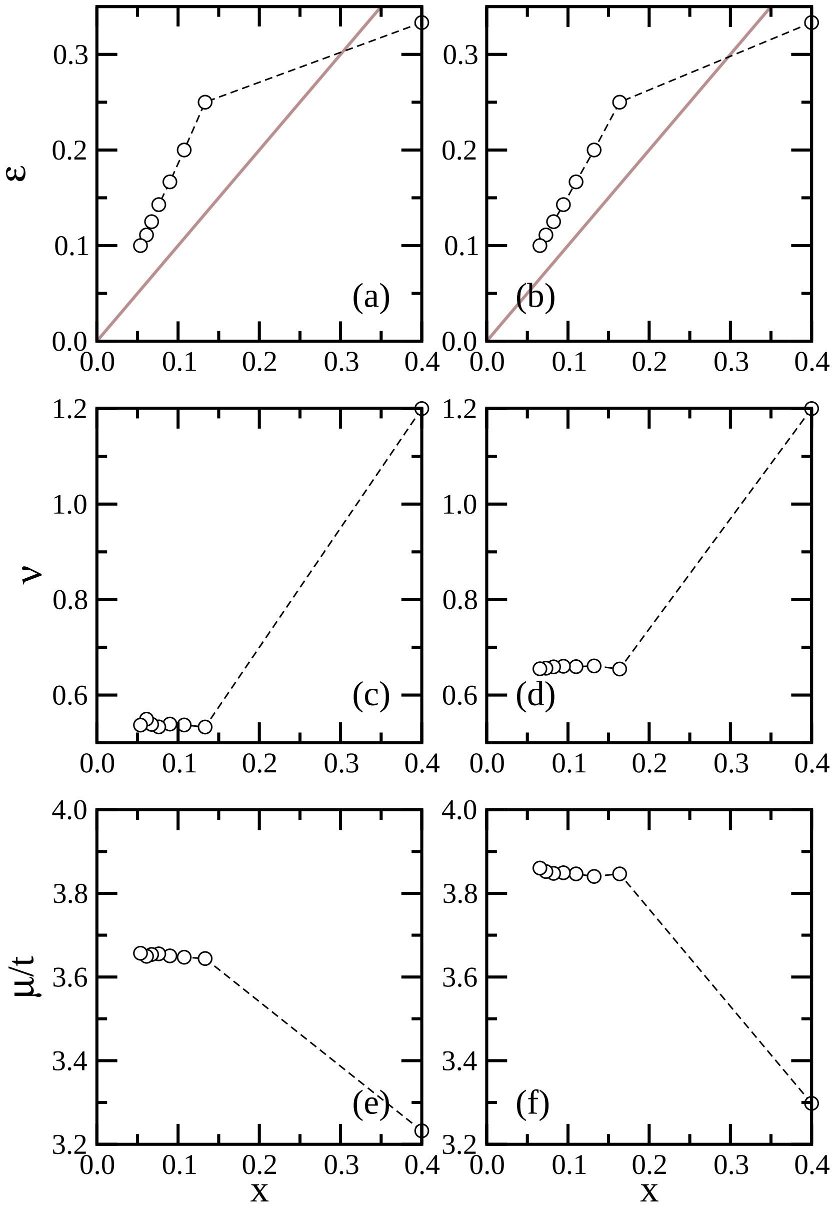

Figure 5.17: Doping dependence of: (a,b) magnetic incommensurability ϵ, (c,d) stripe filling ν, and (e,f) chemical potential μ for the VBC (left) and DBC (right) stripe ground state deduced from Figs. 5.16. Gray solid line in panels (a,b) shows the experimental behavior of ϵ in LSNO.

In order to find out the reason of such a vast discrepancy between the predictions made in the e_g and in the DDH model, let us now investigate closer the properties of idealized filled and half-filled DWs. In particular we shall discuss the local hole density $n_h(l_x)$, local modulated magnetization density $m_\pi(l_x)$, local hole orbital polarization $o_h(l_x)$, and local modulated magnetic orbital polarization

$p_\pi(l_x)$:

$$n_h(l_x) = \sum_\alpha n_{h\alpha}(l_x), \qquad m_\pi(l_x) = (-1)^{l_x}, \sum_{\alpha\sigma} \lambda_\sigma n_{\alpha\sigma}(l_x), \tag{5.72}$$

$$o_h(l_x) = \sum_\alpha \lambda_\alpha n_{h\alpha}(l_x), \qquad p_\pi(l_x) = (-1)^{l_x} \sum_{\alpha\sigma} \lambda_\alpha \lambda_\sigma n_{\alpha\sigma}(l_x), \tag{5.73}$$

where $n_{\alpha\sigma}(l_x)$ is the local orbital charge density,

$$n_{\alpha\sigma}(l_x) = \langle n_{(l_x,0)\alpha\sigma} \rangle, \tag{5.74}$$

whereas $n_{h\alpha}(l_x)$ denotes the local orbital hole density,

$$n_{h\alpha}(l_x) = 1 - \sum_\sigma n_{\alpha\sigma}(l_x). \tag{5.75}$$

Furthermore, important information about the nature of stripe phases is provided by the average local intraorbital double occupancy,

$$D(l_x) = \sum_\alpha n_{\alpha\uparrow}(l_x) n_{\alpha\downarrow}(l_x), \tag{5.76}$$

as well as by two local interorbital double occupancies,

$$D_{xz}^{\sigma\bar{\sigma}}(l_x) = \sum_\sigma n_{x\sigma}(l_x) n_{z\bar{\sigma}}(l_x), \tag{5.77}$$

$$D_{xz}^{\sigma\sigma}(l_x) = \sum_\sigma n_{x\sigma}(l_x) n_{z\sigma}(l_x). \tag{5.78}$$

where $\bar{\sigma} = -\sigma$. To appreciate better the differences between the DDH and e_g model, we compare in Fig. 5.18, local hole $n_h(l_x)$ and modulated magnetization density $m_\pi(l_x)$ of the filled VBC and DBC stripe phase found at temperature $\beta t = 100$ in either model on a 64×64 cluster with $U = 8t$, $J_H = 1.5t$, $E_z = 0$, and $x = 1/8$. For completeness we also show, finite in the e_g model, local hole $o_h(l_x)$ and local modulated magnetic $p_\pi(l_x)$ orbital polarization.

The observed differences, pronounced especially at DWs, follows directly from the fact that each model prefers a different effect helping to reduce double occupancy at those sites. Namely, in the e_g model, large positive $o_h(l_x)$ at DWs means that it is energetically advantageous to optimize the kinetic energy of holes doped into the $|x\rangle$ orbitals, contributing to a wide band. However, in the HA, the only way to optimize the on-site energy is to develop a strong spin polarization which, in turn, would noticeably reduce the kinetic energy gain. On the other hand, one can avoid such disadvantageous suppression by a strong reduction of electron density. This explains clearly larger hole density $n_h(l_x)$ along DWs in the e_g model, as compared to the corresponding value found in the DDH model. Indeed, in the latter case both bands are equivalent, resulting in $o_h(l_x) = p_\pi(l_x) = 0$. Hence this

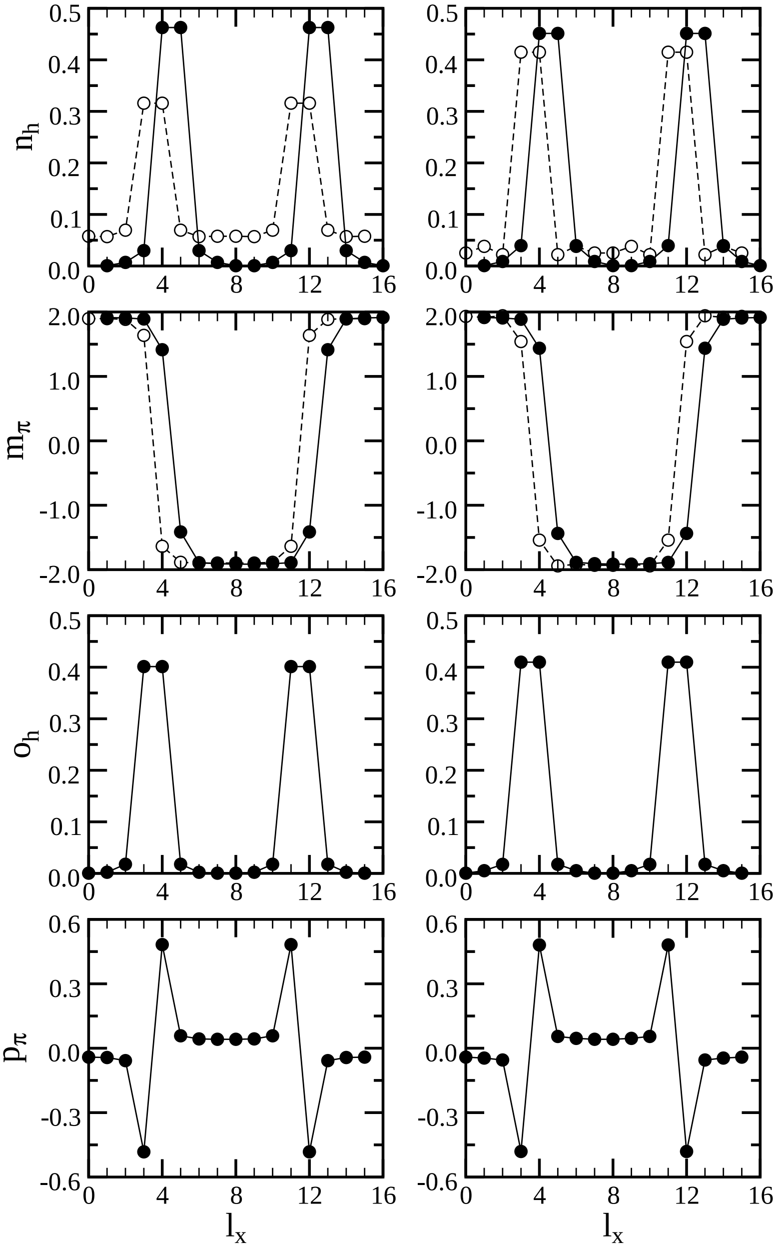

Figure 5.18: Local hole $n_h(l_x)$ (top) and modulated magnetization density $m_\pi(l_x)$ (second row), as well as local hole $o_h(l_x)$ (third row) and local modulated magnetic $p_\pi(l_x)$ orbital polarization (bottom) of the filled VBC (left) and DBC (right) stripe phase found at temperature $\beta t = 100$ in either the DDH (open circles) or e_g (filled circles) model on a 64×64 cluster with $U = 8t$, $J_H = 1.5t$, $E_z = 0$, and $x = 1/8$. For clarity, the e_g results are shifted by one lattice constant from the origin of the coordinate system. In the degenerate Hubbard model $o_h(l_x) = p_\pi(l_x) = 0$.

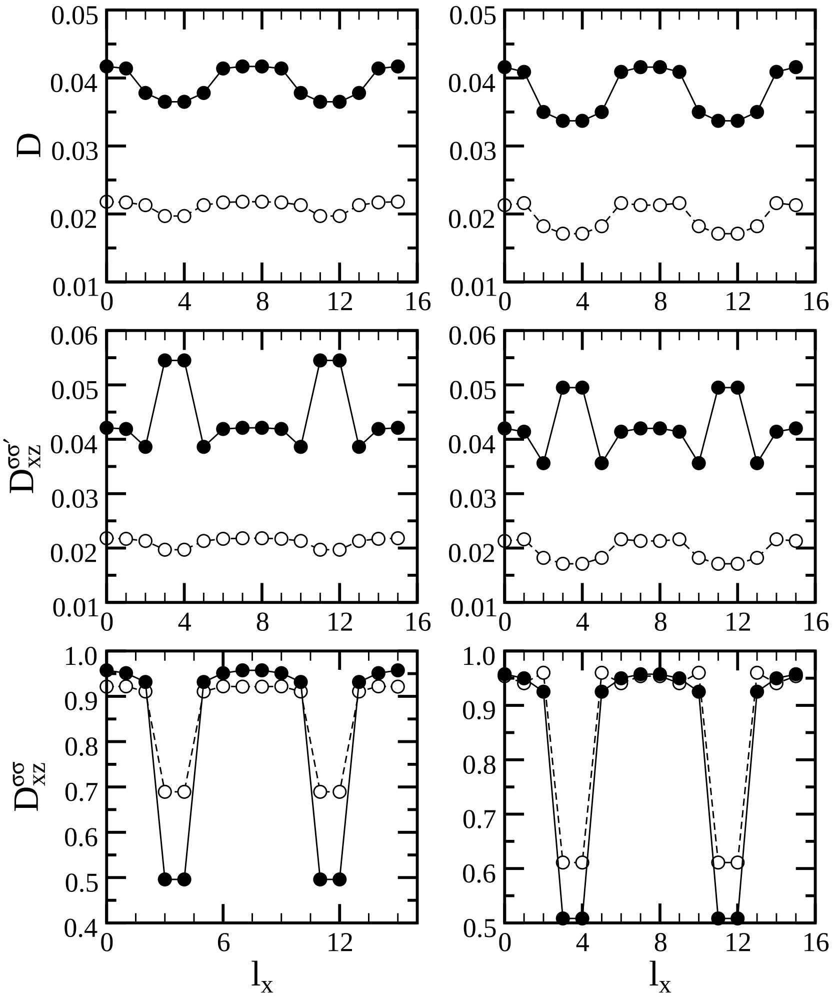

Figure 5.19: Local intraorbital double occupancy $D(l_x)$ (top) and two local interorbital $D_{xz}^{\sigma\bar{\sigma}}(l_x)$ (middle) and $D_{xz}^{\sigma\sigma}(l_x)$ (bottom) double occupancies, of the filled VBC (left) and DBC (right) stripe phase shown in Fig. 5.18. Open (filled) circles denote the results found in the DDH (e_g) model, respectively.

model yields a more localized stripe phase with a larger magnetization $|m_\pi(l_x)|$ at DWs than the one obtained in the e_g model (*cf.* Fig. 5.18).

To verify our conclusion, we show in Fig. 5.19 the average double occupancy (5.76)-(5.78) of the stripe phases shown in Fig. 5.18. Remarkably, in the DDH model (open circles) the on-site energy is predominately optimized by the reduction of the high-energy intraorbital $D(l_x)$ and interorbital $D_{xz}^{\sigma\bar{\sigma}}(l_x)$ double occupancies, so that the system might create even in the low doping regime a large number of DWs in the unit cell and consequently reduce the optimal stripe filling. In contrast, in the e_g model, the Coulomb energy is mainly optimized by the reduction of the low-energy interorbital $D_{xz}^{\sigma\sigma}(l_x)$ double occupancy resulting in a

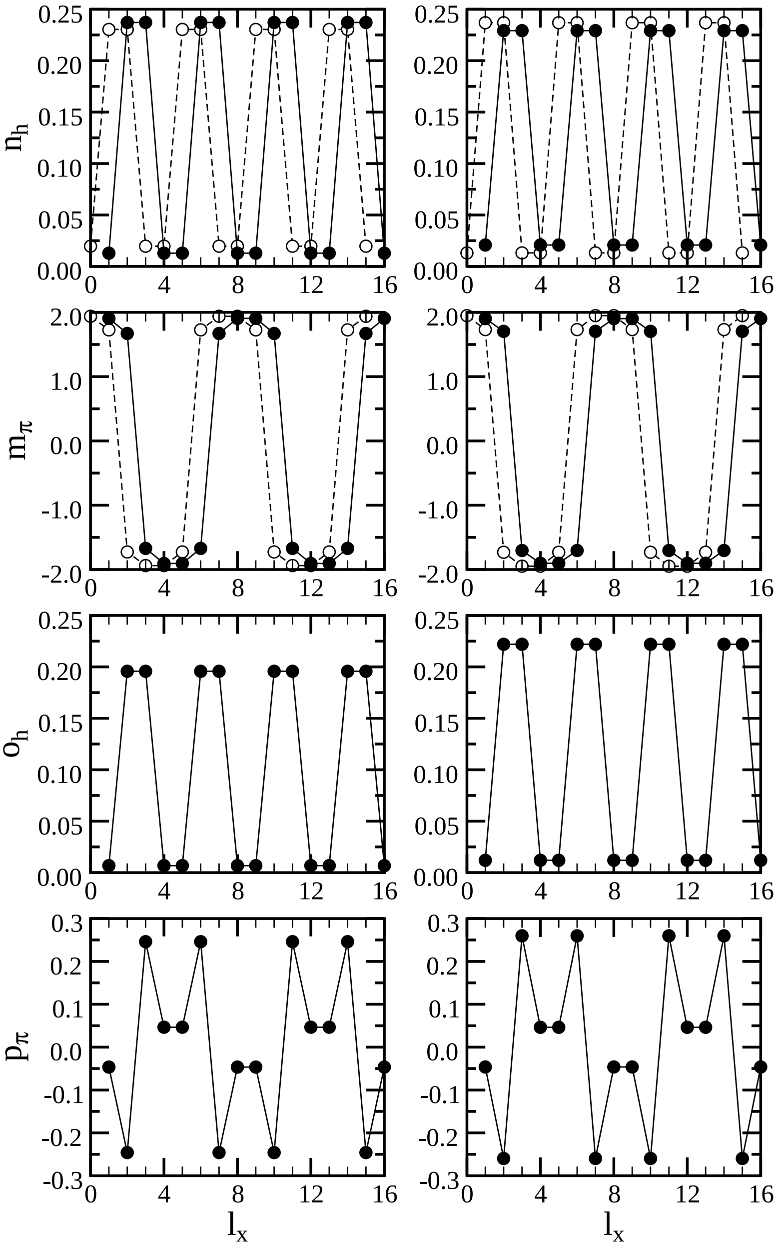

Figure 5.20: Local hole $n_h(l_x)$ (top) and modulated magnetization density $m_\pi(l_x)$ (second row) as well as local hole $o_h(l_x)$ (third row) and local modulated magnetic $p_\pi(l_x)$ orbital polarization (bottom) of the HVBC (left) and HDBC (right) stripe phase found at temperature $\beta t = 100$ in either the DDH (open circles) or e_g (filled circles) model on a 64×64 cluster with $U = 8t$, $J_H = 1.5t$, $E_z = 0$, and $x = 1/8$. For clarity, the e_g results are shifted by one lattice constant from the origin of the coordinate system. In the degenerate Hubbard model $o_h(l_x) = p_\pi(l_x) = 0$.

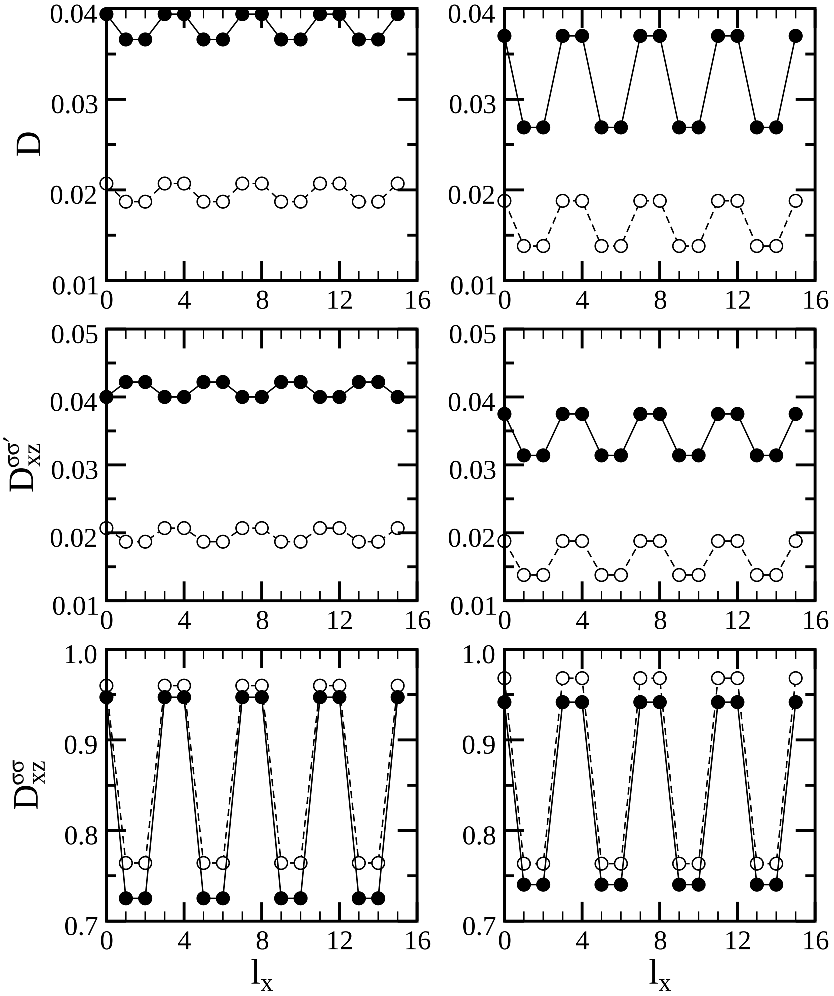

Figure 5.21: Local intraorbital double occupancy $D(l_x)$ (top) and two local interorbital $D_{xz}^{\sigma\bar{\sigma}}(l_x)$ (middle) and $D_{xz}^{\sigma\sigma}(l_x)$ (bottom) double occupancies, of the HVBC (left) and HDBC (right) stripe phase shown in Fig. 5.20. Open (filled) circles denote the results found in the DDH (e_g) model, respectively.

smaller magnetization $|m_\pi(l_x)|$ at DWs as compared to the one found in the DDH model. However, reduced $|m_\pi(l_x)|$ at those sites allows the system to optimize better the kinetic energy gain which apparently overcompensates a large on-site energy only when the optimal filling is close to one hole/Ni site, meaning that for a given doping level, the DWs should be separated by a larger distance as compared to predictions made in the DDH model. On the other hand, a robust stability of the DBC stripe phases with respect the VBC ones, has the origin in a better optimization, by the former, of all double occupancies (5.76)-(5.78).

For completeness, in Fig. 5.20 we compare hole- $n_h(l_x)$ and spin- $m_\pi(l_x)$ density profile of a half-filled vertical bond-centered (HVBC) stripe with a corresponding

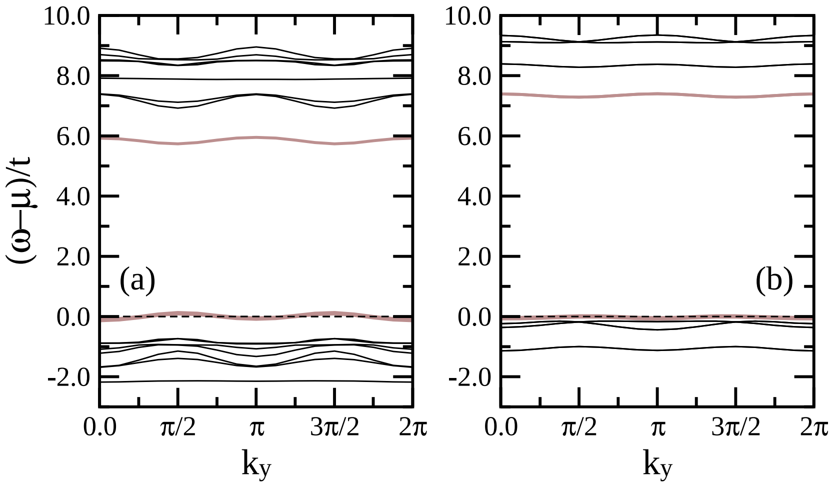

Figure 5.22: Band structure of the HVBC stripe phase as a function of parallel momentum k_y, calculated from the unit cell shown in Fig. 4.1(a) at temperature $\beta t = 50$ either in the e_g (a) or DDH (b) model on a 8×16 cluster with $U/t = 8$, $J_H = 1.5t$, $E_z = 0$, and $x = 1/8$. Black (gray) line corresponds to the bulk (mid-gap) bands, respectively, whereas the dashed line indicates the Fermi level, and show that the lower mid-gap states are partly filled.

profile of a half-filled diagonal bond-centered (HDBC) stripe. Even though the overall shape of the DWs looks very much the same in both models, a larger magnetization $|m_\pi(l_x)|$ at DWs is again found within the DDH Hamiltonian which follows from larger interorbital $D^{\sigma\sigma}_{xz}(l_x)$ double occupancy (*cf.* Fig. 5.21) promoting, due to finite Hund's exchange $J_H = 0.15t$, the on-site high-spin states. In fact, different values of $m_\pi(l_x)$ at these sites has severe consequences for the band structure of the HVBC stripes in both models, shown in Fig. 5.22. First of all, note that due to the AF spin modulation along the BC DWs, one finds a distinct gap between two mid-gap states lying within the Mott-Hubbard gap. Remarkably, the lower mid-gap state is localized just above the LHB in the DDH model, wheraes it is clearly separated, due to smaller on-wall $m_\pi(l_x)$, by a real gap from the LHB in the e_g model. Therefore, in the former it is possible to fill up also the low-lying mid-gap states explaining the reason of substantial suppression of the optimal stripe filling in the DDH model, the situation which is avoided in the e_g model, promoting filled stripes.

The above important difference is also well seen in the DOS, depicted in Fig. 5.23. Fig. 5.23(a) [Fig. 5.23(b)] shows density of states $N_\alpha(\omega)$ (5.70), projected on the orbital $|x\rangle$ ($|z\rangle$), respectively. The corresponding total density of states $N(\omega)$ is shown in Fig. 5.23(c). Here, one finds that the mid-gap bands are formed mainly by the $|x\rangle$ states, which optimizes the kinetic energy of holes doped into the $|x\rangle$ orbitals, whereas the vast majority of the $|z\rangle$ states belongs to the

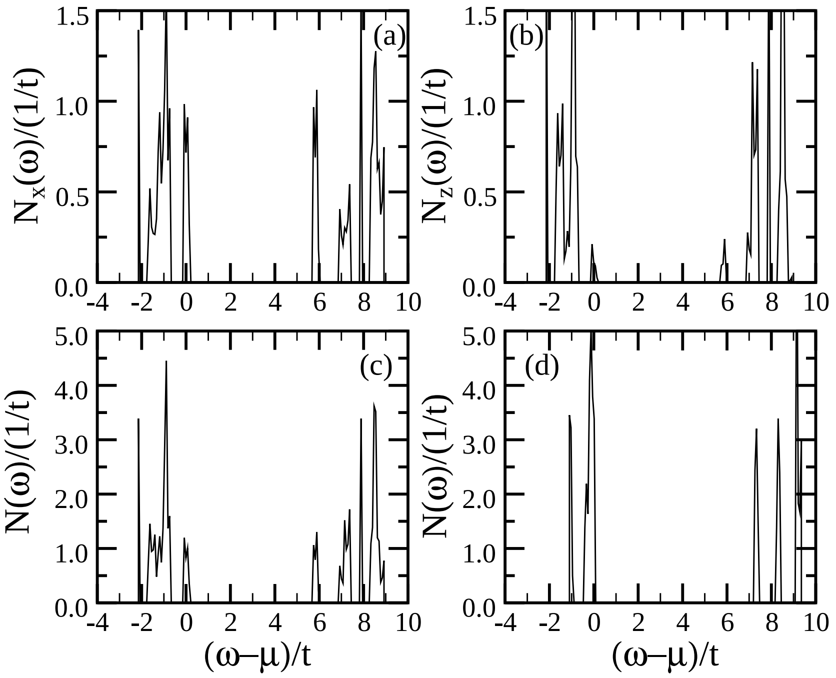

Figure 5.23: Partial densities of states $N_\alpha(\omega)$: (a) projected on $|x\rangle$ orbital, and (b) projected on $|z\rangle$ orbital, as well as (c) total density of states $N(\omega)$ for the HVBC stripe phase obtained in the e_g model. Panel (d) shows for comparison $N(\omega)$ as found in the HVBC stripe phase within in the DDH model. Parameters as in Fig. 5.20

Hubbard bands. In contrast, in the DDH model the lower mid-gap states overlap with the LHB [*cf.* Fig. 5.23(d)].

We summarize our key results in Table 5.7, where we compare the free energy of both the filled and half-filled BC stripe phases, found either in the e_g or DDH model. In the realistic e_g model, one observes a generic tendency to promoting filled stripes over the half-filled ones (*cf.* Table 5.7). Most imoportantly, for the parameters relevant for LSNO, one finds as the lowermost phase experimentally observed *filled* diagonal stripes. In contrast, even though the DDH model with two equivalent orbitals clearly favors diagonal DWs, it stabilizes the *half-filled* diagonal stripes.

In fact, our systematic studies of stripe phases, within the model with e_g orbitals, separated by different lattice spacing varying from $d = 3$ to $d = 11$, have revealed that, in the doping regime where $\epsilon \simeq x$, i.e., for $x \leq 0.2$, the optimal stripe filling in the true ground state is slightly less ($0.86 \leq \nu \leq 0.89$ hole/Ni, depending on the crystal field splitting) than the experimental value of one hole/Ni ion. Nevertheless, we argue that only a realistic model including two e_g orbitals with different hopping elements inducing finite orbital polarization provides a correct

e_g model		DDH model	
phase	F/t	phase	F/t
HDBC	2.5759	VBC	2.8395
HVBC	2.5756	HVBC	2.8354
VBC	2.5629	DBC	2.8172
DBC	2.5508	HDBC	2.8135

Table 5.7: Comparison of the free energy F for the BC stripe phases as obtained at temperature $\beta t = 100$ either in the e_g or DDH model on a 64×64 cluster with $U = 8t$, $J_H = 1.5t$, $E_z = 0$, and $x = 1/8$.

description of doped NiO_2 planes in layered nickelates.

Finally, in Chapter 3 we have seen that in the single-band Peierls-Hubbard model, strong electron-lattice coupling might tip the balance between vertical and diagonal DWs clearly stabilizing the former (*cf.* Fig. 3.14). This is a particularly intriguing question in the light of arguments indicating that LSNO is strongly localized primarily due to a large effect of the electron-lattice coupling [138], whereas neutron scattering experiments suggest that DWs run diagonally across the NiO_2 planes [14, 15, 24–29]. However, it should be emphasized that the realistic e_g model is qualitatively different from the DDH model, in which, by analogy with the results found in the single-band Peierls-Hubbard model, one would also expect stabilization of the vertical DWs in the presence of the Peierls coupling. Hence, a finite electron-lattice coupling in the e_g model does not necessarily have to stabilize vertical DWs, explaining the discrepancy between the theory and experimental findings. This situation suggests that further studies are needed to establish a definite answer to this question.

Chapter 6

Summary and conclusions

The aim of this Thesis was first and foremost to understand the properties of stripe phases and to determine the reasons of differences between the doped layered cuprates and the nickelates. In order to get an insight into the above important questions, we have used two *realistic* models: (i) an extended hopping single-band Hubbard model (t-t'-U) for the cuprates and (ii) a two-band model with the e_g orbitals as appropriate for the nickelates.

First, in Chapter 3, motivated by the pioneering works [5–9] we investigated, using the HA, the relative stability of the filled vertical/horizontal and diagonal stripe phases and discussed the role of finite lattice anisotropy, next-neighbor hopping t', nearest-neighbor Coulomb interaction V, and finally the influence of static Peierls electron-lattice coupling. In particular, it has been found that stripe order always selects the direction of DW's along a smaller hopping direction in the anisotropic model, and that both repulsive V ($V > 0$) and negative t' ($t'/t < 0$), which correspond to the realistic parameters of the superconducting cuprates, enhance the relative stability of the diagonal stripes. Furthermore, we have shown that even such a simple method as the HA is sufficient to demonstrate the solitonic mechanism which primarily stabilizes stripes owing to the hopping perpendicular to the direction of DW's and allows to draw qualitative conclusions about the possible phases. Interestingly, we have found that the static Peierls electron-lattice coupling stabilizes vertical DW's by the bond contractions, especially pronounced on the bonds which connect DW atoms with their neighbors in the transverse direction. They lead to a stronger relative enhancement of the local hopping elements and consequently to a larger kinetic energy gain as compared to the case of diagonal DW's. Next, guided by the observation that the negative t' ($t'/t < 0$) yields a positive kinetic energy and hence its contribution is reduced by expelling holes from the AF domains and reinforcing the stripe order, we have stabilized a half-filled stripe phase involving an on-wall SDW. We argue that such phase not only easily accommodates holes, but also redistributes them around DW's in such manner that the kinetic energy associated with next-neighbor hopping becomes negative despite negative t' and consequently, it takes over in the regime of $t'/t \simeq -0.3$.

In Chapter 4 we reviewed the SRI SB representation of the Hubbard model and have introduced the reciprocal space representation, used in the investigation of stripe phase stability in this Thesis. Having presented the theoretical framework, we then proceeded with an analysis of stability of the idealized filled as well as the half-filled stripes in the t-t'-U model at the doping $x = 1/8$ and have shown that the negative next-neighbor hopping ($t'/t < 0$) favors the latter. We have also emphasized the role a proper treatment of strong electron correlations by comparing the SB charge and spin density profiles with the ones obtained in the HA. With this knowledge of general features of the stripe phases, we have performed a systematic studies of an array of stripe phases by considering variable length of the unit cell. Our findings obtained in t-t'-U model within the SBA agree qualitatively with the experimental data concerning the cuprates and reveal a strong influence of the next-neighbor hopping t' on the optimal filling of DW's. In particular, we have found that the stability of the half-filled DW's, as established in LSCO and Nd-LSCO, requires taking $t'/t < -0.15$. Finally, we have analyzed the melting of stripes in the overdoped regime $x \geq 0.3$. The numerical result that spin and charge order disappear simultaneously led us to the conclusion that the stripe order is a common charge-and-spin instability.

Once we understood the competition between various stripe phases in the t-t'-U model, we considered, in Chapter 5, a degenerated model with two e_g electrons in order to establish the role of the second orbital in stabilizing filled DW's in the nickelates. First, in order to understand better the electronic structure and intersite correlations, we solved exactly a two-site molecule with either e_g or t_{2g} orbitals at quarter-filling and found that the phenomenon of a complementary behavior of the spin and orbital flavors is also a characteristic feature of this model. Next, we addressed the occurrence of orbitally polarized states due to the inequivalent orbitals, and their interplay with FM and AF spin order in the HA, and demonstrated that finite Hund's exchange coupling J_H significantly stabilizes the former order. Having discussed the properties of phases with small unit cells, we have proceeded with applying the reciprocal space representation to the BC stripe phase which is a good candidate for a ground state of the model with finite J_H due to FM order on the rungs. Using the HA we have shown that the filled diagonal BC stripes observed in the nickelates appear naturally within the effective model for e_g electrons, whereas a simplified DDH model, yields instead half-filled DW's in the ground state and hence cannot reproduce the experimental data.

Summarizing, we have developed a simple but powerful approach which allows one to investigate the various stripe phases with a large unit cell and carry out the calculation on large (up to 144×144) clusters. Consequently, our method provides a unique opportunity to study strong changes induced by doping in the electronic structure of a system with DW's. Moreover, it allows us to obtain unbiased results at the low temperature $\beta t = 100$ as well as to eliminate the role of finite size effects. Therefore, the stripe phases found in the present approach are stabilized not due to particular boundary conditions, but they represent a generic feature of the doped strongly correlated electron systems.

At the end, let us address briefly a few problems which remain interesting and timely topics in this field. One of them is to establish the influence of charged impurities on stripe phases. It has been found that the system with DW's is extremely sensitive to the presence of charged impurities and the stripe order is suppressed at sufficiently large impurity concentration, although it can persist in some part of the cluster [206]. In fact, a possible mechanism of destructive influence of the disorder on the stability of DW's could by easily investigated in the present approach by adding a random potential. Furthermore, it would be interesting to examine whether a finite static Peierls electron-lattice coupling in the model with two e_g orbitals stabilizes vertical DW's, as the effective single-band model does, or if it promotes diagonal DW's observed in the layered nickelates. Finally, further studies are needed to establish to what extent, results found within the effective e_g model and the predictions made out of a more realistic multiband model remain in qualitative agreement.

Appendix A

Useful formulas of the SRI SB representation

A.1 Spin density vector

Here we prove the formula for the spin density vector in terms of SB operators,

$$\mathbf{S} = \sum_{\sigma\sigma'\sigma_1} \boldsymbol{\tau}_{\sigma\sigma'} p^\dagger_{\sigma\sigma_1} p_{\sigma_1\sigma'} = \frac{1}{2}\big(p_0^\dagger \bar{\mathbf{p}} + \bar{\mathbf{p}}^\dagger p_0 - i\bar{\mathbf{p}}^\dagger \times \bar{\mathbf{p}}\big). \tag{A.1}$$

Substitution the expression (4.3) for $p_{\sigma\sigma'}$ into (A.1) gives,

$$\sum_{\sigma\sigma'\sigma_1} \boldsymbol{\tau}_{\sigma\sigma'} p^\dagger_{\sigma\sigma_1} p_{\sigma_1\sigma'} = \frac{1}{4}\sum_{\sigma\sigma'\sigma_1} \boldsymbol{\tau}_{\sigma\sigma'}\big(p_0^\dagger \tau_{0,\sigma\sigma_1} + \mathbf{p}^\dagger \boldsymbol{\tau}_{\sigma\sigma_1}\big)\big(p_0 \tau_{0,\sigma_1\sigma'} + \mathbf{p}\boldsymbol{\tau}_{\sigma_1\sigma'}\big). \tag{A.2}$$

A straightforward multiplication yields,

$$\sum_{\sigma\sigma'\sigma_1} \boldsymbol{\tau}_{\sigma\sigma'} p^\dagger_{\sigma\sigma_1} p_{\sigma_1\sigma'} = \frac{1}{4}\sum_{\sigma\sigma'} \boldsymbol{\tau}_{\sigma\sigma'}\Big[\sum_\mu p^\dagger_\mu p_\mu \delta_{\sigma\sigma'} + \mathbf{n}\cdot\boldsymbol{\tau}_{\sigma\sigma'}\Big], \tag{A.3}$$

$$\mathbf{n} = p_0^\dagger \mathbf{p} + \mathbf{p}^\dagger p_0 + i\big(\mathbf{p}^\dagger \times \mathbf{p}\big), \tag{A.4}$$

where we used the relation,

$$\big(\mathbf{A}\cdot\boldsymbol{\tau}_{\sigma\sigma_1}\big)\big(\mathbf{B}\cdot\boldsymbol{\tau}_{\sigma_1\sigma'}\big) = \mathbf{A}\cdot\mathbf{B} + i\big(\mathbf{A}\times\mathbf{B}\big)\cdot\boldsymbol{\tau}_{\sigma\sigma'}. \tag{A.5}$$

Now, we can leave out the first term on the right hand side of (A.3) due to the fact that Pauli matrices are traceless: $\sum_{\sigma\sigma'} \boldsymbol{\tau}_{\sigma\sigma'}\delta_{\sigma\sigma'} = 0$, and multiply Pauli matrices in the remaining term separately for each direction $\alpha = x, y, z$,

$$n_\alpha \sum_{\sigma\sigma'} \tau_{\alpha,\sigma\sigma'}\tau_{\alpha,\sigma\sigma'} = \pm n_\alpha \sum_{\sigma\sigma'} \tau_{\alpha,\sigma\sigma'}\big(\tau_{\alpha,\sigma\sigma'}\big)^{\mathrm{T}} = \pm 2 n_\alpha. \tag{A.6}$$

The upper sign refers to x and z, whereas the lower — to y direction. The last step is to introduce a new operator $\bar{\mathbf{p}} = (p_1, -p_2, p_3)$, which allows to write the final result in a compact form (A.1), in which we took into account that $\big(\mathbf{p}\times\mathbf{p}\big)_\alpha = \mp\big(\bar{\mathbf{p}}\times\bar{\mathbf{p}}\big)_\alpha$, with the sign convention as in (A.6).

A.2 Kinetic energy renormalization operator

It is convenient to express the spin matrix $\underline{z}$,

$$\underline{z} = (e^\dagger \underline{p} + \underline{\tilde{p}}^\dagger d) \frac{\sqrt{1 + e^\dagger e + d^\dagger d + \sum_\mu p_\mu^\dagger p_\mu}}{\sqrt{(1 - d^\dagger d)\underline{\mathcal{I}}_0 - 2\underline{p}^\dagger \underline{p}}\sqrt{(1 - e^\dagger e)\underline{\mathcal{I}}_0 - 2\underline{\tilde{p}}^\dagger \underline{\tilde{p}}}}, \tag{A.7}$$

in terms of its mean-field eigenvalues. However, in order to proceed one needs to determine the eigenvalues of the matrix $\underline{p}$. They are: $p_{1,2} = \frac{1}{2}(p_0 \pm p)$. Therefore, the eigenvalues $z_{1,2}$ and the corresponding eigenvectors $\chi_{1,2}$ of the matrix $\underline{z}$ are given by,

$$\begin{aligned} z_1 &= \frac{1}{\sqrt{2}} \frac{e(p_0 + p) + d(p_0 - p)}{\sqrt{1 - d^2 - \frac{1}{2}(p_0 + p)^2}\sqrt{1 - e^2 - \frac{1}{2}(p_0 - p)^2}}, \quad & \chi_1 &= \frac{1}{\sqrt{2}} \begin{pmatrix} 1 \\ e^{i\Phi} \end{pmatrix}, \\ z_2 &= \frac{1}{\sqrt{2}} \frac{e(p_0 - p) + d(p_0 + p)}{\sqrt{1 - d^2 - \frac{1}{2}(p_0 - p)^2}\sqrt{1 - e^2 - \frac{1}{2}(p_0 + p)^2}}, \quad & \chi_2 &= \frac{1}{\sqrt{2}} \begin{pmatrix} -e^{-i\Phi} \\ 1 \end{pmatrix}, \end{aligned} \tag{A.8}$$

where the angle Φ describes a regular twist of the spin quantization axis.

On the other hand, matrix $\underline{z}$ can be diagonalized by means of a similarity tranformation,

$$\begin{pmatrix} z_1 & 0 \\ 0 & z_2 \end{pmatrix} = \underline{P}^{-1} \underline{z} \underline{P}, \tag{A.9}$$

specified by its eigenvectors,

$$\underline{P} = \frac{1}{\sqrt{2}} \begin{pmatrix} 1 & -e^{-i\Phi} \\ e^{i\Phi} & 1 \end{pmatrix}. \tag{A.10}$$

Hence, one can express $\underline{z}$ in terms of its eigenvalues by applying the inverse similarity tranformation,

$$\underline{z} = \underline{P} \begin{pmatrix} z_1 & 0 \\ 0 & z_2 \end{pmatrix} \underline{P}^{-1} = \begin{pmatrix} z_+ & z_- e^{-i\Phi} \\ z_- e^{i\Phi} & z_+ \end{pmatrix}, \tag{A.11}$$

with,

$$z_+ = \frac{z_1 + z_2}{2}, \qquad z_- = \frac{z_1 - z_2}{2}. \tag{A.12}$$

Appendix B

Papers of the author

1. M. Raczkowski, *Magnetic and orbital ordering in doped manganites*, in: Lectures on the Physics of Highly Correlated Electron Systems VI, edited by F. Mancini, AIP Conference Proceedings Vol. **629**, New York, 2002, p. 203.

2. M. Raczkowski and A. M. Oleś, *Spin stiffness and quantum fluctuations in C–type and A–type aniferromagnets*, Phys. Rev. B **66**, 094431 (2002).

3. M. Raczkowski, B. Normand, and A. M. Oleś, *Vertical and diagonal stripes in the extended Hubbard model*, Phys. Stat. Sol. (b) **236**, 376 (2003).

4. M. Raczkowski and A. M. Oleś, *Vertical stripes stabilized by the Peierls coupling*, Physica C **387**, 82 (2003).

5. M. Raczkowski and A. M. Oleś, *Competition between vertical and diagonal stripe phases in the HF approximation*, in: Lectures on the Physics of Highly Correlated Electron Systems VII, edited by A. Avella and F. Mancini, AIP Conference Proceedings Vol. **678**, New York, 2003, p. 293.

6. R. Frésard, M. Raczkowski, and A. M. Oleś, *Interplay of orbitally polarized and magnetically ordered phases in doped transition metal oxides* , Phys. Stat. Sol. (b) **242**, 370 (2005).

7. M. Raczkowski, A. M. Oleś, and R. Frésard, *Mean-field phase diagram of interacting* e_g *electrons*, Physica B **359-361**, 672 (2005).

8. M. Raczkowski, R. Frésard, and A. M. Oleś, *Melting of the stripe phases in the* t-t'-U *Hubbard model*, Physica B **359-361**, 780 (2005).

9. M. Raczkowski, A. M. Oleś, and R. Frésard, *Half-filled stripes in the* t-t'-U *Hubbard model*, submitted to Phys. Stat. Sol. (c).

Bibliography

[1] M. Imada, A. Fujimori, and Y. Tokura, Rev. Mod. Phys. **70**, 1039 (1998).

[2] S. Maekawa, T. Tohyama, S. E. Barnes, S. Ishihara, W. Koshibae, and G. Khaliullin, *Physics of Transition Metal Oxides*, Springer Verlag, Berlin 2004.

[3] A. M. Oleś, Acta Phys. Polon. B **31**, 2963 (2000).

[4] A. H. Castro Neto and C. Morais Smith, `cond-mat/0304094`.

[5] J. Zaanen and O. Gunnarsson, Phys. Rev. B **40**, 7391 (1989).

[6] D. Poilblanc and T. M. Rice, Phys. Rev. B **39**, 9749 (1989).

[7] H. J. Schulz, J. Phys. (Paris) **50**, 2833 (1989); *ibid.* Phys. Rev. Lett. **64**, 1445 (1990).

[8] M. Kato, K. Machida, H. Nakanishi, and M. Fujita, J. Phys. Soc. Jpn. **59** 1047 (1990).

[9] M. Inui and P. B. Littlewood, Phys. Rev. B **44**, 4415 (1991).

[10] O. Zachar, S. A. Kivelson, and V. J Emery, Phys. Rev. B **57** 1422 (1998); J. Zaanen, Physica C **317** 217 (1999).

[11] S. A. Kivelson and V. J. Emery, Synth. Metals **80**, 151 (1996).

[12] U. Löw, V. J. Emery, K. Fabricius, S. A. Kivelson, Phys. Rev. Lett. **72**, 1918 (1994).

[13] J. M. Tranquada, B. J. Sternlieb, J. D. Axe, Y. Nakamura, and S. Uchida, Nature **375**, 561 (1995).

[14] V. Sachan, D. J. Buttrey, J. M. Tranquada, J. E. Lorenzo, and G. Shirane, Phys. Rev. B **51**, 12742 (1995).

[15] J. M. Tranquada, D. J. Buttrey, and V. Sachan, Phys. Rev. B **54**, 12318 (1996).

[16] C. N. A. van Duin and J. Zaanen, Phys. Rev. Lett. **80**, 1513 (1998).

[17] S. R. White and D. J. Scalapino, Phys. Rev. Lett. **80**, 1272 (1998).

[18] J. M. Tranquada, J. D. Axe, N. Ichikawa, Y. Nakamura, S. Uchida, and B. Nachumi, Phys. Rev. B **54**, 7489 (1996).

[19] J. M. Tranquada, J. D. Axe, N. Ichikawa, A. R. Moodenbaugh, Y. Nakamura, and S. Uchida, Phys. Rev. Lett. **78**, 338 (1997).

[20] N. Ichikawa, S. Uchida, J. M. Tranquada, T. Niemöller, P. M. Gehring, S.-H. Lee, and J. R. Schneider, Phys. Rev. Lett. **85**, 1738 (2000).

[21] P. M. Singer, A. W. Hunt, A. F. Cederström, and T. Imai, Phys. Rev. B **60**, 15345 (1999).

[22] S. Wakimoto, R. J. Birgeneau, Y. Fujimaki, N. Ichikawa, T. Kasuga, Y. J. Kim, K. M. Kojima, S.-H. Lee, H. Niko, J. M. Tranquada, S. Uchida, and M. von Zimmermann, Phys. Rev. B **67**, 184419 (2003).

[23] K. Yamada, C. H. Lee, K. Kurahashi, J. Wada, S. Wakimoto, S. Ueki, H. Kimura, Y. Endoh, S. Hosoya, G. Shirane, R. J. Birgeneau, M. Greven, M. A. Kastner, and Y. J. Kim, Phys. Rev. B **57**, 6165 (1998).

[24] S.-H. Lee and S-W. Cheong, Phys. Rev. Lett. **79**, 2514 (1997).

[25] H. Yoshizawa, T. Kakeshita, R. Kajimoto, T. Tanabe, T. Katsufuji, and Y. Tokura, Phys. Rev. B **61**, R854 (2000).

[26] R. Kajimoto, T. Kakeshita, H. Yoshizawa, T. Tanabe, T. Katsufuji, and Y. Tokura, Phys. Rev. B **64**, 144432 (2001).

[27] S.-H. Lee, J. M. Tranquada, K. Yamada, D. J. Buttrey, Q. Li, and S.-W. Cheong, Phys. Rev. Lett. **88**, 126401 (2002).

[28] P. G. Freeman, A. T. Boothroyd, and D. Prabhakaran, D. González, and M. Enderle, Phys. Rev. B **66**, 212405 (2002).

[29] R. Kajimoto, K. Ishizaka, H. Yoshizawa, and Y. Tokura, Phys. Rev. B **67**, 014511 (2003).

[30] S. R. White and D. J. Scalapino, Phys. Rev. B **60**, R753 (1999).

[31] G. Seibold, E. Sigmund, and V. Hizhnyakov, Phys. Rev. B **57**, 6937 (1998).

[32] G. Seibold, C. Castellani, C. Di Castro, and M. Grilli, Phys. Rev. B **58**, 13506 (1998).

[33] G. Seibold and J. Lorenzana, Phys. Rev. B **69**, 134513 (2004).

[34] D. Góra, K. Rościszewski, and A. M. Oleś, Phys. Rev. B **60**, 7429 (1999).

[35] T. Tohyama, S. Nagai, Y. Shibata, and S. Maekawa, Phys. Rev. Lett. **82**, 4910 (1999).

[36] P. Wróbel and R. Eder, Phys. Rev. B **62**, 4048 (2000).

[37] M. Fleck, A. I. Lichtenstein, E. Pavarini, and A. M. Oleś, Phys. Rev. Lett. **84**, 4962 (2000).

[38] M. G. Zacher, R. Eder, E. Arrigoni, and W. Hanke, Phys. Rev. Lett. **85**, 2585 (2000); *ibid.* Phys. Rev. B **65**, 045109 (2002).

[39] F. Becca, L. Capriotti, and S. Sorella, Phys. Rev. Lett. **87**, 167005 (2001).

[40] J. Riera, Phys. Rev. B **64**, 104520 (2001).

[41] S. A. Kivelson, I. P. Bindloss, E. Fradkin, V. Oganesyan, J. M. Tranquada, A. Kapitulnik, and C. Howald, Rev. Mod. Phys. **75**, 1201 (2003).

[42] A. Damascelli, Z. Hussain, and Z.-X. Shen, Rev. Mod. Phys. **75**, 473 (2003).

[43] G. B. Teitel'baum, B. Büchner, and H. de Gronckel, Phys. Rev. Lett. **84**, 2949 (2000).

[44] H.-H. Klauss, W. Wagener, M. Hillberg, W. Kopmann, H. Walf, F. J. Litterst, M. Hücker, and B. Büchner, Phys. Rev. Lett. **85**, 4590 (2000).

[45] M. Fujita, H. Goka, K. Yamada, and M. Matsuda, Phys. Rev. Lett. **88**, 167008 (2002).

[46] H. Kimura, Y. Noda, H. Goka, M. Fujita, K. Yamada, M. Mizumaki, N. Ikeda, and H. Ohsumi, Phys. Rev. B **70**, 134512 (2004).

[47] M. Fujita, H. Goka, K. Yamada, J. M. Tranquada, and L. P. Regnault, Phys. Rev. B **70**, 104517 (2004).

[48] S. Wakimoto, G. Shirane, Y. Endoh, K. Hirota, S. Ueki, K. Yamada, R. J. Birgeneau, M. A. Kastner, Y. S. Lee, P. M. Gehring, and H. S. Lee, Phys. Rev. B **60**, R769 (1999).

[49] S. Wakimoto, R. J. Birgeneau, M. A. Kastner, Y. S. Lee, R. Erwin, P. M. Gehring, S. H. Lee, M. Fujita, K. Yamada, Y. Endoh, K. Hirota, and G. Shirane, Phys. Rev. B **61**, 3699 (2000).

[50] M. Fujita, K. Yamada, H. Hiraka, P. M. Gehring, S. H. Lee, S. Wakimoto, and G. Shirane, Phys. Rev. B **65**, 064505 (2002).

[51] N. Hasselmann, A. H. Castro Neto, and C. Morais Smith, Phys. Rev. B **69**, 014424 (2004).

[52] M. Matsuda, Y. S. Lee, M. Greven, M. A. Kastner, R. J. Birgeneau, K. Yamada, Y. Endoh, P. Böni, S.-H. Lee, S. Wakimoto, and G. Shirane, Phys. Rev. B **61**, 4326 (2000).

[53] M. Matsuda, M. Fujita, K. Yamada, R. J. Birgeneau, M. A. Kastner, H. Hiraka, Y. Endoh, S. Wakimoto, and G. Shirane, Phys. Rev. B **62**, 9148 (2000).

[54] M. Matsuda, M. Fujita, K. Yamada, R. J. Birgeneau, Y. Endoh, and G. Shirane, Phys. Rev. B **65**, 134515 (2002).

[55] A. W. Hunt, P. M. Singer, K. R. Thurber, and T. Imai, Phys. Rev. Lett. **82**, 4300 (1999).

[56] Y. Ando, K. Segawa, S. Komiya, and A. N. Lavrov, Phys. Rev. Lett. **88**, 137005 (2002).

[57] M. Dumm, S. Komiya, Y. Ando, and D. N. Basov, Phys. Rev. Lett. **91**, 077004 (2003).

[58] B. O. Wells, Y. S. Lee, M. A. Kastner, R. J. Christanson, R. J. Birgeneau, K. Yamada, Y. Endoh, and G. Shirane, Science **277**, 1067 (1997); Y. S. Lee, R. J. Birgeneau, M. A. Kastner, Y. Endoh, S. Wakimoto, K. Yamada, R. W. Erwin, S.-H. Lee, and G. Shirane, Phys. Rev. B **60**, 3643 (1999).

[59] K. Hirota, K. Yamada, I. Tanaka, and H. Kojima, Physica B **241**, 817 (1998).

[60] H. Kimura, K. Hirota, H. Matsushita, K. Yamada, Y. Endoh, S.-H. Lee, C. F. Majkrzak, R. Erwin, G. Shirane, M. Greven, Y. S. Lee, M. A. Kastner, and R. J. Birgeneau, Phys. Rev. B **59**, 6517 (1999); J. M. Tranquada, N. Ichikawa, K. Kakurai, and S. Uchida, J. Phys. Chem. Solids **60**, 1019 (1999).

[61] P. Dai, H. A. Mook, R. D. Hunt, and F. Doğan, Phys. Rev. B **63**, 054525 (2001).

[62] J. L. Tallon, C. Bernhard, H. Shaked, R. L. Hitterman, and J. D. Jorgensen, Phys. Rev. B **51**, 12911 (1995).

[63] P. Dai, H. A. Mook, and F. Doğan, Phys. Rev. Lett. **80**, 1738 (1998).

[64] H. A. Mook, P. Dai, S. M. Hayden, G. Aeppli, T. G. Perring, and F. Doğan, Nature (London) **395**, 580 (1998).

[65] H. A. Mook and F. Doğan, Nature (London) **401**, 145 (1999).

[66] H. A. Mook, P. Dai, F. Doğan, and R. D. Hunt, Nature **404**, 729 (2000).

[67] M. Arai, T. Nishijima, Y. Endoh, T. Egami, S. Tajima, K. Tomimoto, Y. Shiohara, M. Takahashi, A. Garrett, and S. M. Bennington, Phys. Rev. Lett. **83**, 608 (1999).

[68] P. Bourges, Y. Sidis, H. F. Fong, L. P. Regnault, J. Bossy, A. Ivanov, and B. Keimer, Science **288**, 1234 (2000).

[69] H. A. Mook, P. Dai, and F. Doğan, Phys. Rev. Lett. **88**, 097004 (2002).

[70] H. A. Mook and B. C. Chakoumakos, Jour. Superconductivity, **10**, 389 (1997).

[71] C. Howald, H. Eisaki, N. Kaneko, M. Greven, and A. Kapitulnik, Phys. Rev. B **67**, 014533 (2003); A. Kapitulnik, A. Fang, C. Howald, and M. Greven, `cond-mat/0407743`.

[72] A. Ino, C. Kim, M. Nakamura, T. Yoshida, T. Mizokawa, Z.-X. Shen, A. Fujimori, T. Kakeshita, H. Eisaki, and S. Uchida, Phys. Rev. B **62**, 4137 (2000).

[73] A. Ino, C. Kim, M. Nakamura, T. Yoshida, T. Mizokawa, A. Fujimori, Z.-X. Shen, T. Kakeshita, H. Eisaki, and S. Uchida, Phys. Rev. B **65**, 094504 (2002).

[74] A. Ino, T. Mizokawa, K. Kobayashi, A. Fujimori, T. Sasagawa, T. Kimura, K. Kishio, K. Tamasaku, H. Eisaki, and S. Uchida, Phys. Rev. Lett. **81**, 2124 (1998).

[75] X. J. Zhou, P. Bogdanov, S. A. Kellar, T. Noda, H. Eisaki, S. Uchida, Z. Hussain, and Z.-X. Shen, Science **286**, 268 (1999).

[76] X. J. Zhou, T. Yoshida, S. A. Kellar, P. V. Bogdanov, E. D. Lu, A. Lanzara, M. Nakamura, T. Noda, T. Kakeshita, H. Eisaki, S. Uchida, A. Fujimori, Z. Hussain, and Z.-X. Shen, Phys. Rev. Lett. **86**, 5578 (2001).

[77] M. I. Salkola, V. J. Emery, and S. A. Kivelson, Phys. Rev. Lett. **77**, 155 (1996).

[78] V. J. Emery, S. A. Kivelson, and O. Zachar, Phys. Rev. B **56**, 6120 (1997).

[79] P. Wróbel, A. Maciąg, and R. Eder, `cond-mat/0408703`.

[80] A. Ino, T. Mizokawa, A. Fujimori, K. Tamasaku, H. Eisaki, S. Uchida, T. Kimura, T. Sasagawa, and K. Kishio, Phys. Rev. Lett. **79**, 2101 (1997).

[81] T. Noda, H. Eisaki, and S. Uchida, Science **286**, 265 (1999).

[82] K. Yamada, K. Kurahashi, T. Uefuji, M. Fujita, S. Park, S.-H. Lee, and Y. Endoh, Phys. Rev. Lett. **90**, 137004 (2003).

[83] N. Harima, J. Matsuno, A. Fujimori, Y. Onose, Y. Taguchi, and Y. Tokura, Phys. Rev. B **64**, 220507 (2001).

[84] T. Kimura, K. Hatsuda, Y. Ueno, R. Kajimoto, H. Mochizuki, H. Yoshizawa, T. Nagai, Y. Matsui, A. Yamazaki, and Y. Tokura, Phys. Rev. B **65**, 020407(R) (2002).

[85] S. Larochelle, A. Mehta, L. Lu, P. K. Mang, O. P. Vajk, N. Kaneko, J. W. Lynn, L. Zhou, and M. Greven, Phys. Rev. B **71**, 024435 (2005).

[86] J. M. Tranquada, D. J. Buttrey, V. Sachan, and J. E. Lorenzo, Phys. Rev. Lett. **73**, 1003 (1994).

[87] J. M. Tranquada, Y. Kong, J. E. Lorenzo, D. J. Buttrey, D. E. Rice, and V. Sachan, Phys. Rev. B **50**, 6340 (1994).

[88] J. E. Lorenzo, J. M. Tranquada, D. J. Buttrey and V. Sachan, Phys. Rev. B **51**, 3176 (1995).

[89] J. M. Tranquada, J. E. Lorenzo, D. J. Buttrey, and V. Sachan, Phys. Rev. B **52**, 3581 (1995).

[90] J. M. Tranquada, P. Wochner, and D. J. Buttrey, Phys. Rev. Lett. **79**, 2133 (1997).

[91] J. M. Tranquada, P. Wochner, A. R. Moodenbaugh, and D. J. Buttrey, Phys. Rev. B **55**, R6113 (1997).

[92] P. Wochner, J. M. Tranquada, D. J. Buttrey, and V. Sachan, Phys. Rev. B **57**, 1066 (1998).

[93] A. T. Boothroyd, P. G. Freeman, D. Prabhakaran, A. Hiess, M. Enderle, J. Kulda, and F. Altorfer, Phys. Rev. Lett. **91**, 257201 (2003).

[94] P. G. Freeman, A. T. Boothroyd, D. Prabhakaran, M. Enderle, and C. Niedermayer, Phys. Rev. B **70**, 024413 (2004).

[95] K. Ishizaka, Y. Taguchi, R. Kajimoto, H. Yoshizawa, and Y. Tokura, Phys. Rev. B **67**, 184418 (2003).

[96] C. H. Chen, S-W. Cheong, and A. S. Cooper, Phys. Rev. Lett. **71**, 2461 (1993).

[97] E. D. Isaacs, G. Aeppli, P. Zschack, S-W. Cheong, H. Williams, and D. J. Buttrey, Phys. Rev. Lett. **72**, 3421 (1994).

[98] A. Vigliante, M. von Zimmermann, J. R. Schneider, T. Frello, N. H. Andersen, J. Madsen, D. J. Buttrey, D. Gibbs, and J. M. Tranquada, Phys. Rev. B **56**, 8248 (1997).

[99] K. Ishizaka, T. Arima, Y. Murakami, R. Kajimoto, H. Yoshizawa, N. Nagaosa, and Y. Tokura, Phys. Rev. Lett. **92**, 196404 (2004).

[100] J. Li, Y. Zhu, J. M. Tranquada, K. Yamada, and D. J. Buttrey, Phys. Rev. B **67**, 012404 (2003).

[101] J. Zaanen and P. B. Littlewood, Phys. Rev. B **50**, 7222 (1994).

[102] Ya-Sha Yi, Zhi-Gang Yu, A. R. Bishop, and J. T. Gammel, Phys. Rev. B **58**, 503 (1998); R. J. McQueeney, A. R. Bishop, Ya-Sha Yi, and Z. G. Yu, J. Phys.: Condens. Matter **12**, 317 (2000).

[103] J. H. Jung, D.-W. Kim, T. W. Noh, H. C. Kim, H.-C. Ri, S. J. Levett, M. R. Lees, D. McK. Paul, and G. Balakrishnan, Phys. Rev. B **64**, 165106 (2001).

[104] K. Yamamoto, K. Ishizaka, E. Saitoh, S. Shinomori, T. Tanabe, T. Katsufuji, and Y. Tokura, Phys. Rev. B **67**, 014414 (2003).

[105] C. Hess, B. Büchner, M. Hücker, R. Gross, and S-W. Cheong, Phys. Rev. B **59**, R10397 (1999).

[106] A. P. Ramirez, P. L. Gammel, S-W. Cheong, D. J. Bishop, and P. Chandra, Phys. Rev. Lett. **76**, 447 (1996).

[107] S.-W. Cheong, H. Y. Hwang, C. H. Chen, B. Batlogg, L. W. Rupp, Jr., and S. A. Carter, Phys. Rev. B **49**, 7088 (1994).

[108] T. Katsufuji, T. Tanabe, T. Ishikawa, Y. Fukuda, T. Arima, and Y. Tokura, Phys. Rev. B **54**, R14230 (1996).

[109] T. Katsufuji, T. Tanabe, T. Ishikawa, S. Yamanouchi, Y. Tokura, T. Kakeshita, R. Kajimoto, and H. Yoshizawa, Phys. Rev. B **60**, R5097 (1999).

[110] M. Satake, K. Kobayashi, T. Mizokawa, Fujimori, T. Tanabe, T. Katsufuji, and Y. Tokura, Phys. Rev. B **61**, 15515 (2000).

[111] J. Zaanen and A. M. Oleś, Ann. Phys. (Leipzig) **5**, 224 (1996).

[112] L. F. Feiner, J. H. Jefferson and R. Raimondi, Phys. Rev. B **53**, 8751 (1996).

[113] T. Mizokawa and A. Fujimori, Phys. Rev. B **56**, 11920 (1997).

[114] Z. G. Yu, J. Zang, J. T. Gammel, and A. R. Bishop, Phys. Rev. B **57**, R3241 (1998).

[115] A. Sadori and M. Grilli, Phys. Rev. Lett. **84**, 5375 (2000).

[116] J. Lorenzana and G. Seibold, Phys. Rev. Lett. **89**, 136401 (2002).

[117] B. Büchner, M. Breuer, and A. Freimuth, and A. P. Kampf, Phys. Rev. Lett. **73**, 1841 (1994).

[118] B. Normand and A. P. Kampf, Phys. Rev. B **64**, 024521 (2001).

[119] A. P. Kampf, D. J. Scalapino, and S. R. White, Phys. Rev. B **64**, 052509 (2001).

[120] J. M. Tipper and K. J. E. Vos, Phys. Rev. B **67**, 144511 (2003).

[121] D. M. King, Z.-X. Shen, D. S. Dessau, B. O. Wells, W. E. Spicer, A. J. Arko, D. S. Marshall, J. DiCarlo, A. G. Loeser, C. H. Park, E. R. Ratner, J. L. Peng, Z. Y. Li, and R. L. Greene, Phys. Rev. Lett. **70**, 3159 (1993).

[122] N. P. Armitage, F. Ronning, D. H. Lu, C. Kim, A. Damascelli, K. M. Shen, D. L. Feng, H. Eisaki, Z.-X. Shen, P. K. Mang, N. Kaneko, M. Greven, Y. Onose, Y. Taguchi, and Y. Tokura, Phys. Rev. Lett. **88**, 257001 (2002).

[123] T. Yoshida, X. J. Zhou, T. Sasagawa, W. L. Yang, P. V. Bogdanov, A. Lanzara, Z. Hussain, T. Mizokawa, A. Fujimori, H. Eisaki, Z.-X. Shen, T. Kakeshita, and S. Uchida, Phys. Rev. Lett. **91**, 027001 (2003).

[124] T. Tohyama and S. Maekawa, Phys. Rev. B **49**, 3596 (1994).

[125] R. J. Gooding, K. J. E. Vos, and P. W. Leung, Phys. Rev. B **50**, 12866 (1994).

[126] T. Tohyama and S. Maekawa, Phys. Rev. B **67**, 092509 (2003).

[127] T. Tohyama, Phys. Rev. B **70**, 174517 (2004).

[128] D. Duffy and A. Moreo, Phys. Rev. B **52**, 15607 (1995).

[129] B. Normand and A. P. Kampf, Phys. Rev. B **65**, 020509 (2002).

[130] M. Fleck, A. I. Lichtenstein, and A. M. Oleś, Phys. Rev. B **64**, 134528 (2001).

[131] A. Himeda, T. Kato, and M. Ogata, Phys. Rev. Lett. **88**, 117001 (2002).

[132] C. T. Shih, T. K. Lee, R. Eder, C.-Y. Mou, and Y. C. Chen, Phys. Rev. Lett. **92**, 227002 (2004).

[133] T. Kato and M. Kato, J. Phys. Soc. Jpn. **69**, 3972 (2000).

[134] K. Rościszewski and A. M. Oleś, J. Phys.: Condens. Matter **15**, 8363 (2003).

[135] K. Yonemitsu, A. R. Bishop, and J. Lorenzana, Phys. Rev. Lett. **69**, 965 (1992).

[136] K. Yonemitsu, A. R. Bishop, and J. Lorenzana, Phys. Rev. B **47**, 8065 (1993); *ibid.* **47**, 12059 (1993).

[137] A. Dobry, A. Greco, J. Lorenzana, and J. Riera, Phys. Rev. B **49**, 505 (1994); J. Lorenzana and A. Dobry Phys. Rev. B **50**, 16094 (1994).

[138] V. I. Anisimov, M. A. Korotin, J. Zaanen, and O. K. Andersen, Phys. Rev. Lett. **68**, 345 (1992).

[139] E. Dagotto, T. Hotta, and A. Moreo, Phys. Reports **344**, 1 (2001) and references therein.

[140] E. Pavarini, I. Dasgupta, T. Saha-Dasgupta, O. Jepsen, and O. K. Andersen Phys. Rev. Lett. **87**, 047003 (2001).

[141] G. Kotliar and A. E. Ruckenstein, Phys. Rev. Lett. **57**, 1362 (1986).

[142] R. Frésard and P. Wölfle, J. Phys.: Condens. Matter **4**, 3625 (1992).

[143] R. Frésard and W. Zimmermann, Phys. Rev. B **58**, 15288 (1998).

[144] B. Möller and P. Wölfle, Phys. Rev. B **48**, 10320 (1993).

[145] R. Doradziński and J. Spałek, Phys. Rev. B **56**, R14239 (1997); *ibid.* **58**, 3293 (1998).

[146] H. Hasegawa, Phys. Rev. B **56**, 1196 (1997).

[147] R. Frésard and G. Kotliar, Phys. Rev. B **56**, 12909 (1997).

[148] A. Klejnberg and J. Spałek, Phys. Rev. B **57**, 12041 (1998); *ibid.* **61**, 15542 (2000);

[149] R. Frésard and M. Lamboley, J. Low Temp. Phys. **126**, 1091 (2002).

[150] L. F. Feiner and A. M. Oleś, Phys. Rev. B **71**, 144422 (2005).

[151] R. Frésard and P. Wölfle, Int. J. Mod. Phys. B **6**, 685 (1992); *ibid.* 3087(E) (1992).

[152] T. Li, P. Wölfle, and P. J. Hirschfeld, Phys. Rev. B **40**, 6817 (1989).

[153] J. W. Negele and H. Orland, *Quantum Many Particle Systems*, Addison-Wesley 1988.

[154] W. H. Press, S. A. Teukolsky, W. T. Vetterling, and B. P.Flannery, *Numerical Recipes in Fortran 77: The Art of Scientific Computing*, Cambridge University Press, Cambridge 1992.

[155] P. Wróbel, A. Maciąg, and R. Eder, `cond-mat/0408578`.

[156] J. B. Grant and A. K. McMahan, Phys. Rev. B **46**, 8440 (1992).

[157] H. Eskes, A. M. Oleś, M. B. J. Meinders, and W. Stephan, Phys. Rev. B **50**, 17980 (1994).

[158] J. Kanamori, Prog. Theor. Phys. **30**, 257 (1963).

[159] J. Hubbard, Proc. Roy. Soc. (London) A **276**, 238 (1963).

[160] M. C. Gutzwiller, Phys. Rev. Lett. **10**, 159 (1963).

[161] Y. Nagaoka, Phys. Rev. **147**, 392 (1966).

[162] E. H. Lieb, Phys. Rev. Lett. **62**, 1201 (1989).

[163] J. E. Hirsch, Phys. Rev. B **40**, 2354 (1989).

[164] J. E. Hirsch, Phys. Rev. B **43**, 705 (1991).

[165] M. Kollar, R. Strack, and D. Vollhardt, Phys. Rev. B **53**, 9225 (1996).

[166] J. C. Slater, H. Statz, and G. F. Koster, Phys. Rev. **91**, 1323 (1953).

[167] J. H. Van Vleck, Rev. Mod. Phys. **25**, 220 (1953).

[168] L. M. Roth, Phys. Rev. **149**, 306 (1966).

[169] K. I. Kugel and D. I. Khomskii, Sov. Phys. JETP **37**, 725 (1973).

[170] M. Cyrot and C. Lyon-Caen, J. Phys. (Paris) **36**, 253 (1975).

[171] S. Inagaki, J. Phys. Soc. Jpn. **39**, 596 (1975).

[172] A. Klejnberg and J. Spałek, Phys. Rev. B **61** 15542 (2000).

[173] L. Didukh, Yu. Skorenkyy, V. Hankevych, and O. Kramar, Phys. Rev. B **64**, 144428 (2001).

[174] A. Koga, Y. Imai, and N. Kawakami, Phys. Rev. B **66**, 165107 (2002).

[175] S. Florens, A. Georges, G. Kotliar, and O. Parcollet, Phys. Rev. B **66**, 205102 (2002).

[176] Y. Ōno, M. Potthoff, and R. Bulla, Phys. Rev. B **67**, 035119 (2003).

[177] A. Liebsch, Phys. Rev. Lett. **91**, 226401 (2003).

[178] A. Koga, N. Kawakami, T. M. Rice, and M. Sigrist, Phys. Rev. Lett. **92**, 216402 (2004).

[179] A. Liebsch, Phys. Rev. B **70**, 165103 (2004).

[180] S. Florens and A. Georges, Phys. Rev. B **70**, 035114 (2004).

[181] W. Gill and D. J. Scalapino, Phys. Rev. B **35**, 215 (1987).

[182] J. Spałek, A. M. Oleś, and K. A. Chao, Physica A **97**, 552 (1979).

[183] J. Kuei and R. T. Scalettar, Phys. Rev. B **55**, 14968 (1997).

[184] J. E. Hirsch, Phys. Rev. B **56**, 11022 (1997).

[185] H. Sakamoto, T. Momoi, and K. Kubo, Phys. Rev. B **65**, 224403 (2002).

[186] S. Q. Shen, X. C. Xie, and F. C. Zhang, Phys. Rev. Lett. **88**, 027201 (2002).

[187] A. M. Oleś, Phys. Rev. B **28**, 327 (1983).

[188] M. Daghofer, A. M. Oleś, and W. von der Linden, Phys. Rev. B **70**, 184430 (2004).

[189] J. D. Jorgensen, B. Dabrowski, Shiyou Pei, D. R. Richards, and D. G. Hinks, Phys. Rev. B **40**, 2187 (1989).

[190] P. G. Radaelli, D. G. Hinks, A. W. Mitchell, B. A. Hunter, J. L. Wagner, B. Dabrowski, K. G. Vandervoort, H. K. Viswanathan, and J. D. Jorgensen, Phys. Rev. B **49**, 4163 (1994).

[191] M. E. J. Newman and G. T. Barkema, *Monte Carlo Methods in Statistical Physics*, Oxford University Press 1999.

[192] L. F. Feiner, A. M. Oleś, and J. Zaanen, Phys. Rev. Lett. **78**, 2799 (1997).

[193] R. Frésard, M. Raczkowski, and A. M. Oleś, Phys. Stat. Sol. (b) **242**, 370 (2005).

[194] J. Zaanen and A. M. Oleś, Phys. Rev. B **48**, 7197 (1993).

[195] F. Mack and P. Horsch, Phys. Rev. Lett. **82**, 3160 (1999).

[196] T. Hotta and E. Dagotto, Phys. Rev. Lett. **92**, 227201 (2004).

[197] M. Raczkowski and A. M. Oleś, Phys. Rev. B **66**, 094431 (2002).

[198] P. Kuiper, J. van Elp, G. A. Sawatzky, A. Fujimori, S. Hosoya, and D. M. de Leeuw, Phys. Rev. B **44**, 4570 (1991).

[199] H. Eisaki, S. Uchida, T. Mizokawa, H. Namatame, A. Fujimori, J. van Elp, P. Kuiper, and G. A. Sawatzky, S. Hosoya, H. Katayama-Yoshid, Phys. Rev. B **45**, 12513 (1992).

[200] J. Bała, A. M. Oleś, and J. Zaanen, Phys. Rev. B **61**, 13573 (2000).

[201] J. S. Griffith, *The Theory of Transition Metal Ions*, Cambridge University Press, Cambridge, 1971.

[202] A. E. Bocquet, T. Mizokawa, T. Saitoh, H. Namatame, and A. Fujimori, Phys. Rev. B **46**, 3771 (1992).

[203] P. Mahadevan, K. Sheshadri, D. D. Sarma, H. R. Krishnamurthy, and R. Pandit, Phys. Rev. B **55**, 9203 (1997).

[204] J. B. Grant and A. K. McMahan, Physica C **162**, 1439 (1989).

[205] P. Kuiper, J. van Elp, D. E. Rice, D. J. Buttrey, H.-J. Lin, and C. T. Chen, Phys. Rev. B **57**, 1552 (1998).

[206] B. P. Stojkovic, Z. G. Yu, A. L. Chernyshev, A. R. Bishop, A. H. Castro Neto, and N. Grønbech-Jensen, Phys. Rev. B **62**, 4353 (2000).

Glossary

μSR	muon spin rotation, 5
1D	one-dimensional, 1
2D	two-dimensional, 2
AF	antiferromagnetic, 1
AIPES	angle-integrated photoemission spectroscopy, 5
ARPES	angle-resolved photoemission spectroscopy, 5
Ba-LSCO	$La_{2-x-y}Ba_ySr_xCuO_4$, 7
BC	bond-centered, 3
BIS	bremsstrahlung-isochromat spectroscopy, 119
BSCCO	$Bi_2Sr_2CaCu_2O_{8+\delta}$, 10
CDW	charge-density wave, 48
CPT	Cluster Perturbation Theory , 3
DBC	diagonal bond-centered, 25
DDH	doubly degenerated Hubbard, 4
DMFT	Dynamical Mean Field Theory, 3
DMRG	Density Matrix Renormalization Group, 3
DOS	density of states, 4
DSC	diagonal site-centered, 24
DW	domain wall, 1
ED	Exact Diagonalization, 3
Eu-LSCO	$La_{2-x-y}Eu_ySr_xCuO_4$, 7
FM	ferromagnetic, 14
FS	Fermi surface, 12
HA	Hartree Approximation, 3
HDBC	half-filled diagonal bond-centered, 132
HDSC	half-filled diagonal site-centered, 66

HF	Hartree-Fock, 1
HTT	high-temperature tetragonal, 7
HVBC	half-filled vertical bond-centered, 131
HVSC	half-filled vertical site-centered, 45
IC	incommensurate, 5
KR	Kotliar and Ruckenstein, 55
LBCO	$La_{2-x}Ba_xCuO_4$, 7
LCO	$La_2CuO_{4+\delta}$, 8
LHB	Lower Hubbard Band, 43
LNO	$La_2NiO_{4+\delta}$, 13
LSCO	$La_{2-x}Sr_xCuO_4$, 1
LSNO	$La_{2-x}Sr_xNiO_4$, 2
LTO	low-temperature orthorhombic, 6
LTT	low-temperature tetragonal, 6
NCCO	$Nd_{2-x}Ce_xCuO_4$, 13
Nd-LSCO	$La_{2-x-y}Nd_ySr_xCuO_4$, 2
NMR	nuclear magnetic resonance, 5
NQR	nuclear quadruple resonance, 5
NSNO	$Nd_{2-x}Sr_xNiO_4$, 13
PM	paramagnetic, 2
QMC	Quantum Monte Carlo, 3
QP	quasiparticle, 10
SB	slave-boson, 4
SBA	Slave-Boson Approximation, 3
SC	site-centered, 3
SDW	spin-density wave, 4
SRI SB	spin-rotation-invariant slave-boson, 4
STM	scanning tunneling microscopy, 5
TEM	transmission electron microscopy, 5
UHB	Upper Hubbard Band, 43
UPS	ultraviolet photoemission, 5
VBC	vertical bond-centered, 25

VMC	Variational Monte Carlo, 37
VSC	vertical site-centered, 24
XAS	x-ray-absorption, 119
XPS	x-ray photoemission, 5
YBCO	$YBa_2Cu_3O_{6+\delta}$, 9
Zn-LSCO	$La_{2-x}Sr_xCu_{1-y}Zn_yO_4$, 8